

Tunable Mean-Field and Beyond Mean-Field Interaction in a Coherently Coupled Bose-Einstein Condensate

Roy Eid

▶ **To cite this version:**

Roy Eid. Tunable Mean-Field and Beyond Mean-Field Interaction in a Coherently Coupled Bose-Einstein Condensate. Optics [physics.optics]. Université Paris-Saclay, 2025. English. ⟨NNT : 2025UPASP129⟩. ⟨tel-05351608⟩

HAL Id: tel-05351608

https://pastel.hal.science/tel-05351608v1

Submitted on 6 Nov 2025

HAL is a multi-disciplinary open access archive for the deposit and dissemination of scientific research documents, whether they are published or not. The documents may come from teaching and research institutions in France or abroad, or from public or private research centers.

L'archive ouverte pluridisciplinaire **HAL**, est destinée au dépôt et à la diffusion de documents scientifiques de niveau recherche, publiés ou non, émanant des établissements d'enseignement et de recherche français ou étrangers, des laboratoires publics ou privés.



HAL Authorization

THESE DE DOCTORAT

NNT : 2025UPASP129

Tunable Mean-Field and Beyond Mean-Field Interaction in a Coherently Coupled Bose-Einstein Condensate

Interaction Réglable de Champ Moyen et au-delà du Champ Moyen pour un Condensat de Bose-Einstein dans un mélange cohérent de spin

Thèse de doctorat de l'université Paris-Saclay

École doctorale n° 572 : Ondes et matière (EDOM)
Spécialité de doctorat: Physique
Graduate School: Physique. Référent : Institut d'Optique

Thèse préparée dans les unités de recherche **Université Paris-Saclay, Institut d'Optique Graduate School, CNRS, Laboratoire Charles Fabry, 91127, Palaiseau, France**, sous la direction de **Thomas BOURDEL**, chargé de recherche CNRS

Thèse soutenue à Paris-Saclay, le 14 octobre 2025, par

Roy EID

Composition du jury

Membres du jury avec voix délibérative

Frédéric CHEVY Professeur, École Normale Supérieure de Paris Laboratoire de Physique de l'ENS	Président & Rapporteur
Franck PEREIRA DOS SANTOS Directeur de Recherche, Sorbonne Université Laboratoire Temps Espace	Rapporteur
Christine GUERLIN Maîtresse de conférences, Sorbonne Université Laboratoire Kastler Brossel	Examinatrice
Patrick CHEINET Chargé de recherche CNRS, Université Paris-Saclay Laboratoire Aimé Cotton	Examinateur

Membres du jury sans voix délibérative

Thomas BOURDEL Directeur de recherche CNRS, Université Paris-Saclay Laboratoire Charles Fabry	Directeur de thèse

Contents

Contents 3

Remerciements 7

Résumé en français 9

General Introduction 15

1 Theoretical Foundations 21
- 1.1 Chapter Introduction . . . 21
- 1.2 Atomic Properties of ^{39}K . . . 22
  - 1.2.1 Fine Structure . . . 22
  - 1.2.2 Hyperfine Structure . . . 23
  - 1.2.3 Zeeman Splitting . . . 24
- 1.3 Interatomic Interactions and Feshbach Resonances . . . 26
  - 1.3.1 Types of Interactions Between Two Alkali Atoms . . . 26
  - 1.3.2 Interatomic Potentials . . . 28
  - 1.3.3 Influence of Bound States on Scattering Length . . . 30
  - 1.3.4 Multichannel Scattering and Feshbach Resonances . . . 31
- 1.4 From Two-Body to Many-Body Interactions . . . 34
  - 1.4.1 Contact Interactions in the Dilute Limit . . . 34
  - 1.4.2 Mean-Field Description and Gross–Pitaevskii Equation . . . 35
  - 1.4.3 Three-Body Recombination and Atom Losses . . . 36
  - 1.4.4 BEC in Cigar-Shaped Trap: Length Scales and Interaction Regimes 36
  - 1.4.5 Beyond Mean-field Energy . . . 38
- 1.5 Radio-Frequency Coupling Between Zeeman Sublevels in ^{39}K . . . 39
  - 1.5.1 RF Coupling and Dressed-State Picture . . . 39
  - 1.5.2 Coherent Rabi Oscillations and Pulses . . . 40
  - 1.5.3 Adiabatic Passage and Dressed-State Preparation . . . 41
  - 1.5.4 Two-Body Scattering in the Dressed-State Basis . . . 43
- 1.6 Chapter Conclusion . . . 47

2 Experimental Setup and Magnetic Field Stabilization 49
- 2.1 Chapter Introduction . . . 49
- 2.2 Laser Cooling and Optical Setup for Potassium-39 . . . 50
  - 2.2.1 Brief Description of the Cooling Sequence . . . 50
  - 2.2.2 D1 and D2 Optical Table . . . 53

2.3 Magnetic Field Stabilization Technique for Cold Atom Experiments 57
2.3.1 Required Stability for Precision Control 58
2.3.2 Overview of the Old Magnetic Field Control Setup 59
2.3.3 Magnetic Field Noise Characterization 61
2.3.4 System Improvements and Filtering 65
2.3.5 Correlation Measurements 67
2.3.6 Active Magnetic Field Compensation Circuit 69
2.3.7 Ambient Noise Correction 73
2.3.8 Final Ramsey Magnetic Field Characterization 74
2.3.9 Feedback Correction of Residual 50 Hz and Harmonics 76
2.3.10 Characterizing Noise Spectrum 77
2.4 Chapter Conclusion 80

3 Mean-Field Description of an RF-Dressed Bose-Einstein Condensate 81
3.1 Chapter Introduction 81
3.2 Mean-Field Energy Functional in the Dressed Basis 82
3.3 Equation of State and Spin Composition 84
3.4 Physical Interpretation and Low-Density Expansion 85
3.5 Mean-Field Energy: Exact vs Perturbative in Density 87
3.6 Previous Observation in the Low Density Regime 90
3.7 Experimental Protocol for Measuring Population and Nonlinear Behavior of the Interaction Energy 91
3.8 Comparison with Theoretical Predictions 94
3.9 Chapter Conclusion 95

4 Beyond Mean-Field Energy in RF-Dressed BEC and Quantum Droplets 97
4.1 Chapter Introduction 97
4.2 Theoretical Approach 99
4.3 Mechanical stability 103
4.4 Experimental Attempt for Exploring the Droplet Regime 105
4.4.1 Experimental Procedure Description 105
4.4.2 Timing Optimization for Axial Trap Release 107
4.4.3 Estimating Expansion Due to Quantum Pressure and Timing Errors 108
4.4.4 Experimental Determination of the Stability Condition 109
4.5 Chapter Conclusion 113

5 BEC Tunneling Through Single and Double Optical Barriers Using a DMD 115
5.1 Chapter Introduction 115
5.2 Atom Tunneling and Experimental Setup 116
5.2.1 Overview on Quantum Tunneling and DMD 116
5.2.2 Digital Micromirror Device Properties 119
5.2.3 Dipole Potential and Optical Setup 120
5.2.4 Experimental Procedure 126
5.3 Experimental Results of the BEC Tunneling Experiment 131
5.3.1 Single Barrier Transmission: Classical vs Quantum Regime 131
5.3.2 Single Barrier Transmission: Barrier Height vs Barrier Width . . . 134
5.3.3 Double Barrier Transmission: Atomic Fabry-Pérot 136
5.4 Chapter Conclusion 138

General Conclusion and Perspectives **141**

List of Figures **143**

List of Tables **151**

Publications **153**

Bibliography **179**

Remerciements

Il est difficile de clore une thèse sans prendre un moment pour exprimer toute ma gratitude envers celles et ceux qui ont marqué ces dernières années de leur présence, leur aide, leur soutien et leur bienveillance.

Je tiens tout d'abord à remercier chaleureusement mon encadrant, Thomas Bourdel. C'est lui qui m'a donné l'opportunité en m'accueillant pour un stage de master et qui a cru en moi dès le début. Je lui suis profondément reconnaissant pour sa patience, sa pédagogie et le temps qu'il a toujours pris pour m'expliquer, même à plusieurs reprises. Son esprit rigoureux et pragmatique, sa disponibilité constante, que ce soit pour un dépannage, une préparation de présentation, une discussion scientifique ou un simple échange humain et réconfortant, ont été précieux. Merci pour tout.

Je remercie aussi Rosa Tualle-Brouri, responsable du Master, grâce à qui j'ai pu intégrer la formation en physique quantique. Son soutien et sa confiance m'ont permis de saisir l'opportunité de commencer cette thèse et de démarrer un nouveau chapitre en France. Je lui en suis très reconnaissant.

Je souhaite remercier sincèrement les doctorants avec qui j'ai eu la chance de travailler : Alfred Hammond et Lucas Lavoine. Leur implication dès les premières années a permis de poser les fondations d'une expérience robuste, sur laquelle j'ai pu m'appuyer pendant toute ma thèse. Leurs propositions ont ouvert de nouvelles perspectives ; leurs explications m'ont éclairé. Un immense merci à Sara Tiengo, avec qui j'ai partagé deux années de travail intensif. Son engagement, sa bonne humeur, son humour et sa persévérance ont été essentiels pour faire avancer l'expérience et pour rendre cette période à la fois productive et agréable.

Merci également à tous les étudiants en stage avec qui j'ai travaillé : Clément, Luca, Florian, Nathan et enfin Maé Levy, future doctorante sur la manip, à qui je souhaite le meilleur pour la suite.

Je tiens à remercier les membres de mon comité de suivi, Frédéric Druon et Aurélien Perrin, pour leur écoute bienveillante, leurs conseils avisés et leur accompagnement tout au long de ces trois années.

Un grand merci à tous les membres permanents du groupe Gaz Quantiques : Isabelle Bouchoule, David Clément, Denis Boiron, Marc Cheneau, Chris Westbrook, Alain Aspect,

Thomas Chalopin et Vincent Josse. Merci pour les échanges chaleureux pendant les réunions, les idées inspirantes et votre passion communicative pour la recherche.

Merci aussi à tous les doctorants, stagiaires et collègues du laboratoire, pour les bons moments partagés, les discussions, les repas, les bières et les instants simples mais précieux qui donnent du souffle au quotidien de la thèse.

Je remercie l'atelier d'électronique, en particulier Marc Apfel et Gwenaël Brulin, pour leur aide précieuse dans la réalisation du circuit de stabilisation du champ magnétique. Leurs conseils techniques, leur disponibilité et leur expérience ont été essentiels.

Un merci tout particulier à Patrick Georges, directeur du laboratoire, pour son implication, sa disponibilité et son soutien constant envers les doctorants.

Je tiens également à remercier sincèrement les membres de mon jury pour avoir accepté d'évaluer ce travail et d'avoir pris le temps de le lire avec attention. Merci à Patrick Cheinet, Franck Pereira Dos Santos, Frédéric Chevy, Christine Guerlin. Je leur suis reconnaissant.

Je n'oublie pas non plus les amis rencontrés au fil de ces années. Votre présence, vos encouragements, vos sourires et vos conversations m'ont permis de garder le cap, même dans les moments les plus exigeants.

Un immense merci à ma famille, ma source inépuisable de force et d'amour. En particulier, mes parents et ma sœur, vous n'êtes pas seulement une famille, vous êtes le socle sur lequel j'ai pu construire ce parcours. Merci pour votre soutien inconditionnel, vos mots réconfortants, vos prières silencieuses et votre confiance.

Finalement, un grand merci à Sally, qui, même si elle vient d'un domaine totalement différent, a toujours pris le temps de m'écouter, que ce soit quand je parlais sans cesse de physique ou quand je me plaignais du moindre détail. Sa patience, son humour et son soutien constant ont beaucoup compté pendant ces années.

Résumé en français

Dans cette thèse, je présente les résultats de mon travail de doctorat dans le domaine des gaz quantiques et des atomes ultrafroids. Cette introduction générale débute par un bref panorama des fondements de la mécanique quantique, en partant des limites de la physique classique face à plusieurs expériences clés, limites qui ont conduit au développement de la théorie quantique. J'évoque des jalons allant des contributions précoces d'Einstein jusqu'aux expériences d'Alain Aspect, lauréat du prix Nobel de physique en 2022, au début de ma thèse. Je présente ensuite quelques exemples d'effets quantiques macroscopiques, prédits par la théorie et observés expérimentalement. Puis j'illustre le rôle central des interactions dans divers systèmes physiques, en mettant l'accent sur les atomes ultrafroids et les condensats de Bose–Einstein (BEC). Après ces éléments de contexte, je précise les objectifs de nos recherches et propose un résumé du contenu de chaque chapitre.

Fondements de la mécanique quantique

À la fin du XIX^{e} siècle, la mécanique classique et l'électromagnétisme ne parvenaient pas à rendre compte de plusieurs résultats expérimentaux. Par exemple, les interférences de la double fente de Young, le problème du rayonnement du corps noir, qui prédisait une énergie divergente aux courtes longueurs d'onde (la catastrophe ultraviolette), ainsi que l'effet photoélectrique, demeurait inexpliqué par la théorie ondulatoire classique. De plus, les raies de spectres atomiques et la diffusion des rayons X révélaient des comportements exigeant un nouveau cadre théorique.

En 1900, Max Planck résolut le problème du corps noir en introduisant l'idée que l'énergie est émise par des quanta discrets d'énergie $h\nu$ [1]. En 1905, Albert Einstein étendit cette idée pour expliquer l'effet photoélectrique, en proposant que la lumière est constituée de particules, les photons [2]. En 1923, Arthur Compton montra que les rayons X diffusent sur les électrons comme des particules [3]. En 1913, Niels Bohr proposa un modèle de l'atome d'hydrogène où les électrons occupent des orbites quantifiées, expliquant ainsi les raies spectrales discrètes [4]. Plus tard, en 1924, Louis de Broglie introduisit l'idée que des particules comme les électrons possèdent également des propriétés ondulatoires, de longueur d'onde $\lambda = h/p$ [5].

Entre 1925 et 1926, Heisenberg, Born et Jordan élaborèrent la mécanique matricielle, tandis que Schrödinger formula la mécanique ondulatoire et introduisit sa célèbre équation décrivant les particules par des fonctions d'onde [6, 7, 8]. En 1927, Heisenberg énonça également le principe d'incertitude, selon lequel la position et la quantité de mouvement ne peuvent pas être connues simultanément [9].

Niels Bohr introduisit le principe de complémentarité, stipulant qu'un système quantique peut manifester un comportement ondulatoire ou corpusculaire selon la mesure effectuée, mais jamais les deux simultanément [10]. Dirac en proposa plus tard une synthèse en affirmant que la nature choisit l'issue lors de la mesure [11]. D'autres avancées majeures suivirent. L'expérience de Stern–Gerlach (1922) met en évidence la quantification du moment cinétique [12]. En 1925, Pauli formule le principe d'exclusion, interdisant à deux électrons de partager le même état quantique [13]. La même année, Uhlenbeck et Goudsmit introduisirent l'idée de spin de l'électron comme nouvelle propriété quantique [14].

En 1928, Dirac unifia la mécanique quantique et la relativité restreinte, prédit l'antimatière et établit un nouveau formalisme pour la théorie quantique. Son équation décrivit correctement le spin de l'électron et mena en 1932 à la découverte du positron par Carl Anderson [15]. Le débat philosophique autour de la théorie quantique se poursuivit. En 1935, Einstein, Podolsky et Rosen disputaient que la mécanique quantique pourrait être incomplète [16]. En 1964, John Bell montra que si le monde obéit à la fois à la localité et au réalisme, certaines inégalités statistiques, dites inégalités de Bell, doivent être satisfaites [17]. Or, la mécanique quantique prévoit leur violation pour des particules intriquées. Au début des années 1980, Alain Aspect et son équipe testèrent ces inégalités à l'aide de photons intriqués et les mirent en évidence [18].

Phases quantiques macroscopiques de la matière

La physique moderne a révélé que des effets quantiques, à l'échelle atomique, peuvent émerger à des échelles macroscopiques. L'un des premiers exemples est la supraconductivité, découverte en 1911 par Heike Kamerlingh Onnes [19]. En 1957, Bardeen, Cooper et Schrieffer en proposèrent une théorie microscopique fondée sur la formation de paires d'électrons se comportant comme un fluide quantique [20, 21]. Cette théorie, dite BCS, expliqua des propriétés clés des supraconducteurs, dont l'effet Meissner et la quantification des lignes de flux magnétique [22].

Un autre phénomène quantique macroscopique est la superfluidité. En 1937, Kapitza à Moscou [23], et indépendamment John Allen et Don Misener à Toronto [24], découvrirent que l'hélium-4 s'écoule sans viscosité en dessous d'une température critique proche de 2,17 K. En 1972, Osheroff, Richardson et Lee mirent en évidence une phase superfluide dans l'hélium-3 [25]. Lars Onsager avait auparavant prédit que la circulation dans un

superfluide est quantifiée [26], prédiction confirmée par les observations de Rayfield et Reif sur des anneaux de vortex dans l'hélium-4 [27].

En 1980, Klaus von Klitzing découvrit l'effet Hall quantique [28], observant que la résistance Hall d'un gaz d'électrons bidimensionnel, à basse température et fort champ magnétique, prend des valeurs discrètes en unités de h/e^2. Deux ans plus tard, Tsui, Störmer et Gossard mirent en évidence l'effet Hall quantique fractionnaire [29].

La condensation de Bose–Einstein (BEC) constitue un autre exemple majeur d'état quantique macroscopique. Dès 1925, Einstein prédit qu'un gaz de bosons, refroidi à une température ultra-basse, subit une transition de phase vers un unique état quantique de quantité de mouvement nulle. Cet état fut observé pour la première fois en 1995 par Cornell et Wieman, avec des atomes de rubidium-87 refroidis en dessous du microkelvin [30]. Leur travail mit en évidence un pic dans la distribution de la quantité de mouvement, signature de la formation du condensat [31].

Peu après, des BEC furent produits dans d'autres espèces atomiques. L'équipe de Wolfgang Ketterle réalisa un condensat de sodium-23 [32], tandis que l'Université Rice observa des condensats de lithium-7 [33]. En 1998, un BEC d'hydrogène fut démontré [34]. Des BEC de potassium-39 furent obtenus vers 2007 [35], ainsi que des mélanges bi-espèces comme ^{40}K–^{87}Rb [36]. Plus tard, des condensats furent réalisés avec le césium-133 [37], le chrome-52 à interactions dipolaires [38], des alcalino-terreux tels que le strontium-84 [39] et le calcium-40 [40], ainsi que des isotopes d'ytterbium comme ^{170}Yb et ^{174}Yb [41], entre autres.

Interactions dans les atomes ultrafroids et les BEC

Les interactions entre particules sont fondamentales pour comprendre le comportement des systèmes physiques à toutes les échelles. Dans les solides, elles déterminent les structures cristallines et influencent des propriétés physiques et chimiques telles que la compressibilité, le point de fusion ou la conductivité [42]. Par exemple, des forces interparticulaires plus fortes exigent davantage d'énergie (donc des températures plus élevées) pour fondre le solide. Dans les fluides classiques, les interactions gouvernent des propriétés thermodynamiques comme la pression et la viscosité [43]. Dans les plasmas, les forces coulombiennes à longue portée entre ions et électrons engendrent des effets collectifs tels que l'écran de Debye et les oscillations plasma [44]. En physique nucléaire, l'interaction forte lie protons et neutrons (nucléons) au sein du noyau [45]. À l'échelle cosmologique, la gravitation façonne la structure des étoiles et des galaxies [46].

Dans les gaz quantiques ultrafroids, les interactions atomiques peuvent être contrôlées et ajustées, faisant de ces systèmes des plateformes idéales pour explorer la physique quantique à N corps. Dans des condensats de Bose–Einstein dilués, les interactions sont

de courte portée et bien décrites par un seul paramètre : la longueur de diffusion en onde s [47]. On peut alors utiliser un modèle d'interaction de contact. Les résonances de Feshbach permettent de contrôler la longueur de diffusion via un champ magnétique externe, accordant aux gaz ultrafroids un grand avantage pour l'étude des phénomènes collectifs et des transitions de phase [48].

Cette accordabilité a permis la réalisation de solitons de matière dans des BEC, où la dispersion (pression quantique) compense des interactions attractives. En quasi-une dimension, et pour des interactions attractives, Khaykovich *et al.* et Strecker *et al.* ont observé et étudié des solitons brillants dans des BEC de ^{7}Li [49, 50]. À l'inverse, des interactions répulsives soutiennent la formation de solitons sombres, comme démontré dans des expériences sur ^{87}Rb par empreinte de phase [51, 52]. Des travaux récents ont utilisé des quenches d'interaction pour générer des trains de solitons brillants dans des gaz en états habillés [53], et ont exploré des structures solitoniques nouvelles comme les solitons de Peregrine dans des BEC à deux composantes déséquilibrées, ondes de grande amplitude apparaissant puis disparaissant, analogues aux vagues scélérates [54]. Chen *et al.* ont créé des solitons de type Townes dans des gaz de Bose attractifs bidimensionnels, étendant le comportement solitonique au-delà de 1D [55].

Lorsque la longueur de diffusion augmente dans un gaz de Bose, la théorie du champ moyen devient insuffisante et doit être complétée par des effets au-delà du champ moyen (BMF). En 1957, Lee, Huang et Yang ont dérivé la correction de plus bas ordre à l'énergie de champ moyen pour un gaz de Bose à température nulle [56]. Cette correction, d'origine fluctuationnelle, correspond à l'énergie de point zéro des excitations de Bogoliubov [57]. Le groupe de C. Salomon a étudié expérimentalement la dynamique et les propriétés thermodynamiques d'un BEC de ^{7}Li proche du régime fortement corrélé [58]. Plus récemment, la combinaison d'une attraction de champ moyen faible et de fluctuations quantiques répulsives dans un BEC spinoriel a conduit à la formation de gouttelettes quantiques [59]. Cette thèse explore des interactions inédites dans des condensats de Bose–Einstein couplés de manière cohérente, incluant des effets à trois corps et des interactions saturantes au sein de la théorie de champ moyen, ainsi que la formation de gouttelettes quantiques due aux corrections au-delà du champ moyen, et le régime de l'effet tunnel quantique d'atomes ultrafroids non interactifs à travers des barrières optiques.

Plan du manuscrit

Cette thèse a été menée au sein du groupe Gaz Quantiques dirigé par Thomas Bourdel au Laboratoire Charles Fabry, Institut d'Optique Graduate School. J'ai rejoint l'équipe en mars 2021 comme stagiaire de master, en contribuant à la poursuite des travaux initiés par les anciens doctorants Alfred Hammond et Lucas Lavoine [60, 61].

Avant mon arrivée, l'équipe avait déjà installé un dispositif à micro-miroirs numériques (DMD) sur l'expérience, mais il restait à le calibrer et à le caractériser avec les atomes.

Cette calibration a conduit à l'étude de l'effet tunnel quantique d'atomes ultrafroids à travers des barrières optiques [62]. Au début de ma thèse, nous avons mené des simulations numériques pour interpréter les résultats expérimentaux de l'effet tunnel. Je présente cette étude dans le dernier chapitre du manuscrit.

Dans la continuité des travaux antérieurs, nous avons dû améliorer la stabilité du champ magnétique afin d'augmenter la précision et de contrôler les interactions interatomiques. Avec Sara Tiengo, doctorante arrivée après moi, nous avons développé une technique de stabilisation du champ magnétique pour une expérience des atomes froids [63].

À la suite de ces développements techniques, l'objectif principal de ma thèse a été de mesurer l'énergie d'interaction de champ moyen dans un condensat de Bose–Einstein à deux composantes couplé de manière cohérente, puis d'explorer l'émergence du régime de gouttelettes quantiques dans ce système. Sur cette base, je décris brièvement le contenu de chaque chapitre.

Chapitre 1 : Fondements théoriques

Ce chapitre établit les bases théoriques pour décrire un gaz de Bose ultrafroid de ^{39}K. Il couvre la structure atomique, y compris les niveaux hyperfins et Zeeman. J'y rappelle les interactions interatomiques via les potentiels de van der Waals et la théorie de la diffusion, ainsi que les résonances de Feshbach permettant d'ajuster la longueur de diffusion par un champ magnétique. Je présente ensuite brièvement l'approche de champ moyen via l'équation de Gross–Pitaevskii, puis j'aborde les pertes à trois corps, les effets de dimensionnalité dans des pièges allongés et les corrections au-delà du champ moyen à travers le terme de Lee–Huang–Yang. Le chapitre se conclut par une description du couplage radiofréquence, de la préparation des états habillés et des propriétés d'interaction dans la base des états habillés.

Chapitre 2 : Dispositif expérimental et stabilisation du champ magnétique

Le deuxième chapitre décrit le dispositif expérimental permettant de manipuler et de contrôler les atomes de ^{39}K. Après la présentation de la méthode de préparation du BEC, le chapitre introduit une contribution majeure de cette thèse : la stratégie de réduction du bruit de champ magnétique. Cette stratégie s'appuie sur la réalisation d'un circuit électronique avec filtrage passif, compensation active et correction du champ ambiant. Nous calibrons et caractérisons le circuit par des sondes atomiques, interférométrie de Ramsey et spectroscopie d'états habillés, ainsi que par des instruments électroniques, oscilloscope, analyseur de spectre et multimètre numérique. Ce système réduit les fluctuations du champ magnétique en dessous de 100 μG rms, ouvrant la voie à l'étude des interactions dans des gaz de Bose couplés de manière cohérente à faible fréquence Rabi.

Chapitre 3 : Description du champ moyen d'un BEC dans l'état habillé par RF

Dans ce chapitre, nous étudions l'énergie d'interaction de champ moyen d'un condensat de Bose–Einstein habillé de façon cohérente par un champ radiofréquence. Nous développons un cadre théorique pour le fonctionnel d'énergie dans la base des états habillés, dérivons l'équation d'état et analysons la dépendance de l'énergie d'interaction en fonction de la densité, du désaccord en fréquence et de la fréquence de Rabi. Un développement de Taylor à faible densité révèle des termes effectifs à deux et trois corps, tandis que la théorie complète capture des effets de saturation à forte interaction. Des mesures expérimentales de l'énergie de champ moyen dans un BEC de ^{39}K couplé de manière cohérente confirment le caractère non linéaire et saturé de l'énergie en fonction de la densité.

Chapitre 4 : Énergie au-delà du champ moyen dans un BEC dans l'état habillé par RF et gouttelettes quantiques

Ce chapitre explore la formation de gouttelettes quantiques dans un condensat de Bose–Einstein de ^{39}K couplé de manière cohérente. En ajustant l'interaction de champ moyen pour qu'elle soit légèrement attractive et en réglant la fréquence de Rabi afin de rendre l'interaction au-delà du champ moyen (LHY) légèrement répulsive, nous atteignons un régime où l'attraction est équilibrée par les fluctuations quantiques répulsives. La faible énergie caractéristique de ce système pose des défis expérimentaux, discutés en détail dans ce chapitre.

Nos expériences sondent un régime distinct de ceux déjà rapportés pour les gouttelettes quantiques. En particulier, nous travaillons en géométrie unidimensionnelle avec des gouttelettes de taille macroscopique, plus grandes que les gouttelettes 3D typiques. Dans ce régime, la pression quantique est négligeable, contrairement aux études précédentes où elle jouait un rôle central [59]. Cette géométrie et cette échelle facilitent l'imagerie et l'étude directe des gouttelettes.

Chapitre 5 : l'effet tunnel quantique d'un BEC à travers des barrières optiques simples et doubles avec un DMD

Ce chapitre présente le travail expérimental sur le tunnel quantique d'un condensat de Bose–Einstein monocomposante de ^{39}K non interactif à travers des barrières optiques façonnées par un dispositif à micro-miroirs numériques (DMD). Le DMD permet un contrôle spatial du potentiel. En variant la largeur de la barrière par rapport à la longueur d'onde de de Broglie atomique, nous observons une transition du comportement classique au comportement quantique de tunnel, ainsi que des signatures expérimentales d'une interférence de type Fabry–Pérot atomique à travers deux barrières. Nous comparons ces résultats à des simulations de l'équation de Schrödinger, en utilisant une PSF non idéale comme *ansatz* pour le système d'imagerie afin d'interpréter les données.

General Introduction

In this thesis, I present the results of my PhD work in the field of quantum gases and ultracold atoms. This general introduction begins with a brief overview of the foundations of quantum mechanics, starting from the limitations of classical physics in explaining key experiments, which led to the development of quantum theory. I refer to milestones ranging from Einstein's early contributions to the experiments of Alain Aspect, who received the Nobel Prize in Physics in 2022, at the start of my PhD. I then present some examples of macroscopic quantum effects predicted by quantum theory and experimentally observed. Next, I present examples of interactions in various physical systems, emphasizing the central role of interactions in ultracold atoms and Bose–Einstein condensates (BECs). After this general background, I introduce the objectives of our research and provide a summary of the content of each chapter.

Foundations of Quantum Mechanics

At the end of the 19^{th} century, classical mechanics and electromagnetism were unable to explain several experimental results. For example, Young's double-slit interference, the blackbody radiation problem, which predicted infinite energy at short wavelengths (the UV catastrophe), and the photoelectric effect could not be understood using classical wave theory. In addition, atomic line spectra and the scattering of X-rays revealed behaviors that required a new theoretical framework.

In 1900, Max Planck solved the blackbody radiation problem by introducing the idea that energy is emitted in discrete units, or quanta, with energy $h\nu$ [1]. Albert Einstein extended this idea in 1905 to explain the photoelectric effect, proposing that light consists of particles, called photons [2]. In 1923, Arthur Compton showed that X-rays scatter off electrons like particles [3]. In 1913, Niels Bohr proposed a model of the hydrogen atom where electrons occupy quantized orbits, explaining the discrete spectral lines [4]. Later, in 1924, Louis de Broglie introduced the idea that particles like electrons also have wave-like properties, with wavelength $\lambda = h/p$ [5].

Between 1925 and 1926, Heisenberg, Born, and Jordan developed matrix mechanics,

while Schrödinger formulated wave mechanics and introduced his famous equation to describe particles as wavefunctions [6, 7, 8]. In 1927, Heisenberg also formulated the uncertainty principle, which states that position and momentum cannot be measured exactly at the same time [9].

Niels Bohr introduced the principle of complementarity, stating that quantum systems can behave as particles or waves depending on the measurement, but never both at once [10]. Dirac later summarized this by saying that nature chooses the outcome during measurement [11]. Other important developments followed. The Stern–Gerlach experiment in 1922 demonstrated the quantization of angular momentum [12]. Pauli proposed the exclusion principle in 1925, which states that no two electrons can have the same set of quantum numbers [13]. That same year, Uhlenbeck and Goudsmit introduced the idea of electron spin as a new quantum property [14].

In 1928, Dirac combined quantum mechanics with special relativity, predicting the existence of antimatter and introducing a new formalism for quantum theory. His equation accurately described the electron's spin and later led to the discovery of the positron in 1932 by Carl Anderson [15]. The philosophical debate about quantum mechanics continued. In 1935, Einstein, Podolsky, and Rosen argued that quantum mechanics might be incomplete [16]. In 1964, John Bell showed that if the world obeys both locality and realism, then certain statistical inequalities, now called Bell's inequalities, must be satisfied [17]. However, quantum mechanics predicts violations of these inequalities for entangled particles. In the early 1980s, Alain Aspect and his team performed experiments using entangled photons to test Bell's inequalities, which showed clear violations [18].

Macroscopic Quantum Phase of Matter

Modern physics has revealed that quantum effects, which happen at the atomic level, can also emerge at macroscopic scales. One of the earliest examples is superconductivity, discovered in 1911 by Heike Kamerlingh Onnes [19]. In 1957, Bardeen, Cooper, and Schrieffer developed a microscopic theory based on the idea that electrons form pairs and behave as a quantum fluid [20, 21]. This theory, known as BCS theory, explained key properties of superconductors, including the Meissner effect and quantized magnetic flux lines [22].

Another macroscopic quantum phenomenon is superfluidity. In 1937, Kapitsa in Moscow [23], and independently John Allen and Don Misener in Toronto [24], discovered that liquid helium-4 flows without viscosity below a critical temperature near 2.17 K. In 1972, Osheroff, Richardson, and Lee discovered a superfluid phase in helium-3 [25]. Lars Onsager had earlier predicted that circulation in a superfluid should be quantized [26], and this was later observed experimentally by Rayfield and Reif using vortex rings in helium-4 [27].

In 1980, Klaus von Klitzing discovered the quantum Hall effect [28], observing that the Hall resistance in a two-dimensional electron gas at low temperature and strong magnetic field takes discrete values in units of h/e^2. Two years later, Tsui, Störmer, and Gossard observed the fractional quantum Hall effect [29].

Bose–Einstein condensation (BEC) is another prominent example of a macroscopic quantum state. The concept dates back to Einstein in 1925, who predicted that a gas of bosons cooled to an ultra-cold temperature would undergo a phase transition into a single quantum state with zero momentum. This state was first observed experimentally in 1995 by Cornell and Wieman using rubidium-87 atoms cooled below 1 microkelvin [30]. Their work revealed a peak in the momentum distribution of atoms, indicating the formation of a condensate [31].

Soon after, researchers created BECs in other atomic species. Wolfgang Ketterle's group produced a sodium-23 condensate [32], while researchers at Rice University observed lithium-7 condensates [33]. In 1998, hydrogen BEC was demonstrated [34]. Potassium-39 BECs were achieved around 2007 [35], along with dual-species mixtures such as ^{40}K and ^{87}Rb [36]. Later, BECs were realized with cesium-133 [37], chromium-52 with dipolar interactions [38], alkaline-earth atoms like strontium-84 [39] and calcium-40 [40], and ytterbium isotopes such as ^{170}Yb and ^{174}Yb [41], among many others.

Interactions in Ultra-Cold Atoms and BEC

Interactions between particles are fundamental to understanding the behavior of physical systems across all domains of physics. In solids, particle interactions determine crystal structures and influence physical and chemical properties, such as compressibility, melting point, and conductivity [42]. For example, strong interparticle forces require more energy (i.e., higher temperatures) to overcome and melt the solid. In classical fluids, interparticle interactions govern thermodynamic properties such as pressure and viscosity [43]. In plasmas, long-range Coulomb interactions between ions and electrons lead to collective effects such as Debye screening and plasma oscillations [44]. In nuclear physics, the strong nuclear force binds protons and neutrons (nucleons) within atomic nuclei [45]. At cosmological scales, gravitational interactions shape the structure of stars and galaxies [46].

Atomic interactions in ultracold quantum gases can be controlled and tuned, making these systems ideal for exploring many-body quantum physics. In dilute Bose–Einstein condensates, interactions are short-range and well described by a single parameter: the s-wave scattering length [47]. This allows the use of a simple contact interaction model. Feshbach resonances enable tuning of the scattering length via an external magnetic field, making ultracold gases versatile systems for studying collective phenomena and phase transitions [48].

This tunability has enabled the realization of matter-wave solitons in Bose–Einstein

condensates, where dispersion (quantum pressure) balances attractive interactions. In quasi-one-dimensional traps with attractive interactions, Khaykovich *et al.* and Strecker *et al.* observed and studied bright solitons in ^{7}Li BECs [49, 50]. Conversely, repulsive interactions support the formation of dark solitons, as demonstrated in experiments with ^{87}Rb using phase imprinting methods [51, 52]. Recent studies have used interaction quenches to generate trains of bright solitons in dressed-state gases [53], and researchers have investigated novel solitonic structures such as Peregrine solitons in imbalanced two-component BEC, high-amplitude waves that appear and vanish, analogous to rogue waves [54]. Chen *et al.* created Townes-like solitons in attractive two-dimensional Bose gases, extending solitonic behavior beyond one dimension [55].

As the scattering length increases in a Bose gas, mean-field theory becomes insufficient to describe the interaction and must be supplemented by beyond-mean-field (BMF) effects. In 1957, Lee, Huang, and Yang derived the leading-order correction to the mean-field energy for a Bose gas at zero temperature [56]. This correction originates from quantum fluctuations and corresponds to the zero-point energy of the Bogoliubov excitations [57]. The group of C. Salomon experimentally investigated both the dynamics and thermodynamic properties of a ^{7}Li BEC near the strongly interacting regime [58]. More recently, the combination of weak mean field attraction and repulsive quantum fluctuations in a spinor BEC led to the formation of quantum droplets [59]. This thesis investigates novel interactions in coherently coupled Bose-Einstein condensates, including three-body and saturating interaction effects within mean-field theory, as well as the formation of quantum droplets arising from beyond-mean-field corrections, and non-interactive ultracold atom tunneling behavior through optical barriers.

Outline of this Manuscript

I conducted this thesis within the Quantum Gases group led by Thomas Bourdel at the Laboratoire Charles Fabry, Institut d'Optique Graduate School. I joined the team in March 2021 as a Master's intern, contributing to the continuation of the work done by former PhD students Alfred Hammond and Lucas Lavoine [60, 61].

The team had already installed a digital micromirror device (DMD) on the experiment before my arrival, but we still needed to calibrate and characterize it using atoms. This calibration led to the work on the ultra-cold atomic quantum tunneling in an optical barrier [62]. At the beginning of my PhD, we worked on numerical simulations to interpret the tunneling experimental results. I present this study in the final chapter of this manuscript.

Building upon previous work, we needed to enhance magnetic field stability to improve the precision of interatomic interactions. Together with Sara Tiengo, a PhD student who joined the group after me, we developed a magnetic field stabilization technique for a cold atom experiment [63].

Following these technical developments, the main focus of my PhD research was to measure the mean-field interaction energy in a coherently coupled two-component Bose–Einstein condensate (BEC), and subsequently investigate the emergence of the quantum droplets regime in this system. Based on this work, I now briefly describe the content of each chapter.

Chapter 1: Theoretical Foundations

This chapter provides the theoretical foundations for describing an ultracold Bose gas of ^{39}K. It covers the atomic structure, including hyperfine and Zeeman levels. I recall interatomic interactions through Van Der Waals potentials and scattering theory, along with Feshbach resonances, which enable the tuning of the scattering length via a magnetic field. I then briefly introduce the mean-field approach using the Gross–Pitaevskii equation, followed by discussions on three-body losses, dimensionality effects in elongated traps, and beyond mean-field corrections via the Lee-Huang-Yang term. The chapter concludes with a description of the radio-frequency coupling, dressed-state preparation, and interaction properties in the dressed basis.

Chapter 2: Experimental Setup and Magnetic Field Stabilization

The second chapter describes the experimental setup used to control and manipulate ^{39}K atoms. After describing the optical table for preparing the BEC, the chapter introduces a major contribution of this thesis: a strategy to reduce magnetic field noise. This strategy includes building an electronic circuit with passive filtering, active compensation, and ambient field correction. We calibrate and characterize the circuit using atomic probes, such as Ramsey interferometry and dressed-state spectroscopy, as well as electronic devices, including an oscilloscope, a spectrum analyzer, and a digital multimeter. This system reduces magnetic field fluctuations below $100\,\mu$G rms, opening the path for the studies on the interaction in coherently coupled Bose gases at low Rabi frequencies.

Chapter 3: Mean-Field Description of an RF-Dressed Bose-Einstein Condensate

In this chapter, we investigate the mean-field interaction energy of a Bose-Einstein condensate coherently dressed by a radio-frequency field. We develop a theoretical framework for the dressed-state energy functional, derive the equation of state, and analyze the dependence of the interaction energy on density, detuning, and Rabi frequency. A low-density Taylor expansion reveals effective two- and three-body terms, whereas the full theory captures saturation effects at high interaction strengths. Experimental measurements of the mean field energy of the coherently coupled ^{39}K BEC confirm the predicted nonlinear and saturated behavior of the energy as a function of density.

Chapter 4: Beyond Mean-Field Energy in RF-Dressed BEC and Quantum Droplets

This chapter explores the formation of quantum droplets in a coherently coupled Bose-Einstein condensate of ^{39}K atoms. By tuning the mean-field interaction to slightly attractive and adjusting the Rabi frequency to tune the repulsive beyond-mean-field interaction (LHY), we reach a regime where attractive interactions balance repulsive quantum fluctuations. The system's low-energy nature presents experimental challenges, which we will discuss in detail in this chapter.

In our experiments, we investigate a new regime distinct from previously reported quantum droplets. Specifically, we work in a one-dimensional geometry with droplets of macroscopic size, larger than typical 3D quantum droplets. In this regime, quantum pressure is negligible, unlike in previous experiments where it played a central role [59]. This geometry and size make it easier to image and study the droplets directly.

Chapter 5: BEC Tunneling Through Single and Double Optical Barriers Using a DMD

This chapter presents the experimental work on quantum tunneling of a non-interacting single-component ^{39}K Bose-Einstein condensate through optical barriers engineered with a Digital Micromirror Device (DMD). The DMD permits spatial control of the potential. By varying the barrier width relative to the atomic de Broglie wavelength, we observe a transition from classical to quantum tunneling behavior, as well as experimental signatures of atomic Fabry-Pérot interference through two barriers. We compare the results with the Schrödinger equation simulations using a non-ideal ansatz PSF for the imaging system to interpret the data.

CHAPTER

Theoretical Foundations 1

1.1 Chapter Introduction

This chapter provides the theoretical background to understand the interactions and dynamics that govern our experiment with ultracold potassium-39 atoms. We begin by reviewing the atomic structure of ^{39}K, including its fine, hyperfine, and Zeeman splitting, which gives rise to a rich energy-level structure that is sensitive to an external magnetic field. This structure permits us to control the atomic spin states via magnetic field control and light coupling, which form the basis of our state preparation and interaction control in a coherently coupled BEC.

We then introduce the different types of interatomic potentials relevant to ultracold alkali atoms, in particular the van der Waals and short-range exchange potentials, which form the singlet and triplet potentials. These, in turn, lead to the open and closed scattering channels involved in Feshbach physics. Their properties determine the scattering behavior of atoms at low energy, where the scattering length fully characterizes interactions in this low-energy limit. In addition, understanding these potentials is crucial for identifying Feshbach resonances to control the scattering length via a magnetic field, which occur when a closed-channel bound state becomes resonant with the open-channel energy threshold.

We then extend our treatment to many-body systems, introducing the contact interaction potential approximation and mean-field theory. This treatment introduces the Gross–Pitaevskii equation (GPE), which governs the dynamics of a weakly interacting Bose-Einstein condensate. We then introduce beyond mean-field corrections, or the Lee-Huang-Yang (LHY) term, which stems from the quantum fluctuation and corresponds to the zero-point energy of the Bogoliubov excitation spectrum .

Finally, we explore the physics of radio-frequency (RF) coupling between two Zeeman sublevels in ^{39}K. We present the dressed-state formalism, discuss Rabi oscillations and adiabatic sweeps, and analyze the transformation of the interaction Hamiltonian into the dressed-state basis. This formalism enables us to control the scattering length, not

only by adjusting the magnetic field, but also by tuning the Rabi coupling and detuning, providing a versatile tool for controlling the internal spin state, the interaction strength, and accessing low-energy regimes, such as those beyond the mean-field energy. This theoretical foundation chapter lays the groundwork for understanding the experimental results presented in the following chapters. It provides the essential tools to understand the physics of coherently coupled Bose gases.

1.2 Atomic Properties of ^{39}K

Potassium-39 (^{39}K) is an alkali with atomic number $Z = 19$, characterized by a single valence electron outside a closed-shell argon-like core. The ground-state electronic configuration is [Ar]$4s^1$, placing the valence electron in the $4s$ orbital. In spectroscopic notation, it corresponds to the symbol $4^2S_{1/2}$.

1.2.1 Fine Structure

The fine structure of potassium 39, shown in Fig. 1.1, arises from spin-orbit coupling, where the electron's spin $\mathbf{S}$ interacts with its orbital angular momentum $\mathbf{L}$. L. H. Thomas introduced this relativistic correction in 1926 [64] to explain the observed fine structure splitting. The corresponding Hamiltonian is:

$$H_{\mathrm{SO}} = \epsilon_{SO}\, \mathbf{L} \cdot \mathbf{S}, \tag{1.1}$$

where ϵ_{SO} is the spin-orbit coupling function that depends on the radial distribution of the electron wavefunction. For the $4p$ excited state, this interaction splits the degenerate $4P$ level into two states with total angular momentum $J = 1/2$ and $J = 3/2$:

$$E_{4P_{1/2}} = E_{4P} - \frac{1}{2}\epsilon_{SO}, \quad E_{4P_{3/2}} = E_{4P} + \frac{1}{2}\epsilon_{SO}. \tag{1.2}$$

Thus, E_{4P} is the energy of the degenerate $4P$ state before accounting for fine structure splitting. It results in two optical transitions from the ground state ($4S_{1/2}$) to the excited states ($4P_{1/2}, 4P_{3/2}$), known as the D1 and D2 lines [65]:

$$\mathrm{D1} : 4S_{1/2} \rightarrow 4P_{1/2}, \quad \lambda_{\mathrm{D1}} \approx 770.108 \text{ nm}, \tag{1.3}$$

$$\mathrm{D2} : 4S_{1/2} \rightarrow 4P_{3/2}, \quad \lambda_{\mathrm{D2}} \approx 766.701 \text{ nm}. \tag{1.4}$$

The energy difference between the $4P_{1/2}$ and $4P_{3/2}$ levels is the fine structure splitting for the first excited state, given by:

$$\Delta E_{\mathrm{fs}} = E_{4P_{3/2}} - E_{4P_{1/2}} \approx h \times 1.72 \text{ THz}. \tag{1.5}$$

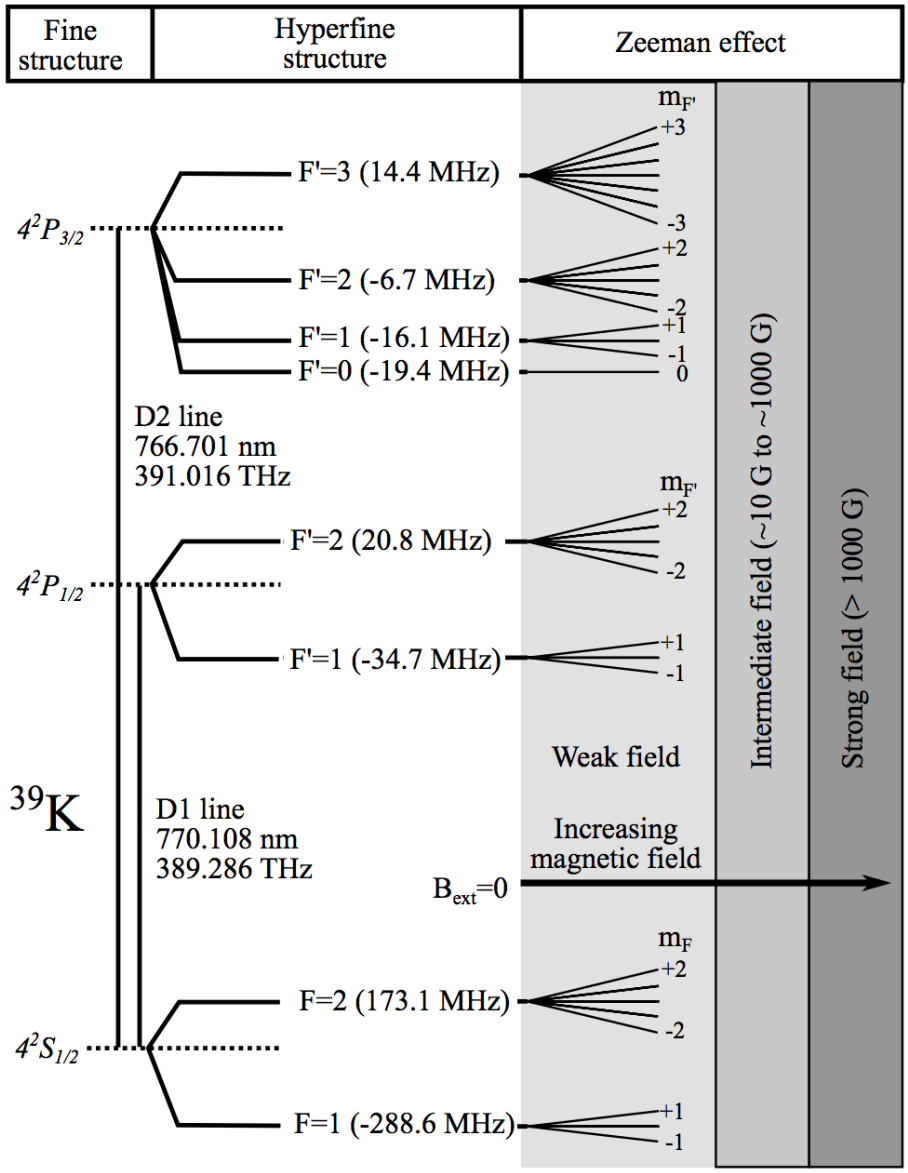


Figure 1.1: Energy level structure of ^{39}K, showing fine structure, hyperfine splitting, and Zeeman level. The Zeeman effect lifts the degeneracy of the hyperfine levels in the presence of an external magnetic field, exhibiting different behaviors in the weak, intermediate, and strong field regimes.

1.2.2 Hyperfine Structure

In addition to fine structure, the nuclear spin of ^{39}K ($I = 3/2$) gives rise to hyperfine interactions by coupling to the total electronic angular momentum $\mathbf{J}$ [66]. The hyperfine Hamiltonian governs the hyperfine structure:

$$H_{hf} = A_{hf}\mathbf{I}\cdot\mathbf{J} + B_{hf}\frac{3(\mathbf{I}\cdot\mathbf{J})^2 + \frac{3}{2}\mathbf{I}\cdot\mathbf{J} - I^2J^2}{2I(2I-1)J(2J-1)} \tag{1.6}$$

where A_{hf} is the magnetic dipole constant, and B_{hf} is the electric quadrupole constant. The first term represents the magnetic dipole interaction, which comes from the coupling between the nuclear magnetic moment and the magnetic field generated by the electrons at the nucleus. This interaction depends on the relative orientation of the nuclear spin $\mathbf{I}$ to the total electronic angular momentum $\mathbf{J}$.

The second term accounts for the electric quadrupole interaction, which describes the interaction of the nuclear quadrupole moment with the electric field gradient produced by the electron cloud. This interaction is present only if the nucleus has a quadrupole moment ($I \geq 1$) and the electronic charge distribution is anisotropic.

For the $4S_{1/2}$ ground state, the orbital angular momentum vanishes ($L = 0$), leading to a spherically symmetric electron charge distribution. Consequently, there is no electric field gradient at the nucleus, and the electric quadrupole interaction vanishes as well ($B_{hf} = 0$). In this case, the hyperfine Hamiltonian simplifies to:

$$H_{hf} = A_{hf}\mathbf{I} \cdot \mathbf{J} \tag{1.7}$$

For the ground state of ^{39}K, the total angular momentum quantum number F takes values: $F = I + J = 2$ and $F = I - J = 1$ and the hyperfine splitting in the ground state is:

$$E_{F=2} = E_{4S_{1/2}} + \frac{3}{4}A_{hf} \text{ and } E_{F=1} = E_{4S_{1/2}} - \frac{5}{4}A_{hf}. \tag{1.8}$$

With $A_{hf}/h \approx 230.86$ MHz, the ground-state hyperfine splitting as shown in Fig.[1.1] is:

$$\Delta E_{\text{hf}} \approx h \times 461.72 \text{ MHz}. \tag{1.9}$$

Since ^{39}K has an integer total spin $(I + J)$ in the ground state, it is a boson and follows Bose-Einstein statistics.

1.2.3 Zeeman Splitting

When an external magnetic field is applied to the potassium atoms, their hyperfine energy levels split due to the Zeeman effect. The Zeeman effect was first observed by Pieter Zeeman in 1896 and later explained using both classical and quantum models [67]. This effect illustrates how atomic levels shift in response to magnetic perturbations. Depending on the relative strength of hyperfine and Zeeman interactions, three regimes arise: the Zeeman regime (weak field), the Breit–Rabi regime (intermediate), and the Paschen–Back regime (strong field) [68, 69]. The Hamiltonian at low field is given by:

$$H_Z = \mu_B \left(g_J \mathbf{J} + g_I \mathbf{I}\right) \cdot \mathbf{B}_{\text{field}}, \tag{1.10}$$

Where μ_B is the Bohr magneton, which defines the strength of the interaction between the total atomic magnetic moment and the external magnetic field. The coefficient g_J is

the Landé g-factor, which describes the coupling strength between the total electronic angular momentum $\mathbf{J}$ and the external magnetic field. Similarly, g_I is the nuclear g-factor, which describes the interaction between the nuclear spin angular momentum $\mathbf{I}$ and the applied magnetic field $\mathbf{B}_{\text{field}}$.

In the Zeeman regime (weak-field limit), where $g_J\mu_B\mathbf{B}_{\text{field}} \ll A_{hf}$, the hyperfine interaction dominates, and the total angular momentum $\mathbf{F} = \mathbf{I} + \mathbf{J}$ remains a good quantum number. The external magnetic field introduces a small perturbation, leading to a linear energy shift: $E = g_F m_F \mu_B \mathbf{B}_{\text{field}}$, where g_F is the hyperfine Landé factor, and m_F is the projection of $\mathbf{F}$ along the field direction.

As the field strength increases, the system enters the Breit-Rabi regime, where $g_J\mu_B\mathbf{B}_{\text{field}} \approx A_{hf}$. The Zeeman interaction becomes comparable to the hyperfine coupling. The total angular momentum F is no longer a good quantum number, and the energy levels split nonlinearly.

In the Paschen-Back regime (strong-field limit), where $g_J\mu_B\mathbf{B}_{\text{field}} \gg A_{hf}$, the Zeeman interaction dominates, fully decoupling $\mathbf{I}$ and $\mathbf{J}$. The good quantum numbers become m_J and m_I, with energy levels splitting linearly: $E = (g_J\mu_B m_J + g_I\mu_N m_I)\,\mathbf{B}_{\text{field}}$.

The hyperfine states $|F, m_F\rangle$ can be decomposed into the uncoupled basis $|m_I, m_S\rangle$ using Clebsch–Gordan coefficients:

$$|F, m_F\rangle = \sum_{m_I, m_S} C^{F m_F}_{I m_I, J m_S} |I, m_I\rangle |J, m_S\rangle. \tag{1.11}$$

This decomposition reveals that each $|F, m_F\rangle$ state is a coherent superposition of electronic spin projections $m_S = \pm 1/2$, which later determines the contributions from singlet and triplet interaction channels.

For ^{39}K, the $F = 1$ manifold states in the uncoupled basis can be written as follows:

$$|F = 1, m_F = 1\rangle = \sqrt{\frac{3}{4}}\left|m_I = \frac{3}{2}, m_S = -\frac{1}{2}\right\rangle - \sqrt{\frac{1}{4}}\left|m_I = \frac{1}{2}, m_S = +\frac{1}{2}\right\rangle \tag{1.12}$$

$$|F = 1, m_F = 0\rangle = \sqrt{\frac{1}{2}}\left|m_I = \frac{1}{2}, m_S = -\frac{1}{2}\right\rangle - \sqrt{\frac{1}{2}}\left|m_I = -\frac{1}{2}, m_S = +\frac{1}{2}\right\rangle \tag{1.13}$$

$$|F = 1, m_F = -1\rangle = \sqrt{\frac{1}{4}}\left|m_I = -\frac{1}{2}, m_S = -\frac{1}{2}\right\rangle - \sqrt{\frac{3}{4}}\left|m_I = -\frac{3}{2}, m_S = +\frac{1}{2}\right\rangle \tag{1.14}$$

Our experiment will later focus on the three Zeeman states of the $F = 1$ manifold, labeled for simplicity as 0, 1, and 2, corresponding respectively to $|1, 1\rangle$, $|1, 0\rangle$, and $|1, -1\rangle$.

We will also plot the energy splittings $E_{10} = E_1 - E_0$ and $E_{21} = E_2 - E_1$, shown in Fig. 1.2. These splittings are relevant for magnetic field noise spectroscopy and precision magnetometry applications, where controlled Zeeman shifts enable high-sensitivity measurements of the magnetic field [70, 71].

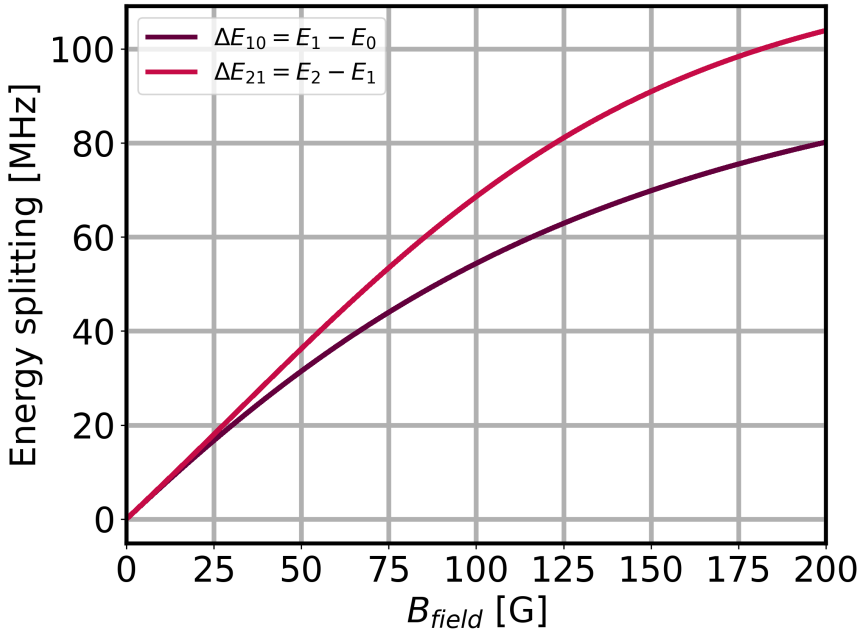


Figure 1.2: Energy splitting between the Zeeman states of the $F = 1$ manifold as a function of the magnetic field. The curves show $\Delta E_{10} = E_1 - E_0$ and $\Delta E_{21} = E_2 - E_1$.

1.3 Interatomic Interactions and Feshbach Resonances

Interactions between neutral atoms are crucial in describing the behavior of ultracold quantum gases, influencing the strength of the Bose-Einstein condensate interaction [72]. This section will provide an overview of the fundamental interaction potential between atoms, analyze their contribution to low-energy scattering, which can form weakly bound molecular states, and discuss the Feshbach resonances [48].

1.3.1 Types of Interactions Between Two Alkali Atoms

The interaction between two neutral alkali atoms arises from a combination of short and long-range interactions, each characterized by distinct potentials and length scales. These

interatomic potentials are essential to understand low-energy scattering phenomena, bound molecular states, and the control of interactions in ultracold gases (Feshbach resonance). Below, we outline the main interaction types relevant to our system :

1. **Van der Waals Interaction**: At large interatomic separation r, two neutral atoms interact via induced dipole-dipole forces. Quantum fluctuations of each atom's electron cloud induce temporary electric dipoles, which in turn polarize the electron cloud of the other atom. The correlated dipoles attract each other, giving rise to a van der Waals potential [73]. In lowest order (second-order perturbation theory):

$$V_{\mathrm{vdW}}(r) = -\frac{C_6}{r^6}, \tag{1.15}$$

where C_6 is the dispersion coefficient. For potassium-39, $C_6 \approx 3897$ atomic units. The characteristic van der Waals interaction range is:

$$r_{\mathrm{vdW}} = \frac{1}{2}\left(\frac{2mC_6}{\hbar^2}\right)^{1/4} \tag{1.16}$$

Where m is the atomic mass. In our case, $r_{\mathrm{vdW}} \approx 77\, a_0$, meaning that for interatomic distances larger than r_{vdW} the interaction is well described by the $-C_6/R^6$ tail, below this distance short-range exchange forces dominate.

2. **Exchange Interaction**: As two potassium atoms approach more closely ($6-10\ a_0$), their electron wavefunctions overlap significantly. The simple $-C_6/r^6$ form is no longer accurate at this short range. Instead, the quantum exchange effects, which dominate, arise from the indistinguishability of electrons and the Pauli exclusion principle [74]. Suppose the two 4s valence electrons occupy an antisymmetric spin state (singlet state). Their spatial wavefunction can be symmetric, allowing the electrons to delocalize between the two nuclei and lower their energy. In contrast, if the electron spins are aligned (triplet state), the spatial wavefunction must be antisymmetric, which keeps the electrons apart and leads to an effective repulsion.

3. **Magnetic Dipole-Dipole Interaction**: A magnetic dipole-dipole interaction arises from the magnetic moments associated with the electron spins. Although significantly weaker than the short-range interaction potentials, it plays a role in magnetic ultracold atomic gases [75]. The magnetic dipole-dipole interaction potential between two magnetic dipoles separated by a distance r is given by:

$$V_{\mathrm{dd}}(r) = \frac{\mu_0}{4\pi}\frac{\mu_B^2 g_J^2}{r^3} \tag{1.17}$$

Where μ_0 is the permeability of free space, μ_B is the Bohr magneton, and r is the separation distance between atoms. The characteristic length scale for the magnetic dipole-dipole interaction, known as the dipolar length r_{dd}, is defined as:

$$r_{\mathrm{dd}} = \frac{\mu_0 \mu_B^2 g_J^2 m}{4\pi\hbar^2} \tag{1.18}$$

The van der Waals and exchange potential length scale for potassium-39 are larger than the dipolar length, which is around $0.02\,a_0$. The Magnetic dipole-dipole interactions are negligible compared to contact interactions. However, they can become relevant when dealing with highly magnetic atoms (such as dysprosium or erbium). Therefore, in the case of potassium atoms, we focus only on the Van der Waals and Short-Range Exchange potential, which are more relevant to our experiment.

1.3.2 Interatomic Potentials

The interatomic potential between two Alkali atoms in ultracold gases is a combination of the two molecular ground-state potentials: the singlet potential $V_S(r)$ and the triplet potential $V_T(r)$. These potentials arise from van der Waals interactions at long range and exchange interactions at short range. Crucially, the form of the potential depends on the symmetry of the two-electron spin configuration, i.e., whether the total electronic spin projection is symmetric (triplet) or antisymmetric (singlet).

In the case of ^{39}K, the total interaction potential is not a pure singlet or triplet but rather a mixture of the two. As previously discussed, these hyperfine states can be decomposed into the uncoupled basis $|m_I, m_S\rangle$ using Clebsch–Gordan coefficients (Eq. 1.11). As a result, each $|F, m_F\rangle$ state contains contributions from both $m_S = +1/2$ and $m_S = -1/2$, meaning the wavefunction has contributions from both singlet and triplet scattering channels.

The singlet potential $V_S(r)$ exhibits a deeper and more negative well than the triplet potential $V_T(r)$. The triplet potential $V_T(r)$ is relatively shallow. For potassium-39 dimers, the well depth of the singlet potential (corresponding to the ground state $X\,^1\Sigma_g^+$) is approximately $D_e \sim 4450$ cm^{-1}, as determined from high-resolution spectroscopy [76]. In contrast, the triplet potential (associated with the $a\,^3\Sigma_u^+$ state) is much less deep, with a depth on the order $D_e \sim 244.5$ cm^{-1} [77].

Different potential models are used to describe interatomic potentials in ultracold gases. Among the most commonly used are the Born–Oppenheimer potentials and the phenomenological Lennard-Jones potential. The Born–Oppenheimer approach offers a detailed and accurate description of molecular potential by treating the electronic energy as a fixed background and solving the nuclear Schrödinger equation [78]. For potassium-39 dimer ($^{39}K_2$), both the singlet and triplet Born–Oppenheimer potentials have been determined and characterized in the literature.

We illustrate these potentials in Fig. 1.3. In particular, Falke et al. conducted precision measurements of the energy gap between asymptotic and well-bound levels in the electronic

ground state ($X\,^1\Sigma_g^+$) of the $^{39}K_2$ molecule, achieving a Level of accuracy of MHz. These measurements allowed for better refinement of ground-state potentials and determined scattering lengths for both the singlet and triplet potentials [79].

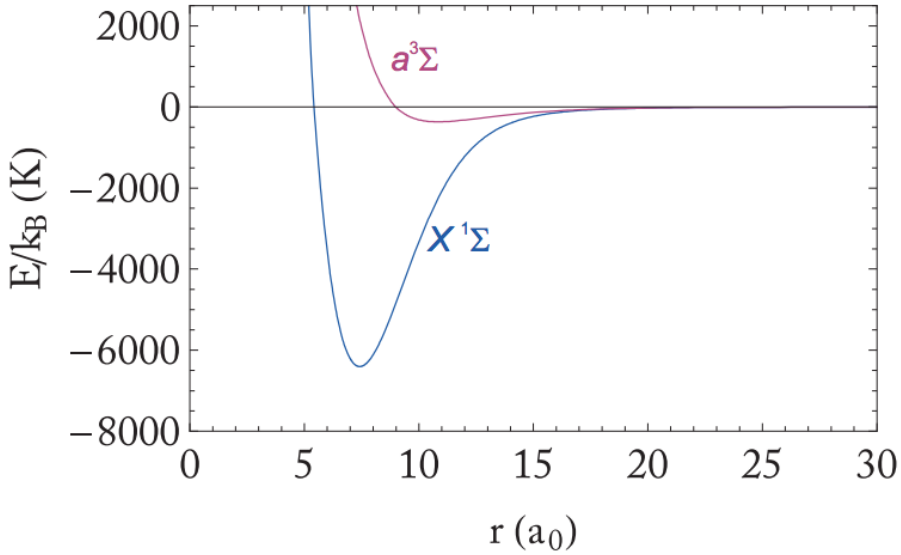


Figure 1.3: Potential energy curves described by the Born Oppenheimer approximation, for the singlet ($X\,^1\Sigma_g^+$) and triplet ($a\,^3\Sigma_u^+$) states of the potassium-39 dimer ($^{39}K_2$). Taken from Tiecke et al. [65].

The Lennard-Jones potential, on the other hand, is an empirical model commonly used to describe van der Waals interactions. It is given by:

$$V_{\mathrm{LJ}}(r) = 4\epsilon \left[\left(\frac{\sigma}{r}\right)^{12} - \left(\frac{\sigma}{r}\right)^{6} \right] \tag{1.19}$$

Where:

- ϵ is the depth of the potential well.
- σ is the distance at which the potential is zero.

It combines a short-range repulsive term with a long-range attractive term. While it is not as precise as the Born-Oppenheimer approach for specific molecular states, Lennard-Jones' potential finds wide applications in molecular dynamics simulations. Researchers frequently use this potential to model the behavior of noble gases [80] and predict the structure of molecular crystals [81]. The simplicity of this potential makes it a practical choice in simulations where computational speed is a priority while still providing a reasonable approximation.

1.3.3 Influence of Bound States on Scattering Length

To understand the behavior of the scattering length and its connection to the appearance of molecular bound states, we start with a few key elements from quantum scattering theory. In ultracold gases, we can describe the interactions between atoms using the framework of two-body scattering at low energy. The relative motion of two atoms of mass m interacting through a central potential $V(r)$ is governed by the time-independent Schrödinger equation:

$$\left[-\frac{\hbar^2}{m}\nabla^2 + V(r)\right]\psi(\vec{r}) = E\psi(\vec{r}), \tag{1.20}$$

where E is the relative energy and $\psi(\vec{r})$ is the wavefunction. For large r, where the potential vanishes, the solution for positive energy $E = \hbar^2k^2/m$ takes the asymptotic form:

$$\psi(\vec{r}) \sim e^{i\vec{k}\cdot\vec{r}} + f(k)\frac{e^{ikr}}{r}, \tag{1.21}$$

where $f(k)$ is the scattering amplitude. For s-wave scattering (dominant at ultracold temperatures), the phase shift $\delta_0(k)$, between the incoming and the outgoing wave, characterizes the interaction and defines the scattering length a via:

$$a = -\lim_{k\to 0}\frac{\delta_0(k)}{k}. \tag{1.22}$$

The corresponding low-energy scattering amplitude is:

$$f_0(k) = \frac{1}{k\cot\delta_0(k) - ik} \approx -a \quad \text{for } k \to 0. \tag{1.23}$$

The phase shift also encodes the presence of bound states. The scattering length becomes large and positive when the potential supports a weakly bound molecular state with small binding energy E_b. In the zero-range limit, this relationship takes the universal form:

$$E_b = -\frac{\hbar^2}{ma^2}. \tag{1.24}$$

To illustrate this connection more explicitly, we now consider a simple model: a three-dimensional square-well potential with a range of r_0 and a depth of U_0. This model can capture the essential physics of how bound-state formation affects the scattering length. The scattering length is small and negative when the well is shallow and does not support any bound state. As U_0 increases, the well reaches a critical depth that supports a new bound state just below the continuum, leading to a divergence in the scattering length, which results in a resonance.

The scattering length for this potential is given by:

$$a(U_0) = -r_0\left(\frac{\tan\left(\sqrt{U_0}\,r_0\right)}{\sqrt{U_0}\,r_0} - 1\right). \tag{1.25}$$

Divergences occur whenever $\sqrt{U_0}\, r_0 = (n + \frac{1}{2})\pi$, corresponding to the appearance of a new bound state at zero energy.

Once a bound state appears, the scattering length becomes significant and positive in value. As the potential depth increases, more bound states emerge periodically, causing another divergence and a sign change in the scattering length. We illustrate this pattern in Fig. 1.4.

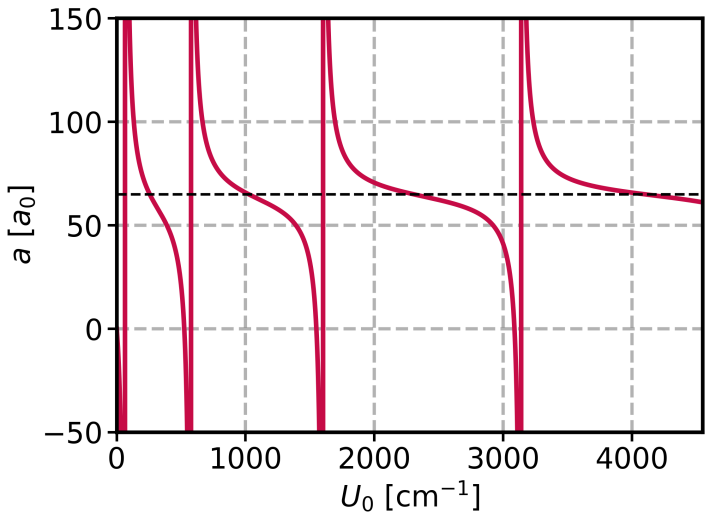


Figure 1.4: Scattering length as a function of potential depth for a square-well potential, showing divergence each time a bound state appears. The horizontal dashed line at $a = r_0$ marks the range of the potential well.

Although the square-well model is simple, it explains the principles underlying the resonance of the scattering length. In real atomic systems, such resonances appear as magnetic Feshbach resonances due to multichannel coupling, where an external magnetic field can tune the energy of a molecular state in a closed channel. To describe this phenomenon, a framework based on multichannel scattering theory is required, which we will discuss briefly in the next section.

1.3.4 Multichannel Scattering and Feshbach Resonances

Collisions between ^{39}K atoms in different hyperfine states involve a complex interplay of spin-dependent potentials and channel couplings. Each hyperfine state $|F, m_F\rangle$ is a superposition of singlet and triplet spin components, Eq. 1.11, and the total interaction potential accounts for this spin mixing as well as the hyperfine and Zeeman contributions as follows:

$$V_{\text{int}}(r) = c_S V_S(r) + c_T V_T(r) + H_{hf} + H_Z, \tag{1.26}$$

where V_S and V_T are the singlet and triplet molecular potentials, and c_S, c_T are coefficients determined by the spin structure of the atomic pair. At ultracold temperatures, the de Broglie wavelength of the atoms is larger than the range of the interaction potential. In this regime, the s-wave scattering dominates, and the multichannel problem should be taken into account.

In multichannel scattering theory, the entrance (or open) channel refers to the pair of atomic states energetically accessible during a collision, typically two atoms in a hyperfine ground state with positive relative kinetic energy. The closed channel consists of pairs of spin states that support a bound molecular state with an energy below the open-channel threshold. The spin-exchange and hyperfine interactions couple the two channels.

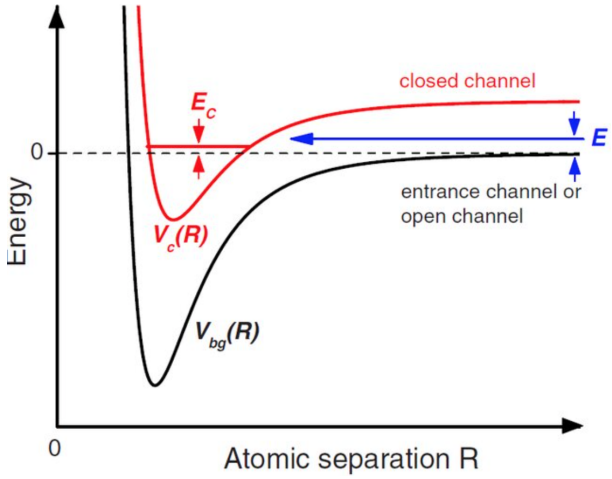


Figure 1.5: Schematic of open and closed channel potentials. A Feshbach resonance occurs when a bound state E_c in the closed channel becomes degenerate with the scattering energy E in the open channel [48].

Even when atoms collide in the open channel, they may undergo a virtual transition to the closed-channel bound state if the bound state energy lies near the continuum threshold. When we tune the magnetic field or, similarly, the bound state energy E_c, if it aligns with the kinetic energy E of the colliding atoms, the two channels couple, and this condition is defined as a Feshbach resonance [48, 47].

Atoms can virtually excite, enter a closed-channel bound state, and then return to the open channel. This resonant coupling modifies the low-energy scattering properties, particularly the s-wave scattering length. Near resonance, the scattering length can be described by:

$$a(B) = a_{\text{bg}} \left(1 - \frac{\Delta}{B - B_0}\right), \tag{1.27}$$

where a_{bg} is the background scattering length far from resonance, B_0 is the resonance position (the field where $a \to \pm\infty$), and Δ is the resonance width. At $B = B_0$, the

scattering length diverges, showing that a closed-channel bound state lies at zero energy. This divergence gives access to regimes such as molecule formation and the emergence of universal few-body phenomena like Efimov states [48].

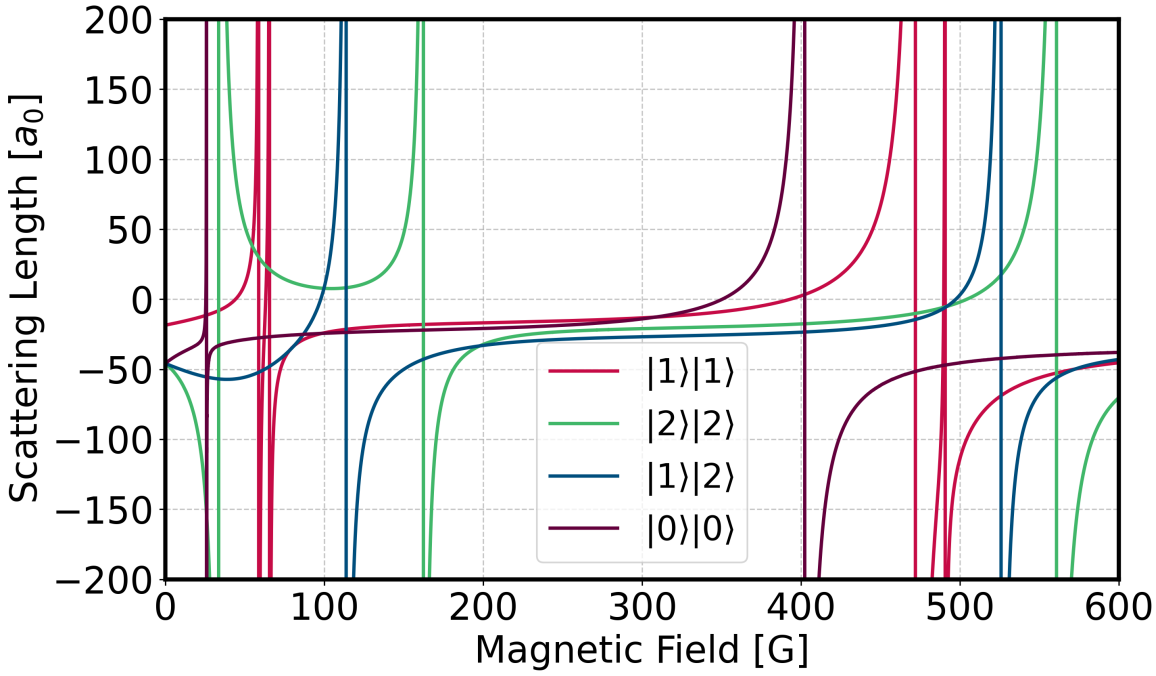


Figure 1.6: Scattering length a_{11}, a_{22}, a_{12} and a_{00} as a function of the magnetic field between the Zeeman states $|0\rangle, |1\rangle, |2\rangle$ of ^{39}K.

A well-characterized Feshbach resonance in ^{39}K occurs near $B_0 = 33.58$ G for atoms prepared in the $|F = 1, m_F = -1\rangle$ state. The resonance is associated with coupling to a bound state in the $|F = 2, m_F = 0\rangle$ closed channel [82].

In our experiments, we prepare atoms in one or two of the three Zeeman states: $|0\rangle$, $|1\rangle$, and $|2\rangle$. We are also interested in the scattering lengths values between the different pairs, particularly $|1\rangle - |1\rangle$, $|2\rangle - |2\rangle$, and $|1\rangle - |2\rangle$ as a function of the magnetic field. For the Final chapter, we are interested in the scattering length for the pair in $|0\rangle - |0\rangle$ around 350 G.

1.4 From Two-Body to Many-Body Interactions

In the previous sections, we demonstrated how a single parameter, the s-wave scattering length a, characterizes the interactions between two atoms in ultracold gases and how it can be tuned using Feshbach resonances. We now extend this understanding to systems with many atoms, which are typical of Bose-Einstein condensates (BECs). How, then, does the simple picture of two-body scattering translate to a quantum degenerate gas composed of thousands or millions of particles? By comparing the different length and energy scales in dilute ultracold gases, we can describe their collective behavior using simple and powerful theoretical tools based on two-body physics.

1.4.1 Contact Interactions in the Dilute Limit

At ultracold temperatures, the thermal de Broglie wavelength $\lambda_{\mathrm{dB}} = h/\sqrt{2\pi m k_B T}$ becomes much larger than the range of the interatomic potential r_{vdW}. This difference justifies replacing the real interaction potential with an effective contact interaction. Moreover, the gas is dilute, meaning that the interparticle spacing $\bar{r} \sim n^{-1/3}$ is also much larger than r_{vdW}, and the probability of three or more atoms coming into close contact is suppressed. Therefore, two-body collisions dominate, and higher-order interactions (three-body or more) are negligible.

In our ultracold gas experiments with ^{39}K, the temperature is typically $T \approx 100\,\mathrm{nK}$, corresponding to a thermal de Broglie wavelength of $\lambda_{\mathrm{dB}} \approx 16700\,a_0$, where a_0 the Bohr radius. The interatomic potential has a characteristic range given by the van der Waals length $r_{\mathrm{vdW}} \approx 77\,a_0$. Thus, the condition $\lambda_{\mathrm{dB}} \gg r_{\mathrm{vdW}}$ is satisfied, allowing us to ignore the detailed structure of the true potential.

The typical density in the center of our trap is $n \approx 2 \times 10^{20}\,\mathrm{m}^{-3}$, so the mean interparticle spacing is $\bar{r} \sim n^{-1/3} \approx 3230\,a_0$, which also satisfies $\bar{r} \gg r_{\mathrm{vdW}}$. Therefore, the gas is dilute, and most interactions involve two-body collisions. It justifies neglecting higher-order few-body interactions in the mean-field theory.

Dimensional analysis shows that a is the only relevant length scale in the low-energy limit. If the relative momentum k of the two particles satisfies $ka \ll 1$, we can replace the interaction potential with a contact pseudopotential V_{pp}, which reproduces the correct scattering length:

$$V_{\mathrm{pp}}(\vec{r}) = g\,\delta(\vec{r})\,\frac{\partial}{\partial r}\,(r\cdot)\,, \quad \text{where} \quad g = \frac{4\pi\hbar^2 a}{m}. \tag{1.28}$$

This potential forces the Bethe-Peierls boundary condition for the relative wavefunction:

$$\varphi(r) \xrightarrow{r\to 0} 1 - \frac{a}{r}, \tag{1.29}$$

Here, $\varphi(r)$ is the radial solution of the two-body Schrödinger equation in the relative coordinate after separating the center of mass and gives rise to the s-wave scattering amplitude:

$$f_0(k) = \frac{1}{k\cot\delta(k) - ik} \approx -\frac{a}{1+ika}. \tag{1.30}$$

In this framework, interactions are effectively pointlike, zero-range, but still produce the correct low-energy physics, as long as we apply an appropriate high-momentum cutoff $\Lambda \sim 1/r_{\text{vdW}}$.

1.4.2 Mean-Field Description and Gross–Pitaevskii Equation

In the many-body context, we describe the condensate using a macroscopic wavefunction $\psi(\vec{r}, t)$, assumed to vary smoothly over the microscopic length scales. It justifies simplifying the two-body interaction to a local contact term:

$$V(\vec{r} - \vec{r}') = g\,\delta(\vec{r} - \vec{r}'), \tag{1.31}$$

where $g = \frac{4\pi\hbar^2 a}{m}$ is the interaction strength determined by the s-wave scattering length a. It leads to the following second-quantized Hamiltonian:

$$\hat{H} = \int d^3\vec{r}\,\hat{\psi}^\dagger(\vec{r})\left(-\frac{\hbar^2}{2m}\nabla^2 + V_{\text{ext}}(\vec{r})\right)\hat{\psi}(\vec{r}) + \frac{g}{2}\hat{\psi}^\dagger(\vec{r})\hat{\psi}^\dagger(\vec{r})\hat{\psi}(\vec{r})\hat{\psi}(\vec{r}), \tag{1.32}$$

where $\hat{\psi}(\vec{r})$ is the bosonic field operator. In the mean-field approximation, we replace the field operator with a classical field $\hat{\psi}(\vec{r}, t) \to \psi(\vec{r}, t)$, leading to the Gross-Pitaevskii energy functional:

$$E_{MF}[\psi] = \int d^3\vec{r}\left[\frac{\hbar^2}{2m}|\nabla\psi|^2 + V_{\text{ext}}(\vec{r})|\psi|^2 + \frac{g}{2}|\psi|^4\right], \tag{1.33}$$

Assuming a uniform cloud of atoms, with a density n, without an external trapping potential, and neglecting quantum pressure (kinetic energy term), the energy per unit volume is given by:

$$\frac{E_{MF}}{V} = \frac{1}{2}gn^2.$$

The corresponding dynamical equation for the condensate wavefunction is known as the nonlinear Schrödinger equation or GPE:

$$i\hbar\frac{\partial\psi}{\partial t} = \left(-\frac{\hbar^2}{2m}\nabla^2 + V_{\text{ext}} + g|\psi|^2\right)\psi. \tag{1.34}$$

The Gross Pitaevskii Equation (GPE) captures the BEC dynamics and has been used to describe vortices, solitons, and collective excitations[83].

1.4.3 Three-Body Recombination and Atom Losses

In ultracold atomic gases, two-body collisions dominate the dynamics under typical dilute conditions. However, at high densities or near a Feshbach resonance where the scattering length $|a|$ becomes large, the three-body recombination rate increases, primarily contributing as a loss mechanism rather than a contribution to the equilibrium energy of the gas.

We can categorize three-body processes as follows:

- **Elastic three-body collisions :** They are usually negligible compared to a 2-body collision and conserve both atom number and energy.
- **Inelastic three-body recombination :** Their effects dominate in experiments, leading to atom loss due to the formation of a molecular bound state.

In an inelastic recombination event, three atoms collide, two bind to form a molecule, and the third carries away the released binding energy. The atom with excess energy typically exceeds the trap depth, and the molecule can no longer be trapped, ejecting both the molecule and the third atom from the trap.

The local atomic density $n(\vec{r}, t)$ decays due to three-body recombination according to the following equation:

$$\frac{dn(\vec{r}, t)}{dt} = -K_3\, n^3(\vec{r}, t), \tag{1.35}$$

Where K_3 is the three-body recombination rate coefficient. Integrating over the trap volume gives the total atom number loss:

$$\frac{dN}{dt} = -L_3 \int d^3r\, n^3(\vec{r}, t). \tag{1.36}$$

At low temperatures, the three-body recombination rate coefficient K_3 depends on the scattering length a. Close to resonances, the scaling is: $K_3 \propto a^4$ [47, 83].

1.4.4 BEC in Cigar-Shaped Trap: Length Scales and Interaction Regimes

A Bose-Einstein condensate confined in an elongated harmonic trap,

$$V_{\text{ext}}(\vec{r}) = \frac{1}{2} m\omega_\perp^2 (x^2 + y^2) + \frac{1}{2} m\omega_z^2 z^2, \tag{1.37}$$

exhibits different behavior due to the interplay between geometry and interactions. In such anisotropic traps, $\omega_\perp \gg \omega_z$, the harmonic oscillator lengths are $a_\perp = \sqrt{\hbar/(m\omega_\perp)}$, and $a_z = \sqrt{\hbar/(m\omega_z)}$. The chemical potential satisfies $\mu = gn(0)$, where $n(0)$ is the peak

density of the atomic cloud, and the condensate wavefunction depends on the ratios μ to trap frequencies.

1. 3D Thomas–Fermi Regime: For $\mu \gg \hbar\omega_\perp, \hbar\omega_z$, interactions dominate and the kinetic energy becomes negligible. The density profile follows an inverted paraboloid:

$$n(\vec{r}) = \frac{\mu}{g}\left(1 - \frac{x^2+y^2}{R_\perp^2} - \frac{z^2}{Z^2}\right), \tag{1.38}$$

valid within the ellipsoidal boundary $\frac{x^2+y^2}{R_\perp^2} + \frac{z^2}{Z^2} \leq 1$. The TF radii are:

$$R_\perp = \sqrt{\frac{2\mu}{m\omega_\perp^2}}, \qquad Z = \sqrt{\frac{2\mu}{m\omega_z^2}}. \tag{1.39}$$

The interplay between the interaction energy and confinement determines the chemical potential :

$$\mu = \frac{\hbar\bar{\omega}}{2}\left(\frac{15Na}{a_{\text{ho}}}\right)^{2/5}, \quad \bar{\omega} = (\omega_\perp^2\omega_z)^{1/3}, \quad a_{\text{ho}} = \sqrt{\frac{\hbar}{m\bar{\omega}}}. \tag{1.40}$$

By integrating the TF profile, we obtain the different energies:

$$E_{\text{total}} = \frac{5}{7}N\mu, \quad E_{\text{trap}} = \frac{3}{7}N\mu, \quad E_{\text{int}} = \frac{2}{7}N\mu. \tag{1.41}$$

2. 1D–3D Crossover Regime: When $\mu \sim \hbar\omega_\perp$, the radial mode is not yet frozen, and the condensate transitions between quasi-1D and 3D. Gerbier *et al.* [84] proposed an interpolation formula:

$$\mu \approx \hbar\omega_\perp\left(1 + \frac{4aN}{a_\perp}\right)^{1/2}. \tag{1.42}$$

This expression recovers:

- the Gaussian ground state for $aN/a_\perp \ll 1$,
- the TF-like behavior when $aN/a_\perp \gg 1$.

The exact density has no simple form but smoothly interpolates between a Gaussian radial envelope and a TF, depending on the interaction strength.

3. Quasi-1D Thomas–Fermi Regime: When $\hbar\omega_z \ll \mu \ll \hbar\omega_\perp$, the radial motion is frozen in its ground state. The effective 1D interaction strength is:

$$g_{1\text{D}} = \frac{g}{2\pi a_\perp^2} = \frac{2\hbar^2 a}{m a_\perp^2}. \tag{1.43}$$

The chemical potential can be written as follows:

$$\mu = \left(\frac{3}{4}Ng_{1\text{D}}\hbar\omega_z\right)^{2/3}. \tag{1.44}$$

The full 3D density is:

$$n(\vec{r}) = \frac{1}{g_{1D}} \left(\mu - \frac{1}{2} m\omega_z^2 z^2 \right) \cdot \frac{1}{\pi a_\perp^2} \exp\left(-\frac{x^2 + y^2}{a_\perp^2} \right), \tag{1.45}$$

We obtain the energy contributions by integrating over the TF axial profile and Gaussian radial confinement:

$$E_{\text{total}} = \frac{3}{5} N\mu, \quad E_{\text{trap}} = \frac{1}{5} N\mu, \quad E_{\text{int}} = \frac{2}{5} N\mu. \tag{1.46}$$

4. 0D Weakly Interacting Regime: If $\mu \ll \hbar\omega_\perp, \hbar\omega_z$, the condensate remains close to the harmonic oscillator ground state. The wavefunction is Gaussian in all directions. The density reads:

$$n(\vec{r}) = \frac{N}{\pi^{3/2} a_\perp^2 a_z} \exp\left(-\frac{x^2 + y^2}{a_\perp^2} - \frac{z^2}{a_z^2} \right). \tag{1.47}$$

The chemical potential approaches the zero-point energy with a mean-field correction:

$$\mu \approx \frac{1}{2}\hbar\omega_\perp + \frac{1}{2}\hbar\omega_z + gn(0), \quad n(0) = \frac{N}{\pi^{3/2} a_\perp^2 a_z}. \tag{1.48}$$

This results in the following approximate energy contributions:

$$E_{\text{total}} \approx \hbar\bar{\omega} + Ngn(0), \quad E_{\text{kin}} \approx \frac{\hbar\bar{\omega}}{2}, \quad E_{\text{trap}} \approx \frac{\hbar\bar{\omega}}{2}, \quad E_{\text{int}} \approx Ngn(0). \tag{1.49}$$

1.4.5 Beyond Mean-field Energy

Beyond the mean-field description, the first quantum correction to the ground state energy of a weakly interacting Bose gas arises from quantum fluctuations around the condensed state. This term represents the sum of the zero-point energies of the Bogoliubov modes. For a single component, Bose gas at zero temperature, the beyond mean field energy term, known as the Lee-Huang-Yang energy, can be written in terms of the dimensionless gas parameter $\sqrt{na^3}$ as follows:

$$\frac{E_{\text{LHY}}}{V} = \frac{1}{2} gn^2 \times \frac{128}{15\sqrt{\pi}} \sqrt{na^3},$$

with $g = 4\pi\hbar^2 a/m$. The LHY term grows more steeply with density than the mean-field term ($\propto n^{5/2}$ vs. n^2), hence becoming relevant when interactions are strong, i.e., when the dimensionless gas parameter approaches 10^{-2}–10^{-1}. However, its derivation strictly assumes the diluteness condition $\sqrt{na^3} \ll 1$ and relies on the validity of the Bogoliubov approximation.

Despite this constraint, several experiments have observed effects beyond the mean-field level by tuning the interaction strength via Feshbach resonances. For instance, the group

of Christophe Salomon measured the equation of state of a homogeneous ^{7}Li BEC and found excellent agreement with the LHY prediction for strong interactions in a single spin component BEC [58].

As a side note, although the healing length $\xi = 1/\sqrt{8\pi na}$ is not central to the derivation of the LHY energy, it carries clear physical significance: it sets the characteristic scale over which the condensate restores its density after a local perturbation. In the context of quantum fluctuations, it also marks the momentum scale ($k \lesssim 1/\xi$) below which Bogoliubov modes significantly contribute to the beyond-mean-field correction, while higher-energy modes become negligible.

1.5 Radio-Frequency Coupling Between Zeeman Sublevels in ^{39}K

This section describes the behavior of a two-level system formed by the Zeeman sublevels $|1\rangle$ and $|2\rangle$ of ^{39}K atoms under radio-frequency (RF) coupling. We introduce the coupled two-level Hamiltonian, its dressed energy eigenstates, and the time evolution, including Rabi oscillations, pulses, and adiabatic sweeps. Those three are essential for preparing internal state mixtures and tuning interactions in our experiment.

1.5.1 RF Coupling and Dressed-State Picture

In the presence of a magnetic bias field B_z, the Zeeman degeneracy is lifted, creating a splitting $\hbar\omega_Z = \hbar|g_F|\mu_B B_z$ between the states $|1\rangle$ and $|2\rangle$. Within typical fields (10–60 G), the splitting lies in the RF domain (7-42 MHz), as shown in Fig. 1.2. An oscillating RF field with frequency ω_{rf} and amplitude B_{rf} perpendicular to B_z can resonantly couple the two states via a magnetic dipole transition. The Rabi frequency quantifies the Rabi coupling strength as:

$$\Omega = \frac{|g_F|\mu_B B_{\text{rf}}}{\hbar},$$

With $B_{\text{rf}} \propto \sqrt{P_{\text{rf}}}$ and P_{rf} is the power of the Radio-Frequency. The RF-driven system is governed by the Hamiltonian in the bare state basis $|1\rangle$ and $|2\rangle$ (in the rotating wave approximation):

$$\hat{H}_{\text{Rabi}} = \frac{\hbar}{2}\begin{pmatrix} \delta & \Omega \\ \Omega & -\delta \end{pmatrix}, \tag{1.50}$$

where $\delta = \omega_{\text{rf}} - \omega_Z$ is the detuning from resonance.

Diagonalizing $\hat{H}_{\text{Rabi}}$ yields the dressed eigenstates:

$$|+\rangle = \cos\left(\frac{\theta}{2}\right)|1\rangle + \sin\left(\frac{\theta}{2}\right)|2\rangle, \qquad |-\rangle = \sin\left(\frac{\theta}{2}\right)|1\rangle - \cos\left(\frac{\theta}{2}\right)|2\rangle, \qquad \cot\theta = \frac{\delta}{\Omega}. \tag{1.51}$$

$$|+\rangle = \sqrt{P_{|1\rangle\to|+\rangle}}|1\rangle + \sqrt{P_{|2\rangle\to|+\rangle}}|2\rangle, \qquad |-\rangle = \sqrt{P_{|1\rangle\to|-\rangle}}|1\rangle - \sqrt{P_{|2\rangle\to|-\rangle}}|2\rangle. \tag{1.52}$$

with eigenenergies $E_{\text{Rabi}|\pm\rangle} = \pm\frac{\hbar}{2}\widetilde{\Omega}$, where $\widetilde{\Omega} = \sqrt{\Omega^2 + \delta^2}$ is the generalized Rabi frequency.

The probability for an atom in the bare state $|2\rangle$ or $|1\rangle$ to be found respectively in the dressed state $|-\rangle$ or $|+\rangle$ is:

$$\cos^2\frac{\theta}{2} = P_{|1\rangle\to|+\rangle} = P_{|2\rangle\to|-\rangle} = \frac{1}{2}\left(1 - \frac{\delta/\Omega}{\sqrt{1+(\delta/\Omega)^2}}\right). \tag{1.53}$$

Similarly, the probability for an atom in the bare state $|2\rangle$ or $|1\rangle$ to be found respectively in the dressed state $|+\rangle$ or $|-\rangle$ is:

$$\sin^2\frac{\theta}{2} = P_{|1\rangle\to|-\rangle} = P_{|2\rangle\to|+\rangle} = \frac{1}{2}\left(1 + \frac{\delta/\Omega}{\sqrt{1+(\delta/\Omega)^2}}\right). \tag{1.54}$$

At resonance ($\delta = 0$), a balanced 50–50 mixture of atoms across the two bare states. As the detuning increases, the overlap becomes asymmetric: for large positive or negative detuning ($|\delta| \gg \Omega$), the bare state aligns predominantly with one of the dressed states, depending on the sign of δ, as shown in Fig. 1.7.

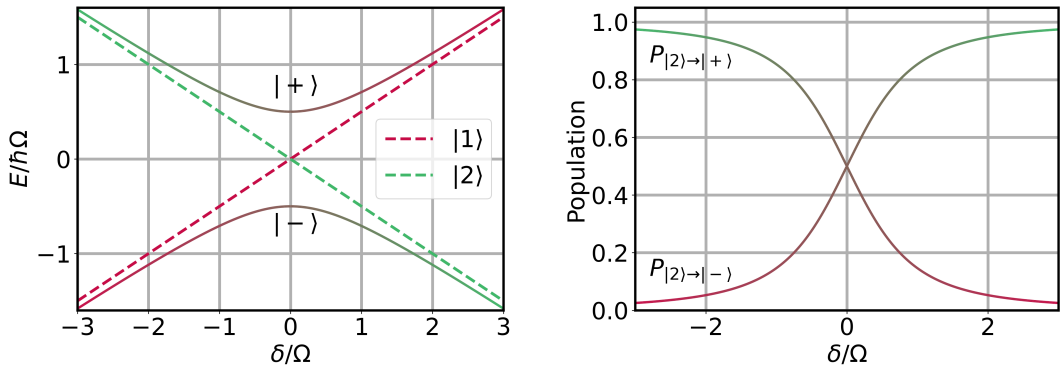


Figure 1.7: (Left) Dressed state energies $E_{\text{Rabi}|\pm\rangle} = \pm\hbar\widetilde{\Omega}/2$ versus detuning. (Right) Projection of the bare state $|2\rangle$ onto the dressed states $|+\rangle$ and $|-\rangle$ as a function of δ/Ω.

1.5.2 Coherent Rabi Oscillations and Pulses

When the system is initially in $|1\rangle$ and subjected to a resonant RF field, the population undergoes sinusoidal oscillations between the two levels:

$$P_{|2\rangle}(t) = \frac{\Omega^2}{\widetilde{\Omega}^2}\sin^2\left(\frac{\widetilde{\Omega}t}{2}\right). \tag{1.55}$$

These are known as Rabi oscillations, as shown in Fig.1.8. On resonance ($\delta = 0 \implies \widetilde{\Omega} = \Omega$), full population inversion occurs with period $2\pi/\Omega$.

By adjusting the pulse duration τ, one can determine the final state:

- A π-pulse ($\tau = \pi/\Omega$) transfers all the population from $|1\rangle$ to $|2\rangle$.
- A $\pi/2$-pulse ($\tau = \pi/(2\Omega)$) creates a coherent superposition $(|1\rangle + |2\rangle)/\sqrt{2}$.

These operations correspond to rotations of the Bloch vector around the x-axis. Since the evolution is not adiabatic, the system does not remain in an eigenstate of the Hamiltonian but oscillates within the bare-state basis. On the Bloch sphere, $|1\rangle$ and $|2\rangle$ lie at the poles, and the state vector precesses around an effective magnetic field.

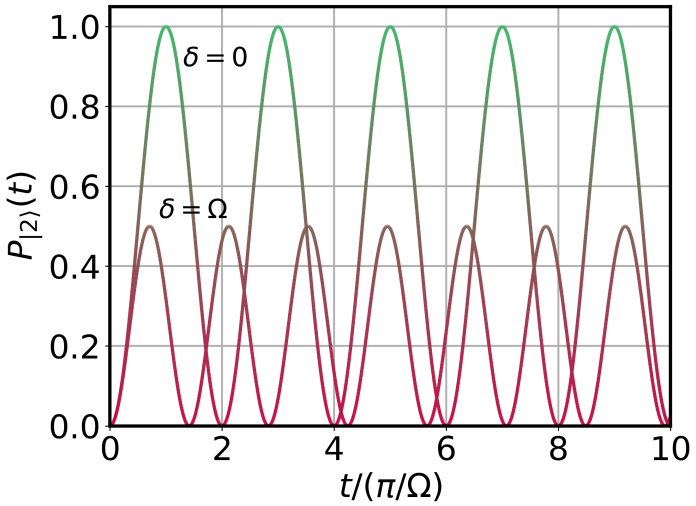


Figure 1.8: Time evolution of the population in state $|2\rangle$ under Rabi coupling for two different detunings: on resonance ($\delta = 0$) and off-resonance ($\delta = \Omega$). The population undergoes full oscillations at the Rabi frequency Ω when $\delta = 0$, leading to complete population transfer. For nonzero detuning, the oscillations occur at the generalized Rabi frequency $\widetilde{\Omega} = \sqrt{\Omega^2 + \delta^2}$ with a lower population transfer. We normalize time to half the Rabi period as $t/(\pi/\Omega)$.

1.5.3 Adiabatic Passage and Dressed-State Preparation

Beyond the regime of Rabi oscillations driven by pulses, coherent state preparation is achieved adiabatically following a dressed eigenstate. This technique involves slowly sweeping the RF frequency, or equivalently the detuning $\delta(t) = \omega_{\mathrm{rf}}(t) - \omega_Z$, across resonance.

Suppose we initially prepare the system in the bare state $|2\rangle$ and sweep the detuning from a large positive value to a large negative value. In that case, the state will evolve along the lower dressed eigenstate $|-\rangle$, resulting in a complete population transfer to $|1\rangle$. This method is known as adiabatic rapid passage, and it enables the preparation of the

dressed state.

The detuning must vary slowly compared to the internal dynamics of the energy gap between dressed states to ensure the adiabatic following. The general adiabaticity condition is:

$$|\dot{\delta}| \ll \delta^2 + \Omega^2, \tag{1.56}$$

This condition ensures that the mixing angle $\theta(t) = \tan^{-1}(\Omega/\delta(t))$ evolves slowly enough for the system to remain in the dressed eigenstate.

Assuming a linear sweep of the form $\delta(t) = \delta_i + \dot{\delta}t$, the sweep rate $\dot{\delta}$ is constant. The crucial constraint occurs when $(\delta = 0)$, where the condition simplifies to:

$$|\dot{\delta}| \ll \Omega^2. \tag{1.57}$$

In this case, if one defines a sweep time t_f for which the detuning is varied linearly from δ_i to δ_f. The total range is $\delta_f - \delta_i$, leading to a sweep rate $\dot{\delta} = (\delta_f - \delta_i)/t_f$, and the adiabaticity condition becomes:

$$t_f \gg \frac{(\delta_f - \delta_i)}{\Omega^2}. \tag{1.58}$$

This condition provides an estimate of the minimum sweep duration for adiabaticity. In our experimental setup, the Rabi frequency $\Omega/2\pi$ can be tuned between 1 kHz and 25 kHz and for the maximum span we do experimentally $(\delta_f - \delta_i) = 18\,\Omega$. Applying the adiabatic condition, the corresponding minimum sweep times are:

- For $\Omega/2\pi = 1$ kHz: $t_f \gg 18/(2\pi \times 1\text{ kHz}) \approx 2.9$ ms,
- For $\Omega/2\pi = 25$ kHz: $t_f \gg 18/(2\pi \times 25\text{ kHz}) \approx 0.12$ ms.

Therefore, for sweep times of a few milliseconds, our system satisfies the adiabaticity criterion over a wide range of Rabi frequencies, ensuring that the atoms follow the dressed eigenstate throughout the sweep and end up in a well-defined internal dressed state.

To illustrate the effect of sweep duration on adiabatic passage, we performed a numerical simulation of the time-dependent Schrödinger equation for a two-level system under a linear frequency sweep, similar to what we do experimentally. The simulation takes a low Rabi frequency of $\Omega/2\pi = 1$ kHz, and initially we start with atoms in the bare state $|2\rangle$. The detuning is linearly swept from $\delta_i = 9\Omega$ to different δ_f over four different total sweep times: $t_f = 1$, 3, 9, and 50 ms. We compute the probability $P_{|2\rangle\to|-\rangle}$ that an atom initially in the bare state $|2\rangle$ ends up in the lower dressed state $|-\rangle$ after the sweep. This gives the projection of the bare state onto the dressed state $|-\rangle$, which is equivalent to $|2\rangle$ at large positive detuning $(\delta_f \gg 0)$ and to $1\rangle$ at large negative detuning $(\delta_f \ll 0)$.

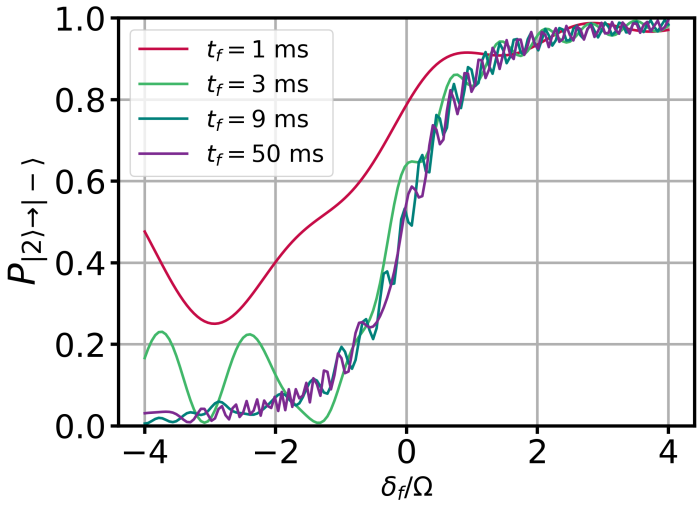


Figure 1.9: Probability of ending in the lower dressed state $|-\rangle$ after a linear RF frequency sweep from $\delta_i = 9\Omega$ to δ_f at a fixed Rabi frequency $\Omega/2\pi = 1$ kHz, for various total sweep durations t_f.

As shown in Fig. 1.9, short sweeps ($t_f = 1$ and 3 ms) fail to satisfy the adiabaticity condition, leading to strong non-adiabatic oscillations and incomplete transfer to the other state. For longer sweeps ($t_f = 9$ ms and 50 ms), the population transfer becomes nearly perfect. To avoid experimental ripples on the sweep curve caused by the abrupt turn-on of the radio-frequency field, we gradually ramp up the RF power. This results in a smoother and more controlled behavior during the sweep.

1.5.4 Two-Body Scattering in the Dressed-State Basis

We analyze how the two-body second-quantized interaction Hamiltonian in the bare state transforms in the dressed-state basis, to describe interactions in a coherently coupled two-component Bose-Einstein condensate. This transformation reveals both elastic and inelastic scattering channels in the dressed basis and allows us to define a tunable interaction strength that depends on the ratio δ/Ω.

We begin with the second-quantized contact interaction Hamiltonian in the bare internal-state basis $\{|1\rangle, |2\rangle\}$:

$$\hat{H}_{\text{int}} = \frac{1}{2}\int d^3\mathbf{r}\left[g_{11}\hat{\psi}_1^\dagger\hat{\psi}_1^\dagger\hat{\psi}_1\hat{\psi}_1 + g_{22}\hat{\psi}_2^\dagger\hat{\psi}_2^\dagger\hat{\psi}_2\hat{\psi}_2 + 2g_{12}\hat{\psi}_1^\dagger\hat{\psi}_2^\dagger\hat{\psi}_2\hat{\psi}_1\right], \tag{1.59}$$

where $g_{ij} = \frac{4\pi\hbar^2 a_{ij}}{m}$ represent the bare interaction strengths, with a_{ij} the s-wave scattering lengths between atoms in internal states i, j.

When a coherent coupling is applied, the single-particle Hamiltonian becomes diagonal in the dressed-state basis. The dressed states $|\pm\rangle$ are superpositions of the bare states $|1\rangle$

and $|2\rangle$. The transformation between field operators in the bare and dressed basis is:

$$\hat{\psi}_1 = \cos\left(\frac{\theta}{2}\right)\hat{\psi}_+ + \sin\left(\frac{\theta}{2}\right)\hat{\psi}_-, \tag{1.60}$$

$$\hat{\psi}_2 = \sin\left(\frac{\theta}{2}\right)\hat{\psi}_+ - \cos\left(\frac{\theta}{2}\right)\hat{\psi}_-. \tag{1.61}$$

Substituting into $\hat{H}_{\text{int}}$ and expanding, we obtain interaction terms written entirely in the dressed basis. These include elastic couplings that preserve the internal state populations and inelastic couplings that allow transitions between dressed states.

The elastic interaction coefficients are:

$$g_{--}^{--} = g_{11}\sin^4\frac{\theta}{2} + g_{22}\cos^4\frac{\theta}{2} + \frac{g_{12}}{2}\sin^2\theta, \tag{1.62}$$

$$g_{++}^{++} = g_{11}\cos^4\frac{\theta}{2} + g_{22}\sin^4\frac{\theta}{2} + \frac{g_{12}}{2}\sin^2\theta, \tag{1.63}$$

$$g_{+-}^{+-} = \frac{g_{11}+g_{22}}{2}\sin^2\theta + 2g_{12}\cos^2\theta. \tag{1.64}$$

The inelastic interaction coefficients, associated with processes such as $|--\rangle \leftrightarrow |+-\rangle$, read:

$$g_{--}^{+-} = \sin\theta\left(-g_{11}\sin^2\frac{\theta}{2} + g_{22}\cos^2\frac{\theta}{2} - g_{12}\cos\theta\right), \tag{1.65}$$

$$g_{++}^{+-} = \sin\theta\left(-g_{11}\cos^2\frac{\theta}{2} + g_{22}\sin^2\frac{\theta}{2} + g_{12}\cos\theta\right), \tag{1.66}$$

$$g_{--}^{++} = \frac{1}{4}(g_{11}+g_{22}-2g_{12})\sin^2\theta. \tag{1.67}$$

To better interpret these expressions, we define the following parameters:

$$\tilde{g} = \frac{g_{11}+g_{22}}{2}, \quad \delta g = \frac{g_{11}-g_{22}}{2}, \quad \bar{g} = \frac{g_{11}+g_{22}-2g_{12}}{4}, \tag{1.68}$$

which we refer to as the mean interaction, interaction asymmetry, and interaction flexibility, respectively.

Applying the previously defined parameters, we rewrite the dressed interaction strengths as follows:

$$\begin{aligned}
g_{--}^{--} &= \tilde{g} - \delta g\cos\theta - \bar{g}\sin^2\theta, & g_{--}^{+-} &= \sin\theta\left(-\delta g + 2\bar{g}\cos\theta\right),\\
g_{++}^{++} &= \tilde{g} + \delta g\cos\theta - \bar{g}\sin^2\theta, & g_{++}^{+-} &= \sin\theta\left(-\delta g - 2\bar{g}\cos\theta\right),\\
g_{+-}^{+-} &= \tilde{g}(1+\cos^2\theta) - 4\bar{g}\cos^2\theta, & g_{--}^{++} &= \bar{g}\sin^2\theta.
\end{aligned}$$

From Eq. 1.53 and 1.54, we can express the trigonometric terms directly in terms of the dimensionless detuning δ/Ω:

$$\cos\theta = \frac{\delta/\Omega}{\sqrt{1+(\delta/\Omega)^2}}, \qquad \cos^2\theta = \frac{(\delta/\Omega)^2}{1+(\delta/\Omega)^2},$$
$$\sin\theta = \frac{1}{\sqrt{1+(\delta/\Omega)^2}}, \qquad \sin^2\theta = \frac{1}{1+(\delta/\Omega)^2}.$$

Substituting these into the previous expressions yields the dressed interaction strength explicitly as a function of δ/Ω:

$$\begin{aligned}
g_{--}^{--} &= \tilde{g} - \delta g \cdot \frac{\delta/\Omega}{\sqrt{1+(\delta/\Omega)^2}} - \bar{g} \cdot \frac{1}{1+(\delta/\Omega)^2}, \\
g_{--}^{+-} &= \frac{-\delta g}{\sqrt{1+(\delta/\Omega)^2}} + \frac{2\bar{g}\cdot(\delta/\Omega)}{1+(\delta/\Omega)^2}, \\
g_{++}^{++} &= \tilde{g} + \delta g \cdot \frac{\delta/\Omega}{\sqrt{1+(\delta/\Omega)^2}} - \bar{g} \cdot \frac{1}{1+(\delta/\Omega)^2}, \\
g_{++}^{+-} &= \frac{-\delta g}{\sqrt{1+(\delta/\Omega)^2}} - \frac{2\bar{g}\cdot(\delta/\Omega)}{1+(\delta/\Omega)^2}, \\
g_{+-}^{+-} &= \tilde{g} \cdot \frac{1+2(\delta/\Omega)^2}{1+(\delta/\Omega)^2} - \frac{4\bar{g}\cdot(\delta/\Omega)^2}{1+(\delta/\Omega)^2}, \\
g_{--}^{++} &= \frac{\bar{g}}{1+(\delta/\Omega)^2}.
\end{aligned}$$

These expressions illustrate how the effective interactions between dressed atoms can be tuned continuously by adjusting the ratio δ/Ω.

These results provide a complete and tunable description of interactions on a dressed basis. Elastic scattering preserves internal-state populations and dominates the dynamics of a condensate that is fully prepared in a single dressed state. In particular, for atoms in the lower dressed state $|-\rangle$, the effective interaction is described by $g_{--}^{--}(\delta/\Omega)$.

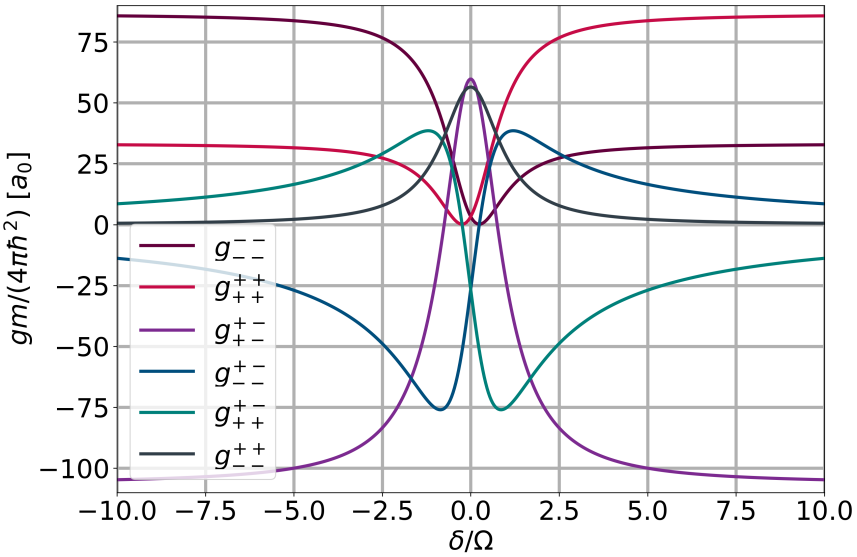


Figure 1.10: Effective two-body scattering length in the dressed-state basis as a function of δ/Ω. The plot shows the elastic interaction strengths g^{--}_{--}, g^{++}_{++}, and g^{+-}_{+-}, as well as the inelastic terms, illustrating the tunability of interactions via detuning to the Rabi ratio. The interaction parameters used for this plot correspond to a data for a magnetic field of 56.85 G, where $g_{11} = 84.3$, $g_{22} = 33.3$, and $g_{12} = -53.21$ (in units of $\frac{m}{4\pi\hbar^2}[a_0]$).

Inelastic processes, such as $|--\rangle \rightarrow |+-\rangle$, can lead to decoherence. However, our experiment confirms these processes don't exist when the dressed-state energy gap $\hbar\Omega$ exceeds the typical kinetic and interaction energy. In this regime, the condensate behaves effectively as a single-component (dressed state) with tunable interactions. This dependence of the two-body interaction strength in the dressed stated on the detuning to Rabi ratio led to the exploration of the LHY energy and the study of the mean-field effective three-body in a coherently coupled BEC [60, 61], and opens the path for exploring the quantum droplet regime and higher-order mean field interactions.

A notable experimental investigation of dressed-state interactions was carried out by Sanz *et al.* [53] who focused first on the elastic interaction in a coherently coupled Bose-Einstein condensate of ^{39}K, in the regime of strong Rabi coupling where it dominates over interaction energy. They prepared the system in the lower dressed state $|-\rangle$ and extracted the effective two-body scattering length a_{--} by measuring the cloud size after a ballistic expansion. Their measurements confirmed that the interactions follow the expected dressed-state interaction strength g^{--}_{--}, as you can see below in Fig 1.11.

However, their study was limited to relatively high Rabi frequencies, typically $\Omega/2\pi = 20\,\text{kHz}$. In the low-$\Omega$ regime, where the Rabi energy becomes comparable to or smaller than the interaction energy, the system no longer follows the two-body mean-field energy alone. Instead, the energy scaling is modified due to the presence of this Rabi coupling.

We will explore this regime in detail in the upcoming chapters. However, magnetic field fluctuations have limited experimental access to this regime. One of the main goals of this work was to overcome these limitations [85] and provide a detailed characterization of the system behavior at low Rabi frequencies.

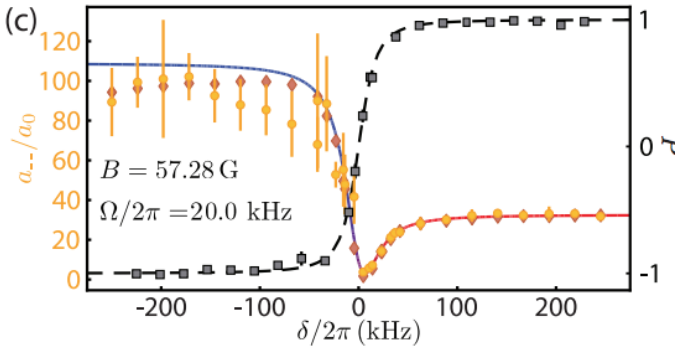


Figure 1.11: Experimental determination of the dressed-state scattering length a_{--} as a function of detuning δ for potassium 39, taken from Ref. [53].

1.6 Chapter Conclusion

This chapter develops the theoretical framework for interpreting and analyzing experiments involving ultracold ^{39}K atoms in coherently coupled spin states. The atomic structure of ^{39}K, including its fine, hyperfine, and Zeeman splitting, permits us to control internal spin state via radio-frequency (RF) coupling. We introduced the dressed-state formalism and analyzed population behavior, including Rabi oscillations and adiabatic passage, which are also necessary for performing state preparation, magnetic field stability measurements, and Ramsey spectroscopy, as discussed in the next chapter.

We have also described the two-body interactions in the bare and dressed basis. In particular, we showed that the scattering length in the dressed basis a_{--} can be tuned with the detuning to the Rabi frequency ratio. This tunability will provide later access to interaction regimes where the mean-field energy deviates from its standard quadratic dependence on density $gn^2/2$, and higher-order nonlinearities or saturation effects appear at low Rabi coupling. These effects will be explored and characterized experimentally and theoretically in Chapter 3.

Beyond mean-field (BMF) corrections, such as the Lee–Huang–Yang (LHY) term in the dressed state, were introduced to account for quantum fluctuations. In our team, we also

study those BMFs in a coherently coupled spin mixture BEC, where we have shown their dependence on the Rabi frequency. In particular, our team experimentally measured this energy in the high Rabi coupling regime [60]. However, access to the low Rabi frequency regime was previously limited by magnetic field noise. In recent work, we developed an improved magnetic field stabilization scheme [85], enabling us to explore the quantum droplet regime even at low Rabi frequencies, where the repulsive LHY term balances the attractive mean-field term. This will be discussed in detail in Chapter 4.

Finally, the scattering properties discussed in this chapter also concern our tunneling experiments. We work in a regime where the scattering length is tuned to zero, lowering interactions and exploring the tunneling of the non-interacting atoms through the optical barrier potential, made with blue detuned light, and controlled with a DMD.

Altogether, the tools and concepts developed in this chapter form the basis for the experimental investigations, giving insight into the many-body physics of coherently coupled Bose gases.

CHAPTER

Experimental Setup and Magnetic Field Stabilization 2

2.1 Chapter Introduction

This chapter presents the experimental setup developed to produce and manipulate quantum degenerate gases of ^{39}K atoms, with a particular emphasis on the magnetic field control system. The first part outlines the laser cooling and trapping sequence used to prepare the atomic sample, including a detailed overview of the D1 and D2 optical setups. Although the optical table is based on work from several previous PhD students, and only a few modifications were made, it is still useful to present it. Since the last optical setup was shown in Lauriane Fouché's thesis, several elements have changed.

The primary focus of this chapter is the implementation of a magnetic field stabilization circuit, a key contribution of this thesis. Precise magnetic field stability is essential for coherent state coupling, tuning the interaction, and the study of quantum droplets. We describe briefly the limitations of the original power supply and progressively introduce improvements, including passive filtering, active compensation circuits, and ambient noise correction.

In particular, the chapter introduces two complementary atomic probe techniques: Ramsey interferometry and dressed-state sweeps for frequency-resolved noise spectroscopy at the Rabi frequency. These methods provide quantitative diagnostics of the magnetic field stability. Through these measurements, we identify the noise sources and develop the necessary electronic circuit for noise correction. The result is a stabilization system capable of maintaining rms magnetic field fluctuations below 100 μG, thereby enabling the studies of a coherently coupled BEC in the low Rabi frequency regime in the next chapters.

2.2 Laser Cooling and Optical Setup for Potassium-39

2.2.1 Brief Description of the Cooling Sequence

It is important to note that the purpose of this section is not to detail or discuss the full optimization procedure of the cooling sequence. This work was not the focus of my PhD and was developed by previous PhD students in previous years. For a more in-depth explanation of the laser cooling strategy, magnetic trapping, and loading optimizations for ^{39}K, we refer the reader to the PhD thesis of Lauriane Fouché [86], Guillaume Berthet [87], and Lucas Lavoine [88].

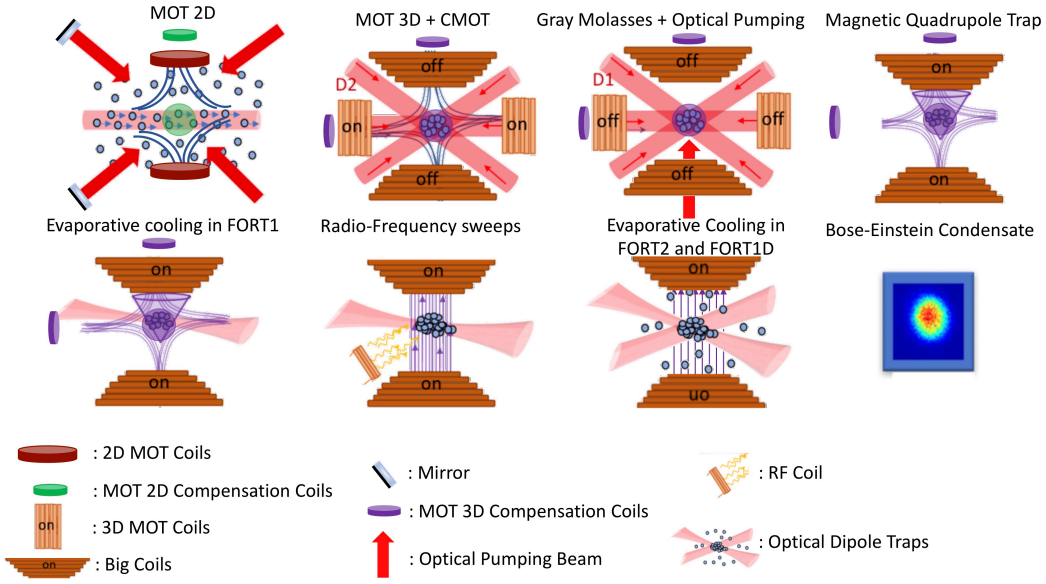


Figure 2.1: Illustration of the experimental sequence used for cooling and trapping ^{39}K atoms, showing the geometry at different stages. We take the figure from the thesis of Lucas Lavoine [88], with additional modifications to reflect the current geometry of the experiment.

The cooling of ^{39}K atoms to quantum degeneracy begins in a vacuum chamber, where a two-dimensional magneto-optical trap (2D MOT) creates a collimated beam of cold atoms. It uses two orthogonal pairs of counter-propagating laser beams addressing the D2 transition Eq. 1.3, with opposite circular polarizations σ^+ and σ^-. A longitudinal push beam tuned to the D2 transition pushes the cooled atoms into the main science chamber with a power of around 0.3 mW.

Anti-Helmholtz 2D MOT coils generate the 2D MOT magnetic field gradient, and we use additional MOT 2D compensation coils along the two axes to fine-tune the quadrupole

center. The laser power is around 95 mW per beam, and the magnetic field gradient is set to 13 G/cm. The resulting atomic beam has a mean longitudinal velocity of approximately 35 m/s and is sufficiently cold and well-collimated to be efficiently captured by the 3D MOT.

In the main science chamber, we capture the atoms with a three-dimensional MOT (3D MOT) based on the D2 transition. The trap uses three orthogonal beam pairs, each with a power of 38 mW. During loading, the magnetic field gradient is around 12 G/cm generated by anti-Helmholtz 3D MOT coils. We use additional MOT 3D compensation coils along the three axes to fine-tune the quadrupole center. Under optimal conditions, the MOT loads up to 2×10^9 atoms within three seconds at a temperature of approximately 3 mK.

As part of recent improvements to the 3D MOT setup, we fixed each of the six MOT beams onto an individual kinematic mount. This configuration allows precise angular tuning of each beam, improving alignment stability. It also simplifies realignment procedures, making it easy to recover the MOT in case of misalignment.

Once the MOT loading is completed, we compress the atoms in a CMOT. During this stage, the magnetic gradient is increased by the 3D MOT Coils to 18 G/cm, and we adjust the detunings for optimal spatial compression. We then apply a gray molasses stage working on the D1 line (Eq. 1.3) immediately after this step. We use a Λ configuration that enables sub-Doppler cooling. It uses three orthogonal beam pairs, each with a 15 mW power. The molasses lasts for 12 ms and cools the ensemble to about 6 μK. The cloud at this point has a root-mean-square size of approximately 1 mm.

We optically pump the atoms into the state $|F = 2, m_F = 2\rangle$ after the molasses cooling stage, which is magnetically trappable and collisionally stable. We apply the optical pumping beam from below the science cell, σ^+, polarized and resonant with the D1 transition, with a maximum power of 4 mW. The transfer duration is about 200 μs.

We then capture the atoms in a magnetic quadrupole trap. At this point, the cloud contains approximately 6×10^8 atoms. This quadrupole trap is a reservoir with a gradient of 120.6 G/cm. Using the 3D MOT compensation coils, we can spatially overlap the quadrupole center with the focus of the first far-off-resonant optical dipole trap (FORT1), formed by a 1550 nm laser beam with a waist of 15 μm and power of up to 19 W as shown on Fig.2.2. The resulting trap depth is about $k_B \times 3$ mK.

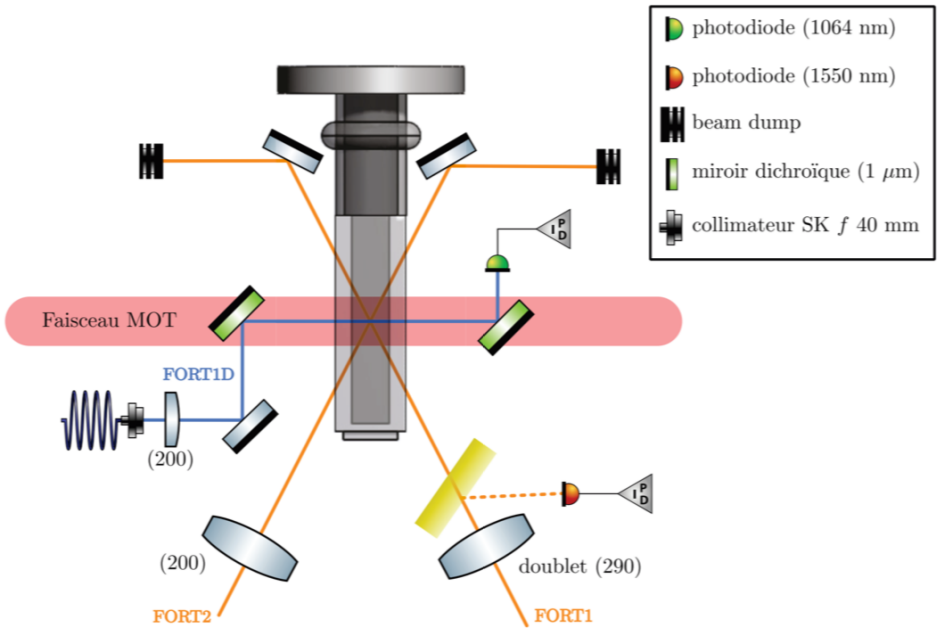


Figure 2.2: Schematic of the optical configuration in the science chamber showing the geometry of the three dipole trapping beams: FORT1 and FORT2 at 1550 nm, and FORT1D at 1064 nm. We use dichroic mirrors (1 μm cutoff) to combine the FORT and MOT beams along the same axes. We place the photodiodes after each beam path. They are integrated into PID feedback loops to actively stabilize laser intensity. Beam dumps eliminate residual light after the chamber. Figure taken from the thesis of Guillaume Berthet [87].

A short stage of evaporative cooling in FORT1, lasting about 100 ms, lowers the temperature to approximately 20 μK and leaves around 5×10^6 atoms. We then transfer the atoms into the state $|2\rangle \equiv |F = 1, m_F = -1\rangle$ through three consecutive adiabatic radio-frequency sweeps.

We perform the final evaporative cooling stage in a crossed optical dipole trap formed by the FORT2 and FORT1D beams. The FORT2 beam is derived from the same 1550 nm laser source as FORT1, but it is shaped independently using the zeroth-order output of an AOM. It delivers up to 14 W of power at the atoms with a waist of 120 μm, providing a trap depth of $k_B \times 50\,\mu$K. Its trapping frequencies are $\omega_r \simeq 2\pi \times 278$ Hz (radial) and $\omega_z \simeq 2\pi \times 0.8$ Hz (axial) at full power.

The FORT1D beam is a 1064 nm infrared beam with a maximum power of 500 mW and a waist of 44 μm at the atoms. This beam provides tight radial confinement with $\omega_r \simeq 2\pi \times 490$ Hz and a weak axial frequency of $\omega_z \simeq 2\pi \times 2.7$ Hz, corresponding to a depth of about $k_B \times 22\,\mu$K at full power.

This final configuration enables efficient evaporation over approximately 2 s, forming a nearly pure Bose-Einstein condensate containing $\sim 1.5 \times 10^5$ atoms at a temperature

below 100 nK, which also provides a platform for experiments involving cigar-shaped traps.

2.2.2 D1 and D2 Optical Table

In this section, I present the current configuration of the optical table used to generate and manipulate the D1 and D2 laser beams required for laser cooling and state preparation of ^{39}K atoms. Lauriane Fouché provided the last comprehensive overview of the optical table [86]. Since then, several PhD students, including Guillaume Berthet [87], Lucas Lavoine [88], and Alfred Hammond [89], have made different modifications and optimizations. However, these were described without a fully updated scheme.

This section aims to present an up-to-date overview of conducting optical table schemes. First, I describe the most recent setup version in detail, showing the geometry, components, and paths of both the D1 and D2 lines. Second, I give approximate power values at different points in the setup. It is useful for future PhD students. It helps them understand what to expect, identify problems like misalignment or power losses, and make upgrades more easily. By presenting a comprehensive overview of the current optical setup, this section serves as both a technical reference and a practical guide for working on the experiment.

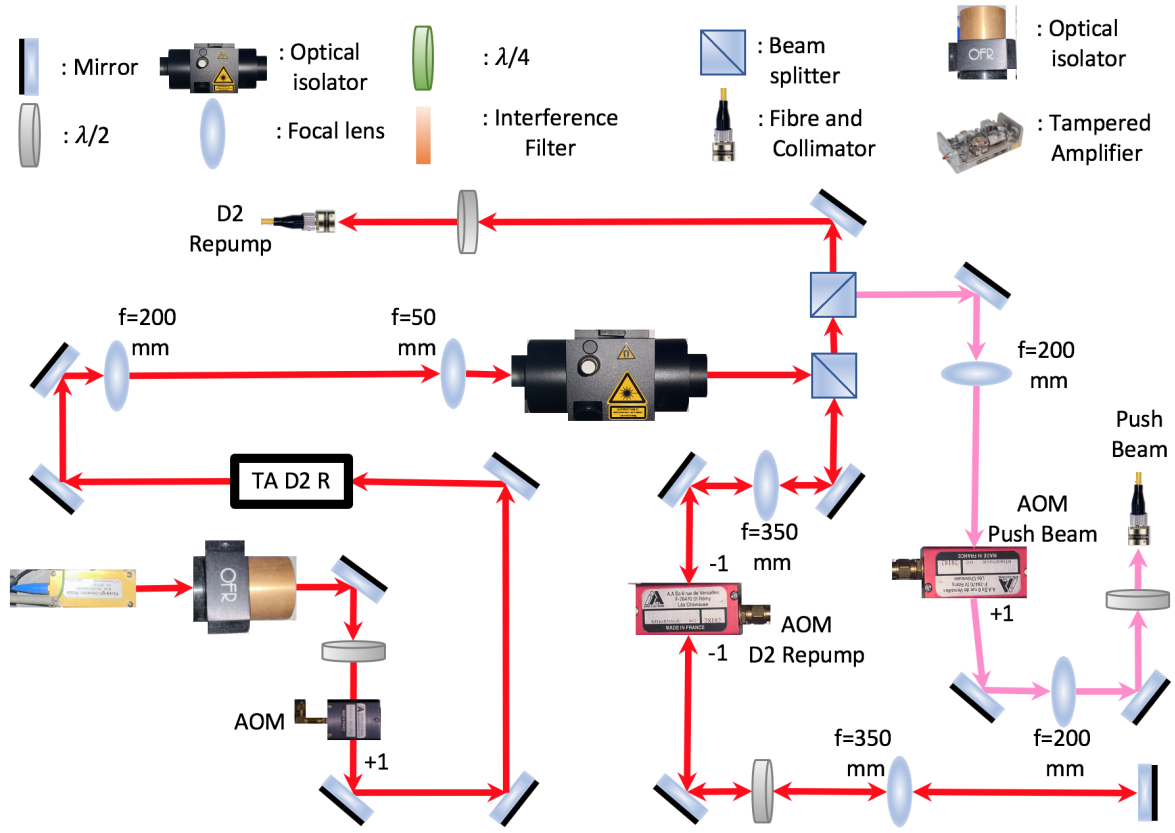


Figure 2.3: Optical setup of the D2 repumper (red path) and the push beam (pink path).

The D2 light used in our experiment's laser cooling and absorption imaging is generated by frequency doubling a fibered telecom laser at 1534 nm. In earlier setups, we produced this light using an extended-cavity diode laser (ECDL) with a linewidth of approximately 2 MHz. This relatively broad linewidth was comparable to the natural linewidth of the D2 transition in ^{39}K ($\Gamma_{\text{at}} \approx 6\,\text{MHz}$), which limited the contrast and precision of absorption imaging. To improve the spectral purity and stability of the imaging light, we upgraded the system to a narrow-linewidth fibered telecom laser (RIO PLANEX, model RIO0195-3-01-1-BP5) with a linewidth of only 2.3 kHz.

The output of the RIO laser at 1534 nm is injected into a Keopsys fibered amplifier and then split into two paths using a fiber splitter. We sent each path into a separate frequency doubler: one for generating the D2 principal light and the other for the D2 repumper. At the output of each doubler, we typically obtain around 70 mW of power at 767 nm.

We show the D2 repumper path (red path) and the push beam for the MOT 2D (pink path) in Fig. 2.3. After frequency doubling, the 767 nm beam is first sent through an AOM to apply an initial frequency shift. We inject it into a tapered amplifier (TA D2 R), which boosts the power to approximately 1.2 W. The amplified beam passes through a double-pass AOM setup, allowing additional frequency adjustment of the repumper. After this stage, we split the beam into two parts. One part is combined with the D2 principal light on a separate optical table and directed later toward the MOT 2D and MOT 3D. We typically measure around 200 mW of power just before fiber injection for this path. The other part is sent toward the push beam fiber (pink path), passing through an additional AOM (AOM push beam) to apply a specific frequency shift required for optimal MOT loading. For the push beam, we typically measure around 4 mW just before fiber injection.

We show the D2 principal path (purple) in Fig. 2.4. After frequency doubling at 767 nm, the light passes through an optical isolator to prevent back-reflection and then enters a beam splitter. We direct a small portion of the beam toward the saturated absorption chamber for frequency stabilization on the D2 transition. The other portion, used for cooling, is sent through a double-pass AOM in the -1 order (AOM D2 Principal). After this, we combine the beam with the repumper on the same optical table before being injected into a fiber for distribution to the MOT 2D and MOT 3D.

The absorption imaging beam path (green), as shown in Fig. 2.4, is derived from the zeroth-order output of the AOM D2 Principal. This light is sent through its own double-pass AOM (Acousto-Optic Modulator) for AOM Absorption Imaging, allowing for precise and tunable detuning, typically used for absorption imaging. After frequency shifting, we inject the beam into a fiber, which delivers it to the absorption imaging axis of the science chamber with a power of around 10 mW. Note that all the atomic images and data taken in this thesis were obtained through fluorescence imaging.

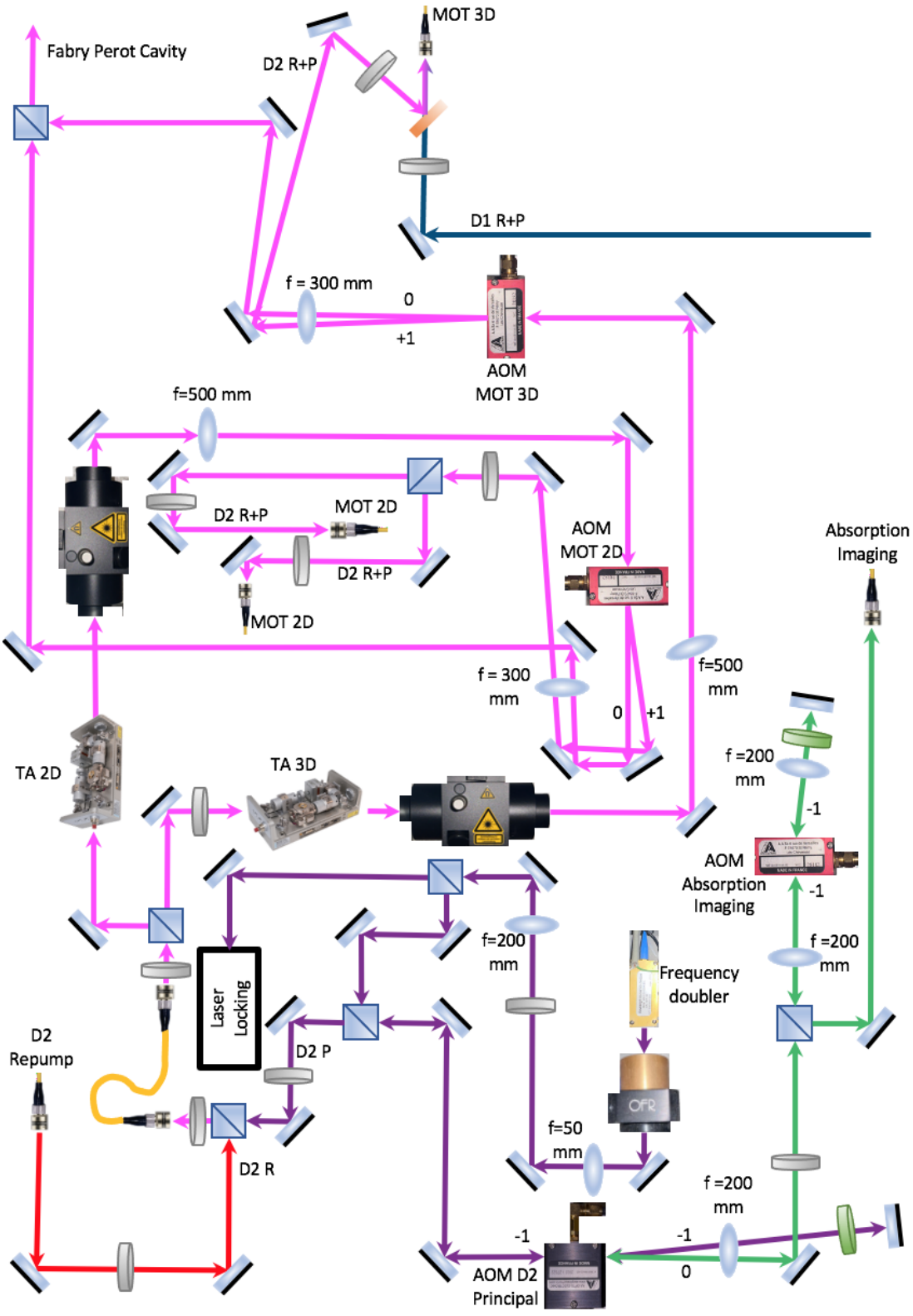


Figure 2.4: Optical setup of the D2 repumper (red path), D2 principal (purple path), absorption imaging (green path), D2 beams for MOT 2D and MOT 3D (magenta path), and the D1 line (blue path).

To ensure long-term stability and consistent alignment of the MOT beams' path (magenta path), we combine the D2 principal and repumper beams into a single polarization-maintaining fiber before distribution. This combined beam, represented by the magenta path in Fig. 2.4, ensures that the output spatial mode remains fixed, independent of optical fluctuations or misalignments. At the fiber output, we typically obtain a power of 75 mW (55 mW Repumper and 20 mW Principal). We split the light into two paths: one directed toward the MOT 2D and the other toward the MOT 3D. We amplify each path using separate Moglabs tapered amplifier devices. We recently installed them to replace the older homemade models. These newer amplifiers have improved the day-to-day stability of the MOT.

After amplification, each beam passes through an optical isolator and an AOM (AOM MOT 2D and AOM MOT 3D) using the +1 order, allowing precise control of each MOT beam's power. We inject the MOT 2D beam into two fibers, with a power of around 300 mW to each MOT 2D beam line. Similarly, the MOT 3D beam has a power of approximately 760 mW before injection. We split this beam using beam splitters into six individual beams to form the 3D MOT configuration. We sent the zeroth order of each AOM to a Fabry-Pérot cavity, which we use to monitor the power balance between the repumper and principal components.

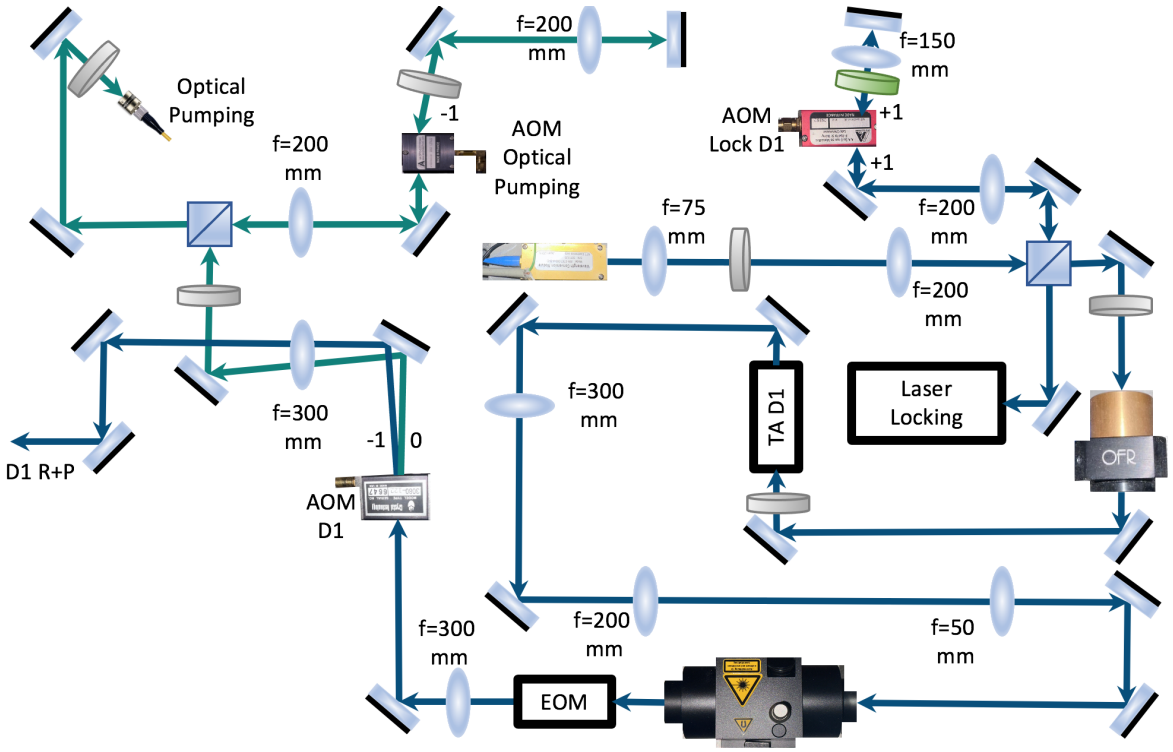


Figure 2.5: Optical setup of the D1 table (blue path) and the optical pumping beam (dark green path).

The D1 light used for optical pumping and state preparation is generated by frequency doubling the output of a fibered telecom laser (Emcore 1782A-NM-040-46-FC-PM). After frequency doubling, we split the resulting 766.7 nm beam into two paths: one directed toward a saturated absorption spectroscopy setup for frequency stabilization and the other used for the experiment. This beam is injected into a tapered amplifier (TA D1), increasing its power to approximately 1.2 W.

To generate both the D1 principal and repumper frequencies, we pass the amplified beam through an electro-optic modulator (EOM) driven at 461.7 MHz. This modulation produces optical sidebands symmetrically spaced around the carrier frequency. The +1 sideband is tuned to address the D1 repumper transition of ^{39}K, while the carrier frequency is used for the principal transition. The remaining sidebands are sufficiently far-detuned from any atomic resonance and therefore do not contribute to the atoms.

Following the EOM, the beam passes through an acousto-optic modulator (AOM D1). We inject the -1 diffraction order from this AOM into the MOT 3D fiber after passing through an interference filter with a power of 300 mW. We direct the zeroth-order beam of the AOM D1 to a second AOM, configured at 180 MHz, in a double-pass configuration (AOM Optical Pumping). We then inject this beam into a separate fiber for the optical pumping with a power of 14 mW before injection.

2.3 Magnetic Field Stabilization Technique for Cold Atom Experiments

Stable magnetic fields are crucial for the accuracy of quantum gas experiments, particularly when probing Zeeman levels, tuning interactions, or achieving high-precision measurements. Applications such as quantum simulation [90], atomic clocks [91], and Feshbach resonance control [48, 92] all rely on magnetic fields with minimal fluctuations. Even for magic transitions where first-order Zeeman shifts vanish, second-order effects remain [93], requiring control at the ppm level or better. In an ultra-cold atomic mixture, magnetic fields enable the tuning of interaction and spin population. For instance, dressing two Zeeman states with a radio-frequency (RF) field allows access to tunable mean-field and beyond-mean-field interaction energy [94, 95]. However, fluctuations in the magnetic field detuning, particularly near the Rabi frequency, can degrade the coherence and stability of such systems.

Passive shielding with high-permeability materials such as μ-metals offers strong suppression [96], but introduces geometric constraints, and they are not compatible with

high fields due to saturation. For this reason, active stabilization techniques have become popular [97, 98]. These approaches involve either feedback loops based on direct magnetic field sensors [99, 100] or current stabilization via transducers [101, 102]. In high-field applications, such as those involving potassium-39, where the magnetic field can reach tens of thousands of Gauss, the dominant noise source is current instability in the coils. While the best commercial current supplies can reach stabilities of 10^{-5}, this is insufficient when we need to control the fluctuations below 100 μG rms on 57 G [103].

2.3.1 Required Stability for Precision Control

The coherent coupling of ultracold atoms in magnetic-field-sensitive spin states demands good control over the magnetic field. In our experiment, we work with the $|F = 1, m_F = -1\rangle$ and $|F = 1, m_F = 0\rangle$ sublevels of ^{39}K, where the energy splitting between the two states depends linearly on the magnetic field at a rate of approximately 0.70 MHz/G. As described in Chapter 1, we use a radio-frequency (RF) field to couple these two states and create dressed states, where the effective interaction depends on both the Rabi frequency Ω and the detuning δ between the atomic transition and the RF frequency.

For the interaction studies in dressed Bose-Einstein condensates presented in Chapters 3 and 4, working at low Rabi frequencies ($\Omega/2\pi \sim 1$ kHz) is crucial for observing the saturating interactions in the mean-field description and the formation of quantum droplets. In this regime, a good control of interactions requires that the ratio δ/Ω be controlled to a precision of below 0.1, and that the system remains in the lower dressed state $|-\rangle$. This requirement imposes a constraint on magnetic field stability, as fluctuations in the field translate into detuning noise $\delta(t)$. The system depends on the ratio δ/Ω, so when Ω is small, it becomes more sensitive to detuning fluctuations.

In our new setup, an rms fluctuation of 100 µG around a field of 57 G corresponds to a detuning rms variation of approximately 70 Hz. In our previous setup, the rms detuning noise was 800 Hz, limiting us to $\Omega/2\pi \gtrsim 7$ kHz. To reach lower Rabi frequencies, we developed an active magnetic field stabilization circuit capable of reducing the detuning noise to below 100 Hz rms, corresponding to a magnetic field stability better than 100 µG, or approximately 2 ppm at 57 G.

However, reducing shot-to-shot fluctuations is not sufficient on its own. Understanding the spectrum of magnetic field noise across different frequencies ν is also important. Our experiment's magnetic field noise spectrum contains ambient low-frequency components (including 50 Hz and harmonics) and a broad background noise from the power supply up to a few kilohertz, thanks to the inductive nature of the coils.

These fluctuations contribute in two distinct ways:

1. low frequency noise below Rabi frequency ($\nu < \Omega/2\pi$) does not induce non-adiabatic

transitions between dressed states. The atoms adiabatically follow the dressed eigenstate $|-\rangle$. However, time-dependent fluctuations of the detuning $\delta(t)$ modify the interaction strength g_{--}^{--} in real time, thus adding unwanted mean-field energy fluctuation into the system.

2. Noise at frequencies near the Rabi frequency ($\nu \sim \Omega/2\pi$) has a qualitatively different effect: it can resonantly couple the dressed states and induce unwanted transitions from $|-\rangle$ to $|+\rangle$. These non-adiabatic transitions modify the energy of the atoms. Atoms in $|+\rangle$ experience different mean field interactions. In particular, the intercomponent interaction strength g_{+-}^{+-} and g_{++}^{++} alter the the mean-field energy.

In summary, achieving precise control of our experiment's dressed-state dynamics requires reducing the magnetic field's shot-to-shot fluctuations and actively correcting the spectrum noise to suppress components near the Rabi frequency. Understanding the spectrum of magnetic field fluctuations is crucial for our stabilization strategy, which we will discuss in detail in the following sections.

2.3.2 Overview of the Old Magnetic Field Control Setup

The old current supply, which was used for magnetic field control, supplies current to large water-cooled coils (Main coils) arranged in a Helmholtz configuration. These coils generate the homogeneous field used in the experiment. IGBTs enable switching between dipole and quadrupole configurations, which are adapted for quadrupole trapping or Feshbach magnetic field control during the sequence.

The magnetic field was generated using two current supplies in parallel, as shown in Fig 2.6:

- The Delta Elektronika SM18-220 was used as the main current supply to generate strong magnetic fields and fast ramps, particularly for the quadrupole configuration. It delivers up to 220 A at 18 V (3300 W) with a relative current stability of 9×10^{-5}. The output current noise is 50 mA rms, measured with a 300 kHz bandwidth (corresponding to 190 mG rms). We also utilize this power supply to generate a uniform magnetic field of approximately 350 G in the experiment described in Chapter 5. However, we use a lower-noise power supply for the stability-sensitive experiments in Chapters 3 and 4, in addition to the active magnetic field stabilization circuit.

- The Delta Elektronika SM170-AR-24 is a low-noise precision power supply capable of delivering up to 24 A in the 0–35 V range (840 W). It delivers a low output current noise of 3 mA rms over a 300 kHz bandwidth, corresponding to 11 mG rms magnetic field fluctuations, and a relative current stability of 9×10^{-5} over 8 hours. A 1 kΩ resistor was placed in parallel with the coils to provide a discharge path for residual current and prevent the power supply's internal capacitance from remaining charged between experimental cycles.

We use a mechanical switch between these two power supplies during the experimental sequence. Switching typically occurs 10 ms after loading the first dipole trap.

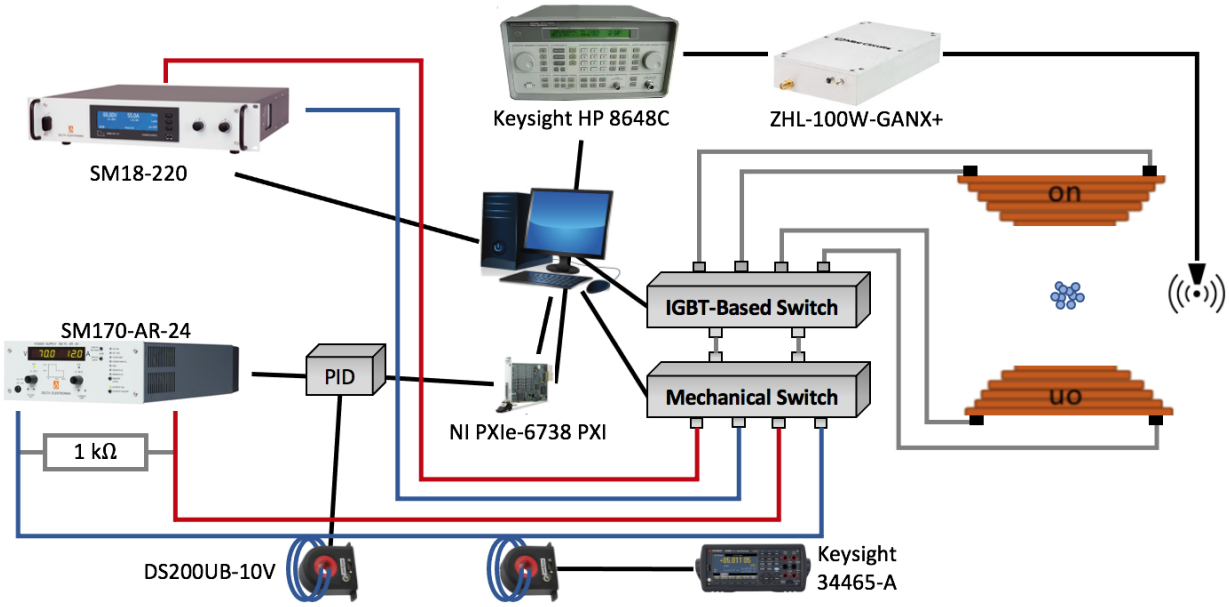


Figure 2.6: Schematic of the old magnetic field control system, showing both power supplies (SM18-220 and SM70-AR-24), switching modules, analog control hardware, and RF components used to generate coherent coupling.

The current polarity in one of the coils is controlled by an electronic IGBT-based switch described in Lucas's Thesis [88], which enables fast switching between dipole and quadrupole modes. F. Moron built this switch, which consists of four IGBT transistors arranged to invert the current through one coil. It also serves as a fast cutoff switch, allowing for current interruption in less than 0.3 ms, which is necessary for time-of-flight imaging. The switch is water-cooled to maintain thermal stability.

The analog control of the magnetic field was handled using NI PXI-6723 cards (13-bit, 32 channels). These exhibit limitations, including glitches up to 80 mV and voltage noise around 0.5 mV over a 1-ms integration time. These artifacts resulted in magnetic field instabilities of up to 4.56 mG rms in the big coils. The system was upgraded to an NI PXI-6738 card (16-bit, 32 channels), which eliminated glitch-related issues and reduced voltage noise. The typical rms noise of 30 µV measured over a 1 ms integration time corresponds to a rms magnetic field fluctuation of about 0.274 mG.

A PID control loop was implemented to stabilize the output of the SM170-AR-24 using a Danisense DS200UB-10V current transducer, which has a range of ±200 A and a voltage output of ±10 V, corresponding to a sensitivity of 50 mV/A. The sensor operates over a bandwidth up to 500 kHz, allowing fast and precise current measurements. Its

total accuracy is better than 1 ppm up to 10 kHz. The cable was passed through the transducer aperture twice, improving the output signal to achieve a sensitivity of 100 mV/A.

Before activation of the PID loop, the magnetic field exhibited short-term fluctuations of approximately 7.22 mG rms (1.9 mA rms) over a 1-ms integration time. We derived this value from the rms current noise measured using a Danisense DS200UB-10V current transducer, which outputs a voltage proportional to the current flowing through the coils. We acquired the voltage signal with a Keysight 34465A digital multimeter. After PID stabilization, the measured field noise was reduced to 1 mG rms (0.26 mA rms). The Keysight 34465A, with its 6½-digit resolution, sub-millivolt sensitivity, and low-noise, ensures sufficient precision to resolve such small variations.

The RF generator (Keysight HP 8648C) produces the RF signal, which is then amplified to a power of up to 100 W, sufficient to reach Rabi frequencies of several tens of kHz. The RF frequency is controlled via analog modulation driven by a National Instruments PXI-6738 card.

2.3.3 Magnetic Field Noise Characterization

Characterizing the magnetic field noise is essential. Our experiment combines three complementary techniques: Ramsey interferometry, dressed-state noise spectroscopy, and direct current noise measurements.

Ramsey Interferometry

Ramsey interferometry provides a highly sensitive, atom-based method for quantifying magnetic field noise, especially at low frequencies. In our experiment, we utilize the Zeeman-sensitive transition between the states $|2\rangle$ and $|1\rangle$ of ^{39}K at a magnetic field of 57 G. The energy splitting between these states is around 40 MHz, with a magnetic sensitivity of 0.70 MHz/G. We perform detuned Ramsey interferometry, which measures the accumulated phase between the two $\pi/2$ pulses, making it suitable for detecting small magnetic field fluctuations.

In a Ramsey sequence performed on resonance, a $\pi/2$ pulse creates an equal superposition of the two spin states, followed by a free evolution time T_{wait}, and then with a second $\pi/2$ pulse, which results in near-complete population transfer from state $|1\rangle$ to state $|2\rangle$. However, this on-resonance Ramsey sequence is not very sensitive to detuning fluctuation.

To have better sensitivity to detuning fluctuations, we perform a slightly detuned Ramsey sequence. The difference is that during the waiting time T_{wait}, the small detuning δ (around 2 kHz) causes the population to oscillate between the two states at the detuning frequency. By measuring the resulting population imbalance as a function of T or δ, we can extract information about the detuning fluctuations. The effective Ramsey time is:

$T = T_{\text{wait}} + \frac{4\tau}{\pi}$, where τ is the finite pulse duration. The probability of finding the atom in state $|2\rangle$ reads:

$$f(T) = \frac{1}{2}\left[1 - C(T)\cos(\delta T)\right], \tag{2.1}$$

where $C(T)$ is the fringe contrast. The formula assumes that the detuning is much lower than the Rabi frequency and includes a correction on the Ramsey time due to the finite pulse time τ. We can achieve the highest sensitivity of the magnetic field at half fringe, for example, when $\delta T = \pi/2$.

In practice, $C(T)$ decays with T due to dephasing effects arising from two different contributions of the detuning fluctuations. The first contribution originates from shot-to-shot variations in the average magnetic field, which cause fluctuations in the global detuning δ. Assuming these fluctuations are Gaussian-distributed with standard deviation σ_δ, the signal acquires a Gaussian envelope.

Another contribution results from magnetic field gradients around the atomic cloud. Atoms at different positions experience slightly different fields and accumulate different phases during the Ramsey sequence. The integrated Ramsey signal also decays with a Gaussian envelope due to inhomogeneous broadening with standard deviation σ_B for a cloud with a Gaussian spatial density distribution.

When both effects are present, they combine in variance, $\sigma_c^2 = \sigma_\delta^2 + \sigma_B^2$, and the contrast becomes:

$$C(T) = C_0 \exp\left[-\frac{1}{2}\sigma_c^2 T^2\right], \tag{2.2}$$

With the effective coherence time:

$$T_{\text{c}} = \frac{\sqrt{2}}{\sigma_c}. \tag{2.3}$$

For a fast Ramsey characterization sequence, we work around the half-fringe condition to probe magnetic field noise, where $\delta T \approx \pi/2$. Around this working point, we have a linear response:

$$f(T) \approx \frac{1}{2} - \frac{C(T)}{2}\left(\delta T - \frac{\pi}{2}\right), \tag{2.4}$$

So, small detuning fluctuations reflects the output signal $f(T)$ variations.

Over repeated realizations, the root-mean-square (rms) fluctuation of the signal, $\text{rms}(f)$, is related to the rms detuning fluctuation $\text{rms}(\delta)$ by:

$$\text{rms}(\delta/2\pi) = \frac{\text{rms}(f)}{\pi C(T) T}. \tag{2.5}$$

Using the Zeeman sensitivity $d\delta/dB$, we can convert this detuning noise into magnetic field noise:

$$\text{rms}(B) = \frac{\text{rms}(\delta)}{d\delta/dB}. \tag{2.6}$$

When the detuning fluctuations exceed the linear response range or when the system does not operate at the half-fringe point, the Ramsey signal becomes nonlinear in δ, and Eq. (2.4) no longer applies.

Noise Spectroscopy via Dressed-State Sweeps

We implement a protocol based on dressed-state sweeps to complement Ramsey interferometry, thereby gaining frequency-resolved information about magnetic field fluctuations near the Rabi frequency Ω. This technique acts as a narrow-band quantum spectrum analyzer, probing noise components at frequencies around Ω. The sequence consists of three main stages:

1. Adiabatic Preparation: The system is initially in a bare spin state, typically $|2\rangle$. We apply an adiabatic sweep of the RF frequency to slowly change the detuning $\delta(t)$ from a large positive value ($\delta \gg \Omega$) to a final value $\delta_f \approx 0$. Thus, the atoms are in the lower dressed state $|-\rangle$ at $\delta = \delta_f$.

2. Noise-Sensitive Hold: The detuning is held constant at $\delta_f \approx 0$ for a duration T_2. The system remains in the dressed state $|-\rangle$. However, magnetic field fluctuations with spectral components near the energy splitting $\hbar\Omega$ can induce transitions to the upper dressed state $|+\rangle$.

3. Readout via Reverse Sweep: A reverse sweep brings the system back, mapping dressed states back onto the bare basis. Atoms in $|-\rangle$ return to $|2\rangle$, while those transferred to $|+\rangle$ project onto $|1\rangle$. The population in $|1\rangle$ thus measures the transition probability $P_{|-\rangle\to|+\rangle}$ accumulated during T_2.

Detuning fluctuations $\delta(t)$ are a time-dependent perturbation that can drive transitions between the dressed states. Using first-order time-dependent perturbation theory, the transition probability reads:

$$P_{|-\rangle\to|+\rangle} = \frac{1}{4}\left|\int_0^{T_2} \delta(t)\, e^{i\Omega t} dt\right|^2 . \tag{2.7}$$

Taking the expectation value over many realizations and using the autocorrelation function $R_\delta(\tau) = \mathbb{E}[\delta(t)\delta(t+\tau)]$, the mean transition probability becomes:

$$\mathbb{E}[P] = \frac{1}{4}\int_{-T_2}^{T_2} (T_2 - |\tau|) R_\delta(\tau) e^{-i\Omega\tau} d\tau. \tag{2.8}$$

This expression is the convolution of the noise autocorrelation with a triangular window function. According to the Wiener–Khinchin theorem, which states that the power spectral density (PSD) is the Fourier transform of the autocorrelation function, equation 2.8 can be rewritten in terms of the PSD $S_{\delta\delta}(\nu)$:

$$\mathbb{E}[P] = \frac{T_2^2}{4}\int_{-\infty}^{\infty} S_{\delta\delta}(\nu)\, \mathrm{sinc}^2\left[\pi T_2(\nu - \Omega)\right] d\nu. \tag{2.9}$$

If the spectral density $S_{\delta\delta}(\nu)$ varies slowly over the bandwidth of the sinc^2 filter, we can approximate it as constant near $\nu = \Omega$. In this case, Eq. (2.9) simplifies to:

$$\mathbb{E}[P](\Omega) \approx \frac{T_2}{4} \cdot S_{\delta\delta}(\Omega). \tag{2.10}$$

This approximation illustrates that, for a hold time T_2, the transition probability becomes proportional to the power spectral density of the detuning noise evaluated at the Rabi frequency $\nu = \Omega$. The sinc^2 filtering function acts as a narrowband spectral window centered at Ω, with a resolution around by $1/T_2$.

In the limit of infinitely long hold times $T_2 \to \infty$, the sinc^2 filter converges to a Dirac delta function δ_D:

$$\lim_{T_2 \to \infty} T_2 \cdot \text{sinc}^2 \left[\pi T_2(\nu - \Omega)\right] = \delta_D(\nu - \Omega), \tag{2.11}$$

In this case, the population measurement would similarly give the same as Eq. 2.10 at $\nu = \Omega$

However, this approximation is valid only when the noise spectrum $S_{\delta\delta}(\nu)$ is flat around the Rabi frequency (white noise). We can write it as:

$$T_2 \gg \frac{1}{\Delta\nu}, \tag{2.12}$$

where $\Delta\nu$ is the characteristic frequency scale over which $S_{\delta\delta}(\nu)$ changes. The measurement duration must be long enough to resolve a narrow spectral frequency. If the condition is not satisfied, the sinc^2 filter spreads over a broader range of frequencies, mixing contributions from different parts of the spectrum. As a result, $\mathbb{E}[P](\Omega)$ no longer reflects the local value of $S_{\delta\delta}(\Omega)$. We must calculate the full convolution in Eq. (2.9) to accurately analyze the noise spectrum.

Direct Current Noise Measurement

Current noise from the current supply, a direct source of magnetic field fluctuations, can be characterized independently of the atomic measurement. Current rms noise is measured using a Keysight 34465A digital multimeter with 6.5-digit resolution, connected to a precision current transducer.

We use the LEM IT 60-S Ultrastab transducer for low-noise current measurements, and later switched to the IT 200-S Ultrastab, which offers slightly better performance. According to the manufacturer's specifications, both models provide excellent accuracy of 4 ppm within a 10 kHz bandwidth. The current sensitivities are 1.667 mA/A for the IT 60-S and 1.0 mA/A for the IT 200-S. Both transducers exhibit a narrow noise peak near 17 kHz due to their internal clock.

We connected the transducer output across a 50 Ω resistor, and a Keysight 34465A multimeter read the signal to measure the current noise bandwidth. The results, shown

in the third column of table 2.1, were converted into magnetic field noise using the coil calibration. These measurements confirm the low-noise performance specified by the manufacturer and demonstrate the system's suitability for high-precision magnetic field noise measurements arising from coil current fluctuations.

The integration time (also referred to as aperture time) of the Keysight 34465A multimeter determines the noise bandwidth of the measurement. Its frequency response is not a simple low-pass filter but has a sinc-squared shape, with a central peak and side lobes. This means the multimeter is most sensitive to noise in the first lobe and least sensitive at the specified frequency. By choosing integration times that are multiples of the LEM transducer's internal clock period (around 17 kHz), we place the transducer's noise peak at a point where the multimeter is least sensitive. This allows us to disregard the transducer's noise and focus solely on the noise from the power supply.

We also use a Rohde & Schwarz FSV signal analyzer to measure the noise power spectral density $S_{II}(\omega)$. These measurements directly characterize the magnetic noise spectrum from current fluctuations and complement the other diagnostics.

2.3.4 System Improvements and Filtering

To further reduce magnetic field noise and improve the current stability, we upgraded the current source powering the coils. The previously used Delta Elektronika SM70-AR-24 supply, which was externally stabilized via a home-built PID system, was replaced by a HighFinesse Unipolar Current Source (UCS) with a 10V/20A. The UCS provides a current stability better than 2.5×10^{-5} (25 ppm) of full scale. Its internal regulation is characterized by a fast switching time of 0.05 ms, as specified in the specifications, corresponding to a bandwidth of below 20 kHz, depending on the jumper configuration and the inductance load. It is not required to have very fast current modulation for the experiment. Thus, slightly reducing the bandwidth will reduce high-frequency current noise.

The current supply provides different outputs (jumpers), J_{11}, J_{12}, and J_{13}, each of which has a distinct internal configuration to balance the trade-off between speed and noise for different application needs. The big coils are characterized by an internal resistance $R_{\text{coil}} = 150\,\text{m}\Omega$ and inductance $L_{\text{coil}} = 175\,\mu\text{H}$. Additionally, we placed an external inductance, L_1, in series with internal resistance, R_1, between the current supply and the coils. We connect both coils $L = L_1 + L_{\text{coil}}$ with internal resistance $R = R_1 + R_{\text{coil}}$ in parallel to a capacitor C_1 to stabilize the voltage, forming a second-order passive low-pass LC filter. We added this filter to reduce the power supply's current noise bandwidth.

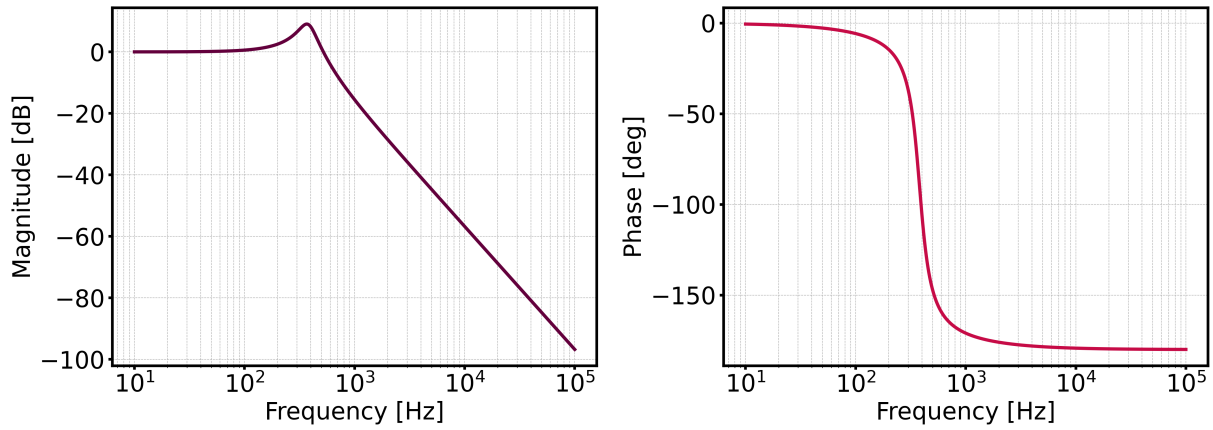


Figure 2.7: Bode diagram showing the amplitude (left) and phase (right) of the transfer function $H(\omega)$, simulated with $R = 150\,m\Omega$, $C_1 = 1\,\text{mF}$, and $L = 175\,\mu\text{H}$. It's a second-order low-pass filter with a resonance peak. At low frequencies, the gain approaches unity, while at high frequencies it attenuates (-40 dB/decade). The phase goes from $0°$ to $-180°$.

The transfer function as shown in fig 2.7 describing the ratio between the current flowing into the coil $I_{\text{coil}}(\omega)$ and the current delivered by the power supply $I_{\text{ps}}(\omega)$, which is given by:

$$H(\omega) = \frac{I_{\text{coil}}(\omega)}{I_{\text{ps}}(\omega)} = \frac{1}{1 + j\omega RC_1 - \omega^2 LC_1}. \tag{2.13}$$

It is important to know that I_{ps} is not an ideal independent source, but instead depends on the load impedance, which is also affected by the filter configuration. For this reason, it is not accurate to interpret $H(\omega)$ as a simple filter. Instead, the current depends on the interplay between the power supply, internal electronics, and the actual impedance at its output. As a result, we chose to experimentally characterize the bandwidth of the power supply for different jumper outputs and for various added external capacitors C_1, rather than relying on the theoretical model using the direct current noise measurement technique previously described.

We carefully tested different configurations to minimize the current noise. Among the three jumper outputs of the UCS, we found that the J_{12} output consistently provided the lowest current noise in the frequency range below 20 kHz, and we adopted it for all subsequent experiments. Our tests also showed that using a capacitor between 220 μF and 1 mF gave the best compromise between noise reduction and bandwidth. In the Ramsey experiments discussed later in this thesis, we used $C_1 = 1\,\text{mF}$.

Aperture Time	Bandwidth	LEM-60 Noise [mG]	0 F [mG]	220μF [mG]	470μF [mG]	690μF [mG]	1mF [mG]	1.22mF [mG]
58 µs	17.24 kHz	0.06	4.06	0.98	0.73	0.71	0.78	0.84
172 µs	5.81 kHz	0.05	1.14	0.98	0.68	0.71	0.78	0.84
516 µs	1.94 kHz	0.03	0.49	0.82	0.60	0.64	0.75	0.81
5 ms	200 Hz	0.02	0.13	0.14	0.16	0.19	0.26	0.31
20 ms	50 Hz	0.01	0.03	0.03	0.03	0.03	0.03	0.04

Table 2.1: Magnetic field noise (in mG rms) measured with the LEM IT 60-S Ultrastab current transducer connected to a Keysight 34465A multimeter, for various filter capacitances C_1 and integration (aperture) times. The third column shows the intrinsic transducer noise floor. We obtained noise values by converting the voltage fluctuations measured across a 50 Ω resistance and using the coil calibration factor.

Finally, we observed that turning on the radio-frequency (RF) field at full power introduced additional current noise, due to electromagnetic interference affecting the UCS. To avoid this, we relocated the current source to a separate room, away from RF signals, which improved stability during the experiment.

After implementing these improvements to the current supply and filtering configuration, we characterized the residual magnetic field noise using Ramsey interferometry, as described in Section 2.3.3. The shot-to-shot fluctuations measured with atoms showed a rms magnetic field noise of approximately 0.9 mG. However, two important limitations remained. First, magnetic field noise components at frequencies $\nu \approx \Omega/2\pi$ were still inducing non-adiabatic transitions to the upper dressed-state at frequencies below 7 kHz. Second, the shot-to-shot magnetic field fluctuations were reduced only to 0.9 mG rms, similar to our old homemade PID. We still needed to achieve better stability for interaction studies, so we developed an active compensation circuit for the magnetic field to address these residual imperfections, which we will describe in the upcoming sections.

2.3.5 Correlation Measurements

Given our ability to measure the current noise of the transducer with a good precision, we decided to attempt a correlation measurement: simultaneously measuring the current in the coil during the sweep experiment and simultaneously measuring the internal population as a function of δ/Ω, as described in Eqs. 1.53 and 1.54. In principle, plotting the measured current and the measured population would allow us to estimate the shot-to-shot current fluctuations contribution of the power supply to the detuning δ.

We synchronized the current measurement with the experimental population measurement. After performing a sweep experiment repeatedly on a thermal atomic cloud to the 50–50 point at $\delta = 0$, we applied a Stern-Gerlach experiment to split the internal spin states spatially. We measured the population $P_{|2\rangle\to|-\rangle}$.

Simultaneously, at the end of the sweep, we measured the coil current using the Keysight 34465A, connected to the LEM transducer, triggered to the experimental cycle with a $172\,\mu$s integration time, which corresponds to an effective bandwidth of approximately 6 kHz. We converted the measured current fluctuations into magnetic field fluctuations using the coil calibration, and then translated them into detuning fluctuations on δ. The Rabi frequency during the sweep was set to $\Omega/2\pi \approx 2.4\,\text{kHz}$.

Figure 2.8 shows the measured population $P_{|2\rangle\to|-\rangle}$ as a function of the measured detuning δ reconstructed from the measured current. For a sweep experiment around the 50–50 point, the expected theoretical slope is 1/2, as predicted by the relation in Eq. 1.54.

We can extract several important results from the data:

- The rms fluctuations of the population P allow us to extract the rms detuning noise seen by the atoms from Eq. 1.53 leading to $\text{rms}(B) \approx 0.9\,\text{mG}$.

- Independently, by analyzing the rms of the measured current fluctuations over a $172\,\mu$s integration time, we obtained $\text{rms}(B) \approx 0.85\,\text{mG}$, which reflects only the noise contribution from the power supply below 6 kHz bandwidth. This value is slightly below the total noise obtained from population fluctuations, indicating the presence of a small residual contribution from an external source of field noise.

- To obtain the residual noise not correlated with the measured current, we subtracted the fitted linear dependence from the experimental population data and computed the rms of the residuals. Applying the same linear relation, we obtain approximately 0.27 mG rms.

This residual noise, which is uncorrelated with the measured coil current, most likely originates from ambient magnetic field fluctuations in the laboratory, as well as 50 Hz line noise and its harmonics. Before analyzing the spectral nature of these residual fluctuations, we developed and implemented an active magnetic field compensation circuit to reduce noise originating from the power supply, as described in the section below.

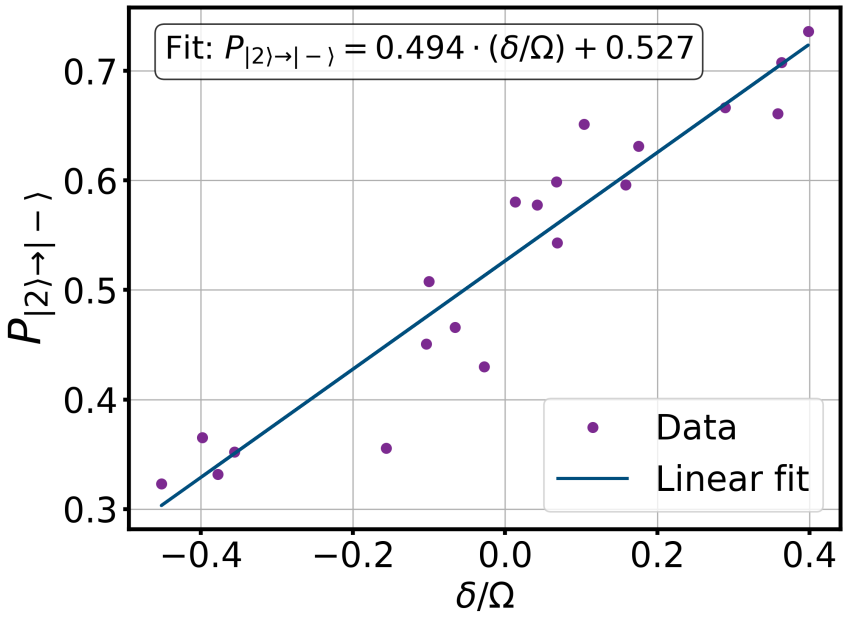


Figure 2.8: Correlation measurement between the measured detuning δ/Ω (obtained from the coil current measurement) and the measured internal state population $P_{|2\rangle\to|-\rangle}$. The linear fit confirms the expected slope of approximately 0.5 at $\delta/\Omega = 0$, consistent with Eq. 1.54.

2.3.6 Active Magnetic Field Compensation Circuit

To go beyond the correlation measurements and suppress current-induced magnetic field noise, we implemented an active magnetic field compensation circuit, as shown in Fig. 2.9. This system injects a feedforward corrective current into a specific compensation coil, which cancels the field fluctuations on the atoms coming from the current supply of the main coils without interfering with it.

The principle of the circuit relies on generating a signal that reflects the deviation between a stable reference current source and the actual current delivered by the main power supply, and reinjects it back into the atoms. This error signal corresponds to the fluctuations and it is obtained by subtracting the current measured from a stable reference current, using the high-precision current transducer (LEM IT 200-S), winding the cable three times around it, as shown in Fig 2.9, capable of detecting fluctuations as small as 16 μA. We measured the power supply current noise within a 17 kHz bandwidth with $C_1 = 1$ mF, which is approximately 205 μA rms. We generated the reference current by a precision voltage source (Stanford Research Systems DC205), connected across a low-temperature-coefficient resistor (VPG Foil Resistors, 100 Ω, ±2 ppm/K).

The DC205 precision voltage source provides excellent long-term stability and low noise. In the ±10 V output range, the device offers a typical 24-hour output stability

of $\pm(1\,\text{ppm} + 3\,\mu\text{V})$ and a rms voltage noise level below $3\,\mu\text{V}$ in the 20 kHz bandwidth, according to the manufacturer's specifications. Operating in 4-wire (remote sensing) mode, the DC205 adapts to the corresponding voltage on the connection wires, ensuring the programmed voltage appears directly across the load resistor. At an output of around 5 V, the current delivered through the resistor is 50 mA, which corresponds to the maximum output current of the DC205 and it can compensate for max currents in the main coils up to 16.667 A and a magnetic field up to 63.334 G on the atoms. The 24-hour stability approximately 8 μ,V corresponds to 0.1 mG on the atoms. Given the rms voltage noise level and resistor specifications, the corresponding current precision below 20 kHz bandwidth on the main coils is better than $10\,\mu$A rms, which corresponds to 0.04 mG, and the thermal drift is limited to approximately $33\,\mu\text{A/K}$ which corresponds to a drift of 0.127 mG/K on the atoms from the main coils.

The differential current signal, representing the difference between the reference and the measured coil current, is converted into a voltage using a transimpedance amplifier (TIA). This stage uses the OPA277PA precision operational amplifier. The TIA uses a feedback resistor $R_f = 1\,\text{k}\Omega$ in parallel with a capacitor $C_2 = 33\,\text{nF}$, forming a low-pass filter with a cutoff frequency $f_c = 1/(2\pi R_f C_2) \approx 4.8\,\text{kHz}$ (C_2 was tested experimentally to identify the optimal value for later correction). This filtering fixes the correction bandwidth, for example, here attenuating high-frequency noise components while correcting the current noise signal within the frequency range of interest.

After the transimpedance amplifier, the resulting error voltage is further amplified through an inverting amplifier (OP97F) to adjust the gain appropriately. This stage uses a fixed input resistor $R_2 = 2.4\,\text{k}\Omega$ and a tunable feedback resistance R_G between a 0–100 kΩ potentiometer, allowing adjustment of the system gain. The gain of the amplifier is given by $G = -R_G/R_2$, enabling a maximum gain of approximately 41. For our experiments, we need a typical gain of around 19 to provide a good correction.

We included a Twin-T notch filter to suppress internal artifacts from the transducer, the narrow clock noise peak at 17 kHz, caused by its internal clock. This filter provides strong attenuation ($-30\,\text{dB}$) at 17 kHz with a full width at half maximum (FWHM) of 0.96 kHz.

We sent the amplified error voltage to a Thorlabs LDC8005 laser current driver. It has a modulation bandwidth of 100 kHz. The LDC8005 has a current noise level of less than 5 μA rms over a 10 MHz bandwidth, corresponding to 10 μG rms. This driver feeds the compensation coil at max with up to 500 mA with an applied 10 V. The compensation coil is adjusted such that 1 A corresponds to a 2.0 G change in magnetic field.

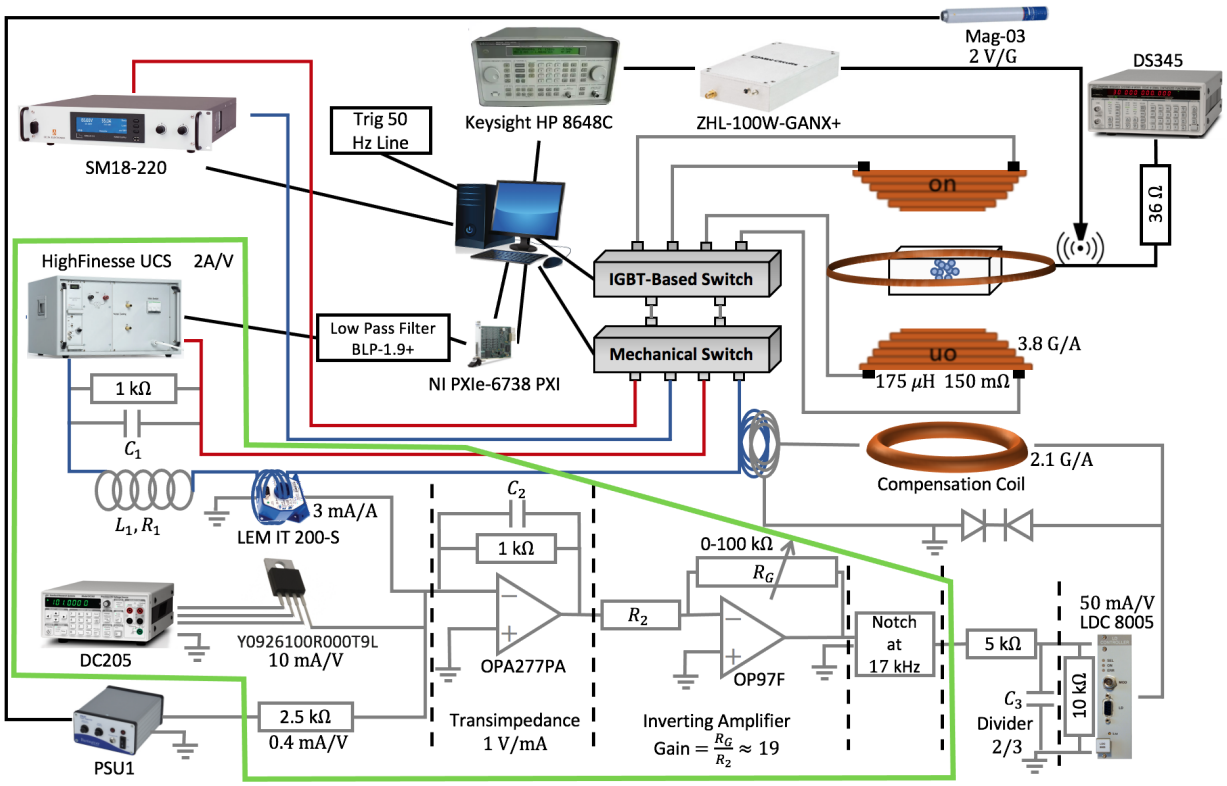


Figure 2.9: Schematic of the active magnetic field compensation circuit. We generate a reference current by applying a stable voltage across a precision resistor and compare it to the current in the main coils, measured by a LEM transducer. The resulting error signal is filtered, amplified, and fed to a current driver, which injects a corrective current into a compensation coil. We include a Twin-T notch filter at 17 kHz to suppress internal transducer noise. We also use a mutual inductance coil to cancel the inductance between the main and compensation coils.

Since the OP97F amplifier can saturate up to 15 V, we apply a voltage divider of ratio 2/3 before the input of the LDC8005 to keep the signal within its acceptable range of 10 V. Given the driver's internal input resistance of 10 kΩ, we place an additional 5 kΩ resistor in series to realize the needed attenuation and to have a safe operation of the LDC driver. In this configuration, the active circuit can correct current fluctuations in the main coil up to approximately ±80 mA or field fluctuations of ±300 mG. Beyond this range, the output voltage would exceed the LDC8005's limit, and the driver would saturate.

A technical challenge arises from the mutual inductance between the large coils and the compensation coil, which can lead to feedback instabilities. To mitigate this effect, we introduced two mutual induction compensation coils: one in series with the big coils and the other in series with the compensation coil. We wound them in opposite directions to cancel their mutual inductances. We calibrate the number of turns experimentally by first measuring the current noise from the power supply using the LEM transducer and a digital multimeter below the 6 kHz bandwidth, with the compensation circuit disabled. We then adjusted the number of windings while activating the compensation circuit, aiming

at maintaining the same noise level with and without compensation.

We abruptly switch off the magnetic field of the main coils during the Stern-Gerlach sequence, leading to a rapid change in magnetic flux. Due to mutual inductance, this sudden variation induces a current spike in the compensation coil. Note that although the system was previously adjusted for mutual inductance, a sudden turn-off introduces high-frequency components that require a different consideration for proper compensation of the mutual inductance. Since the coil is an inductive element, it produces a voltage spike proportional to the rate of current change ($V = L\ dI/dt$), which appears across the output of the LDC8005 driver. To protect the LDC8005 from this overvoltage effect, this could trigger its shutdown protection. We added two Zener diodes in an anti-parallel configuration across the output. These diodes remain inactive under normal conditions but act as a voltage clamp when the output exceeds the Zener threshold in either polarity. They provide a low-resistance path for the induced current, effectively limiting the voltage spike.

The gain of the amplification stage was determined experimentally by adjusting the variable resistor R_G using the Ramsey experiment, as discussed in Eq. (2.1). We first adjusted the gain to its theoretically expected value, ensuring the system remained near the 50-50 population point. To fine-tune the correction, we then intentionally induced a small step change in the magnetic field by varying the current in the main coils by a small amount. We then adjusted the feedback gain in real time by slowly tuning the potentiometer R_G until the Ramsey signal returned to the $50-50$ point. The estimated accuracy is 1%.

To further characterize the compensation circuit performance, we performed a Ramsey measurement. We used a Rabi frequency of approximately 10 kHz, corresponding to $\pi/2$ pulse durations of 25 μs, and a waiting time between the two pulses of 100 μs. At this short evolution time, we were in the linear zone, and the contrast $C(T)$ remained close to 95%, ensuring strong sensitivity to detuning fluctuations. By repeating the experiment over many shots at the 50–50 working point, we extracted the rms magnetic field noise from shot-to-shot variations and found it to be 0.31 mG. This value is comparable to the residual noise observed in the correlation measurements, indicating that our compensation circuit successfully corrected most of the noise originating from the power supply.

The next objective is to further enhance stability by actively correcting for ambient magnetic field fluctuations. This correction includes measuring the ambient magnetic field with a magnetometer, correct for it, and triggering the experiment on the 50 Hz line to synchronize environmental 50 Hz noise across different shots, thereby reducing shot-to-shot fluctuations. We will discuss these strategies and results in the next section.

2.3.7 Ambient Noise Correction

Despite the high performance of the active magnetic field compensation circuit described previously, residual noise from ambient sources, especially the 50 Hz line, can still impact the stability of the magnetic field, To further suppress these effects, we implemented two complementary strategies: synchronization of the experimental sequence to the 50 Hz power line and the integration of an ambient magnetic field sensor into the compensation circuit.

Magnetic field noise from the 50 Hz AC line and its harmonics is a major source of systematic fluctuations in atomic experiments. This noise can vary from shot to shot unless we synchronize the experiment to the 50 Hz line. To address this, we inject the 50 Hz signal directly into the FPGA of the control computer. We convert this signal into a compatible clock used to initiate each experimental cycle at a fixed phase relative to the line. As a result, magnetic perturbations from the 50 Hz line occur at the same phase in each cycle, effectively suppressing their contribution to shot-to-shot noise, while they still exist over an evolution time .

By triggering the 50 Hz line to the experiment, we were able to reduce shot-to-shot fluctuations further. Using a Ramsey experiment centered at the 50–50 point, we were able to reduce the shot-to-shot residual magnetic field fluctuation from 0.31 mG to 0.2 mG. While this does not mean that we eliminate the 50 Hz noise, it now reaches the atoms at a fixed phase in every cycle. For experiments involving time scans at fixed magnetic fields, this introduces a 50 Hz oscillation in the field over time, a point we will address later.

To complement the synchronization strategy and target residual external slow drifts and ambient magnetic field fluctuations, we introduced an additional analog correction path using a high-sensitivity fluxgate magnetometer. We used the Bartington Mag-03 three-axis fluxgate sensor. We placed the sensor approximately 50 cm from the atomic cloud, far enough to avoid sensitivity to the large DC field generated by the Helmholtz coils, but close enough to track ambient fluctuations arising from external sources such as nearby electrical devices or any environmental magnetic noise.

Because the fluxgate sensor measures a different magnetic field than the one seen by the atoms, we needed to determine, for different locations, how sensitive the atoms are to the Gaussmeter measurement. To achieve this, we tested various sensor positions and examined the best correlation measurement, similar to the one obtained with the transducer. We did correlation measurements between the magnetic field noise seen by the atoms (population measurement using Ramsey fringes) and the voltage from the Gaussmeter. All tested spots yielded approximately similar results, indicating that the measurement was insensitive to the position (uniform distribution of magnetic field noise across the lab). We estimated the gain relation from the correlation measurement and connected the magnetometer output to a 2.5 kΩ resistor, chosen to achieve the desired gain. We then connect this resistance to an additional input of the transimpedance amplifier.

This method created a second correction path in the compensation circuit, in addition to the transducer signal.

We found that the correction only works for low-frequency noise and drifts, and it does not directly correct the 50 Hz line noise because it is hard to find a position where the Gaussmeter sees the same 50 Hz field as the atoms, with the same amplitude and phase. This imperfect correction arises because 50 Hz sources in our room or lab are located in various positions near the atoms, making it difficult to find a location where the sensor views the same field as the atoms. As a result, the gain and spatial response for both noise sources differ significantly at all locations. For this reason, we use the Gaussmeter to correct for the large-scale, low-frequency ambient field more effectively.

2.3.8 Final Ramsey Magnetic Field Characterization

After implementing all these stabilization strategies, including active current noise compensation, mutual inductance cancellation, ambient noise correction via a fluxgate sensor, and synchronization of the experimental sequence to the 50 Hz AC line, we performed a full Ramsey interferometric analysis to characterize the residual magnetic field noise.

We performed Ramsey spectroscopy on the $|1\rangle$ to $|2\rangle$ transition in ultracold ^{39}K atoms confined in a crossed optical dipole trap. The atoms experience a magnetic field of 57 G, which sets the Zeeman energy splitting to approximately 40 MHz. The experiment used a cloud of $N \approx 10^6$ atoms at a temperature of $2\,\mu$K in a harmonic trap with frequencies $(\omega_{||}, \omega_{\perp}) = 2\pi \times (62, 300)$ Hz.

The Ramsey sequence consists of two RF $\pi/2$ pulses of $25\,\mu$s each, separated by an evolution time T that we scanned from 0 to 3.5 ms. Each experimental cycle took 11 seconds to complete. We recorded 10 full Ramsey datasets over two hours, each consisting of 70 linearly spaced time points, resulting in a total of 700 data points.

We present the experimental data in Fig. 2.10, showing the population transfer $f(T)$ as a function of time. The blue points represent single-shot measurements. The envelope of the oscillation signals enables us to extract the contrast C(T) of the interferometer, which is better described by a Gaussian curve with an offset (solid blue line) rather than a simple Gaussian decay (dashed blue line). In particular, we previously suppressed the magnetic field gradient, which was measuring 8.9 G/m, and improved the contrast decay. The remaining decay could be due to the magnetic field gradients in the other two directions that we did not compensate for. After averaging over the 10 repetitions of the experiment (black dots in Fig 2.10), this leads to a further decay of the contrast due to the statistical averaging.

To analyze the magnetic field noise, we fit the averaged Ramsey signal $f(T)$ with the

following model:

$$\langle f(T)\rangle = \frac{1}{2}\left[1 - C(T)\,\exp\left(-\frac{1}{2}\sigma^2 T^2\right)\cos(\delta_0(T)\,T + \phi)\right], \tag{2.14}$$

An analysis of the Ramsey data showed a slight variation of the central detuning $\delta_0(T)$ as a function of the evolution time T. We attributed this behavior to the magnetic field oscillation at 50 Hz, which manifests as a phase-dependent shift during the interferometric sequence. Since the maximum Ramsey time (3.5 ms) is much shorter than the 20 ms period of the 50 Hz line, we can approximate the variation of the central detuning as linear:

$$\delta_0(T) = \delta_0(T_{\text{wait}} = 0) + \alpha T.$$

Fitting the experimental data yields $\delta_0(T_{\text{wait}} = 0) = 2\pi \times 1900(5)\,\text{Hz}$ and a slope $\alpha = 2\pi \times 59(3)\,\text{Hz/ms}$.

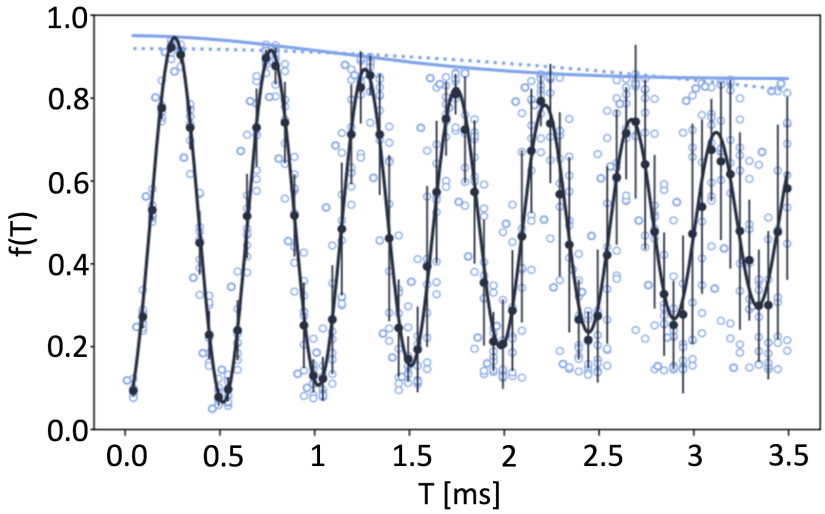


Figure 2.10: Repetitive Ramsey oscillations over 2 hours, showing the fraction f of atoms in state $|1\rangle$ as a function of the evolution time T. Blue circles: single-shot data; black points: average over 10 sequences.

Additionally, we analyzed the standard deviation of $f(T)$ as a function of T, which captures the shot-to-shot fluctuation behavior:

$$\frac{\text{Std}[f(T)]^2}{C(T)^2} = \frac{1}{8}\left(1 + e^{-2\sigma^2 T^2}\cos(2\delta_0 T + 2\phi)\right) - \frac{1}{4}e^{-\sigma^2 T^2}\cos^2(\delta_0 T + \phi). \tag{2.15}$$

Fitting this expression provides the standard deviation of the detuning noise, corresponding to an rms magnetic field fluctuation of $71(4)\,\mu$G. This level of noise is only slightly higher than the value obtained over a shorter 5-minute acquisition window, confirming that the stabilization scheme maintains excellent performance and magnetic field stability over time scales of at least two hours. The data analysis of the Ramsey curve will be detailed further in the thesis of Sara Tiengo.

2.3.9 Feedback Correction of Residual 50 Hz and Harmonics

Even after synchronizing the experimental sequence to the 50 Hz AC line, residual magnetic field oscillations at 50 Hz and its harmonics can still impact atomic coherence. To characterize and eventually correct these contributions, we first quantified their temporal behavior using a phase-resolved Ramsey protocol.

We triggered the experiment on the rising/falling edge of the 50 Hz line signal. We looked at the population as a function of a variable delay time $T_{50\,\mathrm{Hz}}$, which is after the Ramsey sequence: a $\pi/2$ pulse ($25\,\mu$s), followed by a $100\,\mu$s free evolution period, and a second $\pi/2$ pulse ($25\,\mu$s). The system is positioned near the 50-50 point of the Ramsey fringe, operating within the linear response regime previously described.

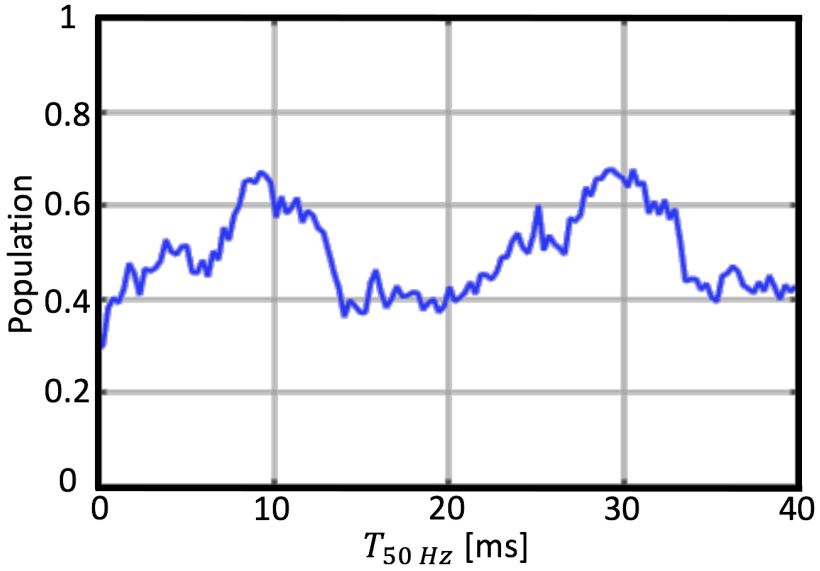


Figure 2.11: population measured after a time $T_{50\,\mathrm{Hz}}$ of a Ramsey sequence. The observed oscillations reflect the magnetic field modulation at 50 Hz and its harmonics experienced by the atoms. We show two full cycles of the line frequency.

By scanning $T_{50\,\mathrm{Hz}}$ over a full 40 ms period (corresponding to two cycles of the 50 Hz line), we directly mapped the time-dependent magnetic field oscillations associated with line noise. The resulting population oscillations reflect the residual magnetic field seen by the atoms as a function of the phase within the 50 Hz cycle, as shown in Fig 2.11.

We then performed a Fourier transform of the measured Ramsey signal as a function of $T_{50\,\mathrm{Hz}}$, showing the spectral content of the residual field fluctuations. This analysis allowed us to identify the amplitudes and frequencies of the dominant components at 50 Hz and harmonics. From the measured population modulation, we infer a peak-to-peak magnetic field fluctuation at 50 Hz of approximately 0.9 mG, representing a deterministic

component of the residual noise. The 50 Hz noise depends on the position of 50 Hz sources in the lab.

Since components remain stable and repeatable from shot to shot, we can cancel them using a pre-programmed corrective signal, as shown in Fig. 2.9. We generate this signal by a DS345 function generator connected to a 36 Ω load, phase-locked to the experimental trigger (or 50 Hz trigger), and injected into an auxiliary compensation coil called comp Y. The comp Y coil has a calibration of 52.3 mG/A. We must calibrate the injected signal each day to account for signal variations. After this feedforward correction, we measured an rms magnetic field fluctuation below 100 μG over the full 40 ms period, while this configuration was not used for the Ramsey sequence in this paper [63] or in subsequent experiments due to the daily calibration overhead.

2.3.10 Characterizing Noise Spectrum

Following the detailed Ramsey characterization of magnetic field fluctuations, we turn to a complementary diagnostic tool: noise spectroscopy via dressed-state sweeps, as described in Section 2.3.3. For our interaction experiments, it is essential to remain in the lower dressed state $|-\rangle$. Magnetic noise at frequencies near Ω can resonantly drive transitions to the upper state $|+\rangle$.

After analyzing the results of the noise spectroscopy sweeps using a hold time $T_2 = 20\,\text{ms}$, we observed that residual noise components below 5 kHz were still visible, and induced unwanted transitions to the upper dressed state $|+\rangle$ as seen in Fig. 2.12.

To identify the source of this noise, we wanted to determine whether it originates from the power supply or the electronic correction circuit itself. We therefore conducted direct noise spectrum measurements using a Rohde & Schwarz FSV signal analyzer. We placed a T-connector before the notch filter, and we connected one branch to the spectrum analyzer, while adjusting the reference current to have 0 V.

To identify the noise contribution of the compensation electronics, we first switched off the power supply and disconnected the Gaussmeter. As shown in Fig. 2.13, the spectrum clearly reveals noise components from the electronics extending up to approximately 5 kHz, and shows the transducer's internal 17 kHz clock artifact. These measurements show that the correction circuit itself introduces non-negligible noise within the frequency band relevant to our Rabi frequency.

Previous measurements showed that both the power supply and the compensation circuit still exhibit noise at frequencies below 7 kHz, which transitions some atoms to the upper dressed state. To address this, we reduced the correction bandwidth of the compensation circuit by increasing the feedback capacitance C_2 in the transimpedance

amplifier. Additionally, we further reduce the power supply's bandwidth so that the correction circuit can work effectively at a lower bandwidth without missing noise components.

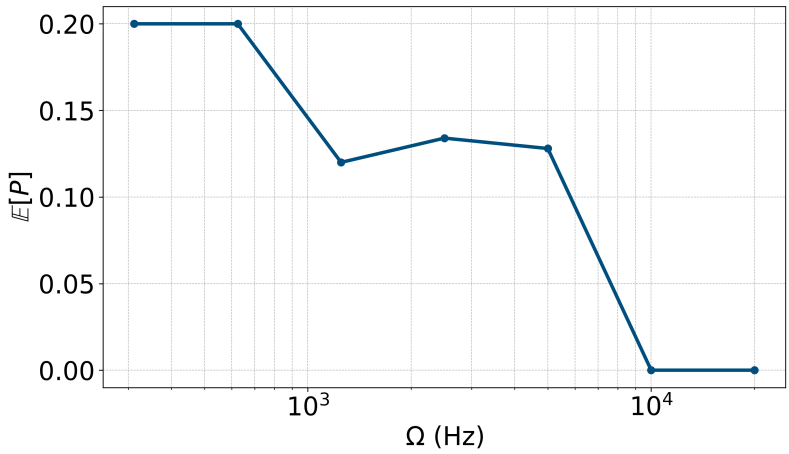


Figure 2.12: Noise spectroscopy measurement: transition probability $\mathbb{E}[P]$ as a function of the Rabi frequency Ω, obtained using dressed-state sweeps with a hold time $T_2 = 20\,\text{ms}$. Each data point corresponds to the mean population transferred to $|1\rangle$, averaged over 5 repetitions. The measurement shows the frequency spectrum of magnetic field noise near the Rabi coupling frequency.

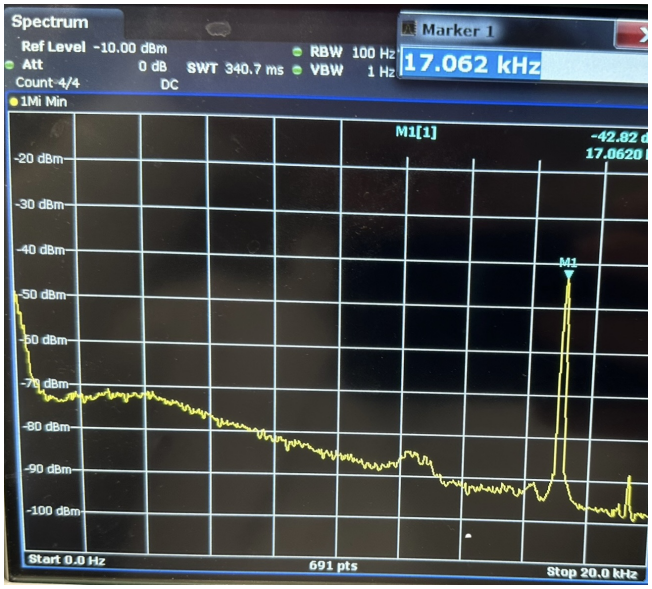


Figure 2.13: Noise spectrum of the compensation electronics measured before the notch with the Rohde & Schwarz FSV analyzer, with the power supply and gaussmeter disconnected. The electronics show broadband noise below 5 kHz and a narrow peak at 17 kHz, corresponding to the LEM transducer's internal clock.

While increasing C_2 or adding a new capacitor at the input of the driver, as shown in Fig 2.9 would reduce high-frequency noise from the electronics, it would also compromise the compensation circuit's ability to respond to fast fluctuations from the power supply which has already noise components below the 5 kHz, potentially leaving noise components uncorrected. For this reason, both filters are important.

We performed a second spectrum analysis while keeping the power supply on and delivering a current of approximately 15 A to the coils. Since the Rohde & Schwarz spectrum analyzer cannot accept DC voltages at its 50 Ω input, we compensated the DC shift using the DC205 precision voltage source. This setup allowed us to isolate and measure the AC noise components. The resulting spectrum measurement is shown in Fig. 2.14.

To further reduce noise in the low-frequency range (below 5 kHz), we focused on limiting the effective bandwidth of the power supply itself. As discussed previously in Eq. (2.13), since the power supply is not an ideal current source and its output depends on the load impedance, modifying C_1 alone did not yield optimal results.



Figure 2.14: Noise spectrum of the compensation electronics measured with the Rohde & Schwarz FSV signal analyzer, with the power supply delivering 15 A. The configuration used $C_1 = 1\,\text{mF}$ and $C_2 = 33\,\text{nF}$. The plots display broadband noise below 5 kHz, with clear spectral features. Left: full spectrum from 10 Hz to 20 kHz with 100 Hz resolution bandwidth. Right: zoomed-in spectrum from 10 Hz to 3 kHz with 20 Hz resolution bandwidth, highlighting prominent 50 Hz harmonics and low-frequency noise contributions from the power supply and compensation circuit.

To overcome this limitation, we decided to increase the inductance in the circuit. As illustrated in Fig. 2.9, we added a high inductance $L_1 = 7.75\,\text{mH}$ in series, with internal resistance $R_1 = 190\,\text{m}\Omega$, positioned away from the atomic cloud. Combined with a capacitance of $C_1 = 200\,\mu\text{F}$, this configuration led to improved performance. By applying a step

function to the current supply, we observed that the magnetic field takes approximately 25 ms to reach its steady-state value. We reduced the internal RMS noise from the power supply (in the band below 5 kHz) from approximately 0.75 mG to 0.3 mG. Furthermore, the spectral analysis showed that the circuit concentrated most of the noise below 1 kHz.

Given this configuration, we also reconsidered the filtering strategy at the input of the current driver. Instead of reducing the transimpedance amplifier bandwidth by increasing C_2, we added a capacitor C_3 as shown in Fig 2.9 to filter the correction signal and the higher frequency noise of the previous electronic components, just before it enters the LDC8005 current driver.

Since the power supply spectrum is now below 1 kHz, this approach allows for more filtering of the compensation signal without compromising correction performance. We tested different values of the filter capacitor C_3, ranging from 33 nF to 100 nF, which corresponds to cutoff frequencies between approximately 700 Hz and 320 Hz. Due to these final optimizations, we were able to reach Rabi frequencies as low as 1 kHz without observing any transfer to the upper dressed state $|+\rangle$, even for long hold times up to 100 ms. We adopted this technique for the experiments presented in Chapters 3 and 4.

2.4 Chapter Conclusion

In this chapter, we have developed and calibrated a magnetic field stabilization system for experiments with ultracold ^{39}K atoms. Starting from the limitations of the original setup, we implemented a series of passive and active filtering to reduce magnetic noise over a broad range of frequencies. These include LC filtering of the power supply, precision current measurement with LEM transducers, and an active compensation circuit capable of reducing noise to sub-milligauss precision.

We characterized the magnetic field noise using Ramsey interferometry and dressed-state noise spectroscopy to demonstrate that the system can achieve relative field stability below 2 ppm on a 57 G bias. Additionally, we diagnosed and suppressed noise near the Rabi frequency, which strongly influences population in the lower dressed state $|-\rangle$, by combining spectral analysis with bandwidth reduction techniques.

Finally, we demonstrated the ability to reach Rabi frequencies as low as 1 kHz without any measurable transfer to the upper dressed state, even for hold times as long as 100 ms. This level of control over magnetic field fluctuations is the path for the high-precision interaction studies presented in the next chapter, where dressed-state stability also facilitates the exploration of beyond-mean-field effects in spinor condensates.

CHAPTER

Mean-Field Description of an RF-Dressed Bose-Einstein Condensate 3

3.1 Chapter Introduction

In many physical systems, the response is linear when the external drive is weak. However, as the strength of the perturbation increases, nonlinearities give rise to a diverse set of phenomena such as harmonic generation, self-focusing, and saturation effects [104, 105, 106]. These nonlinear responses often manifest through higher-order terms in a Taylor expansion of the system's susceptibility. Yet, such expansions are only valid in regimes where the perturbation remains sufficiently small. In the strong-drive limit, saturation becomes dominant, and the system response may deviate from any polynomial expansion.

An example of this effect is in the field of ultracold atomic gases. In dilute Bose-Einstein condensates (BECs), interactions between atoms are typically weak and well described by mean-field theory [83]. The nonlinear term in the energy arises from two-body contact interactions, scaling with the square of the density. At higher precision, quantum fluctuations lead to a correction scaling as $n^{5/2}$, the so-called Lee-Huang-Yang (LHY) term [56], which contributes to form quantum droplets in Bose mixtures [107, 59]. While higher-body interactions are usually negligible in the dilute regime [108, 109, 110], recent studies in our team have shown that coherent coupling between internal states can modify this picture [95].

By coherently coupling a two-component Bose-Einstein Condensate, in the lower dressed state, both may experience reduced two-body interaction [53] and large three-body interactions that are due to possible virtual excitations during collisions [85]. Such three-body processes are increasingly important when the ratio γ of the two-body interaction strength to the coupling strength is increased, and their effects in the equation of state were experimentally measured [60, 61].

In this chapter, we consider the situation where γ is much lower than one and demon-

strate a saturation effect of the interaction mean-field energy. In this regime of strong nonlinear behavior, the equation of state can no longer be described as a Taylor series expansion as a function of the density. The saturation effect is captured within a mean-field framework, as shown below.

The chapter is organized as follows. We first describe the coupled system Hamiltonian and theoretically explain the effect in a homogeneous system (with a given density). Second, we present our experiment using ^{39}K atoms. We explain the preparation of the condensates in the dressed state and the measurement of the interaction energy through one-dimensional time-of-flight expansions. As the experiment lies in the 1D to 3D crossover regime, we finally compare our results with imaginary-time Gross-Pitaevskii simulations including the two spin states and the coupling, as well as the radial trap. A good match, with no fit parameter, confirms our interpretation of the data.

3.2 Mean-Field Energy Functional in the Dressed Basis

We begin by formulating the many-body Hamiltonian for a coherently coupled two-component Bose-Einstein condensate in the second quantization formalism. The field operators $\hat{\psi}_s(\vec{r})$, with $s = 1, 2$, annihilate a boson in spin state s at position $\vec{r}$. The total Hamiltonian includes four contributions: the kinetic energy, the coherent (Rabi) coupling, the two-body interaction, and the external trapping potential:

$$\hat{H} = \hat{H}_{\text{kin}} + \hat{H}_{\text{Rabi}} + \hat{H}_{\text{Int}} + \hat{H}_{\text{ext}}. \tag{3.1}$$

In the following, we consider a spatially uniform system in free space. In this case, we don't consider an external potential. The field operators can be taken as spatially independent, such that $\hat{\psi}_s(\vec{r}) = \hat{\psi}_s$, and we neglect the kinetic energy contribution ($\hat{H}_{\text{kin}} = 0$). The relevant Hamiltonian thus reduces to the Rabi coupling and the interaction terms:

$$\hat{H} = \hat{H}_{\text{Rabi}} + \hat{H}_{\text{Int}}.$$

The Rabi term describes the coherent coupling between spin components as:

$$\hat{H}_{\text{Rabi}} = \hbar \int d\vec{r} \left[\frac{\delta}{2} \left(\hat{\psi}_1^\dagger \hat{\psi}_1 - \hat{\psi}_2^\dagger \hat{\psi}_2 \right) - \frac{\Omega}{2} \left(\hat{\psi}_1^\dagger \hat{\psi}_2 + \hat{\psi}_2^\dagger \hat{\psi}_1 \right) \right], \tag{3.2}$$

where δ is the detuning and Ω is the Rabi frequency of the coupling.

The interaction Hamiltonian accounts for contact interactions between atoms in the same or different spin states:

$$\hat{H}_{\text{Int}} = \frac{1}{2} \int d\vec{r} \left[g_{11}\, \hat{\psi}_1^\dagger \hat{\psi}_1^\dagger \hat{\psi}_1 \hat{\psi}_1 + g_{22}\, \hat{\psi}_2^\dagger \hat{\psi}_2^\dagger \hat{\psi}_2 \hat{\psi}_2 + 2 g_{12}\, \hat{\psi}_1^\dagger \hat{\psi}_2^\dagger \hat{\psi}_2 \hat{\psi}_1 \right], \tag{3.3}$$

where g_{ij} denotes the interaction strength between components i and j.

To compute the energy functional, we apply the mean-field (Gross-Pitaevskii) approximation by replacing the quantum field operators with classical complex fields:

$$\hat{\psi}_s \to \psi_s,$$

where $\psi_s = |\psi_s|\, e^{i\phi_s}$ for spin component s, written in terms of its amplitude $|\psi_s|$ (assumed real and positive) and phase ϕ_s.

Therefore, the total mean-field energy functional is: $E_{MF} = E_{\text{Rabi}} + E_{\text{Int}}$, where

$$E_{\text{Rabi}} = \int d\vec{r} \left[\frac{\hbar\delta}{2}(|\psi_1|^2 - |\psi_2|^2) - \hbar\Omega|\psi_1||\psi_2| \cos(\phi_2 - \phi_1) \right] \tag{3.4}$$

$$E_{\text{Int}} = \frac{1}{2} \int d\vec{r} \left[g_{11}|\psi_1|^4 + g_{22}|\psi_2|^4 + 2g_{12}|\psi_1|^2|\psi_2|^2 \right] \tag{3.5}$$

The ground state corresponds to the configuration that minimizes the total mean-field energy. Among all terms, only the Rabi coupling depends on the relative phase $\phi_2 - \phi_1$, and energy minimization sets this phase difference such that $\cos(\phi_2 - \phi_1) = 1$.

We now consider the system to be in a coherent superposition of the two bare spin states, described by a single macroscopic wave function with global density n. For a uniform gas, the spinor components can be written as:

$$(\ |\psi_1|\ , |\psi_2|\ ) = \sqrt{n}\ (\ \cos(\theta/2)\ , \sin(\theta/2)\ )$$

Where θ is a mixing angle that determines the spin composition of the coherent state. Substituting these expressions into Eqs. (3.4) and (3.5), the energy per particle can be expressed in terms of n and θ as:

$$\frac{E_{\text{Rabi}}}{N} = -\hbar\delta \left(\frac{\cos^2(\theta/2) - \sin^2(\theta/2)}{2} \right) - \hbar\Omega\ \sin(\theta/2)\cos(\theta/2) \tag{3.6}$$

$$\frac{E_{\text{int}}}{N} = \frac{n}{2} \left[g_{11} \sin^4(\theta/2) + g_{22} \cos^4(\theta/2) + 2g_{12} \sin^2(\theta/2)\cos^2(\theta/2) \right] \tag{3.7}$$

To simplify the interaction terms, we apply the parameters $\bar{g}$, $\tilde{g}$, δg defined in Eq 1.68 and using the trigonometric identities $\sin^2(\theta/2) = \frac{1-\cos\theta}{2}$, $\cos^2(\theta/2) = \frac{1+\cos\theta}{2}$, and $\sin(\theta/2)\cos(\theta/2) = \frac{1}{2}\sin\theta$, we can rewrite the mean field energy per particle as:

$$\boxed{\frac{E_{MF}}{N} = -\frac{\hbar\delta}{2}\cos\theta - \frac{\hbar\Omega}{2}\sin\theta + \frac{n}{2}\left[\tilde{g} - \delta g\cos\theta - \bar{g}\sin^2\theta\right]} \tag{3.8}$$

This expression corresponds to the mean-field energy per particle in a general coherent spin state. The first term corresponds to the Rabi energy contribution in the $|-\rangle$, and the

second term corresponds to the interaction strength g_{--}^{--} found previously.

If we perform the substitution $\theta \to \theta + \pi$, which corresponds to a maximization of the energy per particle:

$$\boxed{\frac{E_{MF}}{N} = +\frac{\hbar\delta}{2}\cos\theta + \frac{\hbar\Omega}{2}\sin\theta + \frac{n}{2}\left[\tilde{g} + \delta g\cos\theta - \bar{g}\sin^2\theta\right]} \tag{3.9}$$

The first term corresponds to the Rabi energy in the $|+\rangle$ dressed state, and the second term corresponds to an interaction strength characterized by g_{++}^{++} described previously in chapter 1.

3.3 Equation of State and Spin Composition

We now want to determine the equilibrium configuration by minimizing the total energy per particle with respect to the mixing angle $\theta \in [0, \pi]$, which determines the spin composition of the dressed state. This minimization is equivalent to allowing the system to self-adjust its internal spin mixture to lower its total energy, balancing the Rabi coupling, detuning, and mean-field interaction terms.

Since θ controls the relative population $P_{|1\rangle\to|+\rangle}, P_{|2\rangle\to|+\rangle}, P_{|2\rangle\to|-\rangle}, P_{|1\rangle\to|-\rangle}$ of the bare spin components as shown in Eqs. (1.53) and (1.54), minimizing Eqs. (3.8) and (3.9) with respect to θ yields the equation of state that governs the condensate dressed state spin composition :

$$\boxed{\frac{\delta}{\Omega} = \cot\theta - \frac{n\delta g}{\hbar\Omega} + 2\frac{n\bar{g}}{\hbar\Omega}\cos\theta} \tag{3.10}$$

If we perform the substitution $\theta \to \theta + \pi$,

$$\boxed{\frac{\delta}{\Omega} = \cot\theta - \frac{n\delta g}{\hbar\Omega} - 2\frac{n\bar{g}}{\hbar\Omega}\cos\theta} \tag{3.11}$$

It is often more intuitive to work in terms of relative population. However, expressing θ explicitly in terms of P via the relations given in Eqs. (1.53) and (1.54) leads to a complicated quartic equation in P that doesn't have a simple analytical solution. Therefore, we solve the equation of state numerically. The result is shown below in Fig 3.1.

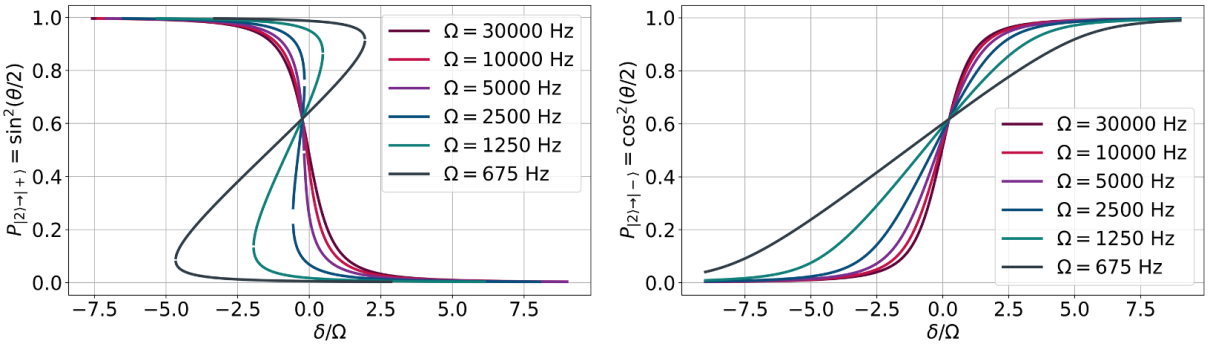


Figure 3.1: The relative population in dressed state as a function of δ/Ω, for several Rabi frequencies Ω. The left panel shows $P_{|2\rangle\to|+\rangle} = \sin^2(\theta/2)$ obtained from Eq. 3.10, while the right panel shows $P_{|2\rangle\to|-\rangle} = \cos^2(\theta/2)$ from Eq. 3.11. The atomic density $n = 2 \times 10^{20}\,\mathrm{m}^{-3}$, and interaction strength $g_{11} = 84.3\,g_0$, $g_{22} = 33.3\,g_0$, $g_{12} = -53.21\,g_0$, where $g_0 = \frac{4\pi\hbar^2}{m}a_0$. For these parameters, the dimensionless interaction coefficients vary as follows: $\epsilon \in [0.031, 1.36]$, $\gamma \in [0.065, 2.89]$.

The population behavior governed by Eqs. (3.11) and (3.10) depends on the dimensionless ratios $\epsilon = \frac{n\delta g}{\hbar\Omega}$ and $\gamma = \frac{n\bar{g}}{\hbar\Omega}$, which quantify the strength of interactions relative to the Rabi energy. As Ω increases (30 kHz), these ratios become small, and the system approaches the non-interacting Rabi-dressed regime. In this limit, the population curves recover the standard dressed-state behavior characterized and presented previously in Fig. 1.7, where the corresponding values of the dimensionless ratios are around 0.031 and 0.065.

In contrast, when we reduce Ω, the interaction energy becomes comparable to or larger than the Rabi energy, and interaction effects start to dominate. We illustrate this in Fig. 3.1 for the lowest Ω case (675 Hz), where the ratios ϵ and γ increases up to 1.36 and 2.89 with a fixed atomic density $n = 2 \times 10^{20}\,\mathrm{m}^{-3}$. Under these conditions, the population curve for the atoms in the lower dressed state exhibits a much smoother transition. In contrast, the atoms in the upper dressed state display bistable and hysteretic behavior.

3.4 Physical Interpretation and Low-Density Expansion

To better understand the influence of interactions on the dressed-state properties, we analyze the equation of state by expressing it in the original bare spin basis. Starting from the dressed-state minimization conditions in Eqs. (3.11) and (3.10), we can rearrange the result into the generic form:

$$\cot\theta = \frac{\delta'}{\Omega} \tag{3.12}$$

where the effective detuning δ' captures the modification of the level splitting induced by mean-field interactions.

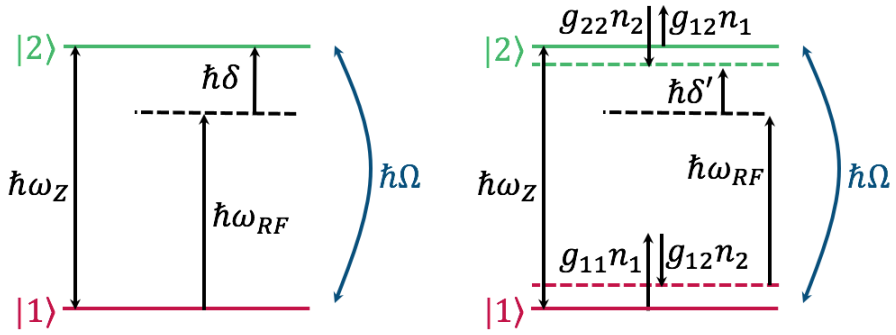


Figure 3.2: Schematic illustration of the interaction-induced shift of the detuning in a two-level Rabi-coupled system. Left: bare two-level system with detuning δ. Right: interacting case, where mean-field shifts result in an effective detuning δ'.

By expressing the densities n_1 and n_2 in the bare spin states, the effective detuning becomes:

$$\delta' = \delta + \frac{1}{\hbar}\left(n_1 g_{11} + n_2 g_{12} - n_2 g_{22} - n_1 g_{12}\right) \tag{3.13}$$

This expression reveals that the two spin components acquire different mean-field energy shifts due to interactions. An atom in spin state $|1\rangle$ sees an energy shift $n_1 g_{11} + n_2 g_{12}$, while an atom in $|2\rangle$ experiences $n_2 g_{22} + n_1 g_{12}$. These shifts the bare detuning δ, effectively shifting the resonance condition and modifying the equilibrium spin mixing angle θ. This interpretation is schematically illustrated in Fig. 3.2.

To better understand the problem, we perform a Taylor expansion of the mean-field energy per particle around the low-density limit, where the dimensionless interaction ratio $\epsilon, \gamma \ll 1$. The energy in Eq. (3.8) then expands as:

$$\frac{E_{MF}}{N}(n) \approx \left.\frac{E_{MF}}{N}\right|_{n=0} + n\left.\frac{d}{dn}\left(\frac{E_{MF}}{N}\right)\right|_{n=0} + \frac{n^2}{2}\left.\frac{d^2}{dn^2}\left(\frac{E_{MF}}{N}\right)\right|_{n=0} + \mathcal{O}(n^3) \tag{3.14}$$

We identify the physical meaning of each term as follows:

- Zeroth-order term: the Rabi energy of a single atom in the lower dressed state:

$$\frac{E_{MF}^{(0)}}{N} = \left.\frac{E_{MF}}{N}\right|_{n=0} = -\frac{\hbar\Omega}{2}\sqrt{1 + \left(\frac{\delta}{\Omega}\right)^2} \tag{3.15}$$

- Linear term: the mean-field interaction energy with a two-body coupling g_{--}^{--} in the dressed basis:

$$\frac{E_{MF}^{(1)}}{N} = n\left.\frac{d}{dn}\left(\frac{E_{MF}}{N}\right)\right|_{n=0} = \frac{n\, g_{--}^{--}(\delta/\Omega)}{2} \tag{3.16}$$

- Quadratic term: a nonlinear correction analogous to an effective three-body interaction:

$$\frac{E_{MF}^{(2)}}{N} = \frac{1}{2}\frac{d^2}{dn^2}\left(\frac{E_{MF}}{N}\right)\Big|_{n=0} = \frac{n^2\, g_3}{3} \tag{3.17}$$

where the effective three-body interaction coefficient g_3 reads:

$$g_3\left(\frac{\delta}{\Omega}, \frac{1}{\Omega}\right) = -\frac{3(\delta g)^2}{4\hbar\Omega}\cdot\frac{1}{\left(1+\frac{\delta^2}{\Omega^2}\right)^{3/2}} - \frac{3\bar{g}^2}{\hbar\Omega}\cdot\frac{\left(\frac{\delta}{\Omega}\right)^2}{\left(1+\frac{\delta^2}{\Omega^2}\right)^{5/2}} + \frac{3\delta g\,\bar{g}}{\hbar\Omega}\cdot\frac{\frac{\delta}{\Omega}}{\left(1+\frac{\delta^2}{\Omega^2}\right)^{2}} \tag{3.18}$$

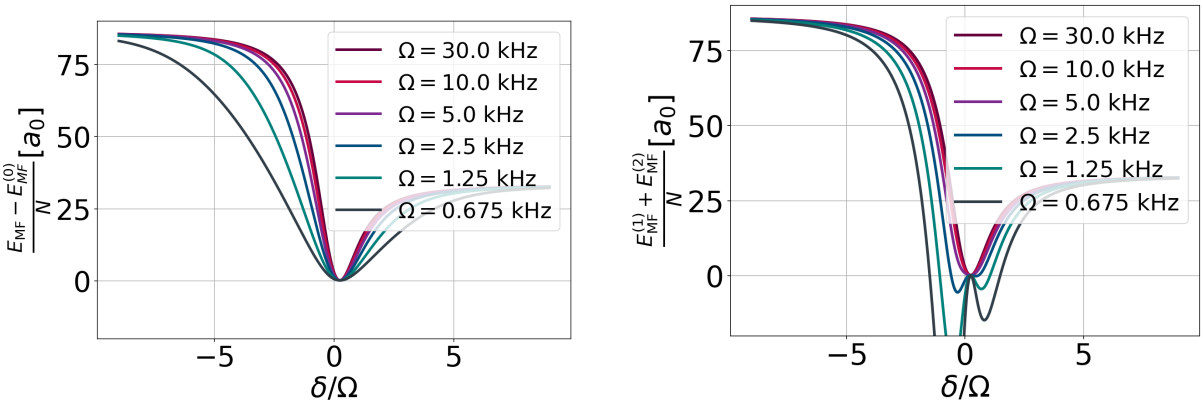
In the previous framework, the quadratic term involving g_3 is a quadratic correction to two-body interactions due to the density dependence of the mixing angle $\theta(n)$. This term can also be understood from a different perspective .

As shown in Ref. [85], this term originates from genuine three-body processes that emerge in the dressed-state basis through a perturbative treatment of the many-body Hamiltonian. Although a full analysis requires going to third-order perturbation theory, the presence of this effective three-body term can already be captured at second order. The detailed derivation and discussion of these contributions are left to the thesis of Sara Tiengo [85].

In the present chapter, we aim to study a highly nonlinear regime, $\gamma \gtrsim 1$, where the previous description is no longer applicable. We would rather rely on the exact solution in the mean-field framework.

3.5 Mean-Field Energy: Exact vs Perturbative in Density

We evaluate the mean-field energy per particle in the dressed state from Eq. (3.8), excluding the zeroth-order term corresponding to the non-interacting Rabi contribution (i.e., the energy of the dressed state at zero density). The mixing angle θ is determined by numerically solving the self-consistent equation of state (3.10). The resulting energy, which includes all orders in density, is shown in the left panel of Fig. 3.3 as a function of δ/Ω. In the right panel, we plot the approximate energy obtained from the Taylor expansion, which includes only the linear and quadratic terms.



(a) Exact mean-field energy (excluding the zeroth-order term), obtained from numerical minimization of the equation of state.

(b) Taylor expansion including two-body and effective three-body interaction terms.

Figure 3.3: Comparison of the interaction energy per particle in a coherently coupled BEC as a function of δ/Ω for various Rabi frequencies. Parameters: atomic density $n = 2 \times 10^{20}\,\mathrm{m}^{-3}$, $g_{11} = 84.3\,g_0$, $g_{22} = 33.3\,g_0$, $g_{12} = -53.21\,g_0$. Energies are expressed in units of $\frac{g_0 n}{2}$, with $g_0 = \frac{4\pi\hbar^2 a_0}{m}$.

These two graphs illustrate how the coupling between Rabi and interatomic interactions influences the condensate energy across different coupling strengths. By comparing the exact and perturbative results, one can identify the range of Rabi frequencies (i.e., values of Ω) for which the Taylor expansion remains valid at a specific atomic density.

At high Rabi frequencies, typically $\Omega = 30\,\mathrm{kHz}$ down to around $10\,\mathrm{kHz}$, both curves left and right in Fig. 3.3 exhibit the same overall behavior. In this regime, where ϵ and γ are small, the system follows the form given by the effective two-body interaction g_{--}^{--} in the dressed basis. This behavior is expected in the limit $\Omega \to \infty$.

However, as Ω decreases, interaction effects become comparable and larger than the Rabi energy. In the left panel, which displays the exact mean-field energy, we observe that the width of the dip in the energy curve broadens significantly when $\Omega \lesssim 5\,\mathrm{kHz}$. This feature reflects a significant modification of the spin composition resulting from interactions. On the right panel, the second-order Taylor expansion fails to capture this behavior: it begins to predict unphysical negative interaction energies at low Rabi frequencies, which is clearly incorrect. This breakdown suggests that higher-order terms and a comprehensive treatment of the energy functional are required in this regime. Our goal is to access this low-Rabi regime experimentally, where the exact mean-field theory becomes crucial for accurately describing the interaction energy.

Finally, for both curves in the far-detuned limits $\delta/\Omega \to \pm\infty$, the system becomes fully polarized in one of the bare spin states $|1\rangle$ and $|2\rangle$. In this case, the interaction energy per particle is given by the corresponding bare-state interaction energy, either $g_{11}n/2$ or

$g_{22}n/2$, depending on the bare spin component.

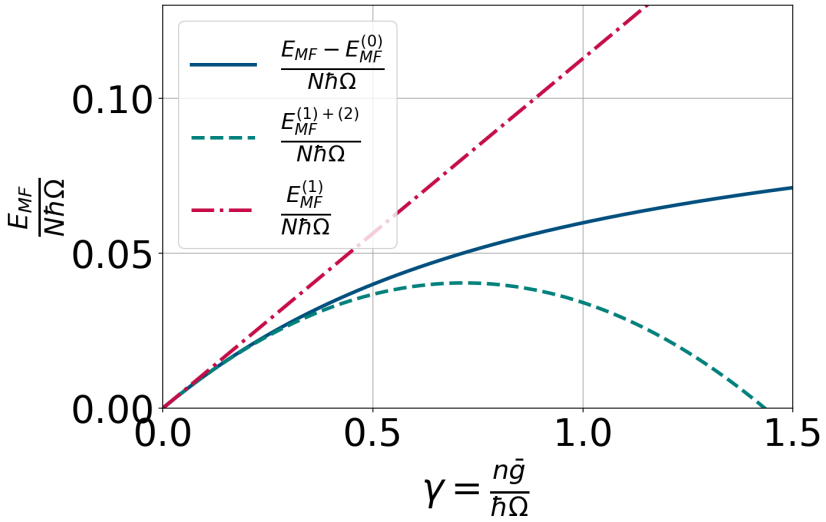


Figure 3.4: Energy per particle per Rabi energy in the $|-\rangle$ dressed state as a function of the dimensionless parameter $\gamma = \frac{n\bar{g}}{\hbar\Omega}$, at fixed $\delta/\Omega = 1$. The solid line shows the full numerical mean-field result (excluding the zeroth-order Rabi term), the dashed curve includes the linear and quadratic terms in density from Taylor expansion, and the dash-dotted line shows only the linear contribution.

To deepen our understanding of the nonlinear interaction energy, we simulate the mean-field energy per particle in the $|-\rangle$ dressed state as a function of the dimensionless interaction parameter $\gamma = \frac{n\bar{g}}{\hbar\Omega}$, while fixing the detuning ratio at $\delta/\Omega = 1$. The energy is normalized by $\hbar\Omega$ and plotted in Fig. 3.4. The plotted curves compare the exact numerical solution (excluding the zeroth-order Rabi contribution) with the first-order (two-body) and second-order (two and three-body) Taylor expansions.

For the exact solution, in the low-density regime where $\gamma \ll 1$, the energy grows linearly with density, with a slope given by $g_{--}^{--}/2$, corresponding to the dressed-state two-body interaction. As γ increases, the energy curve begins to bend due to interaction-induced modification of the spin composition. At large γ, the curve saturates into a new linear regime with a smaller slope, $g_{\min}/2$, where

$$g_{\min} = \frac{g_{11}g_{22} - g_{12}^2}{g_{11} + g_{22} - 2g_{12}}.$$

This effective coupling strength reflects the energy at the minimum of the curve in Fig. 3.3, and can vanish in the case where $g_{12} = \sqrt{g_{11}g_{22}}$.

In comparison, the Taylor expansion at low γ reproduces the linear behavior accurately through the two-body term. As interactions increase, the next-order correction, the

effective three-body term, accounts for the curvature of the energy curve up to a certain value of γ. This defines the regime where the three-body approximation remains valid. However, beyond this point, the expansion fails to capture the correct asymptotic behavior, and only the exact solution can describe the energy in the strong interaction regime.

Experimentally, it is more practical to tune γ by varying the Rabi frequency Ω rather than the density. In this approach, the observed nonlinear behavior of the energy curve manifests as a broadening of the energy dip in the interaction energy versus δ/Ω curves (see Fig. 3.3a). In the high γ regime, the three-body expansion overestimates the energy and may even predict unphysical behavior, underscoring the need for a full non-perturbative treatment.

3.6 Previous Observation in the Low Density Regime

While our experiments aim to explore the density-dependent interaction of coherently coupled Bose-Einstein condensates (BECs), it is helpful to recall previous studies on dressed-state BECs. Two notable demonstrations are particularly relevant: the work by Hammond *et al.* [95] and Sanz *et al.* [53].

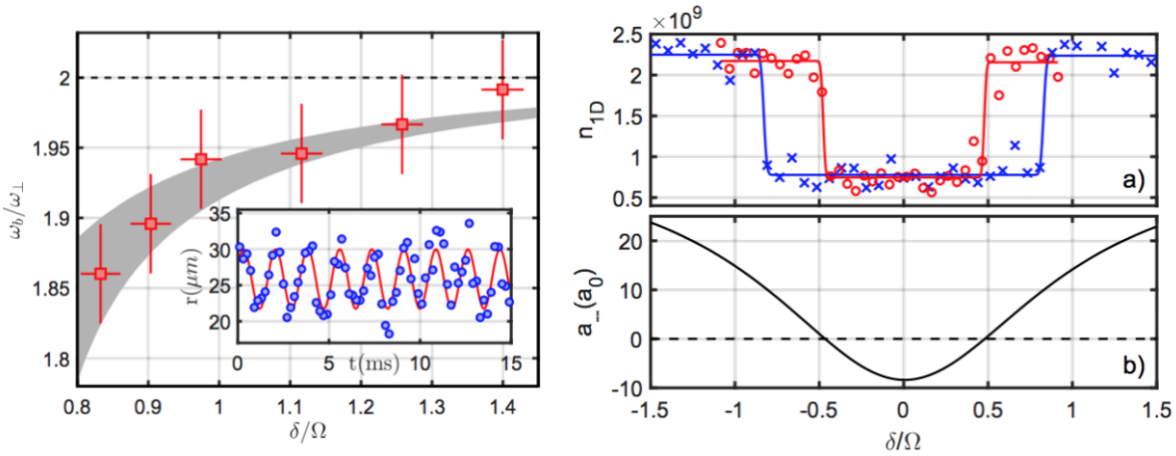


Figure 3.5: Experimental signatures of the three-body interaction term in the dressed-state BEC, taken from Ref. [95]. Left panel: Downshift of the radial breathing mode frequency $\omega_b/\omega_\perp$ measured as a function of δ/Ω in the symmetric interaction configuration where $g_{11} = g_{22}$. The shaded region represents theoretical predictions including the g_3 term. Right panel: Radial collapse observed via a sudden drop in peak 1D density, even in regimes where the dressed two-body scattering length $a_{--} > 0$. This behavior confirms the presence of an attractive term.

Our recent experimental results and analysis are built on earlier work, as presented in Ref. [95], which demonstrated experimentally the presence of the nonlinear three-body term in the energy functional. They performed the study in the symmetric interaction regime where $g_{11} = g_{22}$, which can be realized in ^{39}K by tuning the magnetic field near 54.69 G. In this configuration, the interaction asymmetry term δg vanishes, and the two-body interaction strength in the dressed basis g^{--}_{--} transitions from negative to positive values as a function of δ/Ω.

They demonstrated the presence of the three-body quadratic term from two independent experimental measurements: (1) a downshift of the radial breathing mode frequency in an elongated condensate (left panel in Fig 3.5), and (2) a radial collapse threshold observed even for positive dressed-state scattering length $a_{--}(a_0) > 0$ (right panel in Fig 3.5). These measurements where made in the $\gamma \ll 1$ regime

3.7 Experimental Protocol for Measuring Population and Nonlinear Behavior of the Interaction Energy

Our measurement protocol begins with the preparation of a Bose-Einstein condensate of ^{39}K atoms in the spin state $|2\rangle$, confined in a crossed optical dipole trap with trapping frequencies $(\omega_\perp, \omega_{||}) = (169, 26)$ Hz. We achieved the coherent coupling to the $|1\rangle$ state via a radio-frequency (RF) field of 41.080 MHz. The magnetic field corresponds to $B = 56.85$ G to tune the intra- and interspin scattering lengths to $a_{22} = 84.30\, a_0$, $a_{11} = 33.30\, a_0$, and $a_{12} = -53.21\, a_0$.

To access the interaction energy of the system, the condensate is first adiabatically prepared in the lower dressed state $|-\rangle$, and the axial confinement is then removed to allow for longitudinal expansion. In the long-time ballistic regime, assuming the initial kinetic energy is negligible, the root-mean-square (rms) size σ_{Int} of the cloud after a time-of-flight duration t_{tof} permits us to extract the interaction energy per particle via the relation:

$$\frac{E_{\text{MF}} - E^{(0)}_{MF}}{N} = \frac{m\sigma^2_{\text{int}}}{2t^2_{\text{tof}}}.$$

We fix the RF power, which sets the Rabi frequency Ω. The RF frequency is then swept adiabatically and linearly over $t_{\text{sweep}} = 9$ms from an initial detuning of 9Ω down to δ_f, allowing the condensate to follow the $|-\rangle$ state. The sweep is also slow enough to

allow adiabatic adjustment of the radial density profile. [1]

An experimental challenge is to prevent additional kinetic energy from being transmitted to the atoms in the axial direction during the sweep. We find that if we turn off the longitudinal trap at the end of the 9-ms sweep, the cloud shrinks axially [2], whereas turning it off too early leads to an expansion. To compensate for the effect, we optimize the timing of turning off the longitudinal trap so that the expansion at the minimum of the curve, at low energy, reflects only the mean-field contribution. Although this adjustment should be repeated for each Ω, in practice, this correction is only crucial near $\delta/\Omega|_{\min} = \delta g/\sqrt{4\bar{g}^2 - \delta g^2} \approx 0.24$, where the effective two-body interaction g^{--}_{--} becomes very small. With this procedure, we reduce the residual kinetic energy per particle to a few Hz. This will be explained in detail in the next chapter.

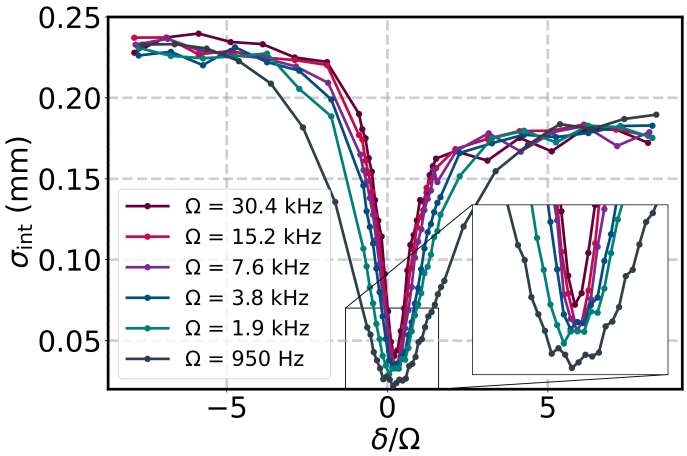


Figure 3.6: Root-mean-square (rms) axial size σ_{int} of the condensate as a function of δ/Ω for different Rabi frequencies Ω, after a time-of-flight $t = 62.6$ ms. The derived quantity $m\sigma^2_{\text{int}}/(2t^2_{\text{tof}})$ reflects the interaction energy per particle. The location of the dip tracks the minimum of the dressed-state coupling g^{--}_{--}, while the broadening of the dip at lower Ω highlights the higher-order nonlinearity.

Figure 3.6 shows the measured rms cloud size σ (from Gaussian fits) as a function of δ/Ω for various values of Ω, after a fixed time-of-flight $t_{\text{tof}} = 62.6$ ms. The extracted quantity $m\sigma^2_{\text{int}}/(2t^2)$ follows the expansion energy of the cloud. Although the density profile is not uniform, the overall trends follow the predictions of Fig 3.3.

[1] This condition is only approximate, by sweeping to $\delta/\Omega < 0$, we observe residual radial oscillations. However, their influence on the longitudinal expansion dynamics is negligible.

[2] This shrinking is due to the decrease of the interaction energy during the RF sweep. Even if the scattering length remains positive throughout, a decreasing a_{--} lowers the mean-field repulsion, allowing the trap to compress the cloud before release.

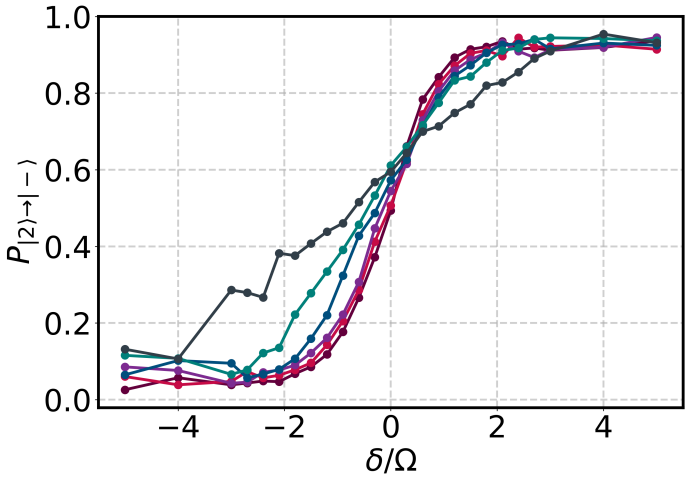


Figure 3.7: Measured population of the bare state $|2\rangle$ after an adiabatic sweep to the lower dressed state $|-\rangle$, shown as a function of δ/Ω for various Rabi frequencies Ω. The data reveal smoother transitions at lower Ω, consistent with the higher-order interaction effects discussed previously. Due to slight imperfections in the preparation procedure, the initial state at large δ/Ω does not reach 100% population in $|2\rangle$, with a residual occupation below 5%.

The expansion energy displays a clear minimum at the detuning corresponding to the minimum of the dressed-state scattering length g_{--}^{--}. For large positive δ/Ω, the cloud behaves like a condensate in the bare $|2\rangle$ state, expanding according to g_{22}. For large negative δ/Ω, the expansion is faster, reflecting the stronger repulsion of the $|1\rangle$ state according to g_{11}. Most notably, the width of the expansion dip broadens significantly as we lower Ω, which is an indication of the strong nonlinear corrections of the equation of state. In the low γ regime, this effect has been previously observed in sodium [111].

We follow a slightly different protocol to measure the spin population in the bare state of the dressed state $|-\rangle$. After preparing the condensate via the adiabatic RF sweep, we don't apply any time-of-flight expansion, and we use a shorter sweep time. Instead, we perform a Stern-Gerlach sequence at the end of the sweep to separate the bare spin components $|1\rangle$ and $|2\rangle$ spatially, allowing us to extract the relative population at the final detuning as shown in Fig 3.7.

This confirms that for the low Ω values, we observe a large change in the population behavior because of mean-field shifts.

3.8 Comparison with Theoretical Predictions

To interpret our experimental measurements of axial expansion, we simulate the imaginary-time 2D Gross-Pitaevski simulations of the spinor wavefunction using the GPELab toolbox. An aspect is that the nature of the confinement changes throughout the RF sweep. Near the minimum expansion size, interactions are weak and the condensate enters a quasi-1D regime, with the radial wavefunction close to the harmonic ground state. Conversely, for large values of $|\delta/\Omega|$, interactions are stronger and the condensate behaves as a fully 3D system.

To account for these effects, we assume adiabatic evolution of the radial wavefunction. For each fixed axial density (treated as a parameter), we compute the radial ground state of the spinor wavefunction. This simulation includes all relevant contributions: trap energy, interaction energy, quantum pressure, and Rabi coupling.

The total energy E_{tot} is obtained by integrating over the axial density profile. By comparing with the experimental observations, we can extract the cloud size using the following expression:

$$\frac{E_{\text{tot}}}{N} - \frac{\hbar\omega_\perp}{2} + \frac{\hbar\tilde{\Omega}}{2} = \frac{m}{2}\frac{\sigma_{\text{int}}^2}{t_{\text{tof}}^2}.$$

we subtract from the computed energy E_{tot} the radial trap energy $\hbar\omega_\perp/2$ and the Rabi energy $-\hbar\tilde{\Omega}/2$. The simulation will be further detailed in the thesis of Sara Tiengo.

The simulations reproduce both the depth and the broadening of the interaction energy dip observed in the experiments without requiring a fitting parameter. Notably, the width of the dip increases as the Rabi frequency Ω is reduced, consistent with the strong γ behavior. Small discrepancies at large negative detuning, where the simulation slightly overestimates the expansion, can be attributed to three-body losses that reduce the effective atom number, as these losses are not included in the simulation. Furthermore, at the point where the two-body coupling almost vanishes (i.e., where $a_{--} \approx 0$), the measured expansion is slightly larger than the mean-field prediction. We interpret this deviation as beyond-mean-field effects due to virtual excitations to the upper dressed state, in agreement with previous theoretical predictions and experimental demonstrations [85, 94].

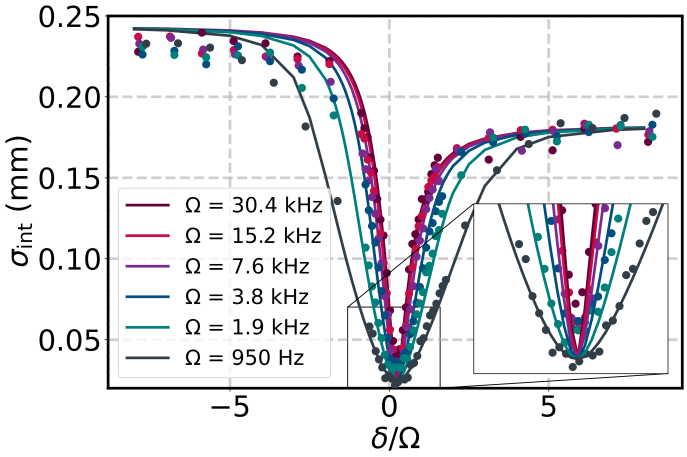


Figure 3.8: comparison between the measured expansion energy and the theoretical predictions from a mean-field simulation based on the Gross–Pitaevskii equation. The plot shows the interaction energy per particle, extracted from the axial cloud size after time-of-flight, as a function of δ/Ω for various Rabi frequencies. The solid lines correspond to the simulated expansion energies assuming adiabatic radial evolution.

This quantitative agreement between the numerical results and our measurements supports the validity of the mean-field saturation effect for interaction energy in RF-dressed BECs. It reveals the nonlinear regimes that extend beyond a simple Taylor expansion in density.

3.9 Chapter Conclusion

In this chapter, we have investigated the mean-field interaction energy of a Bose-Einstein condensate prepared in a coherent state. By developing both an analytical and numerical description of the energy functional, we have demonstrated that the interaction energy exhibits a nontrivial dependence on both the atomic density and the Rabi frequency. The interplay between the Rabi energy and the interaction energy leads to a rich structure in the equation of state, including a low-density regime dominated by two-body interactions, an intermediate regime where effective three-body terms emerge, and a high-density regime characterized by saturation effects.

We demonstrated that, although a Taylor expansion in density captures the initial nonlinearities, it breaks down as the interaction strength becomes comparable to the Rabi coupling energy. In this nonlinear regime, the system no longer responds perturbatively. Instead, the interaction approaches a saturation behavior.

Our experiments, based on the expansion dynamics of a ^{39}K condensate in the dressed state $|-\rangle$, confirm the theoretical predictions. We capture the broadening of the energy dip at low Rabi frequencies through mean-field simulations that account for the crossover geometry and spinor dynamics. This agreement validates the mean-field approach beyond the perturbative limit. It shows how the spin composition is significantly modified to minimize the interaction energy.

These findings open up new possibilities for engineering nonlinear matter-wave systems with tunable effective interactions. The ability to reach a regime where the interaction energy exhibits nonlinear behavior, yet transitions to another two-body regime or even becomes non-monotonic, opens the way for exploring modified ground-state density profiles beyond the standard Thomas-Fermi model, as well as modified collective excitations. Moreover, it motivates future studies of different types of quantum droplets, solitons in the dressed regime.

CHAPTER

Beyond Mean-Field Energy in RF-Dressed BEC and Quantum Droplets 4

4.1 Chapter Introduction

Quantum droplets are ultracold atomic systems in which interactions and quantum fluctuations play a crucial role. A macroscopic cloud that remains stable even without external trapping. This stability comes from a balance between attractive mean-field interactions and repulsive quantum fluctuations. Such droplets go beyond the standard Gross-Pitaevskii description, which predicts collapse when the mean-field interactions are attractive.

The theoretical work by Petrov [107] showed that the quantum correction to the mean-field energy called the Lee-Huang-Yang (LHY) term can stabilize a mixture of two Bose gases with contact interactions. When the interspecies attraction slightly exceeds the intraspecies repulsions ($\sqrt{a_{11}a_{22}} < -a_{12}$ where $a_{11}, a_{22} > 0$ and $a_{12} < 0$), the mean-field energy density that scales like n^2 becomes negative. However, instead of collapsing, the system can be stabilized by quantum fluctuations, which introduce a repulsive LHY energy density that scales as $n^{5/2}$. Those scalings with n allow the formation of a self-bound droplet at an equilibrium density, even in free space. For a certain range of atom numbers and without external trapping, the excitation spectrum of the droplet lies above the particle emission threshold. In this regime, any excitation results in particle loss, causing the droplet to self-evaporate and cool to a temperature of zero.

The quantum droplets were first observed experimentally in strongly dipolar BECs of dysprosium [112, 113] and erbium [114], where the anisotropic long-range dipole-dipole interaction mimics the attractive component required for droplet formation. Soon after, quantum droplets were observed in spin mixtures of potassium-39 by Cabrera et al. [59] and by Semeghini et al. [115], as well as in a heteronuclear bosonic mixture of potassium-41 and rubidium-87 by D'Errico et al. [116] and a mixture of sodium-23 and rubidium-87 by Guo et al. [117] .

Several works have shown that dimensionality might affect the LHY energy in 1D, 2D, and crossover geometries [118, 94, 119], if the healing length for the spin excitation mode is comparable to or larger than the trap dimension. Furthermore, other experiments show the emergence of a supersolid order phase in dipolar systems [120, 121], and study the collective excitations in dipolar supersolids [122]. Further studies have investigated droplets in weakly disordered Bose mixtures [123], and in optical lattices near the Mott transition [124],

Most studies on quantum droplets have focused on incoherent Bose mixtures or dipolar interactions. In contrast, our work explores the droplet regime in coherently coupled Bose-Einstein condensates [125]. This configuration introduces a new degree of control to the LHY energy: the Rabi frequency Ω, where we tune the mean-field energy to zero and measure only LHY energy [60]. This makes coherently coupled mixtures a promising and versatile platform to investigate beyond-mean-field physics and the formation of quantum droplets.

This chapter focuses on the experimental observation of quantum droplets in a Rabi-coupled two-spin-component ^{39}K Bose–Einstein condensate. For a given range of magnetic fields, we prepare the condensate in the lower dressed state by performing an adiabatic sweep at a fixed density. For each magnetic field value, we tune the mean-field energy by varying the ratio δ/Ω, scanning across the point where the mean-field energy reaches a minimum as a function of δ/Ω.

At this minimum, the mean-field interaction energy becomes slightly negative and independent of Ω. At the same time, the Lee-Huang-Yang (LHY) correction remains positive and tunable via the Rabi frequency (increasing with Ω). The objective is to reach a regime where the total energy, as a function of density, exhibits a minimum. This energy minimum corresponds to the droplet regime: the condensate remains stable without shrinking or expanding, as repulsive quantum fluctuations balance the attractive mean-field term.

For a fixed Rabi frequency, there exists a unique equilibrium density at which the system stabilizes. Conveniently, in coherently coupled mixtures, it is experimentally easier to tune the Rabi frequency, and thus the LHY energy, than to control the density. This flexibility contrasts with non-coherent mixtures, where the LHY energy is not tunable, and achieving the droplet regime requires precise adjustments of multiple parameters, including spin mixture, magnetic field, and trap configuration.

Experimentally, we prepare a coherently coupled BEC in a crossed cigar-shaped trap. For our experimental parameters, the LHY energy remains 3D where the healing length for the spin excitation mode is smaller than the trap dimension. We then identify the Rabi frequency at which the axial size of the cloud remains constant during axial expansion. This enables us to compare the data to the theoretical predictions based on the LHY energy expression derived in [60]. Many challenges arise in this low-energy regime. Due to

the smallness of the LHY energy (typically a few tens of Hz), which requires a very good control of all parameters to such a level.

We carefully address the different experimental limitations and implement strategies to reduce their impact. Among these, shot-to-shot magnetic field fluctuations [85], imperfect adiabaticity during RF sweeps, which leads to atoms excited in the upper dressed state that have different interaction strengths, and errors in the axial trap release timing can inject unwanted kinetic energy into the system. To mitigate this, we experimentally determine and calibrate the optimal release time for each value of Ω. In an elongated trap, we find that the contribution of quantum pressure in the axial direction remains negligible in our experiment.

4.2 Theoretical Approach

In this chapter, we first investigate the beyond-mean-field (BMF) energy of a two-component Bose-Einstein condensate coherently coupled via a radio-frequency (RF) field and explore the quantum droplet regime, where repulsive beyond-mean-field corrections compensate attractive mean-field interactions. This regime corresponds to the point where higher-order mean-field interaction effects vanish. As shown in the previous chapter and illustrated in Fig. 3.3a, this regime coincides with the minimum of the mean-field energy curve as a function of δ/Ω. At this point, the mean-field energy minima become independent of the Rabi frequency Ω, while the LHY correction remains Rabi-dependent. This minimum occurs at:

$$\left.\frac{\delta}{\Omega}\right|_{\text{min}} = \frac{1}{2}\frac{g_{11}-g_{22}}{\sqrt{(g_{22}-g_{12})(g_{11}-g_{12})}}.$$

At this point, the mean-field energy per particle takes the simple form:

$$\frac{E_{\text{MF}}}{N} = \frac{g_{\text{min}}}{2}\,n, \qquad \text{with} \qquad g_{\text{min}} = \frac{g_{11}g_{22}-g_{12}^2}{g_{11}+g_{22}-2g_{12}}.$$

We also define the spin composition ratio parameter $\alpha = \sqrt{n_2/n_1}$. At the minimum of the mean-field energy, this corresponds to $\alpha = \sqrt{(g_{11}-g_{12})/(g_{22}-g_{12})}$. As shown in Fig. 4.1, the scattering length a_{min} corresponding to g_{min} becomes negative below a magnetic field of approximately 56.87 G, indicating a transition to a weakly attractive regime. To obtain the relevant scattering lengths, we asked Jasper van de Kraats to compute them using the approach described in [126]. We compare these values with those reported by Simoni et al. [82]. Although neither method provides error bars, we treat the discrepancy between the two predictions as an estimate of the uncertainty. This difference,

on the order of $1\,a_0$ for a_{11}, slightly shifts the point at which the mean-field energy vanishes. An observed shift between the experimental data and theoretical predictions may therefore stem from this uncertainty in the scattering length calculations.

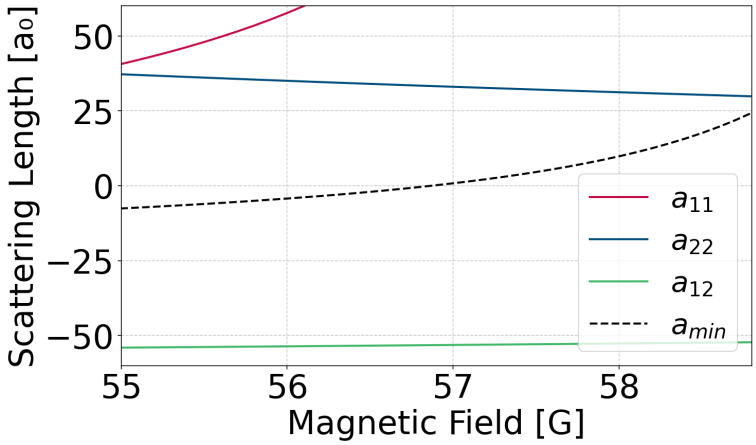


Figure 4.1: The scattering length $a_{\min}, a_{11}, a_{22}, a_{12}$ corresponding to $g_{\min}, g_{11}, g_{22}, g_{12}$, shown as a function of magnetic field for ^{39}K. The region below 56.87 G indicates the weakly attractive regime ($a_{\min} < 0$) where quantum droplet formation becomes possible.

Our goal is to experimentally locate the regime of quantum droplet formation by identifying, for a fixed atomic density, the Rabi frequency at which the repulsive BMF correction nearly cancels this weak, attractive mean-field interaction. The BMF energy at this optimal detuning depends on the Rabi frequency, which can be tuned experimentally. In particular, we seek the point where the derivative of the energy per particle with respect to density vanishes, $\partial(E/N)/\partial n = 0$, the mechanical stable point of self-bound quantum droplets if the energy per particle decreases with density (i.e., $\partial(E/N)/\partial n < 0$), the system tends to reduce its density to lower its energy, leading to expansion. Conversely, if the derivative is positive, $\partial(E/N)/\partial n > 0$, the energy per particle favors higher densities, and the system tends to shrink. The BMF energy is computed analytically from the zero-point fluctuations of the Bogoliubov excitation spectrum, following the expression derived in the supplementary material of Ref. [94].

To compute the beyond mean-field (BMF) correction, we take the formula given by D. Petrov [94]. While we do not detail the full derivation, we briefly outline the physical assumptions underlying the calculation.

Starting from the second-quantized Hamiltonian of a two-component Bose gas with coherent Rabi coupling, we consider a mean-field wavefunction and a quantum fluctuation term. The field operators are then decomposed into a classical mean-field part and a fluctuation operator as follows:

$$\hat{\psi}_i(\mathbf{r}) = \psi_i + \delta\hat{\psi}_i(\mathbf{r}), \quad \text{for } i = 1, 2, \tag{4.1}$$

where ψ_i is the condensate wavefunction of component i, and $\delta\hat{\psi}_i$ represents quantum fluctuations.

Assuming that the system condenses into a spinor state with a fixed spin composition, determined by the Rabi coupling and detuning, we linearize the second-quantized Hamiltonian around the classical condensate field and derive the corresponding Bogoliubov excitation spectrum. The resulting quantum corrections to the mean-field energy arise from the zero-point energy of these Bogoliubov modes and constitute the beyond mean-field (BMF) contribution, often referred to as the Lee-Huang-Yang (LHY) correction.

In our analysis, we directly use the analytical expression for the BMF energy derived from this procedure without reproducing the full derivation. The complete calculation is detailed in the supplementary material of Ref. [94].

In general, the expression for the beyond mean-field (BMF) energy in a two-component Bose-Einstein condensate is significantly more complex than in the single-component case. This complexity arises from the interplay between the system's two fundamental collective excitations: the density mode and the spin mode. The density mode corresponds to in-phase oscillations of the two spin components and is sensitive to the density and interaction strength. In contrast, the interspecies interaction and the Rabi coupling directly influence the spin mode, which corresponds to out-of-phase oscillations between the components.

In the presence of RF coupling, the spin mode develops a gap set by the Rabi frequency and detuning. The BMF correction must account for both branches of the Bogoliubov spectrum, making the general analytical expression intractable. In a specific condition, such as when $g_{\min} = 0$ which corresponds to $g_{12} = -\sqrt{g_{11}g_{22}}$, the spin composition ratio parameter corresponds to $\alpha = \alpha_0 = \left(\frac{g_{11}}{g_{22}}\right)^{1/4}$, only the spin mode contribute. At this point, the corresponding detuning is: $\delta/\Omega = (\sqrt{g_{11}} - \sqrt{g_{22}})/(2(g_{11}g_{22})^{1/4})$. We can then obtain a simplified analytical expression of the LHY correction.

Under these conditions, the LHY (Lee-Huang-Yang) correction takes the simple analytical form:

$$\boxed{\frac{E_{\mathrm{LHY}}}{N}(g_{\min} = 0,\, \alpha = \alpha_0) = -\frac{g_{12}n}{2} \cdot \frac{128}{15\sqrt{\pi}}\sqrt{n(-a_{12})^3} \cdot I(y)} \tag{4.2}$$

where

$$I(y) = \frac{15}{4}\int_0^1 \sqrt{x(1-x)(x+y)}\, dx, \quad \text{with} \quad y = \frac{\hbar\tilde{\Omega}}{-2g_{12}n}, \quad \text{and} \quad \tilde{\Omega} = \Omega \cdot \frac{\alpha_0 + 1/\alpha_0}{2}.$$

In our experiment, the previous condition corresponds to the magnetic field value $B = 56.87\,\mathrm{G}$, where the mean-field interaction vanishes and only the quantum fluctuations remain, we obtain $\alpha_0 = 1.265$ and the corresponding detuning is $\delta/\Omega = 0.237$. However, in

order to stabilize quantum droplets, we require a slightly attractive mean-field interaction, meaning we must move away from the exact $g_{\min} = 0$ condition.

To address this regime, Petrov provided, in a private communication, a first-order expansion of the LHY energy around $g_{\min} = 0$ and $\alpha = \alpha_0$, which reads:

$$E_{\mathrm{LHY}} \approx E_{\mathrm{LHY}}(g_{\min} = 0,\, \alpha = \alpha_0) + \frac{\partial E_{\mathrm{LHY}}}{\partial g_{\min}} g_{\min} + \frac{\partial E_{\mathrm{LHY}}}{\partial \alpha} \cdot (\alpha - \alpha_0), \tag{4.3}$$

and it yields to the compact form:

$$\boxed{\frac{E_{\mathrm{LHY}}}{N} \approx -\frac{g_{12} n}{2} \cdot \frac{128}{15\sqrt{\pi}} \sqrt{n(-a_{12})^3}\, [I(y) + C_J\, J(y) + C_K\, K(y)]\,,} \tag{4.4}$$

With coefficient :

$$C_J = \frac{g_{12} + \sqrt{g_{11} g_{22}}}{g_{12}\,(\alpha_0 + 1/\alpha_0)^2}, \qquad C_K = -\frac{(\alpha_0^2 - 1)(\alpha - \alpha_0)}{4\alpha_0(\alpha_0^2 + 1)}.$$

The additional integrals $J(y)$ and $K(y)$ are defined as:

$$J(y) = \frac{15}{4} \int_0^1 \sqrt{\frac{x}{1-x}(x+y)}\, dx, \quad K(y) = \frac{15}{4} \int_0^1 \sqrt{\frac{x+y}{x(1-x)}} \cdot (2y - 4xy + 4x)\, dx.$$

The eq. 4.4 corrects the analytical form of the LHY energy expression when $g_{\min}$ slightly deviates from zero, and the spin composition ratio shifts away from α_0. While these corrections are minimal, they introduce only a constant offset without significantly changing the overall behavior, it is still instructive to distinguish between the slightly attractive regime we are working in from the one explored by Lavoine et al. in the previous BMF study, which focused on the special case $g_{\min} = 0$ to analyze the overall trend of the LHY energy. In contrast, our goal is to explore whether quantum droplets can form in regimes where $g_{\min} < 0$, i.e., in the presence of a weak attractive mean-field interaction.

The extremely attractive condition for the mean-field interaction that we will be working at corresponds to a magnetic field of approximately 56.61 G, where it reaches $g_{\min} = -1.48\, g_0$, with $g_0 = \frac{4\pi\hbar^2}{m} a_0$. At this point, the bare interaction parameters are: $g_{11} = 74.81\, g_0$, $g_{22} = 33.77\, g_0$, and $g_{12} = -53.33\, g_0$. The corresponding spin composition ratio parameter is: $\alpha = 1.213$, and the detuning to Rabi ratio is $\frac{\delta}{\Omega}\Big|_{\min} = 0.1943$. As a comparison, the leading term in Eq. (4.2) is evaluated at $\delta/\Omega = 0.2$ and $\alpha_0 = 1.220$. For these parameters, the corresponding correction coefficients are: $C_J \approx 0.0138$, and $C_K \approx 2.82 \times 10^{-4}$.

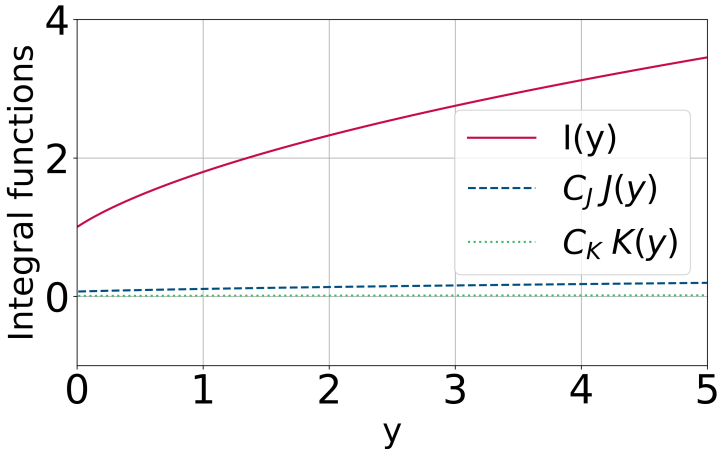


Figure 4.2: Plot of the dimensionless integrals $I(y)$ (solid curve), $C_J\, J(y)$ (dashed curve), and $C_K\, K(y)$ (dotted curve) as a function of $y = \hbar\tilde{\Omega}/(-2g_{12}n)$, appearing in the expression for the LHY energy correction. The small prefactors C_J and C_K, calculated for 56.61 G for potassium 39 atoms, suppress the impact of $J(y)$ and $K(y)$, making $I(y)$ the dominant contribution for our parameters.

We now examine the three dimensionless quantities $I(y)$, $J(y)$, and $K(y)$, which enter Eq. (4.4). As shown in Fig. 4.2, the prefactors C_J and C_K respectively reduce the impact of $J(y)$ and $K(y)$ with respect to $I(y)$. $C_K K(y)$ term is completely negligeable compared to $I(y)$, whereas $C_J J(y)$ amounts to 3 %

4.3 Mechanical stability

We now turn to the question of mechanical stability, which determines whether the condensate forms a stable quantum droplet or, instead, undergoes collapse or expansion. The key criterion is how the total interaction energy per particle evolves with density. If either an increase or a decrease in density effect leads to an increase in energy, the system develops a restoring pressure that counteracts compression, ensuring mechanical stability. In contrast, if the energy per particle decreases with increasing density, the condensate becomes unstable and tends to shrink. Conversely, if decreasing the density lowers the energy, the system is unstable toward expansion. In both cases, the stable point is when the energy exhibits a local minimum as a function of density.

The condition for mechanical stability corresponds to a local minimum of the energy per particle. For a uniformly distributed Bose-Einstein condensate with negligible kinetic

energy, we derive the stable point from:

$$\frac{\partial}{\partial n}\left(\frac{E_{\mathrm{MF}}+E_{\mathrm{LHY}}}{N}\right)=0. \tag{4.5}$$

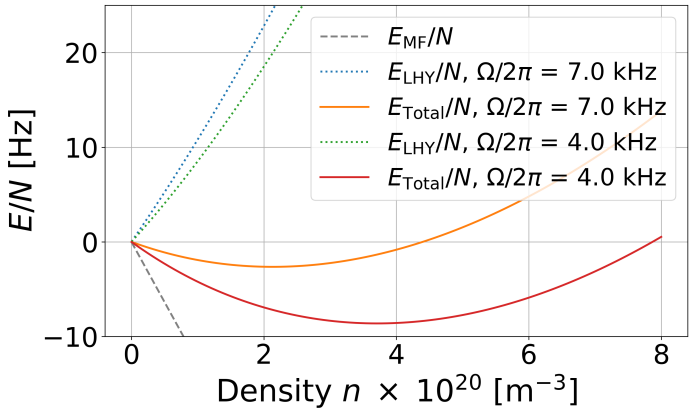


Figure 4.3: Mean-field energy per particle (dashed curve), Lee-Huang-Yang energy per particle, for $\Omega/2\pi = 7$ kHz (blue dotted curve), for $\Omega/2\pi = 4$ kHz (green dotted curve), and total energy per particle as a function of density, for $\Omega/2\pi = 7$ kHz (orange solid curve), for $\Omega/2\pi = 4$ kHz (red solid curve) computed for a magnetic field $B = 56.87\,\mathrm{G}$. The minimum of the total energy per particle indicates the mechanical equilibrium and potential droplet formation at a density around $n \approx 2 \times 10^{20}\,\mathrm{m}^{-3}$ for $\Omega/2\pi = 7$ kHz and at a density around $n \approx 4 \times 10^{20}\,\mathrm{m}^{-3}$ for $\Omega/2\pi = 4$ kHz.

The condition in Eq. 4.5 defines the equilibrium point at which the repulsive beyond mean-field correction balances the attractive mean-field interaction, as shown in Fig. 4.3. The Rabi frequency strongly influences the stability point. At higher Rabi frequencies, the LHY energy rises more steeply with density (blue dotted curve), causing the minimum of the total energy to shift toward lower densities (orange solid curve). Conversely, at lower Rabi frequencies, the LHY correction has a smaller slope (green dotted curve), and the energy minimum appears at higher densities (red solid curve). From an experimental perspective, it is often more convenient to fix the atomic density and vary the Rabi frequency. These minima occur at an energy per particle of $-3\,\mathrm{Hz}$ for $\Omega/2\pi = 7\,\mathrm{kHz}$ and $-9\,\mathrm{Hz}$ for $\Omega/2\pi = 4\,\mathrm{kHz}$.

In our model, we employ the analytical form of the LHY energy, which includes the perturbative corrections $J(y)$ and $K(y)$. The final stability condition reads:

$$\left[I(y)-\frac{2}{3}y\frac{dI(y)}{dy}+C_J\left(J(y)-\frac{2}{3}y\frac{dJ(y)}{dy}\right)+C_K\left(K(y)-\frac{2}{3}y\frac{dK(y)}{dy}\right)\right]=\frac{5\sqrt{\pi}\,g_{\mathrm{min}}}{64\,g_{12}\sqrt{n(-a_{12})^3}}. \tag{4.6}$$

The expressions for the derivatives are given by:

$$\frac{dI(y)}{dy} = \frac{15}{8}\int_0^1 \sqrt{\frac{x(1-x)}{x+y}}\,dx, \tag{4.7}$$

$$\frac{dJ(y)}{dy} = \frac{15}{8}\int_0^1 \sqrt{\frac{x}{(1-x)(x+y)}}\,dx, \tag{4.8}$$

$$\frac{dK(y)}{dy} = \frac{15}{8}\int_0^1 \frac{8x(1-x)+6y(1-2x)}{\sqrt{x(1-x)(x+y)}}\,dx. \tag{4.9}$$

Equation 4.6 provides a direct way to determine the stability condition for a given set of experimental parameters, including the magnetic field (which controls the interaction strengths), the Rabi frequency, and the density. In particular, it highlights how we can tune the interaction between attractive and repulsive via Ω to achieve the formation of stable quantum droplets in the weakly attractive regime ($g_{\min} < 0$). The theoretical values of $g_{\min}$ are smaller than $\sim -3g_0$, so even a small deviation in the theoretical model can shift the expected stability curve, given the weak interaction regime as explained previously in Fig 4.1.

4.4 Experimental Attempt for Exploring the Droplet Regime

4.4.1 Experimental Procedure Description

Our experimental objective is to explore different magnetic field values in the weakly attractive interaction regime where $g_{\min}$ is slightly attractive, in particular within the range 56.87 G to 56.60 G, where $g_{\min}$ varies from 0 to approximately $-1.5\,g_0$. We focus on this working range of magnetic fields because, within the experimentally accessible density of around $2 \times 10^{20}\,\mathrm{m}^{-3}$ and the available Rabi frequency range between 1 kHz and 25 kHz, we are able to explore the droplet regime under experimentally achievable conditions.

The central goal is to prepare the system in the droplet regime, ensuring that we don't inject excess energy during the state preparation. Since quantum droplets form at extremely low energy scales (a few tens of Hz), as shown in Fig. 4.3, the system is particularly sensitive to any form of excitation or imbalance. We must take care of them to avoid additional energy.

We start with a Bose-Einstein condensate in the state $|2\rangle \equiv |F = 1, m_F = -1\rangle$, confined in a cigar-shaped optical dipole trap with trapping frequencies $\omega_r = 2\pi \times 170$ Hz and

$\omega_z = 2\pi \times 26\,\mathrm{Hz}$. The magnetic field is set to values between 56.60 G and 56.87 G, corresponding to a scattering length $a_{22} \in [33.26, 33.79]\, a_0$. At this stage, the condensate is well described by the 3D Thomas–Fermi approximation, with a chemical potential $\mu \approx 930\,\mathrm{Hz}$ much larger than both trap frequencies, justifying the use of the 3D Thomas–Fermi profile. The initial atom number is approximately 1.2×10^5 atoms, determined after a long time of flight. The corresponding peak density is around $1.6 \times 10^{20}\,\mathrm{m}^{-3}$, and the Thomas–Fermi radii are $R_\perp = 4\,\mu\mathrm{m}$ and $Z = 26.6\,\mu\mathrm{m}$, computed from Eqs. (1.39) and (1.40).

In the data analysis, we use Gaussian fits rather than a Thomas–Fermi profile. The corresponding Gaussian rms sizes are $\sim 2\,\mu\mathrm{m}$ in the radial direction and $\sim 13\,\mu\mathrm{m}$ in the axial direction, consistent with our measured experimental sizes.

The next step is to prepare the system in the desired $g_{\min}$. We first fix the magnetic field to define the interaction parameters g_{11}, g_{22}, g_{12}. For each experimental configuration, we fix the Rabi frequency and perform a linear sweep of the detuning-to-Rabi ratio δ/Ω over 9 ms to reach the desired interaction regime defined by $g_{\min}$ at $\delta/\Omega|_{\min}$. After the sweep, we turn off the axial trapping potential and monitor the axial expansion of the condensate as a function of time, which enables us to determine whether the BEC is expanding or contracting under the given conditions. We then repeat the experiment for different Rabi frequencies, either increasing or decreasing Ω, until we identify the configuration where the condensate exhibits neither expansion nor contraction.

We must carefully address two experimental considerations when varying the Rabi frequency. First, we control the RF frequency by driving the RF generator with a computer-controlled voltage signal. We adjust the frequency modulation slope (in kHz/V) for each Rabi frequency, which guarantees that the Landau–Zener sweep always starts from the same initial detuning ratio $\delta/\Omega = 9$ and ends at a well-defined final value $\delta/\Omega|_{\min}$. We can also determine the final detuning value experimentally by scanning δ/Ω and measuring the axial size of the condensate after one-dimensional expansion. The point where the expansion reaches a minimum corresponds to $g_{\min}$, providing a practical way to identify $\delta/\Omega|_{\min}$ for each Rabi frequency.

The total sweep time, 9 ms, is chosen to ensure adiabaticity with respect to the spin degree of freedom, even at the lowest Ω values. In addition, this time is sufficiently large as compared to $1/\omega_\perp$ such that the radial wavefunction can adapt itself adiabatically to the interaction change during the sweep.

In contrast, the axial direction behaves differently. Since the axial trap characteristic time is long compared to the 9-ms sweep time, keeping the axial trap on during the entire interaction sweep leads to axial compression. To avoid injecting additional kinetic energy into the system, the axial confinement must be switched off at a well-defined moment—ideally. This timing is critical, as any extra kinetic energy could mask or distort the measurement of the droplet regime.

Moreover, due to higher-order mean-field interaction effects discussed in the previous chapter, they do not change right from $\delta/\Omega = 9$, but rather begin to vary around $\delta/\Omega \approx 2$ for high Rabi couplings, and around $\delta/\Omega \approx 4$ for low Rabi couplings. As a result, the precise moment to release the axial confinement depends on the Rabi frequency and must be experimentally calibrated for each case. The following section details the procedure we use to determine this optimal release time.

4.4.2 Timing Optimization for Axial Trap Release

We perform an experimental calibration to determine the optimal timing for turning off the axial trap. For each Rabi frequency, we set the magnetic field such that the interaction g_{min} is close to zero. We then scan the timing of the axial trap release during the 9-ms sweep duration and observe the long-time expansion of the BEC (300-400 ms).

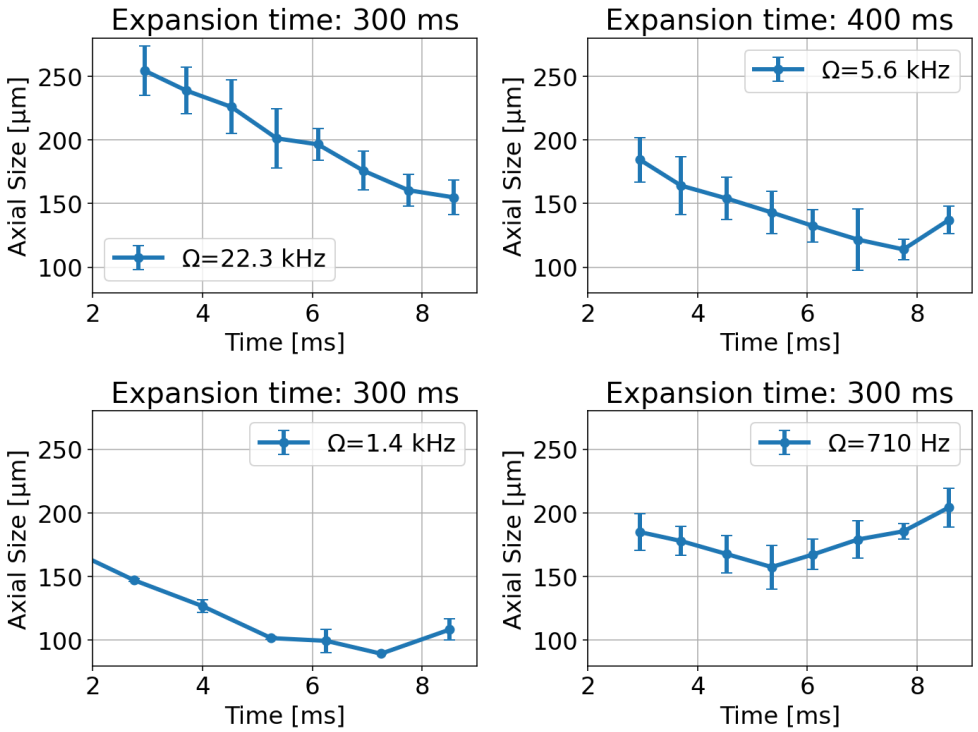


Figure 4.4: Calibration of the optimal axial trap release time for different Rabi frequencies. We scan the time during the sweep at which the axial trap is turned off and extract the resulting size. Each data point is obtained by averaging several measurements in 0.8 ms intervals, and the error bars represent the corresponding standard deviation. The observed minimum in the axial size indicates the moment when the induced shrinking or trap expansion dynamics compensated, resulting in minimal energy.

We optimize the release time by identifying the condition where the expansion profile

exhibits a minimal final size, corresponding to minimal energy input from the sweep, as shown in Fig. 4.4. This calibrated timing is then used for all later measurements to ensure no added excess energy into the system

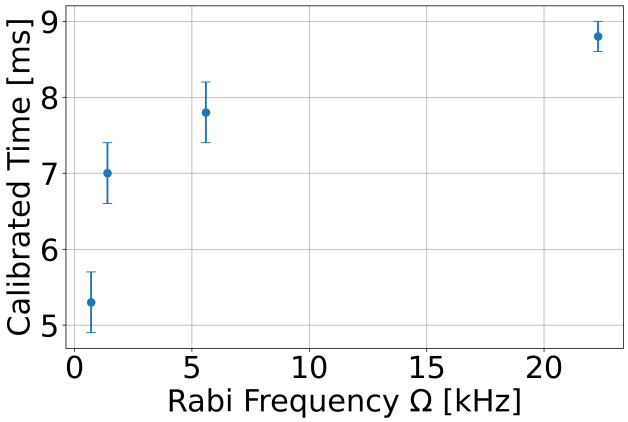


Figure 4.5: Calibrated axial trap release time as a function of Rabi frequency Ω. Each data point corresponds to the optimal timing (within the 9-ms Landau-Zener sweep) at which we turn off the axial trap in order to minimize the added kinetic energy for different Rabi frequencies.

The finite expansion time introduces some uncertainty in this method. Ideally, in the infinite-time limit, the expansion minima would fully reflect the precise time when the initial kinetic energy is compensated. However, since the expansion time is finite, when the cloud initially slowly shrinks before the expansion, we might observe a smaller size compared to the case where the initial cloud is at rest. This effect may thus lead to a slight overestimation of the ideal switching time of the axial trap, which we have not taken into consideration.

4.4.3 Estimating Expansion Due to Quantum Pressure and Timing Errors

To estimate the axial size evolution due to quantum pressure alone, we consider a non-interacting Bose-Einstein condensate described by a 3D Gaussian wavefunction. At the moment of release ($t = 0$), the quantum pressure energy per particle is given by:

$$E_{\mathrm{QP}} = \frac{\hbar^2}{4m}\left(\frac{2}{\sigma_\perp^2} + \frac{1}{\sigma_z^2}\right), \tag{4.10}$$

where $\sigma_\perp$ and σ_z are the radial and axial Gaussian widths, respectively.

After the axial confinement is switched off ($t_{1\mathrm{D}} > 0$), the quantum pressure energy stored in the axial direction is converted into axial kinetic energy of the expanding cloud.

By solving the time-dependent Schrödinger equation for a Gaussian wave packet, one obtains the following evolution for the axial size:

$$\sigma_z(t_{1D}) = \sigma_0\sqrt{1+(\omega\, t_{1D})^2}, \quad \text{with} \quad \omega = \frac{\hbar}{2m\sigma_0^2}. \tag{4.11}$$

For our experimental parameters, the initial axial size is approximately $\sigma_0 \approx 14\,\mu$m, corresponding to $\omega/2\pi \approx 0.7\,$Hz. After a 1D expansion time $t_{1D} = 70\,$ms, the axial size increases by only about 4%, indicating that quantum pressure alone contributes weakly to the observed expansion.

We now consider the contribution arising from a timing mismatch in the switch-off of the axial trap. Ideally, the axial confinement is turned off at a calibrated moment during the sweep when the condensate is locally at equilibrium, meaning that the net force acting on each atom vanishes. In this case, when the trap is turned off, the cloud begins its expansion with zero axial velocity.

However, if the trap is released slightly too early or too late by a time mismatch Δt, the atoms will experience a residual harmonic restoring force. Locally, this results in a force $-m\omega_z^2 r$, leading to an acceleration $\ddot{r} = -\omega_z^2 r$. For a short time Δt, the atoms acquire a residual velocity:

$$\dot{r} \approx -\omega_z^2\, r\, \Delta t. \tag{4.12}$$

Since the overall size of the condensate σ_z is a measure of the spatial distribution of atoms, this translates into an initial axial velocity of the size:

$$\dot{\sigma}_z(0) \approx \omega_z^2\, \sigma_0 \cdot \Delta t, \tag{4.13}$$

where ω_z is the axial trap frequency. This nonzero initial velocity contributes to an extra kinetic energy during expansion, which we minimize and calibrate experimentally. This initial velocity $\dot{\sigma}_z(0)$ leads to an additional expansion during 1D time-of-flight, given by:

$$\sigma_z(t_{1D}) = \sigma_0 + \dot{\sigma}_z(0) \cdot t_{1D}. \tag{4.14}$$

In our experiment, a mismatch of just $\Delta t = 1\,$ms can inject kinetic energy on the order of 7 Hz; such a value is comparable to the droplet binding energy, leading to an increase in axial size of approximately 50% after a 20 ms 1D expansion. This gives an estimation of the effect for our experimental condition.

4.4.4 Experimental Determination of the Stability Condition

We now present the experimental procedure and measurements used to identify the stability condition in the droplet regime. The goal is to find, for each magnetic field, the Rabi frequency at which the condensate exhibits neither expansion nor contraction, indicating mechanical equilibrium.

We begin by fixing the magnetic field, corresponding to a known RF splitting between the Zeeman states. At each Rabi frequency Ω, we perform a linear sweep of the detuning-to-Rabi ratio from $\delta/\Omega = 9$ to the value $\delta/\Omega|_{\min}$. The value of $\delta/\Omega|_{\min}$ is determined experimentally by identifying the detuning at which the axial size of the BEC reaches a minimum after a 1D time-of-flight of $t_{1D} = 60\,\text{ms}$.

For each Rabi frequency, we use the corresponding calibrated axial release time obtained from Fig. 4.5, which minimizes the additional energy introduced during the sweep. We repeat this procedure for different values of the magnetic field.

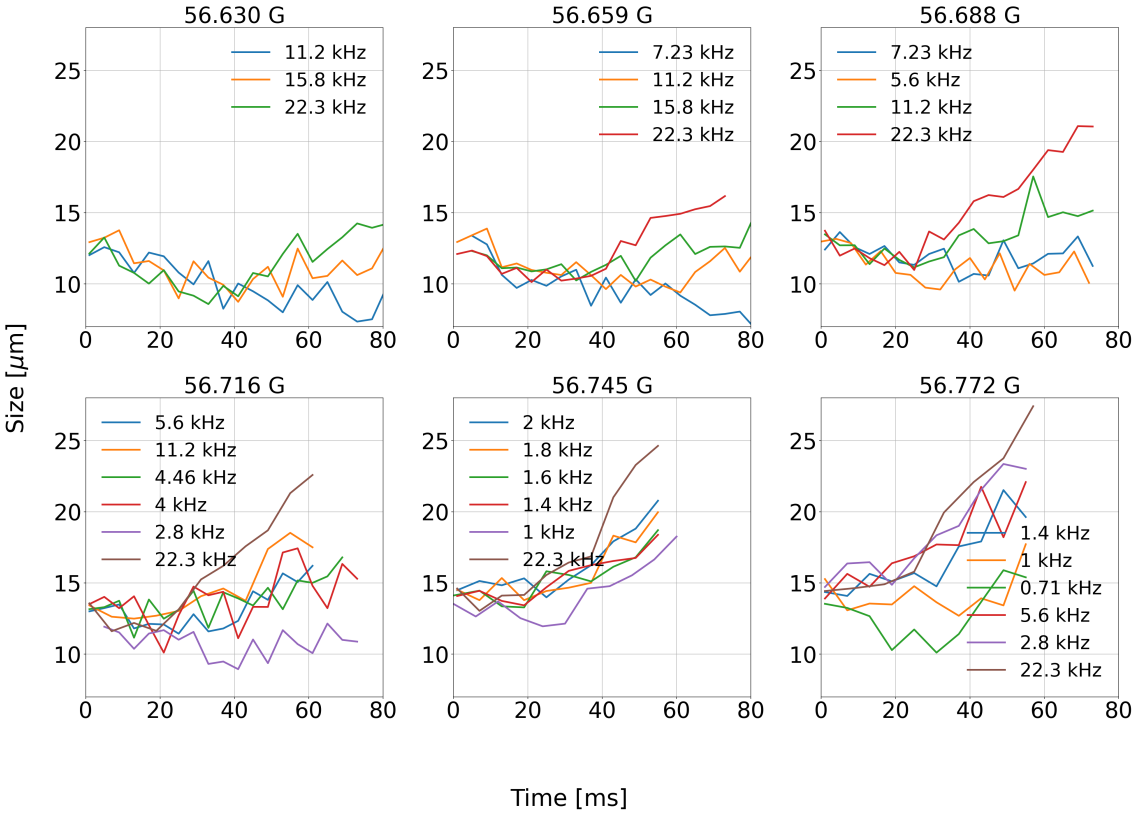


Figure 4.6: Axial size of the BEC as a function of time for various magnetic fields and Rabi frequencies, measured at the minimum of δ/Ω. For each magnetic field, the Rabi frequency corresponding to minimal expansion (or contraction) is identified and used to map the stability condition.

Figure 4.6 shows the axial expansion of the BEC at $\delta/\Omega|_{\min}$ for various magnetic fields and Rabi frequencies. For each magnetic field (i.e., each $g_{\min}$), we try to identify the Rabi frequency at which the cloud size remains constant over time, signaling the stability condition. These values are selected manually by identifying the curve with minimal expansion or contraction. This is very difficult because the cloud sometimes seems to shrink, as it is possible if the axial trap is turned off slightly too late, as compared to the ideal case.

Moreover, due to experimental noise, we cannot determine the extracted Rabi frequencies with high precision. Instead, we evaluate them within a range where the cloud's behavior clearly transitions from expansion to contraction. The error bars that we evaluate do not account for the possibility of a slight initial shrinkage of the cloud. Additionally, there may be a systematic shift toward lower Rabi frequency due to this effect.

The results for the Rabi frequency as a function of the interaction parameters g_{min} are then compared to the theoretical prediction based on the analytical stability condition given in Eq. 4.6, as shown in Fig. 4.7.

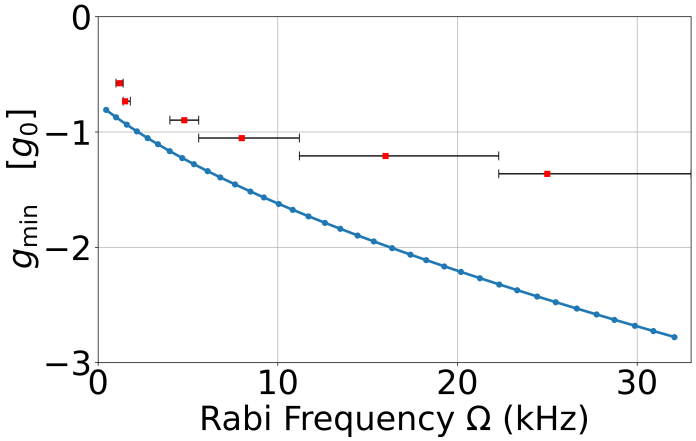


Figure 4.7: Experimental determination of the stability condition for droplet formation. Each red point corresponds to the Rabi frequency Ω at which the BEC exhibits no axial expansion or contraction, extracted from Fig. 4.6. The horizontal error bars represent the uncertainty range where we observe the transition from expansion to contraction. The solid blue curve shows the theoretical prediction based on Eq. 4.6, a fixed density of $1.6 \times 10^{20}\,\text{m}^{-3}$. Note that it might shift up or down by $\sim$0.4 g_0 because of the uncertainties in the theoretical scattering length values. Here, we used the values from J. Kraats based on the Tiemann potential.

The observed discrepancy in Figure 4.7 between experiment and theory may originate from several experimental limitations. The most probable source of error lies in the precise timing of the axial trap release, as discussed in the previous sections [1]. As seen in the high Rabi frequency regime in Fig. 4.6, the initial cloud shrinks due to imprecise timing in switching off the axial trap, which requires additional repulsive LHY energy to counteract. This likely explains why the corresponding data points appear shifted, as a higher Ω was

[1]The stability condition given in Eq. 4.6 is derived for a uniform density. However, the actual density profile in the experiment is Gaussian. To account for this, we integrated the energy density over a Gaussian distribution and re-derived the stability condition accordingly. The resulting correction was found to be important if we consider the average density of the cloud

needed to compensate for the added compression.

Other potential sources of error include magnetic field gradients during expansion, although we compensate for these experimentally to ensure a uniform field across the cloud. Furthermore, a slight inclination of the optical trap may cause center-of-mass motion during expansion, slightly affecting the local field. Still, this effect is also minimal once the initial expansion velocity is set.

The experiment was performed without active cancellation of 50-Hz magnetic noise, which results in magnetic field oscillations of $\Delta B \sim 0.3$ mG. This translates into detuning oscillation of approximately $\Delta\delta \sim 200$ Hz, which can modify the effective interaction strength. While this has no noticeable effect at high Rabi frequencies, its impact becomes more significant at low Rabi couplings.

.

These detuning fluctuations contribute to fluctuations in the effective scattering length according to the approximate expression obtained from [60]:

$$\Delta g_{--}^{--} \approx 48 \left(\frac{\Delta\delta}{\Omega}\right)^2 g_0. \tag{4.15}$$

Numerically, For $\Omega = 2\pi \times 1$ kHz: $\Delta g_{--}^{--} \approx 1\ a_0$ and for $\Omega = 2\pi \times 5$ kHz: $\Delta g_{--}^{--} \approx 0.10\ a_0$. These values indicate that 50 Hz magnetic noise has a negligible effect on the interaction strength for $\Omega \gtrsim 5$ kHz, but can introduce some energy at low Rabi frequencies.

Three-body losses contribute to the reduction of the total atom number and can limit the lifetime of the droplet. In the case of a coherently coupled mixture, these losses are symmetric between the two spin components. This is in contrast to incoherent (non-coupled) mixtures, where asymmetric losses between components can lead to an even shorter droplet lifetime due to population imbalance.

While the 9-ms sweep duration may not be perfectly adiabatic in the radial direction, we verified that the induced radial oscillations remained minimal at the low-energy conditions relevant for droplets. All these effects highlight the system's sensitivity in this weakly interacting regime, where even small imperfections in preparation can significantly influence the observed dynamics.

Nevertheless, the data remain valuable as they reproduce the overall trend predicted by the theory. They also complement earlier studies such as those in Ref. [60], where the LHY energy was measured for fixed $g_{\min} = 0$ at various Rabi frequencies. Our curve shows that for a very small Rabi frequency, the LHY energy is nonzero. Here, our approach, by controlling both the magnetic field and Rabi frequency, gives a broader view of the droplet formation threshold.

4.5 Chapter Conclusion

In this chapter, we have experimentally investigated the formation and stability of quantum droplets in a coherently coupled Bose-Einstein condensate of ^{39}K atoms. By tuning both the magnetic field and the Rabi frequency Ω, we identified the regime where the total mean-field interaction is attractive and the Lee-Huang-Yang (LHY) correction becomes the stabilizing mechanism. Our analysis focused on determining the mechanical equilibrium condition signaled by the absence of axial expansion or contraction.

Although our results do not perfectly match the theoretical predictions, they still follow the expected qualitative trend. Compared to the experimental study by Lavoine et al. [60], which measures the LHY energy at zero mean-field energy for various Ω, our data provide a complementary perspective. In the previous work, strong magnetic noise at low Rabi frequency led to the unwanted population of the upper-dressed state, causing an increase in cloud size and energy. In contrast, our measurements, which involve scanning both the Rabi frequency and magnetic field to determine the droplet regime, clearly reveal that the LHY energy decreases at low Ω. At Ω close to zero, the LHY energy is nonzero and converges toward the LHY energy of a non-coherent mixture, as theoretically expected.

Although some experimental limitations, such as magnetic field noise, interaction sweep, axial trap release timing, etc., prevent a perfect quantitative agreement with theoretical predictions, the data nonetheless reveal a consistent qualitative trend. In particular, the observed stabilization threshold follows the expected behavior derived from the analytical model for beyond-mean-field energy in the dressed-state basis [94]. This approach provides complementary validation to earlier experiments performed at fixed $g_{\mathrm{min}} = 0$ [60] while extending the exploration to the low Rabi frequency regime.

Looking forward, several improvements can enhance the precision of droplet measurements. Notably, shaping the trap geometry using a Digital Micromirror Device (DMD) to generate uniform box potentials [127, 128]. This would allow for more direct comparisons with theoretical models assuming uniform density.

In summary, the present study confirms the viability of coherently coupled mixtures as a rich platform for realizing and characterizing quantum droplets because of the LHY energy dependence on the Rabi frequency. However, it highlights the difficulty of the experiment due to its extremely low energy scale.

CHAPTER

BEC Tunneling Through Single and Double Optical Barriers Using a DMD 5

5.1 Chapter Introduction

This chapter is independent of the others, and we present the experimental observation of classical versus quantum tunneling behavior in cold atoms and our experimental indication of the matter-wave Fabry-Pérot effect in this system Fig.5.1. Experimentalists had never observed directly the quantum regime of tunneling through a single barrier and the Fabry-Pérot effect in cold atom experiments due to several challenges, including the difficulty of creating optical barriers comparable in size to the de Broglie wavelength of the atoms, limitations in numerical aperture, and the complexity of precisely controlling the distance between two barriers [129].

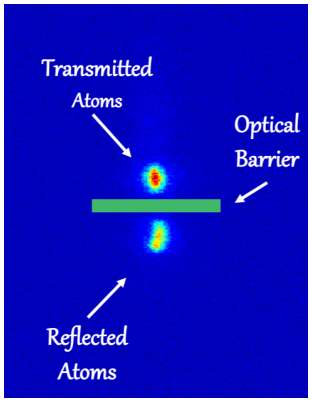


Figure 5.1: Fluorescence image of our ^{39}K Bose-Einstein condensate (BEC) undergoing quantum tunneling. We intentionally add the optical barrier in green to illustrate its position at the center, with the transmitted atom cloud visible on one side and the reflected atom cloud on the other. This image, captured during our tunneling experiment, shows the wave-like behavior of ultra-cold atoms as they interact with the potential barrier.

We divide this chapter into two main parts. The first section provides an overview of quantum tunneling, tracing its historical evolution. We follow this section with a discussion of a recent experiment investigating tunneling phenomena in cold atoms. We then present the specifications and control of our Digital Micro-mirror Device (DMD), and describe the optical setup used to create small barrier sizes, followed by a detailed description of the dipole trap. Finally, we detail the experimental setup and procedure for studying tunneling through single and double optical barriers with cold atoms.

In the second section, we present the experimental results. We first analyze tunneling through a single barrier, demonstrating both the classical and quantum regimes of tunneling. Next, we examine the Fabry-Pérot effect, where we observe a signature of atomic interference made possible by the DMD's versatility. Finally, we compare our results with numerical simulations of the Schrödinger equation, using an ansatz for the barrier potential to fit the experimental data. All of these results are presented in the paper attached at the end of this manuscript [62].

5.2 Atom Tunneling and Experimental Setup

5.2.1 Overview on Quantum Tunneling and DMD

Quantum tunneling is a fundamental phenomenon in quantum mechanics, where a particle can traverse a potential barrier despite having insufficient classical energy to overcome it [130]. This effect arises due to the wave-like nature of matter, as described by the Schrödinger equation [131], which allows for a finite probability of finding a particle beyond an energy barrier. Unlike classical mechanics, where an object must possess energy greater than the barrier to pass through, quantum tunneling permits transmission even when the particle's energy is lower than the potential height.

In the 1920s, physicists first explored this fundamental concept in quantum mechanics as they sought to understand how particles could penetrate energy barriers that would be insurmountable under classical physics. Inspired by Louis de Broglie's 1923 proposal that matter exhibits wave-like properties, early studies drew analogies between light waves and quantum particles [132]. In 1927, Friedrich Hund applied the concept of barrier penetration to molecular spectra, highlighting its role in chemical bonding [133]. Around the same time, Lothar Nordheim and Ralph Fowler explained electron emission from metals using tunneling, leading to the famous Fowler-Nordheim equation [134]. Application of tunneling came in 1928 when George Gamow, along with Ronald Gurney and Edward Condon, formulated a quantum mechanical explanation for alpha decay, showing that particles

could escape atomic nuclei via tunneling [135].

The first experimental confirmations of quantum tunneling emerged in the late 1920s and early 1930s, validating the theoretical framework. One of the earliest demonstrations came from studies of field electron emission, where physicists observed electrons escaping metal surfaces under strong electric fields, as predicted by the Fowler-Nordheim theory in 1928 [136]. In the 1950s, Leo Esaki experimentally confirmed electron tunneling in semiconductors, thereby developing the tunnel diode, a crucial component in high-speed electronics [137]. A decade later, Brian Josephson predicted and experiments soon verified that superconducting electron pairs could tunnel through thin insulating barriers, a phenomenon now known as the Josephson effect, with implications for quantum computing and superconducting circuits [138]. These experiments laid the foundation for the understanding and application of tunneling, including atomic-scale imaging with the scanning tunneling microscope (STM) in the 1980s [139, 140].

Experiments with ultracold atoms have provided direct observations of quantum tunneling. One example is the realization of resonant tunneling in optical lattices, where ultracold atoms confined in periodic potentials tunnel between lattice sites, analogous to electron transport in solids [141, 142, 143] or within a double-well potential [144]. In 1996, Anderson and Kasevich demonstrated quantum tunneling of Bose-Einstein condensates (BECs) in a tilted optical lattice under gravity, observing Wannier-Stark ladders and Bloch oscillations [145, 146, 147]. Furthermore, these experiments not only validate fundamental tunneling theories but also serve as platforms for exploring quantum many-body dynamics, high-precision measurements using matter-wave interferometers [148], and simulating condensed matter systems with high tunability. In configurations where atoms propagate through a waveguide, beam splitting has been achieved via Bragg scattering [149], and quantum reflection from the attractive potential near a solid surface has been experimentally observed [150, 151]. Additionally, physicists investigated tunneling dynamics in transport experiments involving two unbalanced fermionic reservoirs [152].

Unlike these indirect observations, cold atom experiments with tunable potential barriers provide a direct platform for studying quantum tunneling under controlled conditions. Yet many challenges remain, particularly in the low-velocity, thin-barrier limit. Pasquini et al. [153] conducted one of the earliest experiments, where they observed low-velocity quantum reflection of Bose-Einstein condensates (BECs) from a square array of silicon pillars. Marchant et al. extended this idea by investigating the quantum reflection of bright solitons from a narrow attractive potential made by a tightly focused, red-detuned laser beam, showing that nonlinear interactions within a BEC significantly modify the reflection process [154]. Billy et al. [155] introduced the concept of a guided atom laser, where they studied tunneling. More recent work by Ramos et al. [156, 157] has focused on the fundamental timescales of tunneling, using atom-optics analogs of classical knife-edge experiments to measure momentum distributions and directly probing the time spent by an atom within a barrier. However, observations of the quantum tunneling regime (where

the de Broglie wavelength λ_{dB} exceeds the barrier width σ_0) have not yet been achieved.

On the theoretical side. Martin et al. [158] studied the transmission and reflection of BECs through a Gaussian barrier, analyzing how the quantum wavefunction evolves. Manju et al. [159] studied the tunneling dynamics of interacting BECs. More recently, Lindberg et al. [160] investigated the asymmetric tunneling of BECs, examining how external perturbations and barrier asymmetries impact the transmission probability. A study on an atomic Fabry-Pérot interferometer using matter waves, as proposed by Manju et al. [161]. Such an interferometer, based on a double-barrier potential, enables precision measurements of atomic velocity distributions. Despite these theoretical studies, an experimental realization of a Fabry-Pérot interferometer with ultracold atoms remains challenging due to the difficulty of achieving precise control of barrier spacing and optical aberrations. Our work addresses these experiments thanks to the digital micromirror device (DMD) to create tunable optical barriers.

Over the past decade, Digital Micromirror Devices (DMDs) have been demonstrated to be a valuable tool for shaping optical potentials in ultracold atom experiments, enabling single-atom trapping in arbitrary geometries [162] and controlled quantum gases [163]. This is particularly valuable for studying quantum transport, disorder effects, and matter-wave interference, where adjustable potentials are essential.

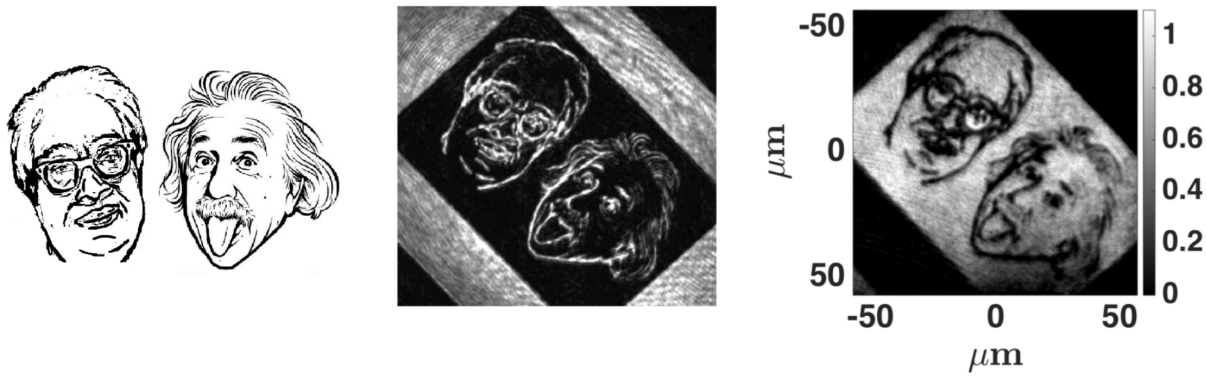


Figure 5.2: Image taken from [164]. The left image represents the binary input pattern. Then, they use the projected pattern to imprint artistic representations of Bose and Einstein on a nearly pure Bose-Einstein condensate (BEC) with $N = 5.2 \times 10^5$ atoms, as shown in the right image. Bright regions correspond to the atoms.

The DMDs can also manipulate BECs and degenerate Fermi gases [127]. Navon et al. [165] used DMDs to realize uniform quantum gases. Tajik et al. [166] implemented tunable 1D traps on an atom chip, and Gauthier et al. [164] developed DMD-based arbitrary potentials for quantum gas experiments. Additionally, A DMD can generate Bragg spectroscopy by creating controlled optical gratings, which enables momentum-resolved excitation measurements, offering insights into many-body interactions and collective excitations [167].

5.2.2 Digital Micromirror Device Properties

A Digital Micromirror Device (DMD) is a high-speed, spatial light modulator consisting of a two-dimensional array of microscopic mirrors, each of which can tilt independently to control the reflection of incident light. Micro-electro-mechanical systems (MEMS) technology fabricates these micromirrors, used for precise optical modulation at high speeds. Each mirror is suspended on a hinge and can switch between two stable states, directing light towards the desired system. This binary control structured light projection, combined with adaptive optics and optical potential, enables a range of applications.

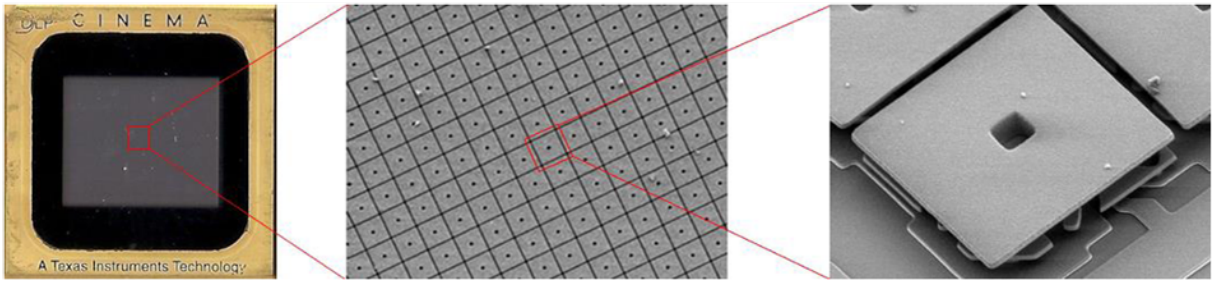


Figure 5.3: A Digital Micromirror Device (DMD) at different magnification levels. The full DMD chip appears in the first image, and the next zoomed-in view shows the micromirror array structure. The final one shows individual micromirrors, each of which can tilt independently to modulate light spatially.

In this work, we use the DLP6500FYE [168], V-Module V-6501 (Vialux), a Texas Instruments DLP (Digital Light Processing) DMD, controlled by DLPC900, which features a 1920×1080 array of micromirrors, each with a pitch of $p = 7.56\ \mu m$. The micromirrors can tilt by $\pm 12°$. The DMD can also be operated in external trigger mode, allowing for synchronization with experimental sequences and ensuring precise timing alignment with the atomic cloud. The device supports frame rates up to 9.523 kHz in binary mode (1-bit depth), well-suited for high-speed optical applications. It utilizes two 16-bit Low Voltage Differential Signaling (LVDS) data buses with a 400 MHz input clock rate, enabling rapid data transfer and synchronized mirror actuation. The DMD operation region is in the 420 – 700 nm wavelength range, with a micromirror reflectivity of approximately 88 % and a 92 % array fill factor. The total active area of the micromirror array measures 14.52 mm $\times$ 8.16 mm. The DMD operational temperature range is 0 ^{circ}C to 90 ^{circ}C. Finally, the DMD can be programmed to display static or moving optical potentials onto the atoms, which we will discuss in the next section.

5.2.3 Dipole Potential and Optical Setup

The optical dipole potential is based on the principles outlined in Grimm et al. [169, 170], where neutral atoms are confined or repelled using a laser beam. The interaction between the induced atomic dipole moment and the oscillating electric field of the laser creates the potential. We can express the resulting potential as: $V(\boldsymbol{r}) = \frac{3\pi c^2}{2\omega_0^3}\frac{\Gamma}{\Delta}I(\boldsymbol{r})$, where c is the speed of light, Γ is the damping rate or the spontaneous decay rate of the excited level, $2\pi \times \omega_0$ the atomic transition frequency and $I(\boldsymbol{r})$ is the intensity profil. For a red-detuned laser ($\Delta < 0$), atoms are attracted to regions of high intensity. For a blue-detuned laser ($\Delta > 0$), atoms are repelled from high-intensity regions and confined in areas of low intensity. The laser power determines the trap depth or barrier height, while the numerical aperture of the optics controls the confinement or barrier size.

The optical setup used in the experiment is shown in Fig. 5.5 and consists of a Verdi V18 laser (Coherent Inc.) with a wavelength of $\lambda = 532$ nm and a maximum power of 15 W, blue-detuned from the atomic transition to serve as a repulsive light source. To control the laser power incident on the Digital Micromirror Device (DMD), it first passes through an Acousto-Optic Modulator (AOM).

To ensure the beam sufficiently covers the active area of the DMD, an afocal telescope consisting of two lenses with focal lengths $f_1 = -12.5$ mm and $f_2 = 250$ mm expands the beam size by a factor of 20 with the laser's initial waist of 1.56 mm. To align with the DMD's blazing condition and optimize power distribution in the desired diffraction order, we tilt the laser at 20° upon incidence.

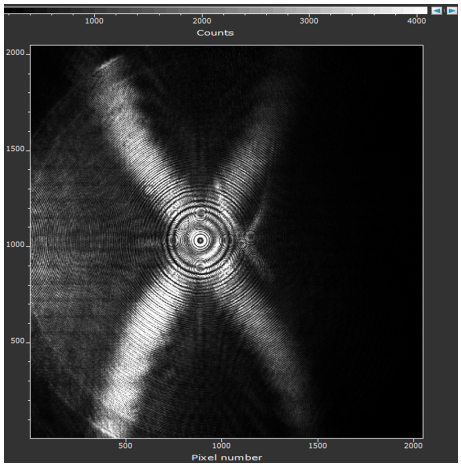


Figure 5.4: Double reflection of a cross pattern projected by the DMD, as seen by the top-view camera. The cross-shaped intensity profile originates from the DMD and undergoes two partial reflections on the walls of the glass science cell before reaching the camera. This reflection pattern is used to align the laser beam with the atomic plane.

The DMD reflects the beam with its micromirror array, directing it in the orthogonal

direction of its surface towards the optical objective, which is positioned at a distance of $L = 1.5$ m. The objective is composed of three chromatic triplet spherical lenses and is placed above the science chamber glass cell. A dichroic mirror reflects the 532 nm light from the DMD while transmitting the 770 nm light used for imaging, since we use this same objective for the top-view imaging camera (absorption imaging).

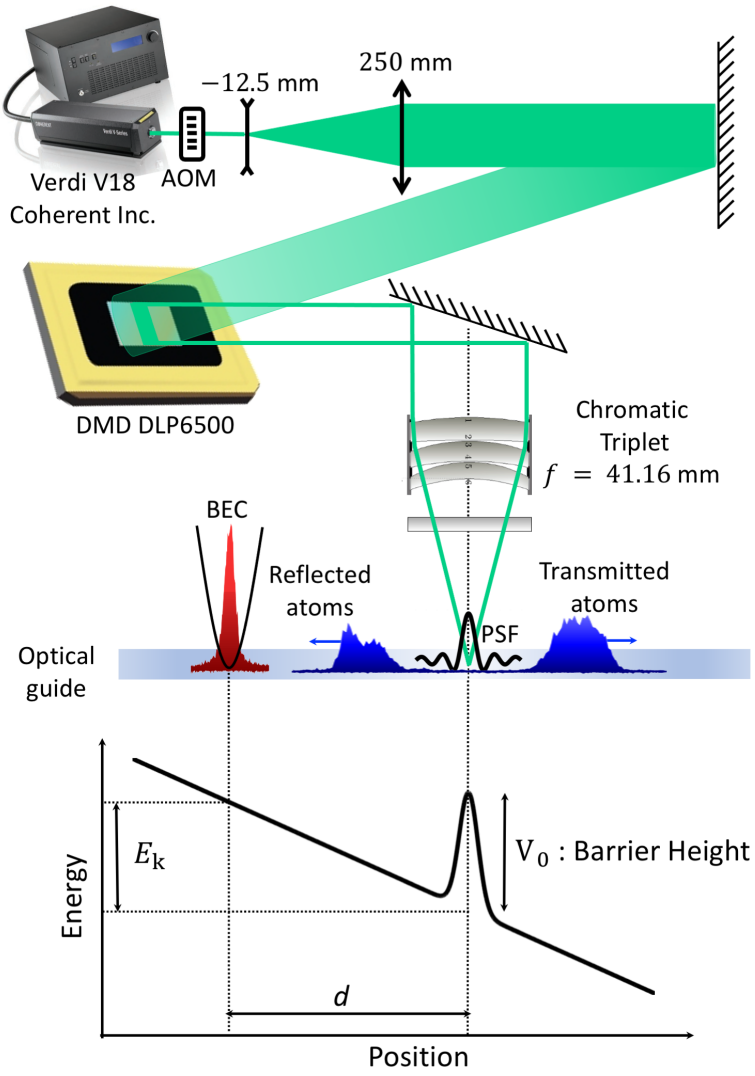


Figure 5.5: Optical setup for the DMD. A 532 nm Verdi V18 laser, its power controlled via an AOM and expanded using an afocal telescope. The beam is incident at 20°. An objective to focus the light in the atomic plane. The lower panels illustrate atomic reflections and transmissions, along with the corresponding energy, which consider the magnetic field gradient (the slope), barrier potential height V_0, kinetic energy of the atoms E_k, and the spatial separation d between the initial position of the BEC and the barrier.

To align the reflected laser beam on the atoms in the science chamber, we display a centered cross pattern on the digital micromirror device (DMD) and use the laser at low

power (0.1 mW). This beam is then aligned to pass through the objective, focusing on the atoms.

The cross pattern becomes visible on the top-view camera due to partial reflections from the glass-cell walls fig.5.4. With the live recording from this camera, we adjust the alignment so that the centers of the reflected cross patterns align with the position of the Bose-Einstein condensate (BEC), which we determine from a single-shot image of the experiment. Once we achieve this alignment, the DMD optical setup will project a 2D potential onto the atomic cloud. We estimated the maximum achievable repulsive potential at focus to be on the order of $V_{0\text{ at }15\text{W}} = 10$ kHz when we activate the Verdi laser at its maximum power output of 15 W and taking into account the fact that only a fraction of the laser power reaches the reflective region of the DMD, as we expanded to obtain flat intensity profil. Additionally, grating diffraction on the DMD reduces the power directed toward the atomic plane.

The objective has a focal length of $f = 41.16$ mm at a wavelength of 532 nm and $f' = 42.7$ mm at 770 nm. The diameter of the circular aperture is $D = 23$ mm. In the following, we will present an analysis of the system's Point Spread Function (PSF), which is crucial for a deeper understanding of the tunneling behavior at the focal point.

Generally, an optical system's Point Spread Function (PSF) represents its response to a point source positioned at infinity. When a collimated beam from this source passes through a lens, it forms an image at the focal plane, subject to diffraction effects. The theoretical PSF is derived using Fourier optics principles, [171].

Diffraction imposes a fundamental limit on the resolution of an optical system. The Rayleigh criterion can quantify the resolution limit, which states that two-point sources are resolvable when their first diffraction minima do not overlap. The angular resolution θ_R is given by

$$\theta_R = 1.22\frac{\lambda}{D}, \tag{5.1}$$

where λ is the wavelength of the incident light, and D is the aperture diameter. the calculated angular resolution is approximately 2.6×10^{-5} rad. This corresponds to a spatial resolution limit σ_{th} at the focal point f , yielding

$$\sigma_{th} = f \cdot \theta_R \approx 1\ \mu\text{m}. \tag{5.2}$$

The Numerical Aperture (NA) is given by

$$\text{NA} = n_{air} \sin(\varphi), \tag{5.3}$$

where n_{air} is the refractive index of the air, and φ is the angle of the aperture at the focal plane. For the objective with a focal length of $f = 41.2$ mm at 532 nm, we find

$$\varphi = \arctan\left(\frac{D}{2f}\right) \approx 0.294 \text{ rad}, \tag{5.4}$$

leading to

$$\mathrm{NA} \approx \sin(\varphi) \approx 0.27 \tag{5.5}$$

The diffraction-limited spot size (Airy disk diameter) is then given by

$$d_{lim} = 1.22\frac{\lambda}{\mathrm{NA}} = 2.3\ \mu\mathrm{m}. \tag{5.6}$$

The theoretical magnification factor M_{th} of the system is determined by the ratio of the distance between the image plane at focus and the lens $\zeta = \frac{f \cdot L}{f+L}$ and the distance between the object and the lens L, given by :

$$M_{th} = \frac{\zeta}{L} \approx \frac{1}{37.44} \tag{5.7}$$

leading to an effective pixel size $p_{eff} = M_{th} \times p \approx 0.2\mu$m, the point spread function (PSF) at the focal plane follows the Airy function distribution, expressed as

$$\mathrm{PSF}(r) = \frac{2J_1(kr\sin\varphi)}{kr\sin\varphi}, \tag{5.8}$$

where J_1 is the first-order Bessel function, $k = \frac{2\pi}{\lambda}$ is the wavenumber, and r is the radial coordinate.

We will use one-dimensional (1D) patterns on the Digital Micromirror Device (DMD) patterns perpendicular to the atom's propagation. In this case, the more relevant quantity is the 1D Point Spread Function (PSF), which theoretically can be expressed as :

$$\mathrm{PSF}(x) = \frac{\sin\left(\frac{\pi x}{\sigma_{th}}\right)}{\frac{\pi x}{\sigma_{th}}}, \tag{5.9}$$

Fraunhofer diffraction describes the far-field diffraction regime, where the propagation distance exceeds the characteristic dimensions of the aperture. In this regime, the Fourier transform determines the diffraction pattern of the aperture function. Consequently, the resulting one-dimensional intensity profile is given by:

$$I(x) = I_0 \cdot \left|t(x) \circledast \mathrm{PSF}(x)\right|^2, \tag{5.10}$$

where $t(x)$ represents the transmission function of the DMD array, and $\circledast$ denotes the convolution product operation.

This study focuses on a potential form of either a single-barrier or a double-barrier structure. The transmission function $t(x)$ can thus be defined as:

$$t(x) = \begin{cases} \Pi\left(\frac{x}{\sigma_0}\right), & \text{for a single barrier,} \\ \Pi\left(\frac{x-\frac{l}{2}}{\sigma_0}\right) + \Pi\left(\frac{x+\frac{l}{2}}{\sigma_0}\right), & \text{for a double barrier.} \end{cases} \tag{5.11}$$

Here, $\sigma_0 = p_{\text{eff}} \times N_{\text{BW}}$, represents the barrier width in microns, $l = p_{\text{eff}} \times N_{\text{BD}}$ the distance between two barriers in microns, where p_{eff} is the effective pixel size in microns, N_{BW} denotes the number of pixels defining a single barrier width and N_{BD} denotes the number of pixels defining a distance between two separate barriers. The function $\Pi(x)$, known as the rectangular or gate function, is defined as:

$$\Pi(x) = \begin{cases} 1, & \text{if } |x| < 1, \\ 0, & \text{otherwise.} \end{cases} \tag{5.12}$$

Theoretically, assuming an ideal optical system free from aberrations, the two cases of the final trapping potentials proportional to the Intensity profiles can be modeled as shown in Fig 5.6:

For a single barrier:

$$V(x) = \frac{V_0}{\pi^2} \left[\text{Si}\left(\frac{\pi}{\sigma_{\text{th}}} \left(x + \frac{\sigma_0}{2} \right) \right) - \text{Si}\left(\frac{\pi}{\sigma_{\text{th}}} \left(x - \frac{\sigma_0}{2} \right) \right) \right]^2. \tag{5.13}$$

For a double-barrier structure:

$$V(x) = \frac{V_0}{\pi^2} \left[\text{Si}\left(\frac{\pi}{\sigma_{\text{th}}} \left(x + \frac{\sigma_0 + \frac{l}{2}}{2} \right) \right) - \text{Si}\left(\frac{\pi}{\sigma_{\text{th}}} \left(x - \frac{\sigma_0 - \frac{l}{2}}{2} \right) \right) \right. \tag{5.14}$$

$$\left. + \text{Si}\left(\frac{\pi}{\sigma_{\text{th}}} \left(x + \frac{-\sigma_0 + \frac{l}{2}}{2} \right) \right) - \text{Si}\left(\frac{\pi}{\sigma_{\text{th}}} \left(x - \frac{-\sigma_0 - \frac{l}{2}}{2} \right) \right) \right]^2.$$

The function $\text{Si}(x)$ is the sine integral function, defined as:

$$\text{Si}(x) = \int_0^x \frac{\sin t}{t} dt. \tag{5.15}$$

The single-barrier potential $V(x)$ influences the barrier's amplitude and width due to the diffraction-limited point spread function (PSF). When the barrier width is below the resolution limit $\sigma_0 < \sigma_{th}$, increasing the number of pixels (N_{BW}) leads to an increase in the barrier height, as shown in Fig [5.6] from $\sigma_0 = 0.6\mu$m to $\sigma_0 = 2\mu$m. However, when $\sigma_0 > \sigma_{th}$, increasing N_{BW} results in a broadening of the barrier width rather than an increase in height. This behavior defines two distinct regimes: the sub-resolution regime, where the barrier height increases with N_{BW}, and the regime where the barrier width broadens. Additionally, the intensity profile does not exhibit a perfectly flat top for larger barriers due to the convolution with the sinc-like function.

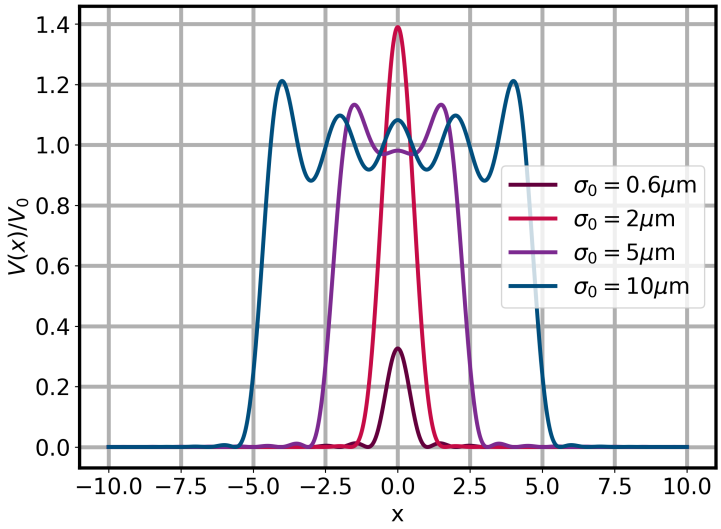


Figure 5.6: Simulated potential profile $V(x)$ for a single barrier taking $\sigma_{th} = 1\mu$m and for different σ_0 values.

For the double-barrier structure, the overlap between the two barriers takes effect as the separation distance l decreases due to the diffraction-limited resolution of the system. When the barriers are far apart, they remain well-separated, each retaining its identity. However, in the sub-resolution regime, where $\sigma_0 < \sigma_{th}$, the sinc-like diffraction tails of each barrier begin to interfere with each other, leading to either constructive or destructive interference in the resulting potential profile. The two regimes occur because the electric field of one barrier's point spread function (PSF) interacts with the maxima or minima of the second barrier's PSF, causing oscillations in the two barrier heights.

As shown in Fig. 5.7, for certain separation distances such as $l = 0.78\,\mu$m, $l = 2.45\,\mu$m, and $l = 4.45\,\mu$m, constructive interference increases the barrier height beyond the expected level for two independent barriers. Conversely, for $l = 1.4\,\mu$m, $l = 3.5\,\mu$m, and $l = 5.5\,\mu$m, destructive interference leads to a reduction in barrier height. As the distance increases, the barriers decouple, and interference effects diminish. When l becomes large, such as $l = 10\,\mu$m, the barriers behave independently.

Aberrations in the optical system can alter the point spread function (PSF), introducing deviations from the ideal diffraction-limited response. Imperfections in the circular lens, particularly at its edges, can cause variations in the wavefront, leading to increased background light and a broader PSF. This effect results in unwanted light spreading beyond the intended regions, potentially modifying the shape of the projected potential barriers. While these aberrations can impact the precision of the optical potentials, we will not discuss them in detail in this section. Instead, we will analyze their effects on the atoms in the results section, comparing the experimental results to the theoretical predictions.

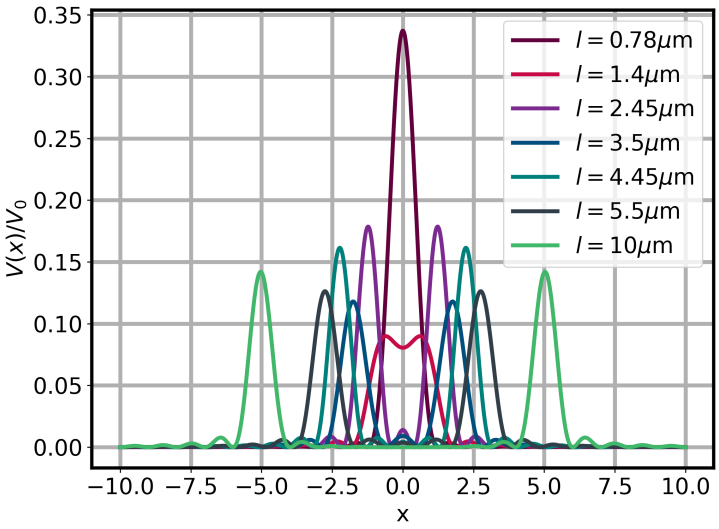


Figure 5.7: Simulated potential profile $V(x)$ for a double-barrier structure taking $\sigma_{th} = 1\mu$m, $\sigma_0 = 0.38\mu$m for different barrier distance l.

5.2.4 Experimental Procedure

In this section, we generate a thermal cloud to verify the focus of our optical system using a box-like potential and an optical lattice to load the atoms, thereby determining the experimental magnification factor. Then, we will describe the main procedure used for the barrier experiments.

For the focus regulation, we begin with a thermal cloud of 10^6 ^{39}K atoms in the $|F = 1, m_F = 1\rangle$ state at a temperature below 1 μK, confined in a harmonic trap with radial and axial trapping frequencies of $\omega_r = 300$ Hz and $\omega_z = 20$ Hz, respectively. The FORT1D beam provides the radial confinement, while the FORT2 beam generates the axial confinement. We then apply a box potential along the axial direction using the DMD and release the axial confinement by ramping down the FORT2 beam to zero. After 40 ms of free expansion along the axial direction, we image the cloud to determine whether the box potential was sufficiently strong to confine the atoms. The box potential has an axial size of 80μm, with potential walls defined by 0.4μm. However, if we are not in focus, the effective potential walls appear significantly broader and lower than expected, so the thermal atoms will have sufficient energy to escape the trap.

To tune the focus, we reduce the power of the green laser to just below the trapping threshold (typically $k_BT/2$) and adjust the vertical position of the objective by ± 10 μm. At each step, we evaluate whether we have more or fewer atoms that escaped the trap. By iterating this process, we determine the best objective position achieving a focus precision of approximately ± 10 μm as shown in Fig. 5.8.

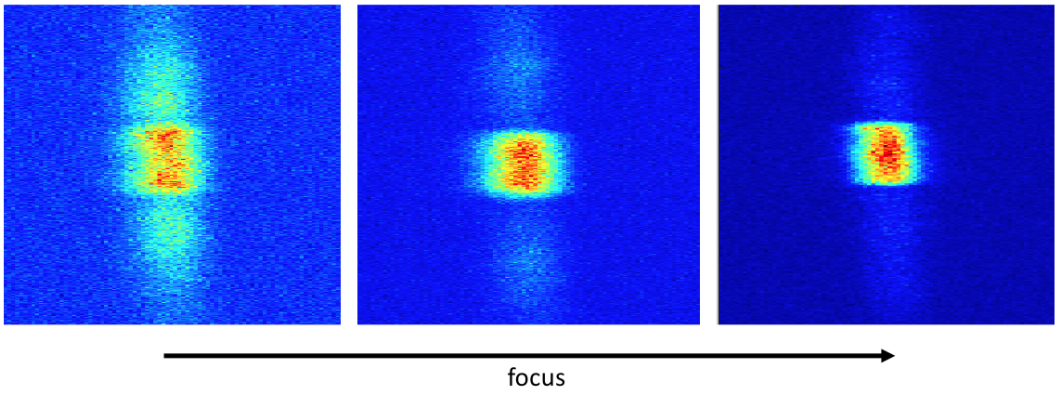


Figure 5.8: Images of the atomic cloud in a box trap as the distance between the objective and atoms is adjusted to achieve the best focus for more trapping.

Once we achieve the focus, we can apply various patterns to the DMD to generate different potentials. However, our initial goal is to determine the magnification factor experimentally.

To measure the magnification factor, we project a periodic potential onto the elongated cloud with a period of 100 DMD pixels corresponding to approximately 756 μm on the DMD. After a wait time of 20 ms, the one-dimensional density profile of the cloud acquires a periodic density modulation. By analyzing this pattern that has a period of $\approx 20\,\mu$m Fig.5.9, we obtain a precise measurement of the magnification factor:

$$M_{exp} = \frac{1}{37.93}$$

With the magnification factor determined experimentally, we now return to preparing the BEC for the tunneling experiment. The experiment begins with a Bose-Einstein condensate (BEC) of ^{39}K atoms in the $|F = 1, m_F = 1\rangle$. The condensation process is achieved through evaporative cooling in a crossed optical dipole trap while maintaining a magnetic field of 393 G. At this field, the interatomic interactions given by the scattering length a are approximately $130\,a_0$, where a_0 is the Bohr radius. We are initially in the Thomas-Fermi approximation.

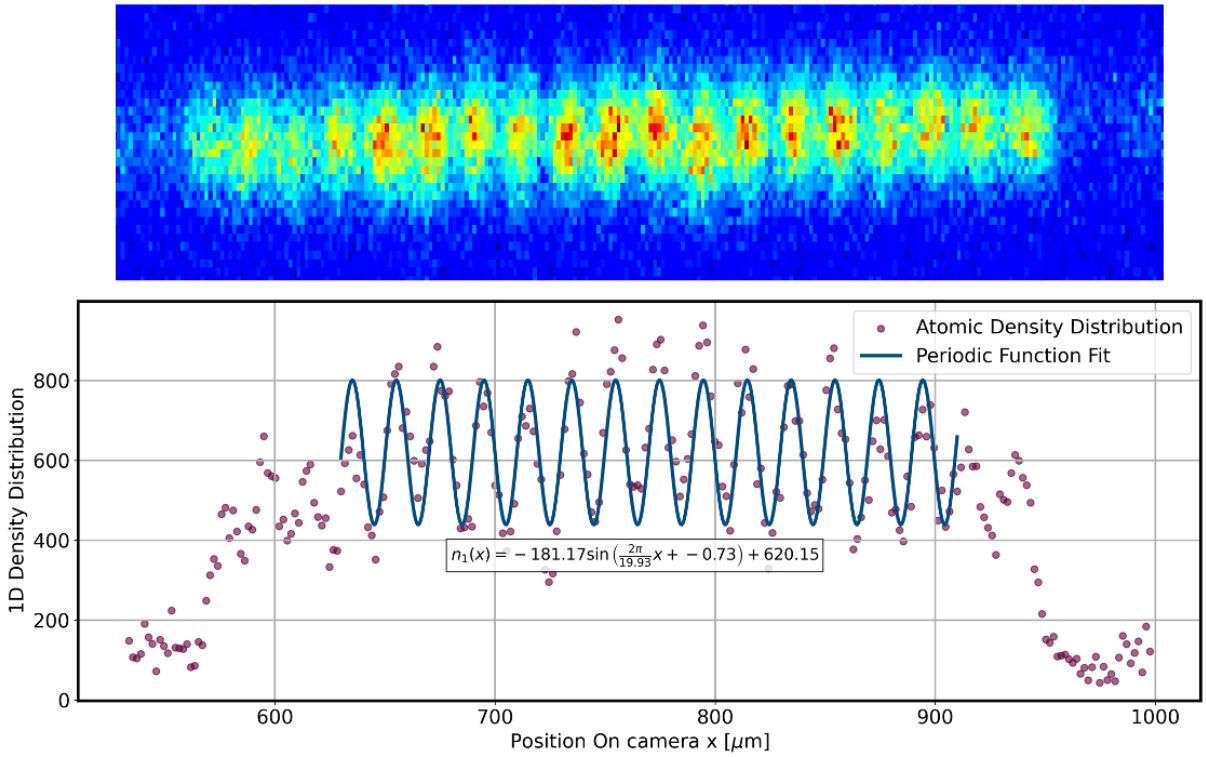


Figure 5.9: Measurement of the magnification factor using a periodic potential. (*Top*) Fluorescence image of the atomic cloud after applying a periodic DMD potential with a period of 100 DMD pixels. (*Bottom*) A one-dimensional atomic density profile was extracted from the image, showing periodic modulation. The fitted sinusoidal function confirms the expected periodicity, allowing experimental determination of the magnification factor.

After preparing the BEC, we adjust the trap parameters over 100 ms to reach the desired experimental conditions. After this time, atoms go to the 0D, 3D Gaussian profile. During this time, we sweep adiabatically the radial and axial trap frequencies from $(\omega_\perp, \omega_\parallel)/2\pi = (115, 47)$ Hz to $(\omega_\perp, \omega_\parallel)/2\pi = (120, 16)$ Hz, and the magnetic field down to 350 G. As the field approaches this value, the scattering length approaches zero, turning the gas into the non-interacting regime.

We scanned the magnetic field to achieve an experimentally non-interacting Bose-Einstein condensate (BEC). We measured the radial expansion of the condensate after a free expansion time of 10.3 ms. We extracted the size from fluorescence images taken after releasing the atoms from the trap, as shown in Fig.5.10. The radial expansion increases for fields above 350 G, indicating a repulsive interaction. Conversely, for fields below 350 G, we enter the collapse regime, where attractive interactions dominate. By locating the field where the size is the smallest, we know that the condensate is in a regime with negligible interactions. The interaction strength in the system is controlled by the magnetic field via a Feshbach resonance, allowing precise control over the scattering length.

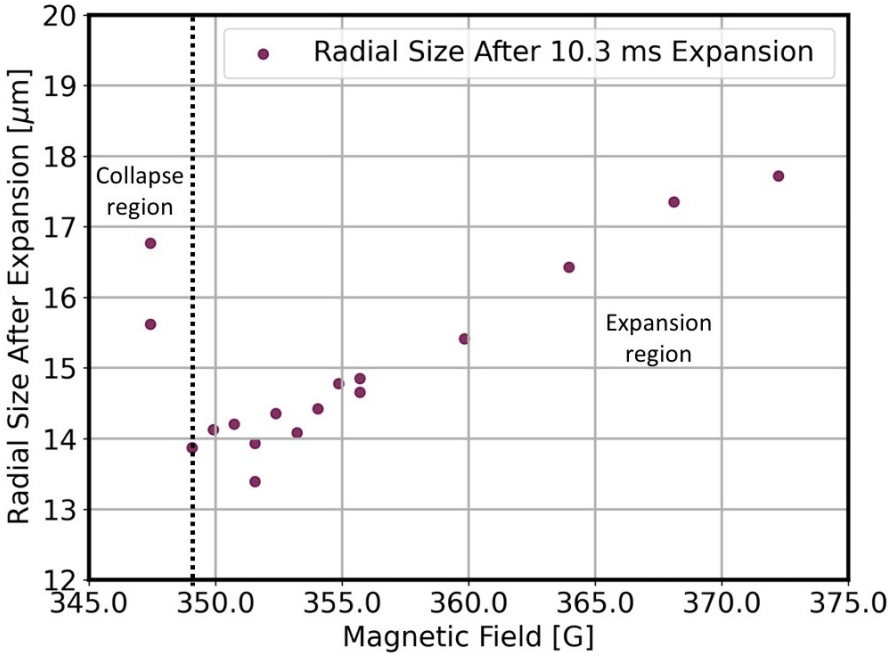


Figure 5.10: Radial size of the BEC after 10.3 ms of expansion as a function of the magnetic field. We observe the collapse regime for fields below 350 G, where attractive interactions lead to collapse. In contrast, the expansion increases for fields above 350 G due to weak repulsive interactions. We chose the field where we had the smallest expansion.

The condensate expands along the waveguide once the longitudinal confinement is removed. Due to the nearly non-interacting nature of the gas, this expansion is extremely slow, corresponding to a mean energy of $h \times 8$ Hz. This energy is equivalent to a velocity spread of $\Delta v_0 \sim 0.35$ mm/s upon release, which is slightly larger than the expected kinetic energy contribution of $h\omega_{\parallel}/8\pi \approx h \times 7.6$ Hz for a non-interacting condensate. Additionally, we observe a residual thermal fraction of approximately 20%, which expands at a faster rate, with a velocity spread of $\Delta v_{\text{thermal}} \sim 2.6$ mm/s. We attribute this thermal component to incomplete evaporative cooling.

The experiment begins by releasing the Bose-Einstein condensate (BEC) into a radial optical waveguide FORT1D. We achieve it by switching off the second optical trapping beam. The atoms propagate along the waveguide. To control the atomic velocity, we add a magnetic field gradient ∇B_x, which we generate by an off-axis coil. The acceleration of the atoms is given by: $\nabla B_x = \frac{m}{\mu_B} g$ where μ_B is the Bohr magneton, m is the mass of a ^{39}K atom, and g is the measured atomic acceleration. This results in a magnetic field gradient of approximately $\nabla B_x \approx 14$ G/m as extracted from the data in Fig 5.11.

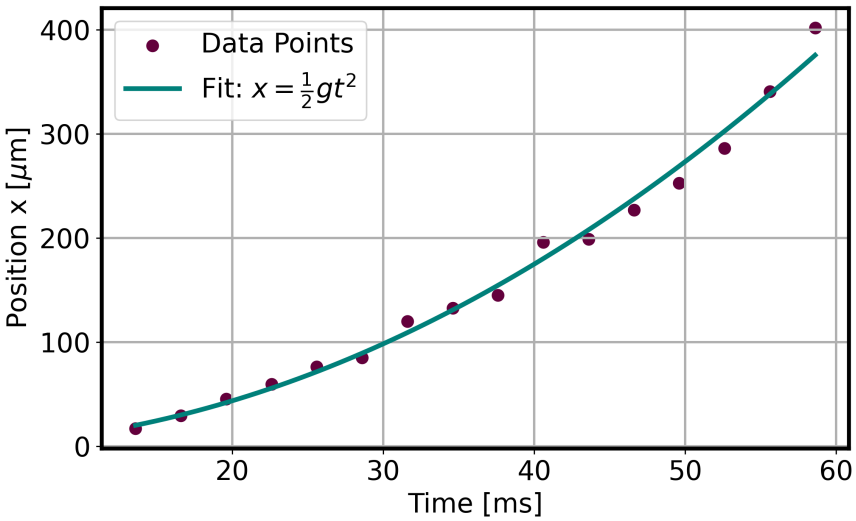


Figure 5.11: Position of the accelerated BEC as a function of time. The points represent the experimental data, while the solid curve is a quadratic fit given by $x = \frac{1}{2}gt^2$. The fitted parameter is $g = 200\,\mathrm{mm/s^2}$, assuming a parabolic trajectory due to uniform acceleration in a magnetic field gradient.

The controlled acceleration sets the atoms' kinetic energy before interacting with the optical barrier. To precisely select the velocity at the moment of interaction, we control the barrier position within a 76 μm range. The propagation time is controlled experimentally, and it varies in the waveguide depending on the chosen velocity. The interaction occurs only once, and the transmitted and reflected atomic clouds become fully spatially separated after the collision. This spatial separation time allows for better imaging and precision of the transmitted and reflected cloud.

The ratio between the atomic de Broglie wavelength, $\lambda_{dB} = h/mv$, and the barrier width, σ, determines how much quantum mechanical effects, such as wave-like tunneling, influence transmission through the potential barrier. The second parameter is the velocity spread, Δv, of the atomic ensemble when it reaches the barrier, which affects the energy distribution and, consequently, the transmission probability.

The velocity spread at the barrier is not determined by Δv_0, the initial velocity spread of the cloud, but by its initial spatial size. This can be understood as follows: the kinetic energy of an atom with initial velocity v_0 at a distance d from the barrier follows:

$$E_k = \frac{1}{2}mv^2 = \frac{1}{2}mv_0^2 + mgd.$$

For our experimental conditions, the contribution from the magnetic field gradient potential energy mgd dominates over the initial kinetic energy, leading to an approximate velocity expression:

$$v \approx \sqrt{2gd}.$$

It gives the relative velocity spread, which we can estimate as:

$$\frac{\Delta v}{v} \approx \frac{\Delta x_0}{2d} \ll 1 \implies \Delta v \approx \frac{2\ g\ \Delta x_0}{v} \tag{5.16}$$

Where $\Delta x_0 \approx 3.5\,\mu$m represents the atomic cloud's initial root-mean-square (rms) size. Importantly, Δv depends on v, implying that by waiting longer before reaching the barrier, the velocity increases while the velocity spread decreases. we find that for $v = 8.6$ mm/s, the velocity spread is approximately $\Delta v \approx 0.16$ mm/s. Similarly, for $v = 3.7$ mm/s, we obtain $\Delta v \approx 0.37$ mm/s. These values demonstrate that waiting longer to reach the barrier results in a higher velocity and a reduced velocity spread.

5.3 Experimental Results of the BEC Tunneling Experiment

5.3.1 Single Barrier Transmission: Classical vs Quantum Regime

We begin with the quantum tunneling in the classical regime, where the atomic de Broglie wavelength is small compared to the actual barrier width ($\lambda_{dB} < \sigma$). In this regime, for a monokinetic atomic beam colliding with a rectangular potential barrier, one expects a sharp step-like transmission function: Atoms with energy greater than the barrier height fully transmit. In comparison, those with lower energy reflect completely.

To test this behavior, we try with high-velocity atoms, specifically at $v = 8.6$ mm/s, corresponding to a de Broglie wavelength of $\lambda_{dB} = 1.2\,\mu$m. The Digital Micromirror Device (DMD) creates a potential barrier using 10 pixels, corresponding to a theoretical width of $\sigma_0 = 1.96\,\mu$m on the atomic cloud. Given this barrier size, when the width is larger than the resolution limit $\sigma_0 > \sigma_{th}$, the actual barrier width takes approximately the theoretical width $\sigma \sim \sigma_0$.

This experiment can also serve as a tool for adjusting the objective focus: by launching the atoms toward the barrier, lowering the laser power, and scanning the focus position, we determine the position where we obtain maximum reflection.

The experimentally measured transmission curve exhibits a step-like behavior, as shown in Fig.5.12, as expected for a classical regime ($\lambda_{dB} < \sigma$), where transmission should drop abruptly as the barrier height surpasses the atomic kinetic energy. However, our data

show a smoother transition rather than a perfectly sharp step.

Primarily, this deviation comes because we are not fully in the classical regime. For the parameters used in our experiment, solving the time-independent Schrödinger equation for a rectangular sharp-edge barrier confirms that the transmission is not completely steep, as the chosen barrier size is not infinitely large. This finite barrier width induces smoothing in the transmission curve. Additionally, the actual barrier shape does not have a perfect rectangular potential but follows the form modeled by Eq.5.13. As a result, the transmission profile deviates from the expected transmission curve for a rectangular barrier found in any textbook or tunneling problem, as can be observed on the solid curve in Fig.5.12. In this case, where the velocity is high, the velocity distribution is small because of the condition shown previously in Eq.5.16

In addition, the transmission curve does not reach 100 % transmission, even for barrier heights much lower than the atomic kinetic energy. This effect is due to a residual thermal fraction ($\sim$ 20%) in the atomic cloud. During acceleration, some thermal atoms have their initial velocities opposite to the acceleration direction, causing them to remain in the reflected region even when the BEC is fully transmitted. Consequently, we always count these atoms as reflected, which lowers the measured transmission.

We try to guess the error bars since we did not perform multiple runs for each data point. These fluctuations arise from uncontrolled dipole oscillations of the atomic cloud in the optical trap. These oscillations introduce small variations in the initial velocity. We display two error bars: one near the 50% transmission region, where transmission is most sensitive to small changes in velocity, and another in a region where transmission is nearly constant and insensitive to fluctuations.

Despite these effects, in the classical regime, we can still determine the barrier height V_0 that allows for 50% transmission, which should correspond to the kinetic energy of the atoms at the 50-50 point. From our data, we have : $V_0 = E_k = \frac{1}{2}mv^2 = h \times 3.6$ kHz. This Measurement provides a direct way to extract the potential height of the barrier and serves as a benchmark for the classical transmission regime, where quantum effects remain negligible.

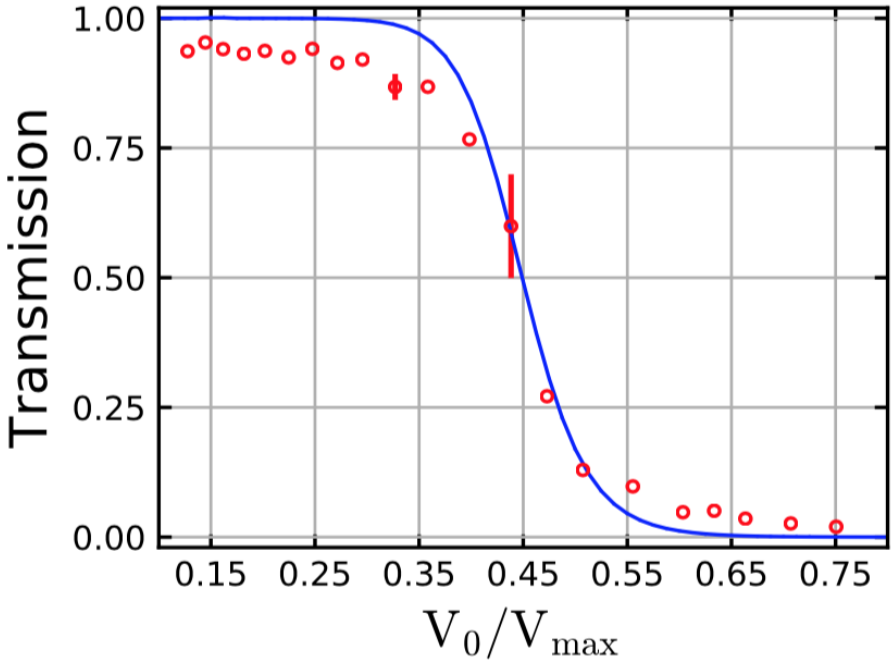


Figure 5.12: Transmission curve in the classical regime with a barrier size of $\sigma_0 = 1.96\,\mu$m and atoms at velocity $v = 8.6$ mm/s, corresponding to a de Broglie wavelength of $\lambda_{dB} = 1.2\,\mu$m. The red scatter points represent the experimental data, while the blue curve is the numerical solution of the 1D time-independent Schrödinger equation, using the potential form described in Eq. (3.14). We scan the barrier height as a percentage of the maximum laser power.

The previous results can be directly compared to the case of low-velocity atoms, where quantum effects become dominant. In this regime, we prepare atoms with a velocity of $v = 3.7$ mm/s, corresponding to a de Broglie wavelength of $\lambda_{dB} = 3.0\,\mu$m. We create the potential barrier using only three pixels on the Digital Micromirror Device (DMD) corresponding to a theoretical width of $\sigma_0 = 0.6\,\mu$m on the atomic cloud but because the width is smaller than the resolution limit $\sigma_0 < \sigma_{th}$, diffraction broaden the actual barrier width to $\sigma \sim \sigma_{th} \sim 1\ \mu$m, meaning that the actual barrier width is now comparable to the resolution of our optical setup.

Unlike in the classical regime, the transmission curve undergoes a qualitative change in behavior. Instead of the step-like, we observe a smooth decay in transmission as a function of barrier height. We expect this behavior in the quantum regime, where $\lambda_{dB} > \sigma$. In this case, the atomic wavepacket does not fully resolve the barrier structure, and a delta-function barrier can theoretically approximate the potential. Under this approximation, the corresponding analytical transmission function accurately describes our experimental data as $T = \left(1 + \left(\frac{V_0}{V_{\text{ref}}}\right)^2\right)^{-1}$, such that V_{ref} is the fitting parameter Fig.5.13.

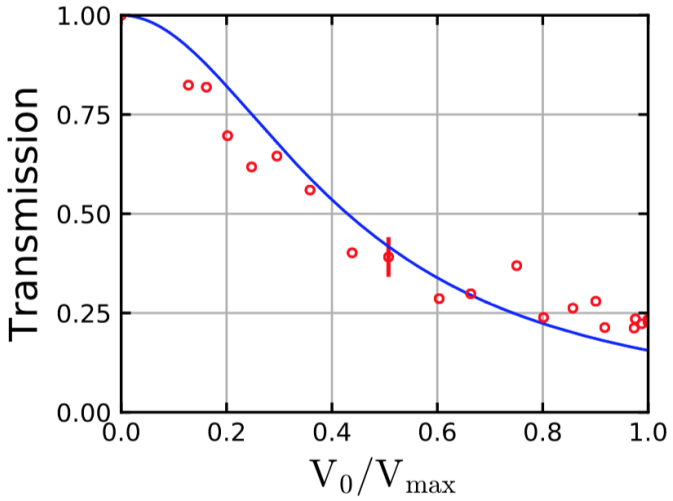


Figure 5.13: Transmission curve in the quantum regime with a barrier created using three pixels on the DMD. The atomic velocity is $v = 3.7$ mm/s, corresponding to a de Broglie wavelength of $\lambda_{dB} = 3.0\,\mu$m. The red scatter points represent the experimental data, while the blue curve corresponds to a fit using the transmission equation described for the delta potential.

We can attribute the small deviations from the theoretical transmission curve to the residual thermal fraction of the atomic cloud. In addition, these atoms at low velocity introduce an extra velocity spread, as verified in Eq.5.16, resulting in an averaging over slightly different transmission curves. However, in the quantum regime, the dominant effect remains the wave-like nature of the atoms, which leads to gradual rather than abrupt changes in transmission probability as the barrier height increases.

This experiment compares the distinction between classical and quantum regimes, showing how atomic transmission through a potential barrier transitions from a step-like behavior in the classical limit to a smooth transmission curve when the atomic wavelength no longer resolves the barrier.

5.3.2 Single Barrier Transmission: Barrier Height vs Barrier Width

In the previous experiments, the transmission curve shape was not very sensitive to the precise shape of the point spread function (PSF). To directly probe the PSF and its width, we conduct another experiment where we tune the laser power required to achieve 50% atomic transmission for different barrier widths at a constant atomic velocity of $v = 5$ mm/s corresponding to 2 μm de Broglie wavelength, check the red scattered point in Fig.5.14.

For our parameters, even though we are not always strictly in the classical regime ($\lambda_{dB} < \sigma$), numerical simulations indicate that the 50% transmission condition corresponds to a barrier height approximately equal to the atomic kinetic energy $V_0 \approx E_{\text{kin}}$.

This experiment, therefore, allows us to measure the relative barrier heights for different barrier widths σ_0, which we can control by adjusting the number of pixels N_{BW} on the DMD.

The precise shape of the potential barrier is the convolution of the PSF with a rectangular aperture function of width σ_0. In the limit of small barrier widths ($\sigma_0 < \sigma_{th}$), the field components interfere constructively, leading to a barrier maximum that scales as σ_0^2. As a result, the laser power required to maintain 50% transmission follows a $1/\sigma_0^2$ dependence. Conversely, for large barrier widths ($\sigma_0 > \sigma_{th}$), the barrier maximum height becomes independent of σ_0, leading to a constant needed power.

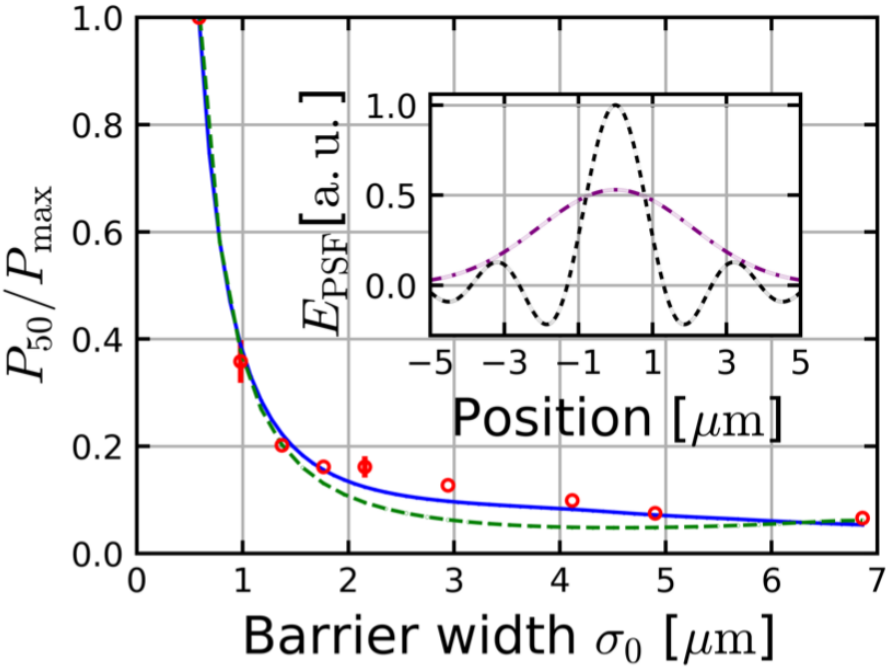


Figure 5.14: Power required for 50% atomic reflection as a function of barrier width. The red scattered points are the experimental data. The green dashed curve represents the expected behavior assuming an ideal sinc-shaped PSF. The solid blue curve corresponds to the PSF model, which includes optical aberrations. The inset shows the Ansatz PSF, consisting of a pure sinc function (dashed curve) and a Gaussian background part (dash-dotted curve), which are the two terms of Eq.5.17.

The experimental results confirm the expected transition between the two limiting behaviors, as shown in Fig.5.14. (red scattered data). This transition occurs when the barrier width σ_0 approaches the optical resolution limit, estimated as $\sigma_{\mathrm{th}} = 1\,\mu$m. While a standard sinc-shaped PSF predicts a potential profile described by Eq.5.13, fitting the data yields to effective resolution of approximately $2.0\,\mu$m, corresponding to $2\sigma_{\mathrm{th}}$. However, this simple model does not fully capture the experimental observations, particularly in the intermediate region of barrier widths ($2 - 5\,\mu$m).

Accurately describing the optical potential requires knowledge of the system's PSF. However, preliminary tests conducted with old PhD students showed discrepancies from the ideal case. Diffraction effects were well-preserved up to an aperture size of the objective of approximately 15 mm. Beyond this, the outer regions of the objective provided a slight diffuse background.

To consider this effect, we model the PSF as a combination of two components: a sinc function corresponding to the central region of the objective and a broader Gaussian background attributed to contributions from the outer region of the objective. We introduce an imaginary Gaussian term in the electric field PSF, which prevents direct interference with the sinc component when raised to the square.

We compute the optical potential using this refined PSF model and compare the simulated transmission to the experimental data. Optimizing the PSF parameters to get the best fit in Fig.5.14, which leads to an amplitude profile of the form:

$$\mathrm{PSF}(x) = \frac{sin\left(\frac{\pi x}{\sigma_{sinc}}\right)}{\frac{\pi x}{\sigma_{sinc}}} + iA_G \exp\left(-\frac{x^2}{2\sigma_G^2}\right), \tag{5.17}$$

where the best-fit values are $\sigma_{\mathrm{sinc}} = 1.30\,\mu$m, $\sigma_G = 2.07\,\mu$m, and $A_G = 0.53$. This model is represented by the solid blue curve in Fig.5.14 and provides a better match to the experimental data.

Although the exact form of the PSF may contain additional complexities, this model captures its key characteristics, including its effective size. This PSF guessing will play a crucial role in the next experiment on transmission through a double-barrier, where interference effects between the two potential barriers are sensitive to the precise shape of the optical potential. Therefore, understanding the PSF is essential for interpreting the results of the double-barrier case, which we will explore in the following section.

5.3.3 Double Barrier Transmission: Atomic Fabry-Pérot

After studying the behavior of atoms transmitted through a single barrier, we now investigate transmission through a double-barrier potential, where quantum interference effects become important. In this set of experiments, we launch the atoms with a velocity of 3.3 mm/s corresponding to a de Broglie wavelength $\lambda_{dB} = 3.1$ μm towards a pair of optical barriers, each created using two pixels on the DMD and set to 75% of the maximum laser power. Under these conditions, the transmission through a single barrier is approximately 70%. By adding a second barrier, we can vary the distance l between them.

We measure the total transmission as a function of the barrier spacing l, as shown in Fig.5.15 (red scattered points). The transmission exhibits oscillatory behavior as l

increases. While such oscillations might suggest Fabry-Pérot-type resonances, a direct interpretation as a simple interferometer is not entirely valid. Two key elements arise:

1. The transmission oscillations do not reach 100%, which we expect for an ideal Fabry-Pérot cavity.

2. The positions of the peaks do not strictly follow the expected spacing of $\lambda_{dB}/2$, where λ_{dB} is the atomic de Broglie wavelength.

For larger barrier separations, the transmission stabilizes around 50%. Two main factors contribute to experimental effects, leading to deviations from the ideal Fabry-Pérot model.

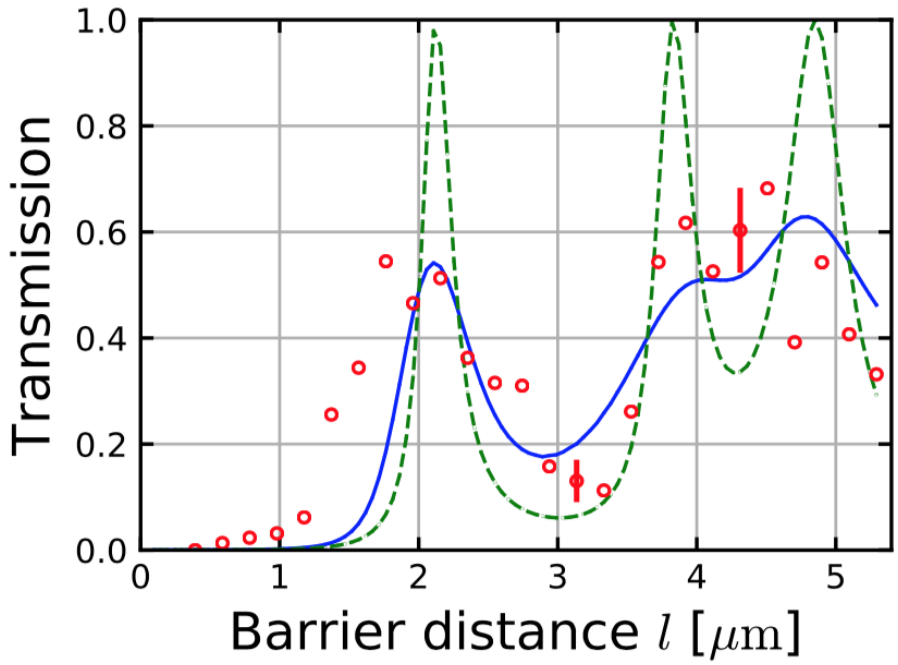


Figure 5.15: Transmission through a double-barrier potential as a function of barrier separation l. The red scatter points represent the experimental data. The dashed green curve corresponds to the monokinetic theoretical simulation using the experimental ansatz PSF from Eq. 5.17. The solid blue curve includes velocity averaging, accounting for the finite velocity spread of the atomic cloud ($\Delta v = 0.25$ mm/s).

For monokinetic atoms with a well-defined velocity, the expected transmission function predicts 100% transmission at specific barrier distances corresponding to Fabry-Pérot resonances. To obtain a more realistic system description, we solve the 1D time-independent Schrödinger equation using the potential profile introduced for the experimentally determined PSF in Eq. 5.17. Considering this potential, we recover the expected Fabry-Pérot-like resonances, where the transmission reaches 100% at specific barrier distances. We show the results in the dashed green curve in Fig.5.15. It is also important to note that the resonance peaks for monokinetic atoms are not evenly spaced and do not correspond to $l = \lambda_{dB}/2$.

This effect arises from the fact that we take a Gaussian background profile for the potential.

In addition, the atoms are not monokinetic but possess a finite velocity distribution, which can blur interference effects by averaging over many transmission curves. We estimate the velocity spread with the experimental parameters to be $\Delta v = 0.25$ mm/s. This effect can be accounted for in simulations by integrating the transmission over the velocity distribution, leading to a broadening and reduction of the expected Fabry-Pérot peaks as demonstrated on the solid blue curve in Fig.5.15. We find that while the first Fabry-Pérot resonance peak remains well-resolved, the second and third peaks merge into a single broader feature due to the oscillatory nature of the PSF, as explained at the beginning of the chapter, which modifies the heights of the barriers. This effect becomes particularly evident at barrier distances of $l \approx 1.9\,\mu$m and $l \approx 3.2\,\mu$m, where the sinus cardinal function is maximally negative and positive, respectively. At $l \approx 1.9\,\mu$m, the barrier height is minimized, while at $l \approx 3.2\,\mu$m, it reaches a maximum. Its the same kind of effect discussed previously in Eq. 5.14 and illustrated in Fig. 5.7 but for $\sigma_{th} = \sigma_{sinc} \approx 1.3\ \mu$m.

The observed transmission oscillations result from both Fabry-Pérot interference and optical effects from the PSF's oscillatory shape. It is difficult to determine which dominates, as isolating one would require simulations without atomic wave nature or experiments without optical interference, both are not feasible.

5.4 Chapter Conclusion

In this chapter, we have explored the quantum tunneling of Bose-Einstein condensates (BECs) through optical barriers created using a Digital Micromirror Device (DMD), distinguishing between classical and quantum regimes. Our experiments have directly observed the transition from step-like classical transmission to smooth quantum tunneling behavior as the de Broglie wavelength of the atoms exceeds the barrier width. The ability to control barrier shapes with the DMD has allowed us to investigate various tunneling conditions, including technical challenges such as velocity distributions, barrier width, and optical aberrations.

The first set of experiments focused on single-barrier transmission, demonstrating how atoms in the classical regime ($\lambda_{dB} < \sigma$) exhibit a sharp transition in transmission, while atoms in the quantum regime ($\lambda_{dB} > \sigma$) experience a decay in transmission probability. These results align with theoretical expectations.

We then investigated the role of the point spread function (PSF) in shaping the optical

barriers. By fitting, we extracted an effective optical system resolution by varying the barrier width and measuring the required laser power for 50% atomic reflection. This analysis revealed that a simple sinc-function PSF model was unable to capture the experimental results. Instead, a model including both a sinc and an additional Gaussian background provided a more accurate description, taking into account the presence of optical aberrations that influence barrier formation.

Building on these insights, we extended our study to double-barrier transmission, where optical interference effects become important. The observed oscillations in transmission as a function of barrier separation suggest a Fabry-Pérot-like effect. Our theoretical analysis, with the ansatz PSF, reproduced the experimental data. We demonstrated that optical interference between barrier regions on the DMD, the wave-nature of the atoms, and velocity averaging play a role in describing the transmission curve. While the first resonance peak remains well-resolved, higher-order peaks become progressively suppressed due to velocity dispersion.

These results provide the first experimental evidence for matter-wave interference in a cold atom Fabry-Pérot interferometer using optical barriers made with DMD. Future work could focus on improving the optical resolution to minimize aberrations and realize moving patterns with the DMD.

Beyond the current work, previous proposals have suggested using a matter-wave Fabry-Pérot interferometer as a gravimeter [172]. Additionally, interactions in atomic collisions with potential barriers remain exciting [173, 174, 175], particularly in the context of bright soliton scattering. Theoretical predictions suggest that soliton scattering on a barrier could lead to the formation of non-classical NOON states [176]. Furthermore, in the presence of interactions, the Fabry-Pérot interferometer is expected to exhibit quantum effects such as squeezing of the outgoing atomic cloud or atomic blockade [177], providing opportunities for future experimental studies.

General Conclusion and Perspectives

This thesis presents my work on studying interactions in a coherently coupled two-spin-component Bose-Einstein condensates (BECs) of potassium-39 atoms. I began by explaining the fundamental theory required to describe these systems, including atomic structure, the interaction between atoms, and how to control these interactions using magnetic fields and Feshbach resonances. I also described the case of a two-level system coupled by radio-frequency fields and how to understand the interactions in the dressed-state basis.

A part of the experimental work focused on improving the stability of the magnetic field. We built and tested a stabilization system that reduced noise to below 100 μG, which is important for performing precise measurements in spinor BECs and controlling the coherent coupling. Using this stable setup, we investigated how the mean-field interaction energy behaves in the dressed-state basis. We found that at low Rabi frequencies or high densities, the energy exhibits nonlinear and saturation effects. These results go beyond the usual mean-field description in a single-component BEC or uncoupled mixture and show the existence of higher-order terms in the energy functional.

We then explored the formation of quantum droplets. By tuning the detuning-to-Rabi ratio δ/Ω, we could reach a regime where slightly attractive mean-field interactions are balanced by repulsive quantum fluctuations (LHY correction). This balance creates self-bound droplets that can exist without any trapping. We observed experimental signatures of this regime and compared them to theoretical predictions.

In the final part of the thesis, I used a Digital Micromirror Device (DMD) to create optical barriers and study tunneling of BECs. I observed both classical and quantum tunneling, as well as interference patterns similar to those of the Fabry-Pérot effect. These results demonstrate how programmable light can be used to investigate the wave-like properties of atoms.

Looking ahead, several directions can be pursued to extend this work. We are currently

developing Bragg diffraction using the DMD, which requires a clean and well-controlled optical potential. To achieve a cleaner potential, we aim to replace the current homemade objective with a more effective commercial one. This upgrade will also enhance the potential for better box trap control of quantum droplets, enabling us to suppress the effects arising from imperfect axial trap turn-off.

Another direction is to investigate the three-body scattering halo. By spatially splitting the BEC into two parts and colliding them using dynamic potentials generated by the DMD, we can explore the role of higher-order interactions in a controlled way. This setup may also allow us to probe new types of droplets that emerge from the interplay between two- and three-body interactions in the upper dressed state. Additionally, it is possible to study the modified Thomas-Fermi profile resulting from the change in interaction scaling. Additionally, we can study modulation instabilities and locally tune interactions using copropagating Raman lasers for coupling the two spin states. This would open the door to studying spatially modulated interactions.

List of Figures

1.1 Energy level structure of ^{39}K, showing fine structure, hyperfine splitting, and Zeeman level. The Zeeman effect lifts the degeneracy of the hyperfine levels in the presence of an external magnetic field, exhibiting different behaviors in the weak, intermediate, and strong field regimes. 23
1.2 Energy splitting between the Zeeman states of the $F = 1$ manifold as a function of the magnetic field. The curves show $\Delta E_{10} = E_1 - E_0$ and $\Delta E_{21} = E_2 - E_1$. 26
1.3 Potential energy curves described by the Born Oppenheimer approximation, for the singlet ($X\,^1\Sigma_g^+$) and triplet ($a\,^3\Sigma_u^+$) states of the potassium-39 dimer ($^{39}K_2$). Taken from Tiecke et al. [65]. 29
1.4 Scattering length as a function of potential depth for a square-well potential, showing divergence each time a bound state appears. The horizontal dashed line at $a = r_0$ marks the range of the potential well. 31
1.5 Schematic of open and closed channel potentials. A Feshbach resonance occurs when a bound state E_c in the closed channel becomes degenerate with the scattering energy E in the open channel [48]. 32
1.6 Scattering length a_{11}, a_{22}, a_{12} and a_{00} as a function of the magnetic field between the Zeeman states $|0\rangle, |1\rangle, |2\rangle$ of ^{39}K. 33
1.7 (Left) Dressed state energies $E_{\text{Rabi}|\pm\rangle} = \pm\hbar\widetilde{\Omega}/2$ versus detuning. (Right) Projection of the bare state $|2\rangle$ onto the dressed states $|+\rangle$ and $|-\rangle$ as a function of δ/Ω. 40
1.8 Time evolution of the population in state $|2\rangle$ under Rabi coupling for two different detunings: on resonance ($\delta = 0$) and off-resonance ($\delta = \Omega$). The population undergoes full oscillations at the Rabi frequency Ω when $\delta = 0$, leading to complete population transfer. For nonzero detuning, the oscillations occur at the generalized Rabi frequency $\widetilde{\Omega} = \sqrt{\Omega^2 + \delta^2}$ with a lower population transfer. We normalize time to half the Rabi period as $t/(\pi/\Omega)$. 41
1.9 Probability of ending in the lower dressed state $|-\rangle$ after a linear RF frequency sweep from $\delta_i = 9\Omega$ to δ_f at a fixed Rabi frequency $\Omega/2\pi = 1$ kHz, for various total sweep durations t_f. 43

1.10 Effective two-body scattering length in the dressed-state basis as a function of δ/Ω. The plot shows the elastic interaction strengths g_{--}^{--}, g_{++}^{++}, and g_{+-}^{+-}, as well as the inelastic terms, illustrating the tunability of interactions via detuning to the Rabi ratio. The interaction parameters used for this plot correspond to a data for a magnetic field of 56.85 G, where $g_{11} = 84.3$, $g_{22} = 33.3$, and $g_{12} = -53.21$ (in units of $\frac{m}{4\pi\hbar^2}[a_0]$). 46

1.11 Experimental determination of the dressed-state scattering length a_{--} as a function of detuning δ for potassium 39, taken from Ref. [53]. 47

2.1 Illustration of the experimental sequence used for cooling and trapping ^{39}K atoms, showing the geometry at different stages. We take the figure from the thesis of Lucas Lavoine [88], with additional modifications to reflect the current geometry of the experiment. 50

2.2 Schematic of the optical configuration in the science chamber showing the geometry of the three dipole trapping beams: FORT1 and FORT2 at 1550 nm, and FORT1D at 1064 nm. We use dichroic mirrors (1 μm cutoff) to combine the FORT and MOT beams along the same axes. We place the photodiodes after each beam path. They are integrated into PID feedback loops to actively stabilize laser intensity. Beam dumps eliminate residual light after the chamber. Figure taken from the thesis of Guillaume Berthet [87]. 52

2.3 Optical setup of the D2 repumper (red path) and the push beam (pink path). 53

2.4 Optical setup of the D2 repumper (red path), D2 principal (purple path), absorption imaging (green path), D2 beams for MOT 2D and MOT 3D (magenta path), and the D1 line (blue path). 55

2.5 Optical setup of the D1 table (blue path) and the optical pumping beam (dark green path). 56

2.6 Schematic of the old magnetic field control system, showing both power supplies (SM18-220 and SM70-AR-24), switching modules, analog control hardware, and RF components used to generate coherent coupling. 60

2.7 Bode diagram showing the amplitude (left) and phase (right) of the transfer function $H(\omega)$, simulated with $R = 150\,m\Omega$, $C_1 = 1\,\text{mF}$, and $L = 175\,\mu\text{H}$. It's a second-order low-pass filter with a resonance peak. At low frequencies, the gain approaches unity, while at high frequencies it attenuates (-40 dB/decade). The phase goes from $0°$ to $-180°$. 66

2.8 Correlation measurement between the measured detuning δ/Ω (obtained from the coil current measurement) and the measured internal state population $P_{|2\rangle\to|-\rangle}$. The linear fit confirms the expected slope of approximately 0.5 at $\delta/\Omega = 0$, consistent with Eq. 1.54. 69

2.9 Schematic of the active magnetic field compensation circuit. We generate a reference current by applying a stable voltage across a precision resistor and compare it to the current in the main coils, measured by a LEM transducer. The resulting error signal is filtered, amplified, and fed to a current driver, which injects a corrective current into a compensation coil. We include a Twin-T notch filter at 17 kHz to suppress internal transducer noise. We also use a mutual inductance coil to cancel the inductance between the main and compensation coils. 71
2.10 Repetitive Ramsey oscillations over 2 hours, showing the fraction f of atoms in state $|1\rangle$ as a function of the evolution time T. Blue circles: single-shot data; black points: average over 10 sequences. 75
2.11 population measured after a time $T_{50\,\mathrm{Hz}}$ of a Ramsey sequence. The observed oscillations reflect the magnetic field modulation at 50 Hz and its harmonics experienced by the atoms. We show two full cycles of the line frequency. . 76
2.12 Noise spectroscopy measurement: transition probability $\mathbb{E}[P]$ as a function of the Rabi frequency Ω, obtained using dressed-state sweeps with a hold time $T_2 = 20\,\mathrm{ms}$. Each data point corresponds to the mean population transferred to $|1\rangle$, averaged over 5 repetitions. The measurement shows the frequency spectrum of magnetic field noise near the Rabi coupling frequency. 78
2.13 Noise spectrum of the compensation electronics measured before the notch with the Rohde & Schwarz FSV analyzer, with the power supply and gaussmeter disconnected. The electronics show broadband noise below 5 kHz and a narrow peak at 17 kHz, corresponding to the LEM transducer's internal clock. 78
2.14 Noise spectrum of the compensation electronics measured with the Rohde & Schwarz FSV signal analyzer, with the power supply delivering 15 A. The configuration used $C_1 = 1\,\mathrm{mF}$ and $C_2 = 33\,\mathrm{nF}$. The plots display broadband noise below 5 kHz, with clear spectral features. Left: full spectrum from 10 Hz to 20 kHz with 100 Hz resolution bandwidth. Right: zoomed-in spectrum from 10 Hz to 3 kHz with 20 Hz resolution bandwidth, highlighting prominent 50 Hz harmonics and low-frequency noise contributions from the power supply and compensation circuit. 79

3.1 The relative population in dressed state as a function of δ/Ω, for several Rabi frequencies Ω. The left panel shows $P_{|2\rangle\to|+\rangle} = \sin^2(\theta/2)$ obtained from Eq. 3.10, while the right panel shows $P_{|2\rangle\to|-\rangle} = \cos^2(\theta/2)$ from Eq. 3.11. The atomic density $n = 2\times10^{20}\,\mathrm{m}^{-3}$, and interaction strength $g_{11} = 84.3\,g_0$, $g_{22} = 33.3\,g_0$, $g_{12} = -53.21\,g_0$, where $g_0 = \frac{4\pi\hbar^2}{m}a_0$. For these parameters, the dimensionless interaction coefficients vary as follows: $\epsilon \in [0.031, 1.36]$, $\gamma \in [0.065, 2.89]$. 85
3.2 Schematic illustration of the interaction-induced shift of the detuning in a two-level Rabi-coupled system. Left: bare two-level system with detuning δ. Right: interacting case, where mean-field shifts result in an effective detuning δ'. 86

3.3 Comparison of the interaction energy per particle in a coherently coupled BEC as a function of δ/Ω for various Rabi frequencies. Parameters: atomic density $n = 2 \times 10^{20}\,\mathrm{m}^{-3}$, $g_{11} = 84.3\,g_0$, $g_{22} = 33.3\,g_0$, $g_{12} = -53.21\,g_0$. Energies are expressed in units of $\frac{g_0 n}{2}$, with $g_0 = \frac{4\pi\hbar^2 a_0}{m}$. 88

3.4 Energy per particle per Rabi energy in the $|-\rangle$ dressed state as a function of the dimensionless parameter $\gamma = \frac{n\bar{g}}{\hbar\Omega}$, at fixed $\delta/\Omega = 1$. The solid line shows the full numerical mean-field result (excluding the zeroth-order Rabi term), the dashed curve includes the linear and quadratic terms in density from Taylor expansion, and the dash-dotted line shows only the linear contribution. 89

3.5 Experimental signatures of the three-body interaction term in the dressed-state BEC, taken from Ref. [95]. Left panel: Downshift of the radial breathing mode frequency $\omega_b/\omega_\perp$ measured as a function of δ/Ω in the symmetric interaction configuration where $g_{11} = g_{22}$. The shaded region represents theoretical predictions including the g_3 term. Right panel: Radial collapse observed via a sudden drop in peak 1D density, even in regimes where the dressed two-body scattering length $a_{--} > 0$. This behavior confirms the presence of an attractive term. 90

3.6 Root-mean-square (rms) axial size σ_{int} of the condensate as a function of δ/Ω for different Rabi frequencies Ω, after a time-of-flight $t = 62.6$ ms. The derived quantity $m\sigma_{\mathrm{int}}^2/(2t_{\mathrm{tof}}^2)$ reflects the interaction energy per particle. The location of the dip tracks the minimum of the dressed-state coupling g_{--}^{--}, while the broadening of the dip at lower Ω highlights the higher-order nonlinearity. 92

3.7 Measured population of the bare state $|2\rangle$ after an adiabatic sweep to the lower dressed state $|-\rangle$, shown as a function of δ/Ω for various Rabi frequencies Ω. The data reveal smoother transitions at lower Ω, consistent with the higher-order interaction effects discussed previously. Due to slight imperfections in the preparation procedure, the initial state at large δ/Ω does not reach 100% population in $|2\rangle$, with a residual occupation below 5%. 93

3.8 comparison between the measured expansion energy and the theoretical predictions from a mean-field simulation based on the Gross–Pitaevskii equation. The plot shows the interaction energy per particle, extracted from the axial cloud size after time-of-flight, as a function of δ/Ω for various Rabi frequencies. The solid lines correspond to the simulated expansion energies assuming adiabatic radial evolution. 95

4.1 The scattering length $a_{\mathrm{min}}, a_{11}, a_{22}, a_{12}$ corresponding to $g_{\mathrm{min}}, g_{11}, g_{22}, g_{12}$, shown as a function of magnetic field for ^{39}K. The region below 56.87 G indicates the weakly attractive regime ($a_{\mathrm{min}} < 0$) where quantum droplet formation becomes possible. 100

4.2 Plot of the dimensionless integrals $I(y)$ (solid curve), $C_J\, J(y)$ (dashed curve), and $C_K\, K(y)$ (dotted curve) as a function of $y = \hbar\tilde{\Omega}/(-2g_{12}n)$, appearing in the expression for the LHY energy correction. The small prefactors C_J and C_K, calculated for 56.61 G for potassium 39 atoms, suppress the impact of $J(y)$ and $K(y)$, making $I(y)$ the dominant contribution for our parameters. 103
4.3 Mean-field energy per particle (dashed curve), Lee-Huang-Yang energy per particle, for $\Omega/2\pi = 7$ kHz (blue dotted curve), for $\Omega/2\pi = 4$ kHz (green dotted curve), and total energy per particle as a function of density, for $\Omega/2\pi = 7$ kHz (orange solid curve), for $\Omega/2\pi = 4$ kHz (red solid curve) computed for a magnetic field $B = 56.87\,\mathrm{G}$. The minimum of the total energy per particle indicates the mechanical equilibrium and potential droplet formation at a density around $n \approx 2 \times 10^{20}\,\mathrm{m}^{-3}$ for $\Omega/2\pi = 7$ kHz and at a density around $n \approx 4 \times 10^{20}\,\mathrm{m}^{-3}$ for $\Omega/2\pi = 4$ kHz. 104
4.4 Calibration of the optimal axial trap release time for different Rabi frequencies. We scan the time during the sweep at which the axial trap is turned off and extract the resulting size. Each data point is obtained by averaging several measurements in 0.8 ms intervals, and the error bars represent the corresponding standard deviation. The observed minimum in the axial size indicates the moment when the induced shrinking or trap expansion dynamics compensated, resulting in minimal energy. 107
4.5 Calibrated axial trap release time as a function of Rabi frequency Ω. Each data point corresponds to the optimal timing (within the 9-ms Landau-Zener sweep) at which we turn off the axial trap in order to minimize the added kinetic energy for different Rabi frequencies. 108
4.6 Axial size of the BEC as a function of time for various magnetic fields and Rabi frequencies, measured at the minimum of δ/Ω. For each magnetic field, the Rabi frequency corresponding to minimal expansion (or contraction) is identified and used to map the stability condition. 110
4.7 Experimental determination of the stability condition for droplet formation. Each red point corresponds to the Rabi frequency Ω at which the BEC exhibits no axial expansion or contraction, extracted from Fig. 4.6. The horizontal error bars represent the uncertainty range where we observe the transition from expansion to contraction. The solid blue curve shows the theoretical prediction based on Eq. 4.6, a fixed density of $1.6 \times 10^{20}\,\mathrm{m}^{-3}$. Note that it might shift up or down by $\sim$0.4 g_0 because of the uncertainties in the theoretical scattering length values. Here, we used the values from J. Kraats based on the Tiemann potential. 111

5.1 Fluorescence image of our ^{39}K Bose-Einstein condensate (BEC) undergoing quantum tunneling. We intentionally add the optical barrier in green to illustrate its position at the center, with the transmitted atom cloud visible on one side and the reflected atom cloud on the other. This image, captured during our tunneling experiment, shows the wave-like behavior of ultra-cold atoms as they interact with the potential barrier. 115

5.2 Image taken from [164]. The left image represents the binary input pattern. Then, they use the projected pattern to imprint artistic representations of Bose and Einstein on a nearly pure Bose-Einstein condensate (BEC) with $N = 5.2 \times 10^5$ atoms, as shown in the right image. Bright regions correspond to the atoms. 118
5.3 A Digital Micromirror Device (DMD) at different magnification levels. The full DMD chip appears in the first image, and the next zoomed-in view shows the micromirror array structure. The final one shows individual micromirrors, each of which can tilt independently to modulate light spatially. 119
5.4 Double reflection of a cross pattern projected by the DMD, as seen by the top-view camera. The cross-shaped intensity profile originates from the DMD and undergoes two partial reflections on the walls of the glass science cell before reaching the camera. This reflection pattern is used to align the laser beam with the atomic plane. 120
5.5 Optical setup for the DMD. A 532 nm Verdi V18 laser, its power controlled via an AOM and expanded using an afocal telescope. The beam is incident at 20°. An objective to focus the light in the atomic plane. The lower panels illustrate atomic reflections and transmissions, along with the corresponding energy, which consider the magnetic field gradient (the slope), barrier potential height V_0, kinetic energy of the atoms E_k, and the spatial separation d between the initial position of the BEC and the barrier. . . . 121
5.6 Simulated potential profile $V(x)$ for a single barrier taking $\sigma_{th} = 1\mu$m and for different σ_0 values. 125
5.7 Simulated potential profile $V(x)$ for a double-barrier structure taking $\sigma_{th} = 1\mu$m, $\sigma_0 = 0.38\mu$m for different barrier distance l. 126
5.8 Images of the atomic cloud in a box trap as the distance between the objective and atoms is adjusted to achieve the best focus for more trapping. 127
5.9 Measurement of the magnification factor using a periodic potential. (*Top*) Fluorescence image of the atomic cloud after applying a periodic DMD potential with a period of 100 DMD pixels. (*Bottom*) A one-dimensional atomic density profile was extracted from the image, showing periodic modulation. The fitted sinusoidal function confirms the expected periodicity, allowing experimental determination of the magnification factor. 128
5.10 Radial size of the BEC after 10.3 ms of expansion as a function of the magnetic field. We observe the collapse regime for fields below 350 G, where attractive interactions lead to collapse. In contrast, the expansion increases for fields above 350 G due to weak repulsive interactions. We chose the field where we had the smallest expansion. 129
5.11 Position of the accelerated BEC as a function of time. The points represent the experimental data, while the solid curve is a quadratic fit given by $x = \frac{1}{2}gt^2$. The fitted parameter is $g = 200\,\mathrm{mm/s^2}$, assuming a parabolic trajectory due to uniform acceleration in a magnetic field gradient. 130

5.12 Transmission curve in the classical regime with a barrier size of $\sigma_0 = 1.96\,\mu$m and atoms at velocity $v = 8.6$ mm/s, corresponding to a de Broglie wavelength of $\lambda_{dB} = 1.2\,\mu$m. The red scatter points represent the experimental data, while the blue curve is the numerical solution of the 1D time-independent Schrödinger equation, using the potential form described in Eq. (3.14). We scan the barrier height as a percentage of the maximum laser power. 133
5.13 Transmission curve in the quantum regime with a barrier created using three pixels on the DMD. The atomic velocity is $v = 3.7$ mm/s, corresponding to a de Broglie wavelength of $\lambda_{dB} = 3.0\,\mu$m. The red scatter points represent the experimental data, while the blue curve corresponds to a fit using the transmission equation described for the delta potential. 134
5.14 Power required for 50% atomic reflection as a function of barrier width. The red scattered points are the experimental data. The green dashed curve represents the expected behavior assuming an ideal sinc-shaped PSF. The solid blue curve corresponds to the PSF model, which includes optical aberrations. The inset shows the Ansatz PSF, consisting of a pure sinc function (dashed curve) and a Gaussian background part (dash-dotted curve), which are the two terms of Eq.5.17. 135
5.15 Transmission through a double-barrier potential as a function of barrier separation l. The red scatter points represent the experimental data. The dashed green curve corresponds to the monokinetic theoretical simulation using the experimental ansatz PSF from Eq. 5.17. The solid blue curve includes velocity averaging, accounting for the finite velocity spread of the atomic cloud ($\Delta v = 0.25$ mm/s). 137

List of Tables

2.1 Magnetic field noise (in mG rms) measured with the LEM IT 60-S Ultrastab current transducer connected to a Keysight 34465A multimeter, for various filter capacitances C_1 and integration (aperture) times. The third column shows the intrinsic transducer noise floor. We obtained noise values by converting the voltage fluctuations measured across a 50 Ω resistance and using the coil calibration factor. 67

Publications

1. R. Eid, A. Hammond, L. Lavoine, T. Bourdel,
   Ultracold-atom quantum tunneling through single and double optical barriers,
   Phys. Rev. A 110, 043316 (2024).

2. S. Tiengo, R. Eid, M. Apfel, G. Brulin, T. Bourdel,
   A simple magnetic field stabilization technique for atomic Bose-Einstein condensate experiments,
   Rev. Sci. Instrum. 96, 063201 (2025).

3. S. Tiengo, R. Eid, T. Bourdel,
   Three-body interactions in Rabi-coupled Bose gases: A perturbative approach,
   Phys. Rev. A 111, 053319 (2025).

4. R. Eid, S. Tiengo, T. Bourdel,
   Saturating interaction in coherently coupled two-component Bose-Einstein condensates,
   Manuscript under preparation.

Ultra-cold atom quantum tunneling through single and double optical barriers

R. Eid, A. Hammond, L. Lavoine, and T. Bourdel*
Laboratoire Charles Fabry, CNRS, Institut d'Optique Graduate School, CNRS, Université Paris-Saclay, , 91127 Palaiseau, France
(Dated: November 12, 2024)

We realize textbook experiments on Bose-Einstein condensate tunneling through thin repulsive potential barriers. In particular, we demonstrate atom tunneling though a single optical barrier in the quantum scattering regime where the de Broglie wavelength of the atoms is larger than the barrier width. Such a beam splitter can be used for atom interferometry and we study the case of two barriers creating an atomic Fabry-Pérot cavity. Technically, the velocity spread of the atoms is reduced due to the use of a ^{39}K Bose-Einstein condensate with no interactions. The potential barriers are created optically and their width is tunable due to the use of a digital micro-mirror device. In addition, our scattering experiments enable *in situ* characterization of the optical aberrations of the barrier optical system.

Particle quantum tunneling is a phenomenon in which a particle passes through a potential energy barrier, which according to classical mechanics should not be passable due to insufficient energy. It is a direct consequence of the wave-nature of matter and is described by the Schrödinger equation [1]. Experimentally, it was first observed for electrons in semiconductors by L. Esaki [2], who then used this effect to build electronic diodes [3]. The scanning tunneling microscope is an important application based on quantum tunneling [4].

Equivalently, atoms can also exhibit quantum (wave) behavior, although they need to be cooled to ultralow temperatures. Ultracold atoms are indeed used both for precision measurements using matter-wave interferometers [5] or for the study of quantum many-body physics [6]. Tunneling of atoms between sites of an optical lattice [7] or of a double well-potential [8] is a commonly observed phenomenon. In a waveguide configuration in which the atoms move, beam splitting was realized through Bragg scattering [9], quantum reflection from the attractive potential close to a solid surface was observed [10, 11] and tunneling was studied in a transport experiment between two unbalanced fermionic reservoirs [12].

In the simple textbook experiment of an atom crossing a single potential barrier, the interesting regime of coherent splitting requires a barrier size σ comparable to the atom de Broglie wavelength $\lambda_{\mathrm{dB}} = h/mv$, where m is the atom mass, v the atom velocity, and h the Planck constant. Unless one uses an advanced technique to create sub-wavelength potential patterns [13], the minimum optical barrier size is limited by diffraction and it thus requires one to reduce and control v to sub-millimeter per second velocities. As a consequence, there have been only a few experiments on quantum tunneling through optical barriers with a moving Bose-Einstein condensate (BEC) [14–18]. The low velocity thin barrier regime, characterized by $\lambda_{\mathrm{dB}} \gg \sigma$ and also called the quantum scattering regime, has never been directly observed. In contrast, numerous theoretical studies have explored atomic tunneling phenomena, considering various barrier shapes and incorporating interactions within BECs [19–21]. Matter-wave Fabry-Pérot interference using two consecutive barriers remains to be observed with potential applications for narrowing the atomic velocity distribution in precision measurements apparatus [22].

In the past ten years, digital micro-mirror devices (DMDs) have been shown to be a great tool to impose arbitrary potentials in ultracold-atom experiments [23–27]. For example, box traps permit one to study gases at a constant density [24, 27] and donut-shape traps are nice for the study of superfluid rotation [28]. Thanks to their versatility and the novel possibilities they offer, DMDs are increasingly used. The optical resolution of such setups is usually measured before their installation in the ultracold atom experiment and not characterized *in situ*.

In this paper we perform atom tunneling experiments through simple and double repulsive optical barriers. The barriers are generated through a DMD setup allowing the adjustment of the barrier width and position. The fine control of the atom velocity is achieved by using a ^{39}K condensate that can be made non-interacting due to Feshbach tuning [29]. For single barriers, we are able to distinctly show the two different regimes of scattering. When $\lambda_{\mathrm{dB}} < \sigma$, the scattering is essentially classical. The transmission curve as a function of barrier height is close to a step function although rounded by quantum effects. When $\lambda_{\mathrm{dB}} > \sigma$, the transmission curve corresponds to the one expected for a δ potential. It is the quantum scattering regime. We then realize double barrier potentials. Interestingly, we observe oscillations of the transmission as a function of the distance between the two barriers. By comparison to numerical simulations, this behavior is interpreted as originating both from atomic Fabry-Pérot interference and from optical interference due to the oscillatory behavior of the point spread-function (PSF) of the optical

* Corresponding author: thomas.bourdel@institutoptique.fr

system. Interestingly, our results with various DMD patterns permit *in situ* characterization of the PSF.

The experiments start with the production of ^{39}K Bose-Einstein condensates in the $|F = 1, m_F = 1\rangle$ state by evaporation at 393 G, where the scattering length a is $\sim$130 a_0 (a_0 is the Bohr radius) in a crossed optical dipole trap [30]. The main horizontal optical trapping beam has a 40-μm waist, creating an atomic waveguide with cylindrical symmetry and the longitudinal confinement comes from a second optical beam with a 150-μm waist. The final preparation stage takes 100 ms in which the trap frequencies are modified from $(\omega_\perp, \omega_\parallel)/2\pi = (115, 47)$ Hz to $(\omega_\perp, \omega_\parallel)/2\pi = (120, 16)$ Hz, and the magnetic field is swept to 350 G in close proximity to the magnetic field where we observe collapse of the condensate due to the change of sign of the scattering length [31]. The gas is then almost non interacting [32]. When the second optical trap is switched off, we observe a very slow expansion of the condensate in the remaining optical waveguide, which corresponds to a mean energy of $h\times$8 Hz or equivalently to a velocity spread upon release $\Delta v_0 \sim 0.35$ mm/s [33]. This is only slightly higher than the kinetic energy $h\omega_\parallel/8\pi$ expected from a non-interacting condensate. There is also a residual $\sim$20% non condensed atomic fraction that expands much faster $\Delta v_{\rm thermal} \sim 2.6$ mm/s.

The optical barriers at 532 nm (Verdi V18, Coherent) are created with an optical setup using a digital micro-mirror devices (DLP-6500, Texas Instrument). The DMD is composed of a matrix of 1920x1080 small square mirrors of pitch size p =7.56 μm. Each of them can take two different angles $\pm$12°. The DMD is illuminated by a large collimated beam at an angle of 24°. We then select only the most intense order of diffraction orthogonal to the DMD that corresponds to the specular reflection and image the DMD plane on the atoms through a custom-made objective. This objective is composed of three spherical lenses and has an overall focal length of 41.16 mm at 532 nm. The numerical aperture is 0.27. The distance from the DMD to the objective is 1.5 m such that the demagnification factor is 38.5 and the effective pixel size in the atomic plane is measured to be p=0.196 μm. The objective design takes into account the glass cell and theoretically gives perfect diffraction-limited performances and an Airy function as PSF. In the following, we use one-dimensional (1D) DMD patterns made of lines perpendicular to the propagation of the atoms. In that case, a more relevant quantity is the 1D amplitude PSF which is theoretically a sinc function. Given the numerical aperture, the first zero of the sinc function should theoretically correspond to $\sigma_{\rm th}$ =1.0 μm in the atomic plane (Fig. 1).

The experiment consists in releasing the Bose-Einstein condensate into the horizontal optical waveguide (by switching off the second optical trapping beam) and accelerating the atoms toward the optical barriers. The longitudinal acceleration is induced by a magnetic field gradient and is g =0.40 m/s^2. The collision with a potential barrier results in partial reflection and transmission of the atomic cloud. The propagation time in the waveguide (between 15 and 30 ms) is chosen such that the atoms meet the barrier once and such that the reflected and transmitted atomic clouds are spatially full separated (Fig. 1). Finally, the main optical trap is switched off and the magnetic field is quickly brought to zero such that after a 1.3 ms time of flight the two transmitted and reflected atomic clouds are simultaneously imaged by fluorescence imaging. The transmission can thus be determined in a single realization of the experiment with no influence of the condensate atom number fluctuation. Choosing the distance d from the initial trap to the barrier position (typ. between 15 and 100 μm), we control the speed of the atoms when they meet the barrier. We can also vary the barrier height through an acousto-optic modulator that modifies the 532 nm light power sent to the DMD. The barrier transmission can then be studied for different conditions. A key parameter is the ratio of the de Broglie wavelength of the atoms $\lambda_{\rm dB} = h/mv$ to the barrier width σ. Another important parameter is the atomic velocity spread Δv when the atoms meet the barrier. Interestingly, since we keep the acceleration on for the whole sequence, Δv is not directly given by Δv_0 [34]. The

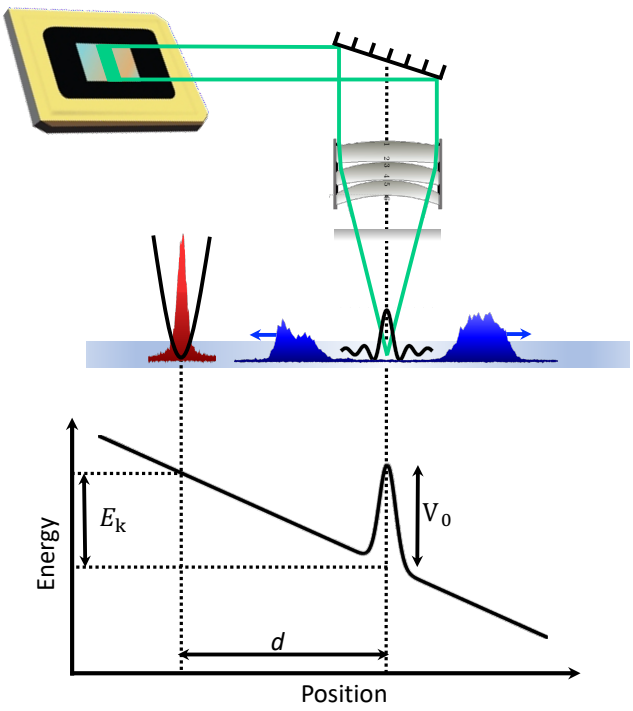


FIG. 1. Schematic of the experiment. A Bose-Einstein condensate is released and accelerated in an optical waveguide toward a potential barrier. This potential is made with a DMD optical setup at 532 nm. The measured quantities are the transmitted and reflected atom numbers after the collision when the two clouds are well separated. An example of a measured longitudinal density profile is shown.

kinetic energy of an atom with an initial velocity v_0 at a distance d from the barrier is $E_k = \frac{1}{2}mv^2 = \frac{1}{2}mv_0^2 + mgd$. For our parameters, the second term dominates such that $v \approx \sqrt{2gd}$ and $\Delta v/v \approx \Delta x/2d \ll 1$ where $\Delta x \approx 3.5\,\mu$m is an estimated rms initial size of the cloud knowing the longitudinal trap frequency and the measured expansion energy.

We first focus on a case of high atom velocity 8.6 mm/s ($\lambda_{dB} = 1.2\,\mu$m) and a barrier made of ten pixels on the DMD, which corresponds to a size $\sigma_0 = 1.96\,\mu$m on the atoms. In that case, we expect diffraction and optical aberrations to only slightly enlarge the barrier width $\sigma \sim \sigma_0$. The transmission as a function of the barrier height is observed to be a step function although smoothed in the region of the transition (Fig. 2). Such a behavior is indeed expected in the classical regime, $\lambda_{dB} < \sigma$. The 50% transmission is then obtained when the barrier height V_0 corresponds to the kinetic energy of the atoms. The data can be directly compared to numerical simulations that consist in solving the 1D time-independent Schrödinger equation for an incoming plane wave. The ratio of the transmitted plane wave to the incoming plane wave amplitudes gives the transmission. The simulation globally matches the experimental data. The fact that the experimental transmission does not really span from 1 to 0 in our data is a consequence of thermal atoms whose behavior is not included in the simulation. For example, some thermal atoms due to their backward initial velocities have not encountered the barrier in the time of the experiment although they are counted as reflected.

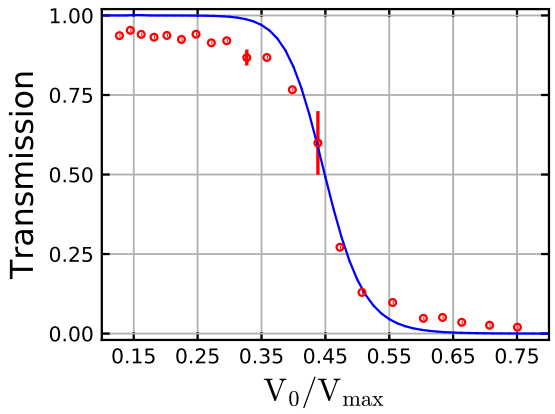


FIG. 2. Transmission in the classical regime $\sigma \sim 2\,\mu$m$> \lambda_{dB} = 1.2\,\mu$m. The transmission is plotted as a function of the barrier height V_0 that is normalized to its maximum value V_{max} obtained at full laser power. The points are single shot experimental data. The solid line is the curve expected from simulations, with the theoretical sinc PSF and assuming no velocity spread of the atoms. The barrier height is the only fit parameter. Some typical statistical error bars are shown.

The previous results can be compared to the situation at low atom velocity 3.7 mm/s ($\lambda_{dB} = 3.0\,\mu$m) and a barrier made of three pixels on the DMD. The size of the potential barrier is then mostly given by the resolution of the imaging system. The transmission curve then qualitatively changes shape with a smooth decaying behavior. Such a behavior is expected in the quantum regime $\lambda_{dB} > \sigma$. In that case, the barrier width is not resolved by the atoms, the barrier can be theoretically replaced by a δ potential and the corresponding analytical transmission curve matches the experimental data. As previously, deviations from the theoretical transmission curve are probably coming from the thermal gas contribution (Fig. 3).

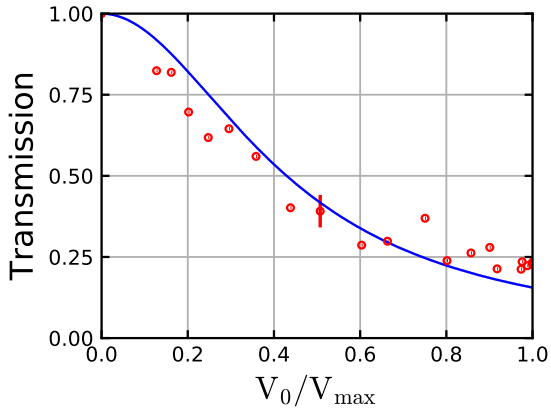


FIG. 3. Transmission in the quantum regime $\sigma \sim 1\,\mu$m$< \lambda_{dB} = 3.0\,\mu$m. The solid line corresponds to the expected transmission for a δ potential barrier $(1/(1+V_0^2/V_{ref}^2)$ and no velocity spread of the atoms. Here V_{ref} is fitted to the data.

In both previous cases, the shape of the transmission curve is not very dependent on the actual PSF of the imaging system. Indeed, in the first case, the barrier width is dominated by the number of pixels creating the potential on the DMD, whereas in the quantum case, the width is not resolved by the atoms. In order to experimentally access the PSF and its width, we turn to a different experiment where we compare at a constant velocity (5 mm/s), the measured 532-nm power that is necessary to reflect 50% of the atoms for different barrier widths (Fig. 4). For our parameters (although we are not always strictly in the classical regime), the 50% transmission is numerically found to correspond to the situations where the barrier height equals the kinetic energy $V_0 = E_{kin}$. Such an experiment thus permits one to measure the relative barrier maxima for barriers made of different numbers of pixels N_{pix} or equivalently of different width σ_0. The exact barrier shape is the absolute value square of the convolution of the amplitude PSF with door functions of variable width $\sigma_0 = N_{pix}p$. In the limit of small σ_0, the barrier maximum is proportional to σ_0^2 as the field interferes constructively. In this case, the 50% transmission power scales as $1/\sigma_0^2$. On the contrary, for large barrier size, we expect the barrier maximum height and thus also the

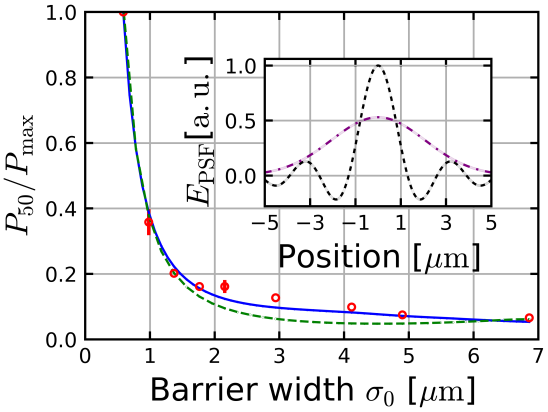


FIG. 4. Optical power P_{50} needed to reflect 50% of the atoms as a function of the barrier width σ_0. The optical power is normalized to its maximum value $P_{\max}$. The mean atomic velocity is 5 mm/s, corresponding to a $\lambda_{\rm dB} = 2.0, \mu$m. The dashed (solid) line corresponds to the numerical result with a sinc PSF with $\sigma_{\rm res} = 2.0\,\mu$m (the ansatz PSF). The real (dash-dotted line) and imaginary (dotted line) parts of the ansatz PSF are plotted in the inset (see the textfor details).

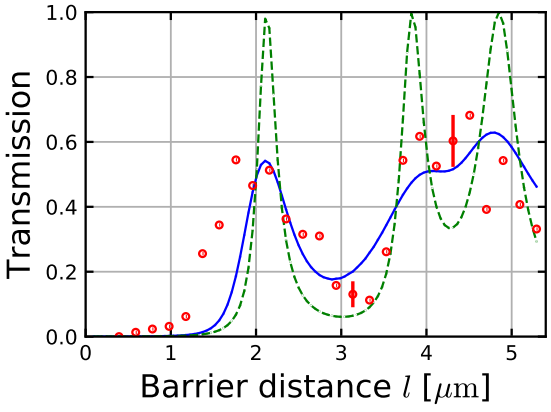


FIG. 5. Transmission through two barriers as a function of the distance between them. The mean atomic velocity is $\sim$ 3.3 mm/s ($\lambda_{\rm dB} = 3.1\,\mu$m). The solid line is the numerical solutions with the ansatz PSF (see the text for details) and a velocity spread $\Delta v = 0.25$ mm/s. The dashed line is the numerical solution for monokinetic atoms. In this last case, the Fabry-Pérot resonance peaks are resolved.

50% transmission power to be independent of σ_0. These two limiting behaviors are experimentally observed (Fig. 4). The change of behavior occurs when the resolution of the imaging system is of the order of σ_0. Assuming a sinc PSF with a resolution $\sigma_{\rm res}$, we can calculate the barrier maximum for each barrier width σ_0. We find that in order to reproduce the observed power ratio between the two limiting regimes, we need $\sigma_{\rm res} \approx 2\sigma_{\rm th} = 2.0\,\mu$m (dashed curve in Fig. 4). However, the whole curve is not well fitted, in particular for barrier widths between 2 and 5 μm. Our results thus point toward a PSF modified by optical aberrations, i.e. not a sinc function. The consideration of a more complex PSF as presented below permits us to better match the observation (solid curve in Fig. 4).

We now turn to transmission experiments through double barriers. In this series of experiments, we use a velocity of 3.3 mm/s, barrier widths of two pixels and 75% of the maximum power available. For such parameters, the transmission through a single barrier is $\sim$70%. We then vary the distance l between the two barriers and, as previously, study the transmission (Fig. 5). Interestingly, the transmission shows oscillations as a function of the barrier distance. However, one should be careful in directly interpreting them as Fabry-Pérot peaks. First, in contradiction to the expectation, they do not reach 100% transmission. Second, the peaks are not precisely positioned at multiples of $\lambda_{\rm dB}/2$. Note that for larger barrier distances, the transmission is essentially constant to $\sim$ 50% [35].

In order to interpret our data, two important ingredients have to be taken into account. First, the atoms have a velocity spread that can eliminate interference effects. It can be estimated to $\Delta v = 0.25$ mm/s from the experimental parameters and can be considered in simulations by averaging the transmission over the velocity distribution. Second the studied barrier distances are not much larger than the resolution of the optical system. We should thus take into account that the barriers have some width and moreover that the optical fields originating from the two DMD regions may interfere as we use coherent light. In principle, the exact calculation of the optical profile requires the knowledge of the amplitude PSF of the optical objective (with its real and imaginary parts), which differs from the theoretical one. In preliminary measurements, prior to the installation on the atoms, the image of a point source (corresponding to the intensity PSF) appeared to be diffraction limited up to a numerical aperture of ~ 0.15. The outer part of the objective only marginally contributed to the reduction of the size of the central image spot and was rather observed to add a broad background. We attribute this effect to imperfectly manufactured (non-spherical) lenses. A reasonable ansatz ampltitude PSF is thus a sinc function originating from the central part of the objective in addition to a Gaussian broader background originating from the outer part of the objective. For simplicity and because there is no reason to assume a given phase relation between the two components, we chose the Gaussian component to be imaginary such that there is no interference with the real sinc function.

With such an ansatz, we can calculate the optical potential and simulate the experimental transmission. We then adjust the PSF parameters to reproduce the experimental findings of both Fig. 4 and 5. We find that the amplitude PSF $\mathrm{E_{PSF}} \propto \mathrm{sinc}(\pi x/\sigma_{\rm sinc}) +$

$iA_{\rm G}\exp(-x^2/2\sigma_{\rm G}^2)$ with $\sigma_{\rm res} = 1.30\,\mu$m, $\sigma_{\rm G} = 2.07\,\mu$m, and $A_{\rm G} = 0.53$ (see the inset in Fig. 4) permits us to reasonably match the data (Fig. 4 and 5). Although, the actual PSF certainly differ from our ansatz, we expect the latter to capture its main features such as its size and its negative real part. Using the previous ansatz PSF, we also plot in Fig. 5, the expected transmission for monokinetic atoms. In that case, the transmission does reach 100% for specific barrier distance corresponding to Fabry-Pérot resonances. The precise resonance positions depend on the atom velocity, leading to a broadening of the transmission peaks after velocity averaging. This sensitivity to the velocity increases as a higher-order Fabry-Pérot resonance (at larger barrier distance) is considered. We thus find that the first Fabry-Pérot resonance peak is resolved but not the second and third ones which merge into a single broad peak. Note also that the monokinetic resonance peaks are not equally spaced. This is due to optical interference between the optical fields originating from the different areas on the DMD. The precise potential barrier heights and positions are slightly affected by the positive to negative oscillations of the amplitude PSF. In particular, for a barrier distance of $\sim 1.9\,\mu$m ($\sim 3.2\,\mu$m), the barrier heights are minimum (maximum), because the sinc function is maximally negative (positive) at those distances. Overall, we thus attribute the observed oscillations in the transmission to a combination of Fabry-Pérot interference and optical interference due to an oscillatory PSF.

In conclusion, we have realized several textbook experiments on atomic transmission through optical barriers. Key advantages of our experiments are the use of non interacting Bose-Einstein condensates and a digital micro-mirror device for the tuning of the barrier characteristics. We clearly demonstrated both the classical and quantum regimes of atomic scattering on a single optical barrier by adjusting both the barrier width and the de Broglie wavelength, or equivalently, the speed of the atoms. We then realized an atomic Fabry-Pérot interferometer based on two potential barriers and were able to resolve the first Fabry-Pérot resonance peak. Interestingly, our setup using a DMD to produce the optical barriers allows for experiments with varying barrier widths and distances permitting an *in situ* estimation of the PSF of the optical system. Technical improvements, such as further reduction of the atom velocity spread using delta-kick cooling technique [36] and/or the engineering of moving barriers using the high switching rate capabilities of DMDs [37, 38] could lead to the observation of a complete atom Fabry-Pérot resonator spectrum.

In the future, the capacity to realize coherent beam splitters from single barriers could be important in the context of atom interferometry. A matter-wave Fabry-Pérot interferometer acting as a gravimeter has been proposed [39]. In addition, our results open prospects for the study of the influence of interactions on collisions with potential barriers [19–21]. Scattering of a bright soliton on a barrier has been predicted to lead to non-classical NOON states [40–43]. In the case of a Fabry-Pérot interferometer, interactions are expected to lead to quantum effects such as squeezing of the outgoing atomic cloud or atomic blockade [44].

This research was supported by CNRS, Ministère de l'Enseignement Supérieur et de la Recherche, Labex PALM, Quantum Paris-Saclay, Région Ile-de-France in the framework of Domaine d'Intérêt Majeur Quantip, Paris-Saclay in the framework of IQUPS, ANR Droplets (Grant No. 19-CE30-0003), and the Simons Foundation (Award No. 563916, localization of waves).

[1] D.J. Griffiths, *Introduction to Quantum Mechanics* (Pearson Prentice Hall, 1995).
[2] L. Esaki, Long journey into tunneling, Nobel Lecture, available at https://www.nobelprize.org/-prizes/physics/1973/esaki/lecture/ (1973).
[3] L. Esaki, New phenomenon in narrow germanium *p-n* junctions, Physical Review A **109**, 603 (1958).
[4] G. Binnig, H. Rohrer, C. Gerber, and E. Weibel, Tunneling through a controllable vacuum gap, Applied Physics Letters **40**, 178 (1982).
[5] A.D. Cronin, J. Schmiedmayer, and D.E. Pritchard, Optics and interferometry with atoms and molecules, Rev. Mod. Phys. **81**, 1051 (2009).
[6] I. Bloch, J. Dalibard, and W. Zwerger, Many-body physics with ultracold gases, Rev. Mod. Phys. **80**, 885 (2008).
[7] M. Greiner, O. Mandel, T. Esslinger, T. Hänsch, and I. Bloch, Quantum phase transition from a superfluid to a Mott insulator in a gas of ultracold atoms, Nature **415**, 39 (2002).
[8] M. Albiez, R. Gati, J. Fölling, S. Hunsmann, M. Cristiani, and M. K. Oberthaler, Direct observation of tunneling and nonlinear self-trapping in a single bosonic josephson junction, Phys. Rev. Lett. **95**, 010402 (2005).
[9] C. M. Fabre, P. Cheiney, G. L. Gattobigio, F. Vermersch, S. Faure, R. Mathevet, T. Lahaye, and D. Guéry-Odelin, Realization of a distributed bragg reflector for propagating guided matter waves, Phys. Rev. Lett. **107**, 230401 (2011).
[10] T. A. Pasquini, Y. Shin, C. Sanner, M. Saba, A. Schirotzek, D. E. Pritchard, and W. Ketterle, Quantum reflection from a solid surface at normal incidence, Phys. Rev. Lett. **93**, 223201 (2004).
[11] F. Shimizu, Specular reflection of very slow metastable neon atoms from a solid surface, Phys. Rev. Lett. **86**, 987 (2001).
[12] S. Häusler, S. Nakajima, M. Lebrat, D. Husmann, S. Krinner, T. Esslinger, and J.-P. Brantut, Scanning gate microscope for cold atomic gases, Phys. Rev. Lett. **119**, 030403 (2017).
[13] Y. Wang, S. Subhankar, P. Bienias, M. Lacki, T.-C. Tsui, M. A. Baranov, A. V. Gorshkov, P. Zoller, J. V.

Porto, and S. L. Rolston, Dark state optical lattice with a subwavelength spatial structure, Phys. Rev. Lett. **120**, 083601 (2018).
[14] T.A. Pasquini, M. Saba, G.B. Jo, Y. Shin, W. Ketterle, D.E. Pritchard, T.A. Savas, and N. Mulders, Low velocity quantum reflection of Bose-Einstein condensates, Physical Review Letters **97**, 093201 (2006).
[15] A.L. Marchant, T.P. Billam, M.M.H. Yu, A. Rakonjac, J.L. Helm, J. Polo, C. Weiss, S.A. Gardiner, and S.L. Cornish, Quantum reflection of bright solitary matter waves from a narrow attractive potential, Phys. Rev. A **93**, 021604(R) (2016).
[16] J. Billy, V. Josse, Z. Zuo, W. Guerin, A. Aspect, and P. Bouyer, Guided atom laser: a new tool for guided atom optics, Ann. de Phys. (France) **32**, 17 (2007).
[17] R. Ramos, D. Spierings, S. Potnis, and A.M. Steinberg, Atom-optics knife edge: Measuring narrow momentum distributions, Phys. Rev. A **98**, 023611 (2018).
[18] R. Ramos, D. Spierings, I. Racicot, and A.M. Steinberg, Measuring the time a tunnelling atom spends in the barrier (2019).
[19] A.M. Martin, R.G. Scott, and T.M. Fromhold, Transmission and reflection of Bose-Einstein condensates incident on a Gaussian tunnel barrier, Physical Review A **75**, 065602 (2007).
[20] P. Manju, K.S. Hardman, M.A. Sooriyabandara, P.B. Wigley, J.D. Close, N.P. Robins, M.R. Hush, and S.S. Szigeti, Quantum tunneling dynamics of an interacting Bose-Einstein condensate through a Gaussian barrier, Physical Review A **98**, 053629 (2018).
[21] D.R. Lindberg, N. Gaaloul, L. Kaplan, J.R. Williams, D. Schlippert, P. Boegel, E.-M. Rasel, and D.I. Bondar, Asymmetric tunneling of Bose–Einstein condensates, J. Phys. B **56**, 025302 (2023).
[22] P. Manju, K.S. Hardman, P.B. Wigley, J.D. Close, N.P. Robins, and S.S. Szigeti, An atomic Fabry–Perot interferometer using a pulsed interacting Bose-Einstein condensate, Scientific Reports **10**, 15052 (2020).
[23] J. Liang, R. Kohn, Jr., M. Becker, and D. Heinzen, 1.5% root-mean-square flat-intensity laser beam formed using a binary-amplitude spatial light modulator, Appl. Opt. **48**, 1955 (2009).
[24] A.L. Gaunt, T.F. Schmidutz, I. Gotlibovych, R.P. Smith, and Z. Hadzibabic, Bose-Einstein condensation of atoms in a uniform potential, Phys. Rev. Lett. **110**, 200406 (2013).
[25] G. Gauthier, I. Lenton, N. Parry, M. Baker, M.J. Davis, H. Rubinsztein-Dunlop, and T.W. Neely., Direct imaging of a digital-micromirror device for configurable microscopic optical potentials, Optica **3**, 1136 (2016).
[26] M. Tajik, B. Rauer, T. Schweigler, F. Cataldini, J. Sabino, F.S. Møller, S.-C. Ji, I.E. Mazets, and J. Schmiedmayer, Designing arbitrary one-dimensional potentials on an atom chip, Opt. Express **27**, 33474 (2019).
[27] N. Navon, R.P. Smith, and Z. Hadzibabic, Quantum gases in optical boxes, Nature Physics **17**, 1334 (2021).
[28] Y.-Q. Zou, É.L. Cerf, B. Bakkali-Hassani, C. Maury, G. Chauveau, P.C.M. Castilho, R. Saint-Jalm, S. Nascimbene, J. Dalibard, and J. Beugnon, Optical control of the density and spin spatial profiles of a planar Bose gas, Journal of Physics B **54**, 08LT01 (2021).
[29] C. D'Errico, M. Zaccanti, M. Fattori, G. Roati, M. Inguscio, G. Modugno, and A. Simoni, Feshbach resonances in ultracold 39K, New Journal of Physics **9**, 223 (2007).
[30] G. Berthet, L. Lavoine, M.K. Parit, A. Brolis, A. Boissé, and T. Bourdel, Observation of the algebraic localization-delocalization transition in a one-dimensional disordered potential with a bias force, Phys. Rev. Res. **2**, 013386 (2020).
[31] E. Donley, N. Claussen, S. Cornish, J. Roberts, E. Cornell, and C. Wieman, Dynamics of collapsing and exploding Bose-Einstein condensates, Nature **402**, 295 (2001).
[32] In this regime of very low scattering length $a < 0.3\,a_0$, the magnetic dipole interaction plays a role comparable to the contact interaction.
[33] We also observe uncontrolled shot-to-shot fluctuations of the mean velocity with a standard deviation of 0.23 mm/s, that we attribute to residual longitudinal dipole oscillations of the cloud prior to release. These are probably the main source of shot-to-shot fluctuation in our transmission data.
[34] F. Damon, F. Vermersch, J. G. Muga, and D. Guéry-Odelin, Reduction of local velocity spreads by linear potentials, Phys. Rev. A **89**, 053626 (2014).
[35] The potential gradient is kept on during the whole sequence. The influence of such a gradient has been studied theoretically [39]. It is expected to play little role in the presented data at small barrier distances and it is not taken into account in our simulations.
[36] H. Ammann and N. Christensen, Delta kick cooling: A new method for cooling atoms, Phys. Rev. Lett. **78**, 2088 (1997).
[37] L.-C. Ha, L.W. Clark, C.V. Parker, B.M. Anderson, and C. Chin, Roton-maxon excitation spectrum of Bose condensates in a shaken optical lattice, Phys. Rev. Lett. **114**, 055301 (2015).
[38] G. Gauthier, T. Bell, A. Stilgoe, M. Baker, H. Rubinsztein-Dunlop, and T. Neely, Dynamic High-Resolution Optical Trapping of Ultracold Atoms (Advances In Atomic, Molecular, and Optical Physics, Academic Press, Vol. 70, 2021) pp. 1–101.
[39] P. Schach, A. Friedrich, J. Williams, W. Schleich, and E. Giese, Tunneling gravimetry, EPJ Quant. Tech. **9**, 20 (2022).
[40] C. Weiss and Y. Castin, Creation and detection of a mesoscopic gas in a nonlocal quantum superposition, Phys. Rev. Lett. **102**, 010403 (2009).
[41] S.L. Cornish, N.G. Parker, A.M. Martin, T.E. Judd, R.G. Scott, T.M. Fromhold, and C.S. Adams, Quantum reflection of bright matter-wave solitons, Physica D: Nonlinear Phenomena **238**, 1299 (2009).
[42] A. Boissé, G. Berthet, L. Fouché, G. Salomon, A. Aspect, S. Lepoutre, and T. Bourdel, Nonlinear scattering of atomic bright solitons in disorder, EPL **117**, 10007 (2017).
[43] P. Naldesi, J. Polo, P.D. Drummond, V. Dunjko, L. Amico, A. Minguzzi, and M. Olshanii, Massive particle interferometry with lattice solitons, SciPost Phys. **15**, 187 (2023).
[44] I. Carusotto, Nonlinear atomic Fabry-Perot interferometer: From the mean-field theory to the atom blockade effect, Phys. Rev. A **63**, 023610 (2001).

A simple magnetic field stabilization technique for atomic Bose-Einstein condensate experiments

S. Tiengo, R. Eid, M. Apfel, G. Brulin, and T. Bourdel[a)]
Université Paris-Saclay, Institut d'Optique Graduate School, CNRS, Laboratoire Charles Fabry, 91127 Palaiseau, France

(Dated: 22 January 2025)

We demonstrate a simple magnetic field stabilization technique in a Bose-Einstein condensate experiment. Our technique is based on the precise measurement of the current fluctuations in the main magnetic field coils and amounts to their compensation using an auxiliary coil. It has the advantage of simplicity as compensation is done using a low inductance coil that can be straightforwardly driven at the relevant frequencies (<1 kHz). The performances of the different components (power supply, current transducer, electronics...) are precisely characterized. In addition, for optimal stability the ambient magnetic field is also measured and compensated. The magnetic field stability around 57 G is measured by Ramsey spectroscopy of magnetic field sensitive radio-frequency transition between two spin states of potassium 39 and the shot-to-shot fluctuations are reduced to 64(7) µG rms, i.e. at the 1×10^{-6} level. In the context of our experiment, this result opens interesting prospects for the study of three-body interactions in Bose-Einstein condensate potassium spin mixtures.

arXiv:2501.11375v1 [cond-mat.quant-gas] 20 Jan 2025

I. INTRODUCTION

A highly stable magnetic field is desirable in many contexts and in particular in quantum technologies, including quantum computing[1], simulation, and sensing[2]. Indeed, the coherence time of quantum systems is often reduced because of magnetic field fluctuations. In particular, neutral atoms or ions are sensitive to the magnetic field because of the Zeeman effect. Even if one works at a 'magic' condition where the Zeeman effect cancels at first order, there is typically also a contribution to second order that is relevant[3]. As a consequence, controlling the magnetic field is crucial in any precision experiment using atoms or ions. This is especially true for clocks[2].

Apart from precision measurements, ultracold atoms are also used in the context of quantum simulation, i.e. the study of well controlled many-body systems[4,5]. The control of the interatomic interaction through magnetically controlled Feshbach (molecular) resonances has led to several major advances in the field[6]. The use of narrow resonances requires a highly stable magnetic field[7–9]. A stable magnetic field is also crucial when working with spin mixtures, either with a magnetic field close to zero to bring the Zeeman energy scale down to the magnitude of the spin-spin interaction energy scale,[10,11] or for the precise control of radio-frequency induced transitions between hyperfine levels[12]. In the latter case, the magnetic field-induced shifts of the transition frequency should be compared to the Rabi-coupling frequency.

The above needs have led to the development of several techniques for magnetic field stabilization. High magnetic permeability materials such as μ-metals are often used as passive magnetic field shields. They are able to efficiently reduce magnetic fluctuations by several (typically ∼6) orders of magnitude[13]. They are used in most metrology experiments and even in some experiments with quantum gases. However, the need for an enclosed geometry and the incompatibility of magnetic shields with strong fields due to saturation effects have driven the development of alternative active stabilization methods[14,15]. The magnetic field can be measured directly with sensors in close proximity to the atoms, and the signal fed back to compensation coils. The magnetic field can then be either stabilized to a low value in a given direction or set to zero in all directions. Due to the lack of high precision fluxgate sensors at high magnetic fields, such a technique is limited to low magnetic fields (typically below 10 G)[16–18].

Some experiments require a stronger magnetic field. It is then usually created with a current (of typically 10 to 500 A) flowing through a pair of coils in Helmholtz configuration. A primary source of magnetic fluctuations are then the current fluctuations. In fact, the best commercially available current supplies have relative current stability in the 10^{-5} range (also depending on the inductance of the coils). The current can be measured to a better accuracy with transducers, and feedback can be applied to the power supply command or to a current controlling MOSFET in order to reduce the current fluctuations[9,19,20]. In addition, environmental magnetic noises such as the 50/60 Hz power line noise or slower drifts can be measured and corrected[9,19]. The experiments are typically also triggered to the 50/60 Hz line.

In our potassium 39 quantum gas experiment, we aim at studying the properties of Bose-Einstein condensates (BEC) in coherent mixtures of hyperfine states with different scattering lengths. A pair of bias coils in Helmholtz configuration produces a bias magnetic field that is used to control the interatomic interaction. In particular, between 33 and 59 G, two hyperfine states offer the specifically interesting situation where the intra-species scattering lengths are positive whereas the inter-species scattering length is negative[21,22]. When a radio-frequency field is frequency swept to bring the condensate in a dressed

a)thomas.bourdel@institutoptique.fr

state, i.e. a coherent superposition of the two spin states, the global mean-field interaction is reduced and higher order terms, such as three-body interactions, may dominate the BEC equation of state[23,24]. Precise study of the consequences on the gas dynamics requires us to work at low Rabi frequencies Ω (of the order of some kilohertz) as the three-body terms increase with $1/\Omega$. An effective control of the detuning of the radio-frequency dressing field as compared to the Rabi frequency requires magnetic field fluctuations in the range of 100 µG, whereas we typically measure magnetic fluctuations of ∼1 mG.

In order to achieve such a performance, we have developed a simple alternative technique to improve the magnetic field stability. In short, we measure the fluctuations of the current in the bias coils and a small proportional current is driven in an auxiliary coil to compensate directly on the magnetic field for these fluctuations. In contrast to a direct proportional-integral-derivative (PID) regulation on the coil current, the proportional gain of the compensation current needs to be precisely set. Nevertheless, our method greatly simplifies the magnetic field stabilization system, as a direct feedback on the current typically has a complex frequency response in the noise frequency range[19]. In our system, we quantify the reduction of the magnetic field noise with the atoms using Ramsey spectroscopy on a radio-frequency transition between two spin states. With the addition of a compensation of the ambient magnetic field noise, we achieve 64(7) µG shot-to-shot rms fluctuations of the magnetic field, corresponding to ∼1 ppm. Finally, we also analyze the residual magnetic field noise over hours by performing repetitive measurements of the full Ramsey oscillations as a function of time. It confirms a ppm stabilization of the magnetic field on such a time scale and permits a more detailed characterization of the residual noise in our setup.

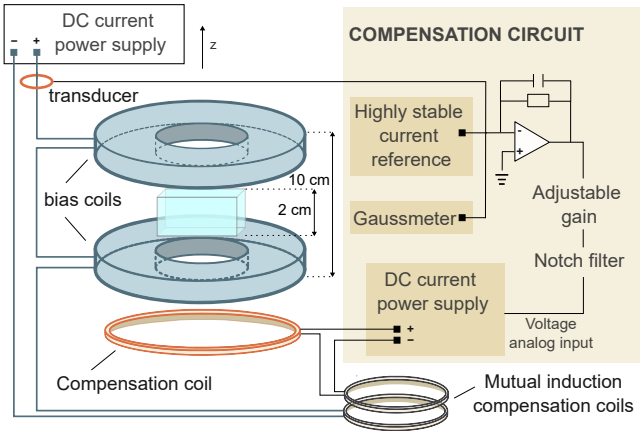


FIG. 1. Schematics of the magnetic field noise compensation circuit. Ultracold ^{39}K atoms are prepared approximately at the center of a glass cell. Two bias coils in Helmholtz configuration generate a magnetic field set in the range 33 to 59 G at the atomic cloud position. A typical value of the current delivered in the bias coils by the stable DC power supply is of 15 A, with relative current stability at the 1×10^{-5} level. A current transducer monitors the main power supply current and its signal is compared with a highly stable DC current reference. The difference gives an error signal that is used as an input for an auxiliary current supply that drives current through a compensation coil, thereby stabilizing the magnetic field. In addition, a gaussmeter is placed close to the atoms, and its signal is added as a supplemental input to the circuit in order to also compensate ambient magnetic field fluctuations. In order to null the mutual induction between the bias coil and the compensation coil circuits, another couple of two small coils is added far from the atom position.

II. CURRENT FLUCTUATION COMPENSATION SETUP

A diagram of the noise stabilization circuit is shown in Fig. 1. Ultracold ^{39}K atoms are prepared in the vacuum glass cell around which two water-cooled bias coils in Helmholtz configuration, with a total DC resistance of 80 mΩ and an inductance of ∼300 µH, produce a bias magnetic field that is used to tune atom interactions. The current through the coils is provided by a low-noise DC current power supply *(HighFinesse UCS 20A/10V with the ultra-high stability option)* with a maximum current of 20 A corresponding to 76 G. To monitor the current in the coils, we use a current transducer *(LEM ultrastab IT 200-S)*. A sensitivity of 3 mA/A is reached by winding the cable 3 times around the sensor. This sensor has very good noise characteristics (significantly below its specifications of 2 ppm of full scale between 0 and 1 kHz, see below for our measured value), although it exhibits clock noise at 17 kHz and harmonics. The noise spectrum of the bias coils current is found to be broad below 1 kHz, and with its main frequency components around 300 Hz[25]. To quantify the DC current noise we use a 6.5 digits multimeter (*Keysight 34465A*) with 176 µs integration time, measuring the rms of the signal after the current transducer. This technique has the advantage of being insensitive to 17 kHz clock noise, while being sensitive to the current noise in the relevant frequency range. At a current of 19 A, from repetitive measurements during a few seconds, we measure a relative rms noise of $\sim 10^{-5}$. Note that this already quite good performance[26] is directly obtained from a commercial power supply which, in fact, already includes a proportional-integrator (PI) feedback loop to stabilize its current[27] . On longer time scales (hours), the mean value of the current also exhibits additional offset jumps at a few 10^{-5} level.

We first focus our magnetic field stabilization strategy on the precise measurement of the current fluctuations and on their compensation. Compensation is performed by sending a current proportional to the measured noise in a compensation coil. The input signal for the compensation circuit is a current error signal, obtained from the subtraction of a highly stable DC current reference from the current provided by the above-mentioned

Noise origin	rms noise [μG])	triggered to 50 Hz
Power-supply (19 A)	630	190
Current transducer	39	23
Reference signal	33	16
noise from electronics	28	6

TABLE I. Rms noises measured at the output voltage of the compensation circuit. The values are extracted from repetitive measurements (over few seconds) using the precision voltmeter with a 176 μs integration time (triggered or not to the 50 Hz line). They are then scaled to magnetic field unit. The power-supply current noise is measured with both the transducer and reference current signals connected. The baseline noise of the current transducer is measured with the transducer serving as the single input of the circuit and the main DC current supply turned off. The reference noise is measured with the reference signal as the only input and at a low reference current input (low DC reference voltage) in order to avoid saturation of the first amplifier. The electronics noise is measured with a 50 Ω resistance as unique input of the circuit.

current transducer. The reference current is produced by a precision voltage source (*Stanford Research system DC205*, stability 1 ppm/24h, 0.3 ppm noise) connected to a highly stable 100 Ω resistance (*VPG Foil Resistors Y0926100R000T9L*, ±2 ppm/K). The difference signal serves as an input for an inverting transimpedance amplifier circuit (OP277BA) with a 1 kΩ feedback resistor. A 33 nF capacitor is added in parallel to the resistor to limit the current noise detection bandwidth, low-pass filtering the signal with a 4.8 kHz cut-off frequency. Note that our method has the advantage that the transducer current is directly subtracted from a reference signal (before any amplification), therefore avoiding the addition of electronic noise prior to the generation of the error signal. A notch filter at 17 kHz further suppresses the transducer clock noise and a variable gain amplifier enables the adjustment of the overall gain for the compensation circuit. The measured noise originating from the different elements are listed in table I, showing that we can indeed precisely measure the current fluctuations from the power supply.

The generated voltage error signal, ranging between 0 to 10 V, is used as an external analog modulation voltage to a laser current supply (*Thorlabs LDC 8005*), which can drive a current between 0 and ± 500 mA through the compensation coil (calibration: 2.0 G/A). This current supply, even connected to the compensation coil, has a 20 kHz bandwidth and a flat frequency response in the frequency range of interest. This is a key advantage of our method as compared to a direct feedback to the main coil circuit, which typically has a complex response in the frequency range of its noise[19]. However, we first have observed that mutual inductive coupling between the main coils and the compensation coil has significant effects and was leading to instabilities of the current compensation system as soon as it was activated. In order to solve this problem, we cancel the mutual induction using an opposite sign mutual coupling between two superimposed coils, each of them in series with either the main coils or the compensation coil (see Fig. 1). Experimentally, the induction can be quantified by measuring the induced voltage in one circuit while modulating the current in the other. The size and number of turns in the mutual inductance compensation coils are adjusted to zero the total mutual induction between the two circuits.

Importantly, we need the magnetic stabilization to work in the presence of radio-frequency fields (between 30 and 50 MHz) used for spin state control. Such fields are found to cause electromagnetic interferences on electronic circuits that are difficult to shield. In practice, in addition to inducing noise at the same frequency, they also lead to small unstable DC offsets in the electronics signals. We solve this issue by moving the main current supply for the Helmholtz coils and the whole compensation circuit to a different room from the one where the vacuum system and the atoms are.

III. RAMSEY INTERFEROMETRY MEASUREMENT OF THE MAGNETIC FIELD

The performance of the stabilization circuit is measured through Ramsey spectroscopy[28] of the transition between the $|\uparrow\rangle = |F = 1, m_F = -1\rangle$ and $|\downarrow\rangle = |F = 1, m_F = 0\rangle$ hyperfine ground states in ^{39}K atoms. The magnetic field is set to 57 G at which the energy gap between the two levels is about 40 MHz and depends linearly on the magnetic field with 0.70 MHz/G. We optically trap $N \approx 1 \times 10^6$ ultracold atoms in the $|\uparrow\rangle$ state at a temperature of 2 μK. The harmonic trap frequencies are $(62 \times 300 \times 300)$ Hz. The radio-frequency field is created by a simple two-loop antenna with a diameter of 2 cm, placed ∼3 cm away from the atoms. Ramsey sequences are performed using radio-frequency $\pi/2$ pulses with a Rabi frequency of 10 kHz (pulse time τ =25 μs). Finally, the optical trap is turned off and another set of coils in quadrupole configuration produces a strong magnetic field gradient, maintained for 2 ms to separate the two spin states by the Stern-Gerlach effect. All currents are then switched off, and, after 1.3 ms, the magnetic field is low enough to image the atoms by resonant fluorescence imaging. In each repetition of the experiment, we can measure the fraction f of atoms that remain in the initial $|\uparrow\rangle$ state. Note that this measurement is not sensitive to total atom number fluctuations and with our signal to noise we estimated a precision of 0.2%, as can be measured using a single $\pi/2$ pulse producing a stable 50/50 mixture[29].

In practice, we slightly detune the radio-frequency from atomic resonance such that we detect oscillations of the atomic fraction as a function of the Ramsey time

T:

$$f \approx \frac{1}{2}\left(1 - C(T)\cos\left(\delta T\right)\right) \quad \text{with } T = T_{\text{wait}} + 4\tau/\pi, \tag{1}$$

where δ is the radio-frequency detuning from resonance and $C(T)$ the contrast of the interferometer, that might depend on T. The above formula[30] assumes that the detuning is much lower than the Rabi frequency and includes a correction on the Ramsey time T due to the finite pulse time τ. The highest magnetic field sensitivity of the signal f is achieved at half fringe, for example when $\delta T \approx \pi/2$. For small deviations around that point, f is linear with the magnetic field noise $f - 1/2 \simeq C(T)(\delta T - \pi/2)/2$. This expression for f also assumes that δ, or equivalently the magnetic field is constant throughout the Ramsey sequence, which is valid as long as T is short as compared to the inverse fluctuation frequencies of the B field. For T_{wait}=100 µs and $\delta \approx 2$ kHz the first half fringe position of f is experimentally realized and here we take repetitive shots to measure to the shot-to-shot variation of the magnetic field. After 100 µs of waiting time, the contrast $C(T)$ of the Ramsey fringes is 0.95(1) (see Sect. V). Our 0.2 % precision on f corresponds to a single-shot precision of 5.3 Hz on the detuning $\delta/2\pi$, or equivalently, of 7.6 µG at each repetition of the experiment. Without compensation of the magnetic field noise, we measure magnetic field rms fluctuations of 0.8 mG over 30 repetitions of the experiments. A single experimental sequence approximately takes 11 seconds to complete, hence the acquisition of 30 shots requires about 5 minutes. In addition, we confirm that the magnetic field noise measured by atomic Ramsey spectroscopy is well correlated with a simultaneous measurement of the bias coil's current.

We now turn to the measurement of the magnetic field with our circuit activated, compensating for the noise of the bias coil current. For the optimal compensation of the magnetic field noise, the variable gain for the compensation current has to be precisely set. This is done by finding the gain for which the magnetic field measured with the atoms is insensitive to a small intentional variable offset in the current of the bias coils. We estimate that the gain is set with a precision of about 1 %. With compensation of the current noise, we then find a reduced rms noise (over 30 repetitions of the experiment and over 5 minutes) corresponding to 136(18) Hz in frequency or equivalently 195(26) µG in magnetic field.

IV. EXTERNAL MAGNETIC FIELD NOISE AND ITS COMPENSATION

In order to analyze the additional variations of the external magnetic field in the vertical direction, a gaussmeter (*Bartington Mag-03*, bandwidth 3 kHz) is placed in the proximity of the atoms. It first detects 50 Hz and harmonics originating from transformer coils connected to the power line. Actually, already for the previous measurements, power supplies fed by the 50 Hz power line were positioned away ($\gtrsim 2$ m) and oriented in such a way to minimize their contribution to the vertical magnetic field at the atom position. This noise contribution can alternatively be zeroed by synchronizing the experiment to the 50 Hz line. In addition, low-frequency drifts (below 0.5 Hz) of the external magnetic field field are identified as the main limitation to our stability. We finally choose the precise gaussmeter position about 50 cm away from the atomic position such that the measured magnetic field is small (below 1 G) and only marginally affected by the current in the bias and compensation coils in order to disentangle the effects from the current noise and from the ambient magnetic field.

We then add the measured external magnetic field to our compensation setup. The gaussmeter output voltage is connected through a 2.5 kΩ resistance (a value chosen to have the proper gain in the compensation) as a supplementary input to the transimpedance amplifier. It now has 3 inputs: the current from the current transducer, the current from the voltage reference and the current originating from the gaussmeter. We then repeat the Ramsey measurements (over 30 shots and 5 minutes), now also synchronized to the 50 Hz line, and found a residual fluctuation of the resonance transition frequency of 45(5) Hz rms, corresponding to 64(7) µG rms. This value is only a factor ~ 2 higher than the noise floor of the compensation system (28 µG if we add the noise contributions from the transducer and from the reference, see TABLE I). Note that our compensation is not really efficient in reducing the 50 Hz modulations, as they differ at the gaussmeter and at the atom position. This is not necessarily a problem since these modulations are first small (if one is careful with the power supply positions) and second deterministic once the experiment is synchronized to the 50 Hz line. If necessary, they could be precisely measured with Ramsey spectroscopy and then feed forward to the compensation circuit[19].

V. ANALYSIS OF RAMSEY OSCILLATIONS ON HOUR TIME SCALE

We now turn to the measurement of the magnetic field stability over hours. Rather than repeating the previous Ramsey spectroscopy measurements, we chose to perform repetitive measurements of Ramsey oscillations of the atomic fraction as a function of time and up to $T = 3.5$ ms (see Fig. 2), as it gives complementary information and brings additional ways of assessing the magnetic field stability. Each Ramsey sequence counts 70 data points (see Fig. 2(a)). Given the typical duration of 11 seconds for each experimental sequence, the acquisition of 10 full datasets with a total of 700 data points requires 2 hours.

Looking at all the transferred fractions f (blue circles in Fig. 2(a)), it is clear that they lie in an envelope func-

tion that we interpret as the single shot contrast $C(T)$ of the interferometer (solid blue line). Indeed, according to the formula (1), single points lies between $(1 - C(T))/2$ and $(1 + C(T))/2$. The reduction of the contrast $C(T)$ over time does not come from shot-to-shot magnetic field fluctuations but rather from an inhomogeneous broadening of the atomic resonance or from decoherence effects. For instance, a residual magnetic field gradient leads to an inhomogeneous broadening of the detuning δ because of the Gaussian spatial atomic distribution. We have indeed observed that the decay of $C(T)$ has been significantly reduced after nulling a residual magnetic field gradient (initially of 8.9 G/m) along the elongated direction of the cloud. The remaining decay could be due to the magnetic field gradients in the other two directions that we did not compensate and/or to a mean-field shift that depends on the density (we estimate the mean-field shift of the resonant frequency to be 150 Hz at our peak density). In addition, we find that a simple Gaussian decay (dashed blue line) does not perfectly fit the measured contrast decay, which appears almost constant in the range $2\,\text{ms} < T < 3.5\,\text{ms}$. This behavior can probably be associated with the atom radial oscillations in the optical trap leading to a partial time averaging of the inhomogeneous frequency shifts in these directions at long Ramsey times T only.

The shot-to-shot variation of the magnetic fields is reflected in the dephasing of the Ramsey oscillations. After averaging over the 10 repetitions of the experiment (black dots in Fig. 2(a)), this leads to a further decay of the contrast. Assuming a Gaussian distribution of the radio-frequency detuning with mean $\delta_0(T)$ and standard deviation σ, we fit the averaged data with the following function

$$\text{Mean}[f] = \frac{1}{2}\left(1 - C(T)\cdot e^{-\frac{1}{2}(\sigma T)^2}\cdot\cos\left(\delta_0(T)T + \phi\right)\right). \tag{2}$$

We include the possibility of a slight variation of $\delta_0(T)$ as a function of T as it is visible after careful data analysis. In fact, it comes from deterministic 50 Hz ambient magnetic field fluctuations.[31] In practice, since the maximum Ramsey time 3.5 ms is small as compared to 20 ms, we can assume a linear behavior $\delta_0(T) = \delta_0(T_{\text{wait}} = 0) + \alpha T$. From the fit, we extract $\delta_0(T_{\text{wait}} = 0) = 2\pi\times 1900(5)$ Hz, $\alpha = 2\pi\times 59(3)$ Hz/ms and the standard deviation of the detuning σ, corresponding to a residual magnetic field rms noise 71(4) µG. This value is only slightly higher than the one obtained on 30 shots and 5 minutes, showing that we are also able to maintain excellent magnetic field stability over two hours. Note that our measured magnetic field stability also implies an excellent mechanical and thermal stability of the bias coils, as it corresponds to a variation of distance between the two coils of $\sim$0.1 µm[32].

We conclude our analysis of the Ramsey fringes data with the study of the standard deviations of f as a function of time T (see Fig. 2(b)). For Gaussian noise, the expected function describing the standard deviation of f,

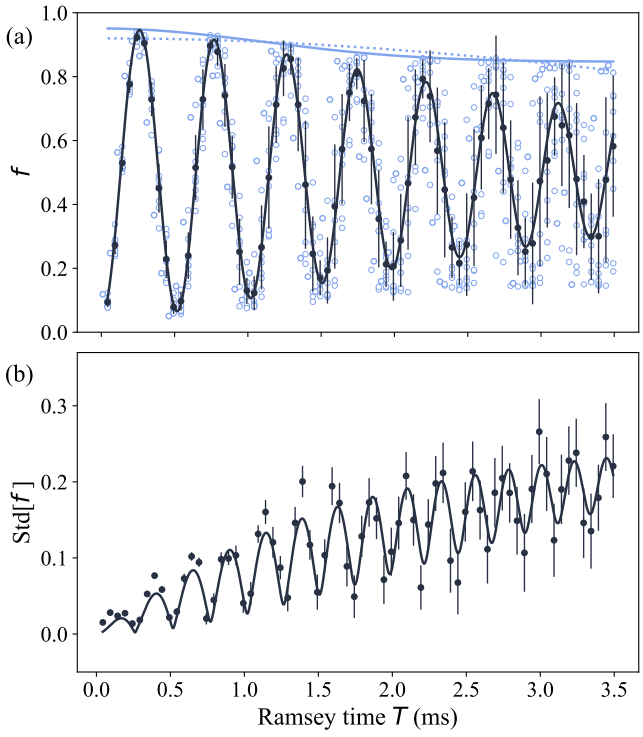


FIG. 2. Repetitive measurements of Ramsey oscillations as a function of time T up to 3.5 ms. (a) Individual measurements of the transfer fraction f (blue circles). The envelope of the oscillation signals allow us to extract the contrast $C(T)$ of the interferometer which is found to be better fitted by a Gaussian with an offset (solid blue line) rather than a simple Gaussian decay (dashed blue line). The average of the 10 measurements Mean[f] with their standard deviations Std[f] is also plotted (black dots) and is fitted (solid black line) in order to extract the magnetic field fluctuations (see text). (b) Standard deviation of the atom fraction f as a function of the waiting time T from 10 repetitions of the Ramsey experiment. The error bars are estimated from simulated data using Monte-Carlo sampling of the noise because it is difficult to extract them from only 10 experimental realizations. The fit with equation 3 permits us to evaluate the magnetic fluctuations.

can be derived

$$\frac{\text{Std}[f]^2}{C(T)^2} = \frac{1}{8}\left(1 + e^{-2\sigma^2T^2}\cos(2\delta_0(T)T + 2\phi)\right) - \frac{1}{4}e^{-\sigma^2T^2}\cos^2(\delta_0(T)T + \phi) \tag{3}$$

We then fit this function to our measured standard deviation and extract a residual noise corresponding to 69(2) µG, a value that is in agreement with the previous estimation. We can note a tendency of the fit to underestimate the measured standard deviation at short times T. This may indicate that the amount of magnetic field noise slightly depends on the integration time T as can be expected if there is residual noise in the frequency range 300 Hz-1 kHz, that is averaged out at long Ramsey time

$T > 1\,\mathrm{ms}$. The overall quality of the fit assuming a constant σ nevertheless indicates that the residual magnetic field noise is dominated by shot-to-shot fluctuations.

VI. CONCLUSIONS

In conclusion, we have shown a new method for stabilizing the magnetic field around 57 G without the use of a magnetic field shield. It mainly amounts to a compensation the fluctuations of current in the coils that produce the magnetic field. This is done through its precise measurement and driving a compensation current in a low inductance auxiliary coil. Such a method has the advantage to circumvent the problem of the complex frequency response of the main circuit due to the high inductance of the main coils. To further improve the magnetic field stability, we also have implemented a compensation of the ambient magnetic field noise. Detailed characterization of our system performances through repetitive Ramsey measurements of the magnetic field using the atoms was performed and we find rms magnetic field fluctuations of $64(7)\,\mu\mathrm{G}$ on 5 minutes and of $71(4)\,\mu\mathrm{G}$ on two hours. Although we have not taken specific data to assess it, given the specifications of the circuit components, good stability is expected and indeed experimentally seems to be maintained over days and weeks. Interestingly, our method can be straightforwardly applied to other systems in order to improve the magnetic field stability. In the context of our experiment, such a magnetic field stability opens prospects for the study of Bose-Einstein condensates in a coherent spin superposition because of dressing by a radio-frequency field. In particular, the consequences of the emerging three-body interactions[23,24] in the equation of state of condensates will be studied.

ACKNOWLEDGMENTS

We thank L. Lavoine and A. Hammond for early developments on current noise measurements. This research was supported by CNRS, Ministère de l'Enseignement Supérieur et de la Recherche, Labex PALM, Quantum Paris-Saclay, Région Ile-de-France in the framework of Domaine d'Intérêt Majeur Quantip, PEPR Quantique Dyn1D, Paris-Saclay in the framework of IQUPS, ANR Droplets (Grant No. 19-CE30-0003), and the Simons Foundation (Award No. 563916, localization of waves).

[1] J. I. Cirac and P. Zoller, "Quantum computations with cold trapped ions," Phys. Rev. Lett. **74**, 4091–4094 (1995).
[2] A. D. Ludlow, M. M. Boyd, J. Ye, E. Peik, and P. O. Schmidt, "Optical atomic clocks," Rev. Mod. Phys. **87**, 637–701 (2015).
[3] L. Sárkány, P. Weiss, H. Hattermann, and J. Fortágh, "Controlling the magnetic-field sensitivity of atomic-clock states by microwave dressing," Phys. Rev. A **90**, 053416 (2014).
[4] I. Bloch, J. Dalibard, and W. Zwerger, "Many-body physics with ultracold gases," Rev. Mod. Phys. **80**, 885–964 (2008).
[5] X. Li, S. Wang, X. Luo, Y.-Y. Zhou, K. Xie, H.-C. Shen, Y.-Z. Nie, Q. Chen, H. Hu, Y.-A. Chen, X.-C. Yao, and J.-W. Pan, "Observation and quantification of the pseudogap in unitary Fermi gases," Nature **626**, 288–293 (2024).
[6] C. Chin, R. Grimm, P. Julienne, and E. Tiesinga, "Feshbach resonances in ultracold gases," Reviews of Modern Physics **82** (2010).
[7] A. Marte, T. Volz, J. Schuster, S. Dürr, G. Rempe, E. G. M. van Kempen, and B. J. Verhaar, "Feshbach resonances in rubidium 87: Precision measurement and analysis," Phys. Rev. Lett. **89**, 283202 (2002).
[8] A. Ciamei, S. Finelli, A. Trenkwalder, M. Inguscio, A. Simoni, and M. Zaccanti, "Exploring ultracold collisions in ^{6}Li$-^{53}$Cr fermi mixtures: Feshbach resonances and scattering properties of a novel alkali-transition metal system," Phys. Rev. Lett. **129**, 093402 (2022).
[9] M. Borkowski, L. Reichsöllner, P. Thekkeppatt, V. Barbé, T. van Roon, K. van Druten, and F. Schreck, "Active stabilization of kilogauss magnetic fields to the ppm level for magnetoassociation on ultranarrow feshbach resonances," Review of Scientific Instruments **94** (2023).
[10] B. Pasquiou, E. Maréchal, G. Bismut, P. Pedri, L. Vernac, O. Gorceix, and B. Laburthe-Tolra, "Spontaneous demagnetization of a dipolar spinor bose gas in an ultralow magnetic field," Phys. Rev. Lett. **106**, 255303 (2011).
[11] C. Rogora, R. Cominotti, C. Baroni, D. Andreoni, G. Lamporesi, A. Zenesini, and G. Ferrari, "Progress toward a zero-magnetic-field environment for ultracold-atom experiments," Phys. Rev. A **110**, 013319 (2024).
[12] R. Cominotti, C. Rogora, A. Zenesini, G. Lamporesi, and G. Ferrari, "Ultracold atomic spin mixtures in ultrastable magnetic field environments," Europhysics Letters **146**, 45001 (2024).
[13] A. Farolfi, D. Trypogeorgos, G. Colzi, E. Fava, G. Lamporesi, and G. Ferrari, "Design and characterization of a compact magnetic shield for ultracold atomic gas experiments," Review of Scientific Instruments **90** (2019).
[14] C. J. Dedman, R. Dall, L. Byron, and A. Truscott, "Active cancellation of stray magnetic fields in a bose-einstein condensation experiment," Review of scientific instruments **78** (2007).
[15] K. Xiao, L. Wang, J. Guo, M. Zhu, X. Zhao, X. Sun, C. Ye, and X. Zhou, "Quieting an environmental magnetic field without shielding," Review of Scientific Instruments **91** (2020).
[16] X.-T. Xu, Z.-Y. Wang, R.-H. Jiao, C.-R. Yi, W. Sun, and S. Chen, "Ultra-low noise magnetic field for quantum gases," Review of Scientific Instruments **90** (2019).
[17] Z.-X. Duan, W.-T. Wu, Y.-T. Lin, and S.-J. Yang, "Simple and active magnetic-field stabilization for cold atom experiments," Review of Scientific Instruments **93** (2022).
[18] A. Hesse, K. Köster, J. Steiner, J. Michl, V. Vorobyov, D. Dasari, J. Wrachtrup, and F. Jendrzejewski, "Direct control of high magnetic fields for cold atom experiments based on nv centers," New Journal of Physics **23**, 023037 (2021).
[19] B. Merkel, K. Thirumalai, J. Tarlton, V. Schäfer, C. Ballance, T. Harty, and D. Lucas, "Magnetic field stabilization system for atomic physics experiments," Review of Scientific Instruments **90** (2019).
[20] R. Thomas and N. Kjærgaard, "A digital feedback controller for stabilizing large electric currents to the ppm level for feshbach resonance studies," Review of Scientific Instruments **91** (2020).
[21] C. D'Errico, M. Zaccanti, M. Fattori, G. Roati, M. Inguscio, G. Modugno, and A. Simoni, "Feshbach resonances in ultracold 39K," New Journal of Physics **9**, 223 (2007).
[22] D. S. Petrov, "Quantum mechanical stabilization of a collapsing bose-bose mixture," Phys. Rev. Lett. **115**, 155302 (2015).
[23] L. Lavoine, A. Hammond, A. Recati, D. S. Petrov, and T. Bourdel, "Beyond-mean-field effects in rabi-coupled two-component bose-einstein condensate," Phys. Rev. Lett. **127**, 203402 (2021).
[24] A. Hammond, L. Lavoine, and T. Bourdel, "Tunable three-body interactions in driven two-component bose-einstein condensates," Phys. Rev. Lett. **128**, 083401 (2022).

[25] Note that we also have added a 1 µF capacitor in parallel to the power supply to slightly reduce the current noise and also its typical frequencies.

[26] A small fraction of this relative noise ($\sim 3\,10^{-6}$ rms) originates from the power supply's external analog input which is driven by one output channel of a digital-to-analog converter card (*National Instrument PCIe-6738*).

[27] In this configuration, trying to further stabilize the current by applying some feedback to its analog command quickly leads to current oscillations.

[28] N. F. Ramsey, "A molecular beam resonance method with separated oscillating fields," Phys. Rev. **78**, 695–699 (1950).

[29] The $\pi/2$ pulse actually puts each atom in a coherent spin superposition. It theoretically results in binomial distribution of the number of atoms in each spin state with rms fluctuations of f that amount to $1/2\sqrt{N}$ =0.05%. Our measured detection noise is only 4 times this shot-noise limit.

[30] J. Vanier and C. Audoin, *The Quantum Physics of Atomic Frequency Standards* (CRC Press, 1989).

[31] Precisely, $\delta_0(T)$ is the ensemble and time averaged of the Ramsey detuning over the time T.

[32] In our experiment, we found that the good long term stability could only be observed with at least 2 s wait time between the magnetic quadrupole trap step, where the bias coils are used with 200 A for about 1 s, and the Ramsey interferometer sequence. This observation could have both a mechanical (because of the force between the two coils) or a thermal (because of the heat deposited in the coils) origin.

Three-body interactions in Rabi-coupled Bose gases: a perturbative approach

S. Tiengo, R. Eid, and T. Bourdel*
Université Paris-Saclay, Institut d'Optique Graduate School, CNRS, Laboratoire Charles Fabry, 91127 Palaiseau, France

(Dated: March 28, 2025)

In ultracold atomic gases, radio-frequency coupling between two spin states can lead to atoms being in a stable coherent superposition of the two states (dressed states). When the two-body interactions (scattering lengths) are different between the two states, it offers the possibility not only to control the interatomic interaction but also to modify the equation of states with emerging three-body terms with different signs and scalings with the parameters. We derive these terms in a unified perturbation framework and show that they correspond to genuine three-body processes found at different orders in perturbation theory. Our work justifies the introduction of contact three-body interactions in dressed-state systems when the spin degree of freedom is integrated out.

arXiv:2503.21270v1 [cond-mat.quant-gas] 27 Mar 2025

I. INTRODUCTION

Ultracold quantum gases are model many-body systems that permit one to access a variety of physical phenomena, such as superfluidity or phase transitions [1]. A key simplification comes from the fact that they are dilute systems with a dominating two-body interaction that, in addition, can be modeled by a contact interaction [2]. In this context, the scattering length a is the only quantity that fully characterizes the interaction strength. Importantly, the scattering lengths can be modified through diffusion (Fano-Feshbach) resonances by tuning the magnetic field [3]. This degree of control and the versatility of the external potential allows for versatile and quantitative studies (or quantum simulations) of complex many-body problems such as the BEC-BCS transition for fermions [4–7], the Mott-transition [8], the Berenzinski-Kosterlitz-Thouless superfluid transition in 2D [9] or the generalized hydrodynamics in 1D [10] for bosons.

Physics can be made even richer when mixtures are used such that different two-body interactions may coexist [11]. For bosons, this has led to the observation of phase separation for repulsive interspecies interaction [12] and quantum droplets for attractive interspecies interaction [13, 14]. Coupling between two spin states (for example, using a radio-frequency field) adds another degree of freedom. Competition between spin interaction and coupling can lead to bistability [15] or ferromagnetism phenomena [16] in the spin degree of freedom. Coherent coupling also leads to an alternative way of controlling the two-body interaction [17]. Indeed, the effective interaction then varies with the spin composition of the dressed state, which can be controlled by the detuning of the coupling field. In this configuration, it was also shown that three-body interaction terms either positive or negative emerge in the equation of state and may play a dominant role in the dynamics of Bose-Einstein condensates. These terms were found to appear either from mean-field shift of the energy difference between the two spin states [18], or in complex calculations beyond the mean field in the limit of large coupling [19]. These experimental demonstrations of controllable three-body interactions without strong enhancement of losses in ultra-cold dilute gases came in a context where such interactions have been considered in numerous theoretical works [20–35].

In this paper, we perform perturbation theory as a function of the interaction strengths and up to the third order. We recover the three-body interaction terms for a Bose gas with coherent coupling between two spin states in a unified framework at different orders in perturbation. We first treat the problem of a homogeneous condensate in the dressed state and calculate the modification of its ground-state energy. This calculation directly links to previous results on the equation of states [18, 19]. Second, few-body scattering processes [28] are considered and calculated. Our results justify the introduction of a contact three-body interaction term in an effective Hamiltonian in the reduced Hilbert space, in which the spin excitations are no longer considered. Finally, a generalization of the calculations to one dimension (1D) is presented.

II. HAMILTONIAN IN THE DRESSED-STATE BASIS

In the second quantization formalism, the single particle and the interaction Hamiltonians H_0 and H_{int} in a coupled two-component homogeneous Bose system of volume V read:

* thomas.bourdel@institutoptique.fr

$$H_0 = \sum_{\mathbf{p}} \left(\frac{\mathbf{p}^2}{2m} + \frac{\hbar\delta}{2} \right) a^\dagger_{\uparrow\mathbf{p}} a_{\uparrow\mathbf{p}} + \sum_{\mathbf{p}} \left(\frac{\mathbf{p}^2}{2m} - \frac{\hbar\delta}{2} \right) a^\dagger_{\downarrow\mathbf{p}} a_{\downarrow\mathbf{p}} + \sum_{\mathbf{p}} \frac{\hbar\Omega}{2} (a^\dagger_{\uparrow\mathbf{p}} a_{\downarrow\mathbf{p}} + a^\dagger_{\downarrow\mathbf{p}} a_{\uparrow\mathbf{p}}), \tag{1}$$

$$H_{\text{int}} = \frac{1}{2V} \sum_{\mathbf{p}_1+\mathbf{p}_2=\mathbf{p}_3+\mathbf{p}_4} (g_{\uparrow\uparrow} a^\dagger_{\uparrow\mathbf{p}_3} a^\dagger_{\uparrow\mathbf{p}_4} a_{\uparrow\mathbf{p}_1} a_{\uparrow\mathbf{p}_2} + g_{\downarrow\downarrow} a^\dagger_{\downarrow\mathbf{p}_3} a^\dagger_{\downarrow\mathbf{p}_4} a_{\downarrow\mathbf{p}_1} a_{\downarrow\mathbf{p}_2} + 2g_{\uparrow\downarrow} a^\dagger_{\uparrow\mathbf{p}_3} a^\dagger_{\downarrow\mathbf{p}_4} a_{\uparrow\mathbf{p}_1} a_{\downarrow\mathbf{p}_2}), \tag{2}$$

where m is the atomic mass, $\hbar$ the reduced Planck constant, δ the coupling detuning, and Ω the Rabi frequency of the coupling between the two spin states. $a^\dagger_{\sigma\mathbf{p}}$ and $a_{\sigma\mathbf{p}}$ are the creation and annihilation operators of a particle with a certain spin σ in the $\{\uparrow,\downarrow\}$ basis and momentum $\mathbf{p}$. In the interaction Hamiltonian appear the three coupling constants $g_{\sigma\sigma'} = 4\pi\hbar^2 a_{\sigma\sigma'}/m$ for the $\sigma-\sigma'$ contact interactions with scattering lengths $a_{\sigma\sigma'}$.

In order to perform perturbation theory, we first diagonalize the single particle Hamiltonian H_0 by a rotation to the dressed-state basis $|+\rangle$, $|-\rangle$, thus introducing the related operators

$$\begin{aligned} a_{+\mathbf{p}} &= \cos\theta a_{\downarrow\mathbf{p}} + \sin\theta a_{\uparrow\mathbf{p}}, \\ a_{-\mathbf{p}} &= \sin\theta a_{\downarrow\mathbf{p}} - \cos\theta a_{\uparrow\mathbf{p}}, \end{aligned} \tag{3}$$

where θ is the mixing angle such that $\text{cotan}(2\theta) = \delta/\Omega$. In this description, θ evolves from 0 to $\pi/2$ and is $\pi/4$ at resonance (that is, for $\delta = 0$). In this rotated basis H_0 reads:

$$\begin{aligned} H_0 = &\sum_p \frac{\mathbf{p}^2}{2m} (a^\dagger_{+\mathbf{p}} a_{+\mathbf{p}} + a^\dagger_{-\mathbf{p}} a_{-\mathbf{p}}) \\ &+ \sum_p \frac{\hbar\tilde{\Omega}}{2} (a^\dagger_{+\mathbf{p}} a_{+\mathbf{p}} - a^\dagger_{-\mathbf{p}} a_{-\mathbf{p}}), \end{aligned} \tag{4}$$

where $\tilde{\Omega} = \sqrt{\Omega^2 + \delta^2}$. In the same basis, the interaction Hamiltonian [36] is

$$\begin{aligned} H_{\text{int}} = &\frac{1}{2V} \sum_{\mathbf{p}_1+\mathbf{p}_2=\mathbf{p}_3+\mathbf{p}_4} \\ \Big(&g_1 a^\dagger_{+\mathbf{p}_3} a^\dagger_{+\mathbf{p}_4} a_{+\mathbf{p}_1} a_{+\mathbf{p}_2} \\ &+ g_2 a^\dagger_{-\mathbf{p}_3} a^\dagger_{-\mathbf{p}_4} a_{-\mathbf{p}_1} a_{-\mathbf{p}_2} \\ &+ g_3 a^\dagger_{+\mathbf{p}_3} a^\dagger_{-\mathbf{p}_4} a_{+\mathbf{p}_1} a_{-\mathbf{p}_2} \\ &+ g_4 (a^\dagger_{+\mathbf{p}_3} a^\dagger_{+\mathbf{p}_4} a_{-\mathbf{p}_1} a_{-\mathbf{p}_2} + a^\dagger_{-\mathbf{p}_3} a^\dagger_{-\mathbf{p}_4} a_{+\mathbf{p}_1} a_{+\mathbf{p}_2}) \\ &+ g_5 (a^\dagger_{+\mathbf{p}_3} a^\dagger_{+\mathbf{p}_4} a_{+\mathbf{p}_1} a_{-\mathbf{p}_2} + a^\dagger_{+\mathbf{p}_3} a^\dagger_{-\mathbf{p}_4} a_{+\mathbf{p}_1} a_{+\mathbf{p}_2}) \\ &+ g_6 (a^\dagger_{+\mathbf{p}_3} a^\dagger_{-\mathbf{p}_4} a_{-\mathbf{p}_1} a_{-\mathbf{p}_2} + a^\dagger_{-\mathbf{p}_3} a^\dagger_{-\mathbf{p}_4} a_{+\mathbf{p}_1} a_{-\mathbf{p}_2}) \Big). \end{aligned} \tag{5}$$

The first three terms of the Hamiltonian correspond to elastic collisions between two atoms in the dressed states, with, respectively, g_1, g_2, g_3 as the interaction strength coefficients. The last three terms with coupling constants g_3, g_4 and g_5, instead describe scattering events that do not preserve the particle dressed state (inelastic collisions).

The dependence of the coupling coefficients on the mixing angle (or equivalently on the detuning δ/Ω) is:

$$\begin{aligned} g_1 &= g_{\downarrow\downarrow}\cos^4\theta + g_{\uparrow\uparrow}\sin^4\theta + \frac{1}{2} g_{\uparrow\downarrow}\sin^2 2\theta \\ g_2 &= g_{\downarrow\downarrow}\sin^4\theta + g_{\uparrow\uparrow}\cos^4\theta + \frac{1}{2} g_{\uparrow\downarrow}\sin^2 2\theta \\ g_3 &= (g_{\downarrow\downarrow} + g_{\uparrow\uparrow})\sin^2 2\theta + 2g_{\uparrow\downarrow}\cos^2 2\theta \\ g_4 &= \frac{1}{4}(g_{\downarrow\downarrow} + g_{\uparrow\uparrow} - 2g_{\uparrow\downarrow})\sin^2 2\theta \\ g_5 &= \sin 2\theta (g_{\uparrow\uparrow}\sin^2\theta - g_{\downarrow\downarrow}\cos^2\theta + g_{\uparrow\downarrow}\cos 2\theta) \\ g_6 &= \sin 2\theta (g_{\uparrow\uparrow}\cos^2\theta - g_{\downarrow\downarrow}\sin^2\theta - g_{\uparrow\downarrow}\cos 2\theta). \end{aligned} \tag{6}$$

The precise description of higher-order interaction processes is especially relevant in conditions where the usual two-body collisions is reduced thanks to the compensation between positive and repulsive bare coupling constants. In such a situation, higher-order interactions will play an important role. It occurs in particular when the intraspecies coupling constant $g_{\uparrow\uparrow}$ and $g_{\downarrow\downarrow}$ are positive whereas $g_{\uparrow\downarrow}$ is negative, conditions that can be met in potassium 39 [37]. As an example, the coupling constants g_2, g_3, g_4, g_6 are plotted for the second and third

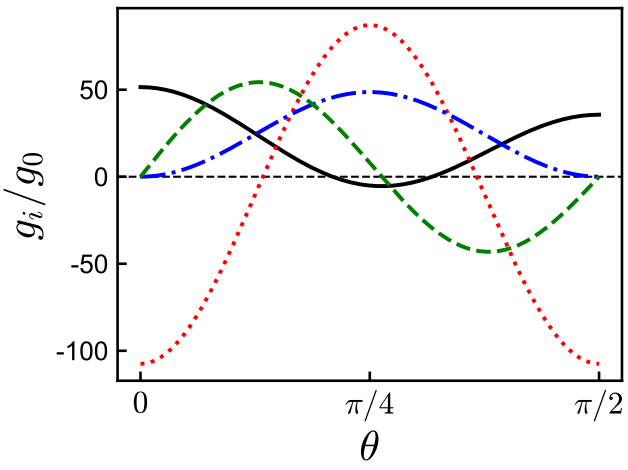


FIG. 1. g_2 (black solid line), g_3 (red dotted line), g_4 (blue dash-dotted line), g_6 (green dashed line) as a function of the mixing angle θ and normalizes to $g_0 = 4\pi\hbar^2 a_0/m$, where a_0 is the atomic Bohr radius. $a_{\uparrow\uparrow} = 51.5\,a_0$, $a_{\downarrow\downarrow} = 35.6\,a_0$, $a_{\uparrow\downarrow} = -53.7\,a_0$.

lowest states of ^{39}K at a magnetic field of 55.6 G in Fig.1. If $\theta = 0$ or $\theta = \pi/2$ (i.e. $\delta/\Omega \to \pm\infty$), we find only elastic collisions and the original Hamiltonian in the non-rotated internal state basis. In the vicinity of the resonance $\delta \approx \pi/4$, $|-\rangle$-$|-\rangle$ interactions are reduced as g_2 is close to zero. Note that $g_6 \propto \frac{\partial g_2}{\partial \theta}$ such that g_6 vanishes when g_2 is minimal.

III. PERTURBATIVE EXPANSION OF THE CONDENSATE ENERGY

We first perform perturbation theory in order to calculate the ground state energy corresponding to a Bose-Einstein condensate in state $|-, \mathbf{p} = \mathbf{0}\rangle$. The unperturbed ground state is $|\psi_0\rangle = \frac{1}{\sqrt{N!}}(a^\dagger_{-,\mathbf{p}=0})^N |0\rangle$, where N is the atom number. At the first order in perturbation theory, the correction to the energy is given by the expectation value of $H_{\rm int}$ in the unperturbed ground state

$$E^{(1)} = \langle\psi_0| H_{\rm int} |\psi_0\rangle . \tag{7}$$

Among all the terms of $H_{\rm int}$, only the term multiplied by the coupling constant g_2 allows two colliding atoms to remain in the dressed state $|-\rangle$. There is therefore a single term in the sum that contributes at the first order

$$\begin{aligned} E^{(1)} &= \frac{g_2}{2V} \langle\psi_0| a^\dagger_{-,\mathbf{p}=0} a^\dagger_{-,\mathbf{p}=0} a_{-,\mathbf{p}=0} a_{-,\mathbf{p}=0} |\psi_0\rangle \\ &= g_2 \frac{N(N-1)}{2V} \simeq g_2 \frac{N^2}{2V}. \end{aligned} \tag{8}$$

The first order correction (eq. 8) corresponds to the standard mean-field interaction energy with a coupling constant g_2 that varies with the detuning δ/Ω.

The energy correction at the second order is given by

$$E^{(2)} = \sum_i \frac{\langle\psi_0| H_{\rm int} |\psi_i\rangle \langle\psi_i| H_{\rm int} |\psi_0\rangle}{E_0 - E_i}, \tag{9}$$

where the sum is taken over all possible intermediate states $|\psi_i\rangle \neq |\psi_0\rangle$. We can recognize that the terms of $H_{\rm int}$ that contribute to the second order are those multiplied by the coupling constants g_2, g_4, and g_6. At the second order the energy correction is given by

$$\begin{aligned} E^{(2)} = &-\frac{g_2^2 N^2}{2V^2} \sum_{\mathbf{p}\neq 0} \frac{m}{\mathbf{p}^2} - \frac{g_4^2 N^2}{2V^2} \sum_{\mathbf{p}\neq 0} \frac{1}{2\hbar\tilde{\Omega} + \mathbf{p}^2/m} \\ &- \frac{g_6^2 N^2}{4V^2} \sum_{\mathbf{p}\neq 0} \frac{1}{\hbar\tilde{\Omega} + \mathbf{p}^2/m} - \frac{g_6^2 N^3}{4V^2 \hbar\tilde{\Omega}} \end{aligned} \tag{10}$$

Note that we have omitted the terms that are not extensive ($\propto N$) in the thermodynamic limit (i.e. for large N and V, with constant density $n = N/V$). The last term originates from the term with all momenta equal to 0 and scales as N^3 because there are three a_{-0} or $a^\dagger_{-0}$ in the corresponding Hamiltonian term. It corresponds to the negative three-body energy contribution calculated at the mean field level, taking into account a density-dependent shift of the detuning [18].

The first three terms are divergent at large $\mathbf{p}$. This is a consequence of the unphysical nature of the contact potential in 3D, which needs to be regularized, for example, by adding a momentum cutoff in $H_{\rm int}$. An alternative way is to renormalize the coupling constant, which is equivalent to removing the divergent parts in the sums [38]. After such a procedure, the first term disappears, whereas the two other terms are renormalized

$$E^{(2)} = \frac{(2\sqrt{2} g_4^2 + g_6^2) N^2 \sqrt{\hbar\tilde{\Omega}}}{2V} \frac{m^{3/2}}{8\pi\hbar^3} - \frac{g_6^2 N^3}{4V^2 \hbar\tilde{\Omega}}. \tag{11}$$

In the specific case, where g_2 is minimal and zero ($g_6 = 0$), we exactly recover the renormalization of the two-body interaction due to beyond-mean-field effects calculated from a Bogoliubov type approach in the limit of large coupling as compared to the interaction energy $\hbar\Omega \gg gN/V$ [19].

Let us now consider third-order perturbation theory. Generally, it reads:

$$E^{(3)} = \sum_i \sum_j \frac{\langle\psi_0| H_{\rm int} |\psi_i\rangle \langle\psi_i| H_{\rm int} |\psi_j\rangle \langle\psi_j| H_{\rm int} |\psi_0\rangle}{(E_i - E_0)(E_j - E_0)}. \tag{12}$$

In principle, the sum includes terms with g_4 or g_6. Since, if g_6 is non zero, there is already a three-body contribution at the second-order of perturbation, we focus on the case where $g_6 = 0$. In that case, the only non-zero terms are of the form

$$\begin{aligned} &(g_4 a^\dagger_{-0} a^\dagger_{-0} a_{+\mathbf{p}_1} a_{+(-\mathbf{p}_1)})(g_3 a^\dagger_{+\mathbf{p}_2} a^\dagger_{-0} a_{+\mathbf{p}_2} a_{-0}) \\ &\qquad (g_4 a^\dagger_{+\mathbf{p}_3} a^\dagger_{+(-\mathbf{p}_3)} a_{-0} a_{-0}), \end{aligned} \tag{13}$$

where the $\mathbf{p} = 0$ are imposed by the fact that there is no atoms in $|-, \mathbf{p} \neq 0\rangle$ in $|\psi_0\rangle$.

The specific case of $\mathbf{p}_1 = \mathbf{p}_2 = \mathbf{p}_3 = 0$ can be neglected in the thermodynamic limit as it scales as $(N/V)^3$. For $\mathbf{p}_1 \neq 0$, $\mathbf{p}_2$ and $\mathbf{p}_3$ have to take the same value up to a sign. There are thus 4 equivalent terms and

$$\begin{aligned} E^{(3)} &= \frac{g_4^2 g_3 N^3}{2V^3} \sum_{\mathbf{p}\neq 0} \frac{1}{(2\hbar\tilde{\Omega} + \mathbf{p}^2/m)^2} \\ E^{(3)} &= \frac{g_4^2 g_3 n^3}{16\pi\sqrt{2\hbar\tilde{\Omega}}} \frac{V m^{3/2}}{\hbar^3}. \end{aligned} \tag{14}$$

Again, it is exactly the positive value found in the Bogoliubov approach in the limit of large coupling $\hbar\Omega \gg gn$ [19]. The pertubation theory permits us to find in a unified framework two-body and three-body interaction terms in the equation of state that were previously found in mean-field and beyond mean-field approaches. However, the perturbative expansion is less general than the Bogoliubov approach; it does not resolve the problem when $\hbar\Omega$ is not large compared to gn. In particular, perturbation theory cannot recover the nonanalytical Lee-Huang-Yang $N^{5/2}$ energy scaling for vanishing Ω [13].

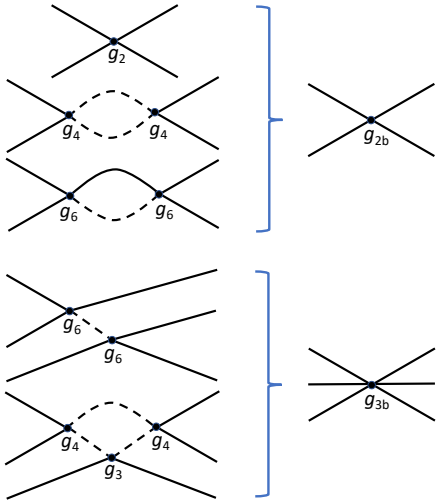


FIG. 2. Feynman diagrams corresponding to the possible scattering events. The plain and dashed lines represent the $|-\rangle$ and $|+\rangle$ state, respectively. The three first diagrams correspond to two-body scattering at first and second order in perturbation theory and contributes to g_{2b} in the effective interaction Hamiltonian. The two last diagrams correspond to three-body scattering at the second and third-order and contributes to g_{3b} in the effective interaction Hamiltonian.

IV. THREE-BODY SCATTERING IN PERTURBATION THEORY

The above calculation shows that the two- and three-body terms in the equation of state of a coherently dressed condensate can be found in perturbation theory. In this section, we show that they actually correspond to few-particle collisions, whose strength can be deduced from perturbative scattering theory. The corresponding Feynman diagrams are shown in Fig. 2.

Let us first consider two-body elastic collisions from the initial state $\left|\psi_i^{2b}\right\rangle = a^\dagger_{-p_1}a^\dagger_{-p_2}\left|0\right\rangle$ to the final state $\left|\psi_f^{2b}\right\rangle = a^\dagger_{-p_3}a^\dagger_{-p_4}\left|0\right\rangle$. Scattering theory tells that we should consider the matrix elements $\left\langle\psi_f^{2b}\right| T \left|\psi_i^{2b}\right\rangle$, where T is called the scattering matrix and can be expressed as

$$T = H_{\rm int} + H_{\rm int}G_0H_{\rm int} + H_{\rm int}G_0H_{\rm int}G_0H_{\rm int} + H_{\rm int}G_0H_{\rm int}G_0H_{\rm int}G_0H_{\rm int} + ..., \quad (15)$$

$$\text{where } G_0 = \frac{1}{H_0 - E_0}, \quad (16)$$

a form that is suited in order to apply perturbation theory.

If we restrict to the first order (i.e. the first diagram in Fig. 2 or Born approximation), only the g_2 term of the Hamiltonien contributes, and the matrix element has the same non-zero value for any value of the momenta that ensure total momentum conservation. It corresponds to the usual two-body s-wave scattering amplitude that leads to an isotropic scattering halo. The second-order terms include as before contributions originating from g_2, g_4, and g_6, and the sums need to be regularized at high momenta with the usual renormalization of the coupling constant. Remarkably, for collisions at low momenta, i.e. such that $p^2/m \ll \hbar\Omega$, one can neglect the corresponding kinetic terms in the denominator such that the exact same type of terms as in the previous energy calculation appears. We thus find two additional terms up to the second-order in perturbation (corresponding to the second and third diagrams in Fig 2)

$$\left\langle\psi_f^{2b}\right| T \left|\psi_i^{2b}\right\rangle \approx 2g_2/V + \frac{(2\sqrt{2}g_4^2 + g_6^2)\sqrt{\hbar\tilde{\Omega}}}{4\pi V}. \quad (17)$$

This result can be simply interpreted as a modification of the scattering length due to the coupling. This correction can also be found from an exact calculation of two-body scattering in the presence of coupling (see supplemental material in [19])

We now consider three particles in the $|-\rangle$ dressed state with momenta p_1, p_2, p_3 and ask the question if they can elastically scatter to other momenta p_1', p_2', p_3'. We thus consider $\langle -p_1', -p_2', -p_3'| T |-p_1, -p_2, -p_3\rangle$. For simplicity, we consider the case where all momenta are different. At the second order in perturbation, the only terms in $H_{\rm int}$ that allow us to change the three momenta are g_2^2 and g_6^2 because they need to annihilate two atoms in $|-\rangle$ and create at least one atom in $|-\rangle$. The g_2^2 term disappears with the renormalization of the coupling constant. The term $\propto g_6^2$ (fourth diagram in Fig. 2) first annihilates two $|-\rangle$ particles among the three, creates one in $|+\rangle$ and one in $|-\rangle$ with one of the final momenta, second annihilates the last initial $|-\rangle$ particle and the $|+\rangle$ particle, and creates the 2 other $|-\rangle$ particles with the final momenta. There are 9 possible intermediate states. If all momenta are small $p^2/m \ll \hbar\Omega$, the matrix element reduces to

$$\left\langle\psi_f^{3b}\right| H_{\rm int}G_0H_{\rm int} \left|\psi_i^{3b}\right\rangle = \frac{9g_6^2}{V^2\hbar\tilde{\Omega}} \quad (18)$$

with no momentum dependence.

At the third order in perturbation theory, there are several possible terms, including g_4 or g_6. Similarly to before, we consider the case $g_6 = 0$, so that there is no three-body scattering at the second order. In that case, there is a single possible diagram (the fifth in Fig. 2). There remains one integration over a momentum which is not diverging and we find (after careful counting of the number of terms that contributes)

$$\left\langle\psi_f^{3b}\right| H_{\rm int}G_0H_{\rm int}G_0H_{\rm int} \left|\psi_i^{3b}\right\rangle = \frac{9g_4^2g_3}{4\pi V^2\sqrt{2\hbar\tilde{\Omega}}}. \quad (19)$$

Interestingly, for symmetric conditions ($g_{\uparrow\uparrow} = g_{\downarrow\downarrow}$ and $\delta = 0$), the latter term can was previously found in a exact three-body calculation [28].

The above results show that two- and three-body interactions are also found in few-body scattering with the initial Hamiltonian. In the perturbative framework, the na-

ture of the three-body interactions is clear. They correspond to higher-order scattering with intermediate states that have a different spin.

Given the success of the perturbative expansion, it is tempting to continue the expansion to higher orders. However, we expect that the fourth order will not be accurate as corrections from short-range physics are then expected [20, 34]. Moreover, three-body recombination losses typically scale as a^4 [39] and also have to be considered at this level of perturbative expansion.

V. EFFECTIVE HAMILTONIAN

The above perturbative results justify an effective interaction Hamiltonian H_{eff} in an Hilbert space reduced to the dressed state $|-\rangle$ with contact three-body interaction

$$H_{\text{eff}} = \frac{g_{2\text{b}}}{2V} \sum_{\mathbf{p_1'}+\mathbf{p_2'}=\mathbf{p_1}+\mathbf{p_2}} a^\dagger_{p_2'} a^\dagger_{p_1'} a_{p_2} a_{p_1} \tag{20}$$

$$+ \frac{g_{3\text{b}}}{3V^2} \sum_{\mathbf{p_1'}+\mathbf{p_2'}+\mathbf{p_3'}=\mathbf{p_1}+\mathbf{p_2}+\mathbf{p_3}} a^\dagger_{p_3'} a^\dagger_{p_2'} a^\dagger_{p_1'} a_{p_3} a_{p_2} a_{p_1}, \tag{21}$$

where $g_{2\text{b}} = V \left\langle \psi_f^{2b} \right| T \left| \psi_i^{2b} \right\rangle /2$ and $g_{3\text{b}} = V^2 \left\langle \psi_f^{3b} \right| T \left| \psi_i^{3b} \right\rangle /12$. The numerical factors come from the number of permutations of the different momenta, and the corresponding two-body and three-body diagrams are shown on the right of Fig. 2. This effective Hamiltonian is constructed to give the same matrix elements as the ones found previously, thus leading to the same low-energy physics as the real system with the dressing field and possible virtual spin excitations. It also leads to previously calculated ground-state energy shifts, when applied to a condensate in the $|-\rangle$ state in the Born approximation. Higher-order terms originating from the effective Hamiltonian can be neglected at the level of accuracy of the initial third-order perturbation theory.

VI. GENERALIZATION TO 1D SYSTEMS

In an elongated trap, the confinement may be such that the radial excitations of the gas correspond to the highest energy scale of the problem. In the simple case of a radial harmonic trap with frequency $\omega_\perp/2\pi$, it requires $g_{\sigma\sigma'} n \ll \hbar\omega_\perp$ as well as $\Omega \ll \omega_\perp$. In the absence of copupling ($\Omega = 0$), 1D quantum droplets have been predicted [40]. With coupling, 1D perturbation calculations can be done similarly to the 3D ones. The only difference is that the sums over the momenta are 1D rather than 3D. It is actually simpler because there is no divergence, and no renormalization of the coupling constants is necessary. The 1D coupling constants for a harmonic trap can be approximated by $g^{1\text{D}}_{\sigma\sigma'} = 2\hbar\omega_\perp a_{\sigma\sigma'}$ in the limit $a_{\sigma\sigma'} \ll \sqrt{\hbar/m\omega_\perp}$ [41].

The three-body interaction arising at the second-order in perturbation (and also found at the mean-field level) is not modified. This is expected as the calculation involves only spin excitations with no momentum change. On the contrary, the renormalization of the two-body interaction and the emergence of a three-body interaction are modified. In the simple case where $g_6 = 0$:

$$E^{(2)} = -\frac{(g_4^{1\text{D}})^2 N^2 \sqrt{m}}{4L\sqrt{2\hbar\tilde{\Omega}}\hbar}, \tag{22}$$

$$E^{(3)} = \frac{(g_4^{1\text{D}})^2 g_3^{1\text{D}} N^3}{32\sqrt{2}L^2} \frac{1}{(\hbar\tilde{\Omega})^{3/2}} \frac{\sqrt{m}}{\hbar}, \tag{23}$$

where L is the size of the 1D system. The sign of the dominant two-body term is now negative, in contrast to the 3D case. This may be expected since for $\Omega = 0$, the beyond-mean-field correction is negative in 1D [40]. In addition, the scaling with Ω is modified as compared to the 3D case. These corrections can also be found in a beyond-mean-field approach in the presence of a coupling similarly to what was done in 3D [19].

VII. CONCLUSION

In this paper, we have performed a perturbative treatment of the interactions in a Bose dressed system with competing interactions. This has been done not only for the energy of a condensate but also for the two-body and three-body scattering problems. Our approach permits us to nicely explain the origin of the different kinds of three-body interactions in a unified framework at different orders in perturbation theory. It justifies the use of an effective Hamiltonian that includes a contact three-body interaction term when conditions for a valid perturbative expansion are met. The control of three-body interactions through radio-frequency-dressing appears as an important addition to the atomic gas toolbox. Precise calculations of the values of g_{2b} and g_{3b} for specific experimental conditions ($a_{\uparrow\uparrow}$, $a_{\uparrow\downarrow}$, ,$a_{\downarrow\downarrow}$, δ, Ω) are straightforward. Interestingly, losses and short-range physics corrections would appear only at higher-order order in the expansion and are thus expected to be negligible compared to the three-body interactions found in the present work.

For compensating two-body interactions (with scattering lengths of opposite signs between the different spins), the dressing permits one to reach situations where the two-body interactions are reduced, such that higher-order three-body interaction terms are sizable and may even dominate the equation of state. This is in contrast to single-component dilute Bose gases where three-body interactions are usually negligible and/or associated with losses when the scattering length is increased [34]. Previous experimental works on three-body interactions in dressed Bose gases have focused on the modification of

the equation of states [18, 19]. Future works may directly detect the specific collision halos that would originate from three-body collisions. This could be done by studying the collision between two condensates under conditions such that there are no two-body collisions ($g_{2b} = 0$) but only three-body collisions ($g_{3b} = 0$).

ACKNOWLEDGMENTS

This research was supported by CNRS, Ministère de l'Enseignement Supérieur et de la Recherche, Quantum Paris-Saclay, Région Ile-de-France in the framework of Domaine d'Intérêt Majeur Quantip (H3B), France 2030 in the framework of PEPR Quantique (ANR-23-PETQ-0001), the Simons Foundation (Award No. 563916, localization of waves), France and Chicago collaborating in the sciences.

[1] I. Bloch, J. Dalibard, and W. Zwerger, Many-body physics with ultracold gases, Rev. Mod. Phys. **80**, 885 (2008).

[2] C. W. M. Inguscio, S. Stringari, ed., *Bose-Einstein Condensation in Atomic Gases*, Proceedings of the International School of Physics "Enrico Fermi", Vol. 140 (IOS Press, Amsterdam, 1999).

[3] C. Chin, R. Grimm, P. Julienne, and E. Tiesinga, Feshbach resonances in ultracold gases, Rev. Mod. Phys. **82**, 1225 (2010).

[4] C. A. Regal, M. Greiner, and D. S. Jin, Observation of resonance condensation of fermionic atom pairs, Phys. Rev. Lett. **92**, 040403 (2004).

[5] M. Bartenstein, A. Altmeyer, S. Riedl, S. Jochim, C. Chin, J. H. Denschlag, and R. Grimm, Crossover from a molecular bose-einstein condensate to a degenerate fermi gas, Phys. Rev. Lett. **92**, 120401 (2004).

[6] M. W. Zwierlein, C. A. Stan, C. H. Schunck, S. M. F. Raupach, A. J. Kerman, and W. Ketterle, Condensation of pairs of fermionic atoms near a feshbach resonance, Phys. Rev. Lett. **92**, 120403 (2004).

[7] T. Bourdel, L. Khaykovich, J. Cubizolles, J. Zhang, F. Chevy, M. Teichmann, L. Tarruell, S. J. J. M. F. Kokkelmans, and C. Salomon, Experimental study of the BEC-BCS crossover region in lithium 6, Phys. Rev. Lett. **93**, 050401 (2004).

[8] M. Greiner, O. Mandel, T. Esslinger, T. Hänsch, and I. Bloch, Quantum phase transition from a superfluid to a Mott insulator in a gas of ultracold atoms, Nature **415**, 39 (2002).

[9] Z. Hadzibabic, P. Krüger, M. Cheneau, B. Battelier, and J. Dalibard, Berezinskii-Kosterlitz-Thouless crossover in a trapped atomic gas, Nature **441**, 1118 (2006).

[10] M. Schemmer, I. Bouchoule, B. Doyon, and J. Dubail, Generalized hydrodynamics on an atom chip, Phys. Rev. Lett. **122**, 090601 (2019).

[11] C. W. M. Inguscio, S. Stringari, ed., *Quantum Mixtures with Ultra-cold Atoms*, Proceedings of the International School of Physics "Enrico Fermi", Vol. 211 (IOS Press, Amsterdam, 2025).

[12] D. S. Hall, M. R. Matthews, J. R. Ensher, C. E. Wieman, and E. A. Cornell, Dynamics of component separation in a binary mixture of Bose-Einstein condensates, Phys. Rev. Lett. **81**, 1539 (1998).

[13] D. S. Petrov, Quantum mechanical stabilization of a collapsing Bose-Bose mixture, Phys. Rev. Lett. **115**, 155302 (2015).

[14] C. R. Cabrera, L. Tanzi, J. Sanz, B. Naylor, P. Thomas, P. Cheiney, and L. Tarruell, Quantum liquid droplets in a mixture of Bose-Einstein condensates, Science **359**, 301 (2018).

[15] T. Zibold, E. Nicklas, C. Gross, and M. K. Oberthaler, Classical bifurcation at the transition from Rabi to Josephson dynamics, Phys. Rev. Lett. **105**, 204101 (2010).

[16] R. Cominotti, C. Rogora, A. Zenesini, G. Lamporesi, and G. Ferrari, Ultracold atomic spin mixtures in ultrastable magnetic field environments, Europhysics Letters **146**, 45001 (2024).

[17] J. Sanz, A. Frölian, C. S. Chisholm, C. R. Cabrera, and L. Tarruell, Interaction control and bright solitons in coherently coupled Bose-Einstein condensates, Phys. Rev. Lett. **128**, 013201 (2022).

[18] A. Hammond, L. Lavoine, and T. Bourdel, Tunable three-body interactions in driven two-component Bose-Einstein condensates, Phys. Rev. Lett. **128**, 083401 (2022).

[19] L. Lavoine and T. Bourdel, Beyond-mean-field crossover from one dimension to three dimensions in quantum droplets of binary mixtures, Phys. Rev. A **103**, 033312 (2021).

[20] T. T. Wu, Ground state of a Bose system of hard spheres, Phys. Rev. **115**, 1390 (1959).

[21] A. Gammal, T. Frederico, L. Tomio, and P. Chomaz, Atomic Bose-Einstein condensation with three-body interactions and collective excitations, Journal of Physics B: Atomic, Molecular and Optical Physics **33**, 4053 (2000).

[22] A. Gammal, T. Frederico, L. Tomio, and F. Abdullaev, Stability analysis of the d-dimensional nonlinear Schrödinger equation with trap and two- and three-body interactions, Physics Letters A **267**, 305 (2000).

[23] T. Köhler, Three-body problem in a dilute Bose-Einstein condensate, Phys. Rev. Lett. **89**, 210404 (2002).

[24] A. Bulgac, Dilute quantum droplets, Phys. Rev. Lett. **89**, 050402 (2002).

[25] S. Tan, Three-boson problem at low energy and implications for dilute Bose-Einstein condensates, Phys. Rev. A **78**, 013636 (2008).

[26] V. Kumar, R. Radha1, and M. Wadati, Phase engineering and solitons of Bose–Einstein condensates with two- and three-body interactions, J. Phys. Soc. Jpn **79**, 074005 (2010).

[27] A. F. M. Crosta, S. Trillo, The Whitham approach to dispersive shocks in systems with cubic–quintic nonlinearities, New J. Phys. **14**, 093019 (2012).

[28] D. S. Petrov, Three-body interacting bosons in free space,

Phys. Rev. Lett. **112**, 103201 (2014).
[29] D. S. Petrov, Elastic multibody interactions on a lattice, Phys. Rev. A **90**, 021601 (2014).
[30] K. Zloshchastiev, Stability and metastability of trapless Bose-Einstein condensates and quantum liquids, Zeitschrift für Naturforschung A **72**, 677 (2017).
[31] R. Killip, T. Oh, O. Pocovnicu, and M. Vişan, Solitons and scattering for the cubic–quintic nonlinear Schrödinger equation on $\mathbb{R}^3$, Arch. Rational Mech. Anal **225**, 469 (2017).
[32] J. D'Incao, Few-body physics in resonantly interacting ultracold quantum gases, J. Phys. B: At. Mol. Opt. Phys. **51**, 043001 (2018).
[33] Y. Sekino and Y. Nishida, Quantum droplet of one-dimensional bosons with a three-body attraction, Phys. Rev. A **97**, 011602 (2018).
[34] P. M. A. Mestrom, V. E. Colussi, T. Secker, and S. J. J. M. F. Kokkelmans, Scattering hypervolume for ultracold bosons from weak to strong interactions, Phys. Rev. A **100**, 050702 (2019).
[35] W. Zwerger, Quantum-unbinding near a zero temperature liquid–gas transition, J. Stat. Mech. , 103104 (2019).
[36] C. P. Search and P. R. Berman, Manipulating the speed of sound in a two-component Bose-Einstein condensate, Phys. Rev. A **63**, 043612 (2001).
[37] C. D'Errico, M. Zaccanti, M. Fattori, G. Roati, M. Inguscio, G. Modugno, and A. Simoni, Feshbach resonances in ultracold 39 K, New Journal of Physics **9**, 223 (2007).
[38] C. J. Pethick and H. Smith, *Bose–Einstein Condensation in Dilute Gases*, 2nd ed. (Cambridge University Press, 2008).
[39] E. Braaten and H.-W. Hammer, Universality in few-body systems with large scattering length, Physics Reports **428**, 259 (2006).
[40] D. S. Petrov and G. E. Astrakharchik, Ultradilute low-dimensional liquids, Phys. Rev. Lett. **117**, 100401 (2016).
[41] M. Olshanii, Atomic scattering in the presence of an external confinement and a gas of impenetrable bosons, Phys. Rev. Lett. **81**, 938 (1998).

Saturating interaction in coherently coupled two-component Bose-Einstein condensates

R. Eid, S. Tiengo, M. Lévy, and T. Bourdel*
Université Paris-Saclay, Institut d'Optique Graduate School, CNRS, Laboratoire Charles Fabry, 91127 Palaiseau, France
(Dated: July 8, 2025)

Rabi-coupled spinor Bose-Einstein condensates, with competing intra- and interspecies interactions, enables independent control of two- and three-body interactions. We show that coupling can also drive the system into a strongly nonlinear regime of saturating interaction. More precisely, the equation of state interpolates between low- and high-density regimes described by two different two-body scattering lengths. Interestingly, the transition can be determined by the strength of the coupling. We experimentally demonstrate this saturation phenomenon by measurements of the interaction energy of a Bose-Einstein condensate as a function of the detuning and of the strength of the Rabi coupling in spin mixtures of potassium 39.

I. INTRODUCTION

For a small perturbation, a physical system usually responds according to linear response theory. As the perturbation increases, the response may become non-linear giving rise to a wide variety of physical phenomena (solitons, bistability, chaotic behavior, etc...). [1]. Nonlinear response is often modeled by the addition of other response terms in powers of the perturbation. Such a Taylor expansion approach explains the higher harmonic generation in a system driven at a single frequency, as is commonly observed in nonlinear optics [2]. The Taylor expansion of the nonlinear response is not always valid for large perturbations, as many physical systems exhibit saturation of their response at large driving amplitudes. Typical examples are the magnetic or electric responses of materials that saturate when the maximum polarization is reached. In optics, saturation of the non-linear index of refraction, of absorption, or of the gain in amplifiers is also commonly observed [3].

In the physics of dilute atomic Bose-Einstein condensates, the non-linearity primary comes from the interaction between atoms [4] which are characterized by the scattering length a. In the case of a single-component Bose-Einstein condensate in the weak interaction regime $na^3 \ll 1$, where n is the atomic density, the energy density is dominated by the mean-field interaction scaling as n^2. Beyond this paradigm, quantum fluctuations are responsible for the Lee-Huang Yang term scaling non-analytically as $n^{5/2}$ in the energy density [5]. In bosonic mixtures, this term is responsible for the stabilization of quantum droplets [6, 7]. Higher-order interaction terms, for example, corresponding to a three-body interaction, are usually negligible in the dilute regime $na^3 \ll 1$ [8–10].

However, this paradigm is no longer valid in the presence of coupling between two spin states, i.e. when the condensate is in a dressed state that is a coherent superposition of two spin states. A condensate in a dressed state may experience both reduced usual two-body interactions [11] and large three-body interactions that are due to possible virtual excitations during collisions [12]. Such three-body processes are increasingly relevant as the ratio γ of the two-body interaction strength to the Rabi coupling strength increases. Their effects on the equation of state were experimentally measured through modifications in the condensate dynamics [13].

In this paper, we consider the situation where $\gamma \gtrsim 1$ and demonstrate a saturation of the interaction energy as a function of γ, a effect that can be captured in a mean-field framework. In this regime of strong nonlinear behavior, the equation of state can no longer be described as a Taylor series expansion as a function of the density, with terms scaling as n^p describing p-body interactions.

The paper is organized as follows. We first describe the coupled system Hamiltonian and theoretically explain the saturation of the interaction energy in a homogeneous system (with a given density). Second, we present our experiment using ^{39}K atoms. We explain the preparation of the condensates in the dressed state and the measurement of the interaction energy through one-dimensional time-of-flight expansions. As the experiment lies in the 1D to 3D crossover regime, we finally compare our results with imaginary-time Gross-Pitaevskii simulations including the two spin states and the Rabi coupling, as well as the radial trap. A good match, with no fit parameter, confirms our interpretation of the data.

II. THEORETICAL DESCRIPTION

Consider a Bose gas in a volume V consisting of N atoms of mass m with two coupled internal states, $\sigma = \uparrow, \downarrow$. The three relevant interaction constants $g_{\sigma\sigma'} = 4\pi\hbar^2 a_{\sigma\sigma'}/m$ are related to the scattering lengths $a_{\sigma\sigma'}$ and $\hbar$ the reduced Planck constant. In an homogeneous system with total density n, the mean field energy for a

* thomas.bourdel@institutoptique.fr

condensate in the spinor state $(\phi_\uparrow, \phi_\downarrow)$ reads

$$\frac{E_{MF}}{V} = -\frac{\hbar\Omega}{2}(\phi_\uparrow^*\phi_\downarrow + \phi_\downarrow^*\phi_\uparrow) + \frac{\hbar\delta}{2}(|\phi_\uparrow|^2 - |\phi_\downarrow|^2) + \sum_{\sigma\sigma'} \frac{g_{\sigma\sigma'}}{2} |\phi_\sigma|^2 |\phi_{\sigma'}|^2 \quad (1)$$

, where δ is the coupling detuning and Ω the Rabi coupling strength. The ground state is found upon minimization of the energy with respect to the internal state. The first term fixes the relative phase of the spinor that we can thus write $(\phi_\uparrow, \phi_\downarrow) = \sqrt{n}(\sin(\theta/2), \cos(\theta/2))$ with $\theta \in [0, \pi]$. The energy is then

$$\frac{E_{MF}}{N} = -\frac{\hbar\Omega}{2}\sin\theta - \frac{\hbar\delta}{2}\cos\theta + \frac{gn}{2} - \frac{\Delta g n}{4}\cos\theta - \frac{\bar{g}n}{2}\sin^2\theta, \quad (2)$$

where N is the total atom number, $g = (g_{\uparrow\uparrow} + g_{\downarrow\downarrow})/2$, $\Delta g = g_{\uparrow\uparrow} - g_{\downarrow\downarrow}$, and $\bar{g} = (g_{\uparrow\uparrow} + g_{\downarrow\downarrow} - 2g_{\uparrow\downarrow})/4$.

The minimization of Eq 2 as a function of θ gives the following implicit equation for the spin composition

$$\cot\theta = \frac{\delta}{\Omega} + \alpha - 2\gamma\cos\theta, , \quad (3)$$

where $\alpha = \frac{\Delta g n}{2\hbar\Omega}$ and $\gamma = \frac{\bar{g}n}{\hbar\Omega}$. The spin magnetization and, equivalently, the mixing angle θ thus depend not only on δ/Ω but also on the density n. For $\alpha \ll 1$ and $\gamma \ll 1$, the deviation can be calculated at the first order in perturbation. It was experimentally observed [14]. At the same order in perturbation, we find two- and three-body corrections on the interaction energy, generalizing the results from [13] to the asymmetric case

$$\frac{E_{MF}}{N} \approx \epsilon_- + g_2\frac{n}{2} + g_3\frac{n^2}{3} \quad (4)$$

$$\text{with } \epsilon_- = -\hbar\sqrt{\Omega^2 + \delta^2}/2,$$

$$g_2 = g - \frac{\bar{g}}{1 + \delta^2/\Omega^2} - \frac{\Delta g}{2}\frac{\delta/\Omega}{\sqrt{1 + \delta^2/\Omega^2}},$$

$$g_3 = -\frac{3\bar{g}^2}{\hbar\Omega}\frac{\delta^2/\Omega^2}{(1 + \delta^2/\Omega^2)^{5/2}} + \frac{3\bar{g}\Delta g\delta/\Omega}{2\hbar\Omega\,(1 + \delta^2/\Omega^2)^2} - \frac{3\Delta g^2}{16\hbar\Omega\,(1 + \delta^2/\Omega^2)^{3/2}}.$$

ϵ_- is the one-body energy of the lower-dressed state $|-\rangle$. The two-body coupling constant $g_2(\delta/\Omega)$ corresponds to the interaction between two atoms in $|-\rangle$. It interpolates between $g_{\uparrow\uparrow}$ and $g_{\downarrow\downarrow}$, reaching intermediately a minimum $g_{\min}$ if the experimentally relevant case $a_{\uparrow\downarrow} < a_{\uparrow\uparrow}, a_{\downarrow\downarrow}$. This two-body term was experimentally measured in [11]. The three-body coupling constant $g_3(\delta/\Omega, \Omega)$ scales as $1/\Omega$ and was also experimentally demonstrated [13].

We now consider the non-pertubative case where the interactions are not small as compared to Ω corresponding to $\gamma \gtrsim 1$. Then we should numerically solve Eq. 3, and insert the result in Eq. 2. In Fig. 1, we plot the mean field interaction energy per particle $E_{\rm int}/N = (E_{\rm MF}(n)/N - \epsilon_-)$ as a function of the parameter γ for a detuning $\delta/\Omega = 1$ and for scattering lengths that are relevant to our experiment with ^{39}K. We observe that the interaction energy first grows linearly with the density because of a positive coupling constant in the dressed state. Then it bends because of attractive three-body interactions g_3. When γ further increases, the energy per particle tends to saturate. A Taylor expansion as a function of density is no longer valid for large γ. In fact, in the limit $\gamma \gg 1$, the system minimizes its energy by choosing the condensate spin state corresponding to a minimal interaction $\cos\theta = \alpha/2\gamma = \Delta g/4\bar{g}$ and a pure two-body interaction is recovered with the coupling constant $g_{\min}$. In the case $a_{\uparrow\downarrow} = -\sqrt{a_{\uparrow\uparrow}a_{\downarrow\downarrow}}$, $g_{\min} = 0$ and the condensate in the dressed state has an interaction energy that saturates to a constant value.

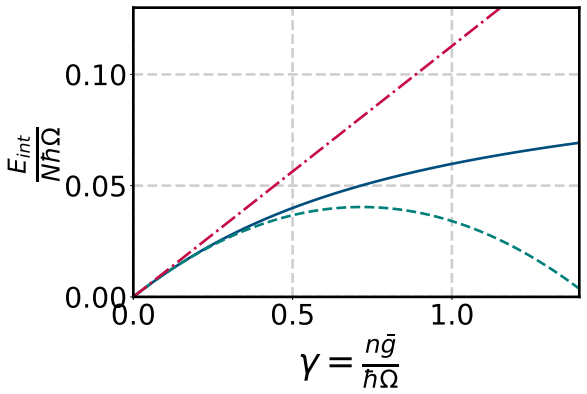


FIG. 1. Interaction energy per particle $E_{\rm int}/N = (E_{\rm MF}/N - \epsilon_-)$ as a function of γ. The specific parameters are $\delta/\Omega = 1$, $a_{\uparrow\uparrow} = 86.4\,a_0$, $a_{\downarrow\downarrow} = 33.2\,a_0$, and $a_{\uparrow\downarrow} = -53.2\,a_0$, where a_0 is the atomic Bohr radius. The solid blue curve is the exact mean-field calculation, the dash-dot red line is the linear two-body results, and the dash green curve is the quadratic two- plus three-body approximation (Eq. 4.

The previous results can be experimentally investigated by modifying Ω in order to change γ over a significant range. In Fig. 2, we thus plot the interaction energy as a function of δ/Ω for different values of γ assuming an homogeneous density n. For small values of γ, the energy is only weakly modified by non-linear effects, whereas for $\gamma \gtrsim 1$, the effect is large. The saturation of the interaction energy at large γ appears as an enlargement of the interaction energy drop as a function of δ/Ω. In particular, for $\gamma \gg 11$, the width of the dip increases linearly with γ. Note that in this regime, the Taylor expansion up to three-body interaction is very wrong. Even for $\gamma = 1$ (blue dashed curve in Fig. 2, it would lead to negative mean-field energies although the interaction energy is always positive for the chosen scattering lengths.

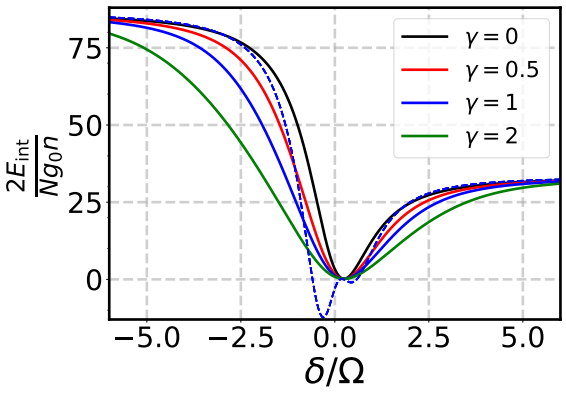


FIG. 2. Interaction energy per particle as a function of the detuning δ/Ω for different values of γ. The scattering lengths are the same as in Fig. 1. The interaction energy is normalized such that it gives the scattering length in unit of a_0 in the regime where the interactions are two-body ($g_0 = 4\pi\hbar^2 a_0/m$). The bare scattering length $a_{\uparrow\uparrow}$ and $a_{\downarrow\downarrow}$ are thus found for large values of $|\delta/\Omega|$. The solid lines corresponds to the exact mean-field calculation for different values of γ. The blue dashed-line corresponds to the two- plus three-body approximation given by Eq. 4.

III. EXPERIMENTAL RESULTS AND ADJUSTMENT

The experiment starts with a ^{39}K Bose-Einstein condensate with $N = 1.3 \times 10^5$ atoms in the $|F = 1, m_F = -1\rangle = |\downarrow\rangle$ spin state in a crossed optical dipole trap with oscillation frequencies $167 \times 167 \times 26$ Hz. The coupling to the state $|F = 1, m_F = 0\rangle = |\uparrow\rangle$ is performed through a radio frequency (RF) field. The magnetic field $B = 56.82$ G is chosen so that the scattering lengths are $a_{\uparrow\uparrow} = 84.3\,, a_{\downarrow\downarrow} = 33.3\,, a_{\uparrow\downarrow} = -53.2\,,$ where a_0 is the atomic Bohr radius [15]. In short, the measurement idea is to first prepare the dressed state $|-\rangle$ and then monitor the longitudinal expansion of the cloud once the weak longitudinal confinement is removed. At long times of flight t, the expansion is ballistic and we can simply deduce the expansion energy from the relation $E_{\rm exp}/N = m\sigma^2/t^2/2$, where σ is the measured rms size of the cloud. For our condition, this expansion energy predominantly reflects the initial interaction energy as the initial kinetic energy is negligible (see below).

The experiment is repeated with different radio frequency powers or equivalently different Rabi coupling frequencies $\Omega/2\pi$ between 0.95 and 30 kHz. These values of Ω are chosen in order to explore both the regimes of weak ($\gamma \ll 1$) and strong ($\gamma \gtrsim 1$) non linear interaction. The measurements at 0.95 kHz Rabi frequency are made possible by a precise control of the detuning δ down to $\sim$100 Hz. This level of control requires a ppm magnetic field stability and is obtained thanks to a feedforward compensation of both the current in the bias coils and of the external magnetic field [16].

The dressed state $|-\rangle$ is prepared with an adiabatic passage technique from the state $|\downarrow\rangle$. The RF detuning is linearly swept from 9Ω to the desired final value δ. The total sweep time τ =9 ms is chosen in order to be adiabatic with respect to the spin degree of freedom even at the lowest Ω values. In addition, this time is sufficiently large as compared to $1/\omega_\perp$ such that the radial wavefunction can adiabatically adapt itself to the interaction change during the sweep[17].

In the longitudinal direction, the cloud dynamics is much slower and the interaction change because of the RF sweep can almost be considered as a sudden quench. This approximation is not strictly true. If the RF sweep is done with (resp. without) the longitudinal trap on, the atomic cloud starts to slightly shrink (resp. expands). We reduce this residual effect by adjusting the time at which the longitudinal trap is turned off during the RF sweep. The most appropriate time does depend on the final value of δ/Ω and also on Ω (through the high non-linear effects). Since the additional kinetic energy is only relevant when the interaction energy is small, i.e. for $\delta/\Omega \approx 0.24$, where $a_- \approx 0$. We thus adjust the trap extinction time at this point for each value of Ω. In practice, this is done by looking at the minimal longitudinal expansion at a long time of flight of 300 ms. We find that the proper extinction time varies from 0.5 ms before the end of the sweep for large Ω to 5 ms before for $\Omega \approx 1$ kHz. The precision of this adjustment permits us to reduce the initial kinetic energy per particle to below 6 Hz, a negligible quantity as compared to the measured interaction energies.

In Fig. 3, we plot the rms size of the condensate (from a Gaussian fit) after a time of fight $t = 62.6$ ms as a function of δ/Ω and for different values of Ω. Each data set shows a minimum around the value $\delta/\Omega \approx 0.24$ where the two-body coupling constant g_2 in the $|-\rangle$ dressed state is minimum. For large and positive δ/Ω, the expansion corresponds to the one of the condensate in $|\downarrow\rangle$ with the scattering length $a_{\downarrow\downarrow}$. For large and negative δ/ω, the expansion is even faster, as the scattering length $a_{\uparrow\uparrow}$ is larger. A striking feature is that the width of the expansion drop is significantly larger as Ω decreases. This behavior qualitatively follows the theoretical expectation from Fig. 2 although the initial density is not homogeneous. Even without quantitative analysis, we can thus say that in our experiment the strongly non-linear regime corresponding to $\gamma \gtrsim 1$ is reached.

Let us turn to a more quantitative analysis with a numerical simulation of the experimental situation. We have to take into account that the nature of the confinement changes depending on the parameters. Around the expansion minimum, the interaction energy is small and the condensate is in a quasi-1D regime (the radial wavefunction is close the trap radial ground state). In contrast, for large $|\delta/\Omega|$ and for the initial condensate, the interactions are stronger and the condensate is effectively 3D. In order to account for these behaviors, we numeri-

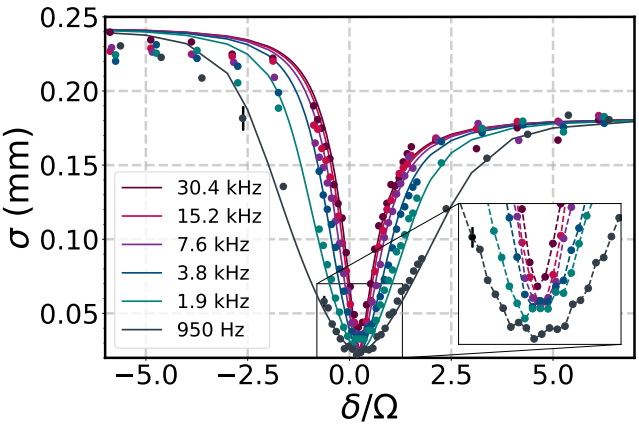


FIG. 3. Size after expansion of condensates in the $|-\rangle$ dressed state as a function of the detuning δ/Ω and for different value of Ω (see legend). The points correspond to the experimental measurements and some typical error bars are shown. In the main graph, the solid line corresponds to the mean-field numerical simulation as described below. At $\delta/\Omega \approx 0.24$, the two-body scattering length is already minimal and all theoretical curves are superimposed. The inset shows an enlargement of the experimental data at low $\delta//\Omega$. The points are linked by dashed lines for clarity. The theoretical lines are omitted in the inset because the theoretical model does not capture the vertical offsets between the curves (see text).

cally calculate the radial profile of the spinor condensate wavefunction when the interactions are modified during the sweep. This is done in a spinor Gross-Pitaevski simulation. In this framework, the previously discussed mean-field effects giving rise to the saturating interactions in the equation of states are naturally included.

In more detail, we assume an adiabatic following of the radial wavefunction and thus search for the radial ground state as a function of the 1D density. This is done through 2D Gross-Pitaevski simulations of the spinor wavefunction in imaginary time using the GPELab toolbox [18]. We then calculate the total energy $E_{\rm tot}$, which includes potential, kinetic and interaction contributions. Finally, we integrate the energy along the longitudinal trap direction, assuming that the density profile is the one of the initial condensate, i.e. a 3D Thomas-Fermi profile at rest. After a significant expansion, the mean kinetic energy per particle can be estimated from $m\sigma^2/2t^2$ and corresponds to $E_{\rm tot}/N - \hbar\omega_\perp/2 - \epsilon_0$, where the two last terms come from the fact that the condensate adiabatically evolves to the non-interacting spinor ground state (with energy ϵ_0) and to the radial ground state during expansion (with energy $\hbar\omega_\perp/2$).

With the above procedure, we are able to reproduce the experimental results without any fitting parameter. The results for large $|\delta/\Omega|$ are well reproduced. The slightly smaller size at large and negative δ/Ω can be attributed to the $\sim$ 20% losses that are experimentally observed and are due to three-body recombination processes. A smaller atom number reduces the interaction energy as compared to the simulation where no losses are included. The width of the minimum expansion drop as a function of Ω is also well reproduced, showing that the saturation of the mean-field interaction energy is well captured.

Looking carefully at the experimental results, one can notice that the observed minimum size (at $\delta/\Omega \approx 0.24$ is higher when Ω increases (see inset in Fig. 3). This behavior is not reproduced in the above mean-field approach, where, at this point, the interaction corresponds to a pure two-body interaction with a scattering length $a_{\rm min}$, that is independent of Ω. We attribute this behavior to beyond mean field effects due to virtual excitations to the $|+\rangle$ states, leading to a slight increase of the minimal interaction energy when Ω increases [12, 19]. In the context of this paper, we do not focus on this residual energy shift as its magnitude is much lower than the dominant mean-field effects studied above and its quantitative measurement would require an improved precision.

IV. CONCLUSION

In this paper, we have shown that the shape equation of state of a coherently driven spinor condensate can be tuned. For some parameters, the interaction term evolves from two-body repulsive interaction at low densities, through a regime that can be described with additional three-body interaction at intermediate density, to yet another regime of two-body interaction with a reduced two-body constant at large density. This second two-body interaction can be either positive or negative, depending of the involved spin-dependent scattering lengths. If this second two-body scattering length is close to zero (as in our work), it leads to an equation of state with a saturating interaction as a function of the density.

Our findings open the way to novel non-linear effects in the physics of condensates. Already, at equilibrium, we anticipate density profiles that differ from the usual Thomas-Fermi profiles. The condensate excitation dynamics (vortices, solitons, low energy excitation modes) will also be modified. In our configuration, the speed of sound decreases at high densities, in contrast to the usual behavior for a Bose-Einstein condensate with repulsive interactions.

ACKNOWLEDGMENTS

This research was supported by CNRS, Ministère de l'Enseignement Supérieur et de la Recherche, Quantum Paris-Saclay, Région Ile-de-France in the framework of Domaine d'Intérêt Majeur Quantip (H3B), France 2030 in the framework of PEPR Quantique (ANR-23-PETQ-0001), the Simons Foundation (Award No. 563916, localization of waves), France and Chicago collaborating in the sciences.

[1] S. H. Strogatz, *Nonlinear Dynamics and Chaos: With Applications to Physics, Biology, Chemistry, and Engineering*, 3rd ed. (CRC Press, Boca Raton, FL, 2024) p. 616.

[2] Y.-R. Shen, *The Principles of Nonlinear Optics* (Wiley-Interscience, New York, 1984).

[3] R. W. Boyd, *Nonlinear Optics*, 4th ed. (Academic Press, 2020).

[4] P. Pitaevskii, Lev and S. Stringari, *Bose–Einstein Condensation* (Clarendon Press, Oxford Univ. Press, Oxford, UK, 2003) p. 382.

[5] T. D. Lee, K. Huang, and C. N. Yang, Eigenvalues and eigenfunctions of a bose system of hard spheres and its low-temperature properties, Physical Review **106**, 1135 (1957).

[6] D. S. Petrov, Quantum mechanical stabilization of a collapsing bose–bose mixture, Physical Review Letters **115**, 155302 (2015).

[7] C. R. Cabrera, L. Tanzi, J. Sanz, B. Naylor, P. Thomas, P. Cheiney, and L. Tarruell, Quantum liquid droplets in a mixture of bose–einstein condensates, Science **359**, 301 (2018).

[8] E. Braaten and A. Nieto, Renormalization effects in a dilute bose gas, Phys. Rev. B **55**, 8090 (1997).

[9] T. Köhler, Three-body problem in a dilute Bose-Einstein condensate, Phys. Rev. Lett. **89**, 210404 (2002).

[10] P. M. A. Mestrom, V. E. Colussi, T. Secker, and S. J. J. M. F. Kokkelmans, Scattering hypervolume for ultracold bosons from weak to strong interactions, Phys. Rev. A **100**, 050702 (2019).

[11] J. Sanz, A. Frölian, C. S. Chisholm, C. R. Cabrera, and L. Tarruell, Interaction control and bright solitons in coherently-coupled bose–einstein condensates, Physical Review Letters **128**, 013201 (2022).

[12] S. Tiengo, R. Eid, and T. Bourdel, Three-body interactions in rabi-coupled bose gases: A perturbative approach, Phys. Rev. A **111**, 053319 (2025).

[13] A. Hammond, L. Lavoine, and T. Bourdel, Tunable three-body interactions in driven two-component bose-einstein condensates, Phys. Rev. Lett. **128**, 083401 (2022).

[14] A. Farolfi, A. Zenesini, R. Cominotti, D. Trypogeorgos, A. Recati, G. Lamporesi, and G. Ferrari, Manipulation of an elongated internal josephson junction of bosonic atoms, Phys. Rev. A **104**, 023326 (2021).

[15] E. Tiemann, P. Gersema, K. K. Voges, T. Hartmann, A. Zenesini, and S. Ospelkaus, Beyond born-oppenheimer approximation in ultracold atomic collisions, Phys. Rev. Res. **2**, 013366 (2020).

[16] S. Tiengo, R. Eid, M. Apfel, G. Brulin, and T. Bourdel, A simple magnetic field stabilization technique for atomic bose-einstein condensate experiments, Review of Scientific Instruments **96**, 063201 (2025).

[17] This is not strictly the case in particular for negative δ where residual radial oscillations have been observed after the sweep. However, we estimate that these radial oscillations do not significantly affect our longitudinal expansion results.

[18] X. Antoine and R. Duboscq, Gpelab, a Matlab toolbox to solve gross–pitaevskii equations I: computation of stationary solutions, Computer Physics Communications **185**, 2969 (2014).

[19] L. Lavoine, A. Hammond, A. Recati, D. S. Petrov, and T. Bourdel, Beyond-mean-field effects in rabi-coupled two-component bose-einstein condensate, Phys. Rev. Lett. **127**, 203402 (2021).

Bibliography

[1] Max Planck. “Ueber das Gesetz der Energieverteilung im Normalspectrum”. *Annalen der Physik* 309 (1901), pp. 553–563.

[2] A. Einstein. “Über einen die Erzeugung und Verwandlung des Lichtes betreffenden heuristischen Gesichtspunkt”. *Annalen der Physik* 322 (1905), pp. 132–148.

[3] Arthur H. Compton. “A Quantum Theory of the Scattering of X-rays by Light Elements”. *Physical Review* 21 (1923), pp. 483–502.

[4] N. Bohr. “I. On the constitution of atoms and molecules”. *The London, Edinburgh, and Dublin Philosophical Magazine and Journal of Science* 26 (1913), pp. 1–25.

[5] Louis de Broglie. “Recherches sur la théorie des Quanta”. PhD thesis. Migration - université en cours d’affectation, 1924.

[6] W. Heisenberg. “Über quantentheoretische Umdeutung kinematischer und mechanischer Beziehungen.” *Zeitschrift für Physik* 33 (1925), pp. 879–893.

[7] Max Born and Pascual Jordan. “7. Zur Quantenmechanik”. *Wellenmechanik*. De Gruyter, 2022, pp. 210–237.

[8] E. Schrödinger. “Quantisierung als Eigenwertproblem”. *Annalen der Physik* 384 (1926), pp. 361–376.

[9] W. Heisenberg. “Über den anschaulichen Inhalt der quantentheoretischen Kinematik und Mechanik”. *Zeitschrift für Physik* 43 (1927), pp. 172–198.

[10] N. Bohr. “The Quantum Postulate and the Recent Development of Atomic Theory1”. *Nature* 121 (1928), pp. 580–590.

[11] P. A. M. Dirac and J. C. Polkinghorne. “The Principles of Quantum Mechanics”. *Physics Today* 11 (1958), pp. 32–33.

[12] Walther Gerlach and Otto Stern. “Der experimentelle Nachweis der Richtungsquantelung im Magnetfeld”. *Zeitschrift für Physik* 9 (1922), pp. 349–352.

[13] W. Pauli. “Über den Zusammenhang des Abschlusses der Elektronengruppen im Atom mit der Komplexstruktur der Spektren”. *Zeitschrift für Physik* 31 (1925), pp. 765–783.

[14] G. E. Uhlenbeck and S. Goudsmit. “Spinning Electrons and the Structure of Spectra”. *Nature* 117 (1926), pp. 264–265.

[15] Carl D. Anderson. “The Positive Electron”. *Physical Review* 43 (1933), pp. 491–494.

[16] A. Einstein, B. Podolsky, and N. Rosen. “Can Quantum-Mechanical Description of Physical Reality Be Considered Complete?” *Physical Review* 47 (1935), pp. 777–780.

[17] J. S. Bell. “On the Einstein Podolsky Rosen paradox”. *Physics Physique Fizika* 1 (1964), pp. 195–200.

[18] Alain Aspect, Jean Dalibard, and Gérard Roger. “Experimental Test of Bell’s Inequalities Using Time-Varying Analyzers”. *Physical Review Letters* 49 (1982), pp. 1804–1807.

[19] H. Kamerlingh Onnes. “Further experiments with liquid helium. C. On the change of electric resistance of pure metals at very low temperatures etc. IV. The resistance of pure mercury at helium temperatures”. *Koninklijke Nederlandse Akademie van Wetenschappen Proceedings Series B Physical Sciences* 13 (1910), pp. 1274–1276.

[20] J. Bardeen, L. N. Cooper, and J. R. Schrieffer. “Microscopic Theory of Superconductivity”. *Physical Review* 106 (1957), pp. 162–164.

[21] J. Bardeen, L. N. Cooper, and J. R. Schrieffer. “Theory of Superconductivity”. *Physical Review* 108 (1957), pp. 1175–1204.

[22] W. Meissner and R. Ochsenfeld. “Ein neuer Effekt bei Eintritt der Supraleitfähigkeit”. *Naturwissenschaften* 21 (1933), pp. 787–788.

[23] P. Kapitza. “Viscosity of Liquid Helium below the lambda-Point”. *Nature* 141 (1938), pp. 74–74.

[24] J. F. Allen and A. D. Misener. “Flow of Liquid Helium II”. *Nature* 141 (1938), pp. 75–75.

[25] D. D. Osheroff, R. C. Richardson, and D. M. Lee. “Evidence for a New Phase of Solid ${\mathrm{He}}^{3}$”. *Physical Review Letters* 28 (1972), pp. 885–888.

[26] L. Onsager. “Statistical hydrodynamics”. *Il Nuovo Cimento (1943-1954)* 6 (1949), pp. 279–287.

[27] G. W. Rayfield and F. Reif. “Quantized Vortex Rings in Superfluid Helium”. *Physical Review* 136 (1964), A1194–A1208.

[28] K. v. Klitzing, G. Dorda, and M. Pepper. “New Method for High-Accuracy Determination of the Fine-Structure Constant Based on Quantized Hall Resistance”. *Physical Review Letters* 45 (1980), pp. 494–497.

[29] D. C. Tsui, H. L. Stormer, and A. C. Gossard. “Two-Dimensional Magnetotransport in the Extreme Quantum Limit”. *Physical Review Letters* 48 (1982), pp. 1559–1562.

[30] M. H. Anderson, J. R. Ensher, M. R. Matthews, C. E. Wieman, and E. A. Cornell. “Observation of Bose-Einstein Condensation in a Dilute Atomic Vapor”. *Science* 269 (1995), pp. 198–201.

[31] E. A. Cornell and C. E. Wieman. “Nobel Lecture: Bose-Einstein condensation in a dilute gas, the first 70 years and some recent experiments”. *Reviews of Modern Physics* 74 (2002), pp. 875–893.

[32] K. B. Davis, M. -O. Mewes, M. R. Andrews, N. J. van Druten, D. S. Durfee, D. M. Kurn, and W. Ketterle. “Bose-Einstein Condensation in a Gas of Sodium Atoms”. *Physical Review Letters* 75 (1995), pp. 3969–3973.

[33] C. C. Bradley, C. A. Sackett, J. J. Tollett, and R. G. Hulet. “Evidence of Bose-Einstein Condensation in an Atomic Gas with Attractive Interactions”. *Physical Review Letters* 75 (1995), pp. 1687–1690.

[34] Dale G. Fried, Thomas C. Killian, Lorenz Willmann, David Landhuis, Stephen C. Moss, Daniel Kleppner, and Thomas J. Greytak. “Bose-Einstein Condensation of Atomic Hydrogen”. *Physical Review Letters* 81 (1998), pp. 3811–3814.

[35] G. Roati, M. Zaccanti, C. D’Errico, J. Catani, M. Modugno, A. Simoni, M. Inguscio, and G. Modugno. “$^{39}\mathrm{K}$ Bose-Einstein Condensate with Tunable Interactions”. *Physical Review Letters* 99 (2007), p. 010403.

[36] M. H. T. Extavour, L. J. LeBlanc, T. Schumm, B. Cieslak, S. Myrskog, A. Stummer, S. Aubin, and J. H. Thywissen. “Dual-Species Quantum Degeneracy of 40K and 87Rb on an Atom Chip”. *AIP Conference Proceedings* 869 (2006), pp. 241–249.

[37] Tino Weber, Jens Herbig, Michael Mark, Hanns-Christoph Nägerl, and Rudolf Grimm. “Bose-Einstein Condensation of Cesium”. *Science* 299 (2003), pp. 232–235.

[38] Axel Griesmaier, Jörg Werner, Sven Hensler, Jürgen Stuhler, and Tilman Pfau. “Bose-Einstein Condensation of Chromium”. *Physical Review Letters* 94 (2005), p. 160401.

[39] Simon Stellmer, Meng Khoon Tey, Bo Huang, Rudolf Grimm, and Florian Schreck. “Bose-Einstein Condensation of Strontium”. *Physical Review Letters* 103 (2009), p. 200401.

[40] Sebastian Kraft, Felix Vogt, Oliver Appel, Fritz Riehle, and Uwe Sterr. “Bose-Einstein Condensation of Alkaline Earth Atoms: $^{40}\mathrm{Ca}$”. *Physical Review Letters* 103 (2009), p. 130401.

[41] Takeshi Fukuhara, Seiji Sugawa, and Yoshiro Takahashi. “Bose-Einstein condensation of an ytterbium isotope”. *Physical Review A* 76 (2007), p. 051604.

[42] *Ashcroft Solid State*. 848 pp.

[43] L. D. Landau and E. M. Lifshitz. *Fluid Mechanics: Volume 6*. Elsevier, 2013. 549 pp.

[44] Francis F. Chen. *Introduction to Plasma Physics and Controlled Fusion*. 3rd. Vol. 1. Springer, 2016.

[45] Samuel S. M. Wong. *Introductory Nuclear Physics*. John Wiley & Sons, 1998. 480 pp.

[46] Stuart L. Shapiro and Saul A. Teukolsky. *Black holes, white dwarfs and neutron stars. The physics of compact objects*. 1983.

[47] C.J. Pethick and H. Smith. *Bose-Einstein Condensation in Dilute Gases*. 2nd. Cambridge University Press, 2008.

[48] Cheng Chin, Rudolf Grimm, Paul Julienne, and Eite Tiesinga. "Feshbach resonances in ultracold gases". *Reviews of Modern Physics* 82 (2010), pp. 1225–1286.

[49] Kevin E. Strecker, Guthrie B. Partridge, Andrew G. Truscott, and Randall G. Hulet. "Formation and propagation of matter-wave soliton trains". *Nature* 417 (2002), pp. 150–153.

[50] L. Khaykovich, F. Schreck, G. Ferrari, T. Bourdel, J. Cubizolles, L. D. Carr, Y. Castin, and C. Salomon. "Formation of a Matter-Wave Bright Soliton". *Science* 296 (2002), pp. 1290–1293.

[51] S. Burger, K. Bongs, S. Dettmer, W. Ertmer, K. Sengstock, A. Sanpera, G. V. Shlyapnikov, and M. Lewenstein. "Dark Solitons in Bose-Einstein Condensates". *Physical Review Letters* 83 (1999), pp. 5198–5201.

[52] J. Denschlag, J. E. Simsarian, D. L. Feder, Charles W. Clark, L. A. Collins, J. Cubizolles, L. Deng, E. W. Hagley, K. Helmerson, W. P. Reinhardt, S. L. Rolston, B. I. Schneider, and W. D. Phillips. "Generating Solitons by Phase Engineering of a Bose-Einstein Condensate". *Science* 287 (2000), pp. 97–101.

[53] J. Sanz, A. Frölian, C. S. Chisholm, C. R. Cabrera, and L. Tarruell. "Interaction Control and Bright Solitons in Coherently Coupled Bose-Einstein Condensates". *Physical Review Letters* 128 (2022), p. 013201.

[54] A. Romero-Ros, G. C. Katsimiga, S. I. Mistakidis, S. Mossman, G. Biondini, P. Schmelcher, P. Engels, and P. G. Kevrekidis. "Experimental Realization of the Peregrine Soliton in Repulsive Two-Component Bose-Einstein Condensates". *Physical Review Letters* 132 (2024), p. 033402.

[55] Cheng-An Chen and Chen-Lung Hung. "Observation of Scale Invariance in Two-Dimensional Matter-Wave Townes Solitons". *Physical Review Letters* 127 (2021), p. 023604.

[56] T. D. Lee, Kerson Huang, and C. N. Yang. "Eigenvalues and eigenfunctions of a Bose system of hard spheres and its low-temperature properties". *Physical Review* 106 (1957), pp. 1135–1145.

[57] L. Landau. "On the Theory of Superfluidity". *Physical Review* 75 (1949), pp. 884–885.

[58] Nir Navon, Swann Piatecki, Kenneth Günter, Benno Rem, Trong Canh Nguyen, Frédéric Chevy, Werner Krauth, and Christophe Salomon. "Dynamics and Thermodynamics of the Low-Temperature Strongly Interacting Bose Gas". *Physical Review Letters* 107 (2011), p. 135301.

[59] C. R. Cabrera, L. Tanzi, J. Sanz, B. Naylor, P. Thomas, P. Cheiney, and L. Tarruell. "Quantum liquid droplets in a mixture of Bose–Einstein condensates". *Science* 359 (2018), pp. 301–304.

[60] L. Lavoine, A. Hammond, A. Recati, D. S. Petrov, and T. Bourdel. "Beyond-Mean-Field Effects in Rabi-Coupled Two-Component Bose-Einstein Condensate". *Phys. Rev. Lett.* 127 (2021), p. 203402.

[61] A. Hammond, L. Lavoine, and T. Bourdel. "Tunable Three-Body Interactions in Driven Two-Component Bose-Einstein Condensates". *Phys. Rev. Lett.* 128 (8 2022), p. 083401.

[62] R. Eid, A. Hammond, L. Lavoine, and T. Bourdel. "Ultracold-atom quantum tunneling through single and double optical barriers". *Physical Review A* 110 (2024), p. 043316.

[63] S. Tiengo, R. Eid, M. Apfel, G. Brulin, and T. Bourdel. "A simple magnetic field stabilization technique for atomic Bose-Einstein condensate experiments". *Review of Scientific Instruments* 96 (2025), p. 063201.

[64] L. H. Thomas. "The Motion of the Spinning Electron". *Nature* 117 (1926), pp. 514–514.

[65] T. G. Tiecke. "Properties of Potassium". 2011.

[66] A. A. Michelson. "APPLICATION OF INTERFERENCE METHODS TO SPECTROSCOPIC MEASUREMENT". *Publications of the Astronomical Society of the Pacific* 4 (1892), p. 190.

[67] A. J. Kox. "The discovery of the electron: II. The Zeeman effect". *European Journal of Physics* 18 (1997), p. 139.

[68] G. Breit and I. I. Rabi. "Measurement of Nuclear Spin". *Physical Review* 38 (1931), pp. 2082–2083.

[69] Klaus Hentschel. "Paschen—Back Effect". *Compendium of Quantum Physics*. Ed. by Daniel Greenberger, Klaus Hentschel, and Friedel Weinert. Berlin, Heidelberg: Springer, 2009, pp. 468–470.

[70] Zhu Ma, Chengyin Han, Zhi Tan, Haihua He, Shenzhen Shi, Xin Kang, Jiatao Wu, Jiahao Huang, Bo Lu, and Chaohong Lee. "Adaptive cold-atom magnetometry mitigating the trade-off between sensitivity and dynamic range". *Science Advances* 11 (2025), eadt3938.

[71] Jinyang Li, Gour Pati, Renu Tripathi, and Selim M. Shahriar. "Spin-squeezed vector atomic magnetometry" (2025).

[72] A. Einstein. "Quantentheorie des einatomigen idealen Gases". *Sitzungsberichte der Preußischen Akademie der Wissenschaften* (1925), pp. 3–14.

[73] Henry Margenau and N. R. Kestner. *Theory of Intermolecular Forces*. Pergamon Press, 1971. 420 pp.

[74] W. J. Mullin and G. Blaylock. "Quantum statistics: Is there an effective fermion repulsion or boson attraction?" *American Journal of Physics* 71 (2003), pp. 1223–1231.

[75] K.-K. Ni, S. Ospelkaus, D. J. Nesbitt, J. Ye, and D. S. Jin. "A dipolar gas of ultracold molecules". *Physical Chemistry Chemical Physics* 11 (2009), pp. 9626–9639.

[76] Claude Amiot, Jean Vergès, and Carlos E. Fellows. "The long-range potential of the K2 X 1+g ground electronic state up to 15 Å". *The Journal of Chemical Physics* 103 (1995), pp. 3350–3356.

[77] Guoxing Zhao, Warren T. Zemke, J. T. Kim, Bing Ji, H. Wang, J. T. Bahns, W. C. Stwalley, Li Li, A. M. Lyyra, and C. Amiot. "New measurements of the a3+u state of K2 and improved analysis of long-range dispersion and exchange interactions between two K atoms". *The Journal of Chemical Physics* 105 (1996), pp. 7976–7985.

[78] M. Born and R. Oppenheimer. "Zur Quantentheorie der Molekeln". *Annalen der Physik* 389 (1927), pp. 457–484.

[79] Stephan Falke, Horst Knöckel, Jan Friebe, Matthias Riedmann, Eberhard Tiemann, and Christian Lisdat. "Potassium ground-state scattering parameters and Born-Oppenheimer potentials from molecular spectroscopy". *Physical Review A* 78 (2008), p. 012503.

[80] Gabor Rutkai, Monika Thol, Roland Span, and Jadran Vrabec. "How well does the Lennard-Jones potential represent the thermodynamic properties of noble gases". *Molecular Physics* 115 (2017), pp. 1104–1121.

[81] Xipeng Wang, Simón Ramírez-Hinestrosa, Jure Dobnikar, and Daan Frenkel. "The Lennard-Jones potential: when (not) to use it". *Physical Chemistry Chemical Physics* 22 (2020), pp. 10624–10633.

[82] C. D'Errico, M. Zaccanti, M. Fattori, G. Roati, M. Inguscio, G. Modugno, and A. Simoni. "Feshbach resonances in ultracold ^{39}K". *New J. Phys.* 9 (2007), p. 223.

[83] Lev Petrovič Pitaevskij and Sandro Stringari. *Bose-Einstein condensation*. Updated edition. International series of monographs on physics. Oxford: Oxford university press, 2016.

[84] F. Gerbier. "Quasi-1D Bose-Einstein condensates in the dimensional crossover regime". *Europhysics Letters* 66 (2004), p. 771.

[85] S. Tiengo, R. Eid, and T. Bourdel. "Three-body interactions in Rabi-coupled Bose gases: A perturbative approach". *Phys. Rev. A* 111 (5 2025), p. 053319.

[86] Lauriane Fouche. "Gaz quantiques de potassium 39 à interactions contrôlables". These de doctorat. Palaiseau, Institut d'optique théorique et appliquée, 2015.

[87] Guillaume Berthet. "Désordre et interactions dans les gaz quantiques bosoniques". These de doctorat. Université Paris-Saclay (ComUE), 2019.

[88] Lucas Lavoine. "Mélange de spin dans un condensat de Bose-Einstein : Gouttelette quantique et couplage cohérent". These de doctorat. université Paris-Saclay, 2022.

[89] Alfred Hammond. “Collective effects in RF-dressed 39 potassium ultra-cold gases”. These de doctorat. université Paris-Saclay, 2023.

[90] Immanuel Bloch, Jean Dalibard, and Wilhelm Zwerger. “Many-body physics with ultracold gases”. *Reviews of Modern Physics* 80 (2008), pp. 885–964.

[91] Andrew D. Ludlow, Martin M. Boyd, Jun Ye, E. Peik, and P. O. Schmidt. “Optical atomic clocks”. *Reviews of Modern Physics* 87 (2015), pp. 637–701.

[92] A. Marte, T. Volz, J. Schuster, S. Dürr, G. Rempe, E. G. M. van Kempen, and B. J. Verhaar. “Feshbach Resonances in Rubidium 87: Precision Measurement and Analysis”. *Physical Review Letters* 89 (2002), p. 283202.

[93] L. Sárkány, P. Weiss, H. Hattermann, and J. Fortágh. “Controlling the magnetic-field sensitivity of atomic-clock states by microwave dressing”. *Physical Review A* 90 (2014), p. 053416.

[94] L. Lavoine, A. Hammond, A. Recati, D. S. Petrov, and T. Bourdel. “Beyond-Mean-Field Effects in Rabi-Coupled Two-Component Bose-Einstein Condensate”. *Physical Review Letters* 127 (2021), p. 203402.

[95] A. Hammond, L. Lavoine, and T. Bourdel. “Tunable Three-Body Interactions in Driven Two-Component Bose-Einstein Condensates”. *Physical Review Letters* 128 (2022), p. 083401.

[96] Arturo Farolfi, Dimitrios Trypogeorgos, Giacomo Colzi, Eleonora Fava, Giacomo Lamporesi, and Gabriele Ferrari. “Design and characterisation of a compact magnetic shield for ultracold atomic gas experiments”. *Review of Scientific Instruments* 90 (2019), p. 115114.

[97] C. J. Dedman, R. G. Dall, L. J. Byron, and A. G. Truscott. “Active cancellation of stray magnetic fields in a Bose-Einstein condensation experiment”. *The Review of Scientific Instruments* 78 (2007), p. 024703.

[98] Kangda Xiao, Li Wang, Jun Guo, Maohua Zhu, Xiuchao Zhao, Xianping Sun, Chaohui Ye, and Xin Zhou. “Quieting an environmental magnetic field without shielding”. *The Review of Scientific Instruments* 91 (2020), p. 085107.

[99] Xiao-Tian Xu, Zong-Yao Wang, Rui-Heng Jiao, Chang-Rui Yi, Wei Sun, and Shuai Chen. “Ultra-low noise magnetic field for quantum gases”. *The Review of Scientific Instruments* 90 (2019), p. 054708.

[100] Zhi-Xin Duan, Wei-Tao Wu, Yue-Tong Lin, and Sheng-Jun Yang. “Simple and active magnetic-field stabilization for cold atom experiments”. *The Review of Scientific Instruments* 93 (2022), p. 123201.

[101] B. Merkel, K. Thirumalai, J. E. Tarlton, V. M. Schäfer, C. J. Ballance, T. P. Harty, and D. M. Lucas. “Magnetic field stabilization system for atomic physics experiments”. *Review of Scientific Instruments* 90 (2019), p. 044702.

[102] Mateusz Borkowski, Lukas Reichsöllner, Premjith Thekkeppatt, Vincent Barbé, Tijs van Roon, Klaasjan van Druten, and Florian Schreck. "Active stabilization of kilogauss magnetic fields to the ppm level for magnetoassociation on ultranarrow Feshbach resonances". *The Review of Scientific Instruments* 94 (2023), p. 073202.

[103] Ryan Thomas and Niels Kjærgaard. "A digital PID controller for stabilizing large electric currents to the ppm level for Feshbach resonance studies". *Review of Scientific Instruments* 91 (2020), p. 034705.

[104] Steven H. Strogatz. *Nonlinear Dynamics and Chaos: With Applications to Physics, Biology, Chemistry, and Engineering*. 3rd. Boca Raton, FL: CRC Press, 2024, p. 616.

[105] Yuen-Ron Shen. *The Principles of Nonlinear Optics*. New York: Wiley-Interscience, 1984.

[106] Robert W. Boyd. *Nonlinear Optics*. 4th ed. Academic Press, 2020.

[107] D. S. Petrov. "Quantum mechanical stabilization of a collapsing Bose–Bose mixture". *Physical Review Letters* 115 (2015), p. 155302.

[108] E. Braaten and A. Nieto. "Renormalization effects in a dilute Bose gas". *Phys. Rev. B* 55 (13 1997), p. 8090.

[109] Thorsten Köhler. "Three-Body Problem in a Dilute Bose-Einstein Condensate". *Phys. Rev. Lett.* 89 (21 2002), p. 210404.

[110] P. M. A. Mestrom, V. E. Colussi, T. Secker, and S. J. J. M. F. Kokkelmans. "Scattering hypervolume for ultracold bosons from weak to strong interactions". *Phys. Rev. A* 100 (5 2019), p. 050702.

[111] A. Farolfi, A. Zenesini, R. Cominotti, D. Trypogeorgos, A. Recati, G. Lamporesi, and G. Ferrari. "Manipulation of an elongated internal Josephson junction of bosonic atoms". *Phys. Rev. A* 104 (2 2021), p. 023326.

[112] Igor Ferrier-Barbut, Holger Kadau, Matthias Schmitt, Matthias Wenzel, and Tilman Pfau. "Observation of Quantum Droplets in a Strongly Dipolar Bose Gas". *Physical Review Letters* 116 (2016), p. 215301.

[113] Matthias Schmitt, Matthias Wenzel, Fabian Böttcher, Igor Ferrier-Barbut, and Tilman Pfau. "Self-bound droplets of a dilute magnetic quantum liquid". *Nature* 539 (2016), pp. 259–262.

[114] L. Chomaz, S. Baier, D. Petter, M.J. Mark, F. Wächtler, L. Santos, and F. Ferlaino. "Quantum-Fluctuation-Driven Crossover from a Dilute Bose-Einstein Condensate to a Macrodroplet in a Dipolar Quantum Fluid". *Physical Review X* 6 (2016), p. 041039.

[115] G. Semeghini, G. Ferioli, L. Masi, C. Mazzinghi, L. Wolswijk, F. Minardi, M. Modugno, G. Modugno, M. Inguscio, and M. Fattori. "Self-Bound Quantum Droplets of Atomic Mixtures in Free Space". *Physical Review Letters* 120 (2018), p. 235301.

[116] C. D'Errico, A. Burchianti, M. Prevedelli, L. Salasnich, F. Ancilotto, M. Modugno, F. Minardi, and C. Fort. "Observation of quantum droplets in a heteronuclear bosonic mixture". *Physical Review Research* 1 (2019), p. 033155.

[117] Zhichao Guo, Fan Jia, Lintao Li, Yinfeng Ma, Jeremy M. Hutson, Xiaoling Cui, and Dajun Wang. "Lee-Huang-Yang effects in the ultracold mixture of $^{23}\mathrm{Na}$ and $^{87}\mathrm{Rb}$ with attractive interspecies interactions". *Physical Review Research* 3 (2021), p. 033247.

[118] D. S. Petrov and G. E. Astrakharchik. "Ultradilute Low-Dimensional Liquids". *Physical Review Letters* 117 (2016), p. 100401.

[119] Paweł Zin, Maciej Pylak, Tomasz Wasak, Mariusz Gajda, and Zbigniew Idziaszek. "Quantum Bose-Bose droplets at a dimensional crossover". *Physical Review A* 98 (2018), p. 051603.

[120] L. Tanzi, E. Lucioni, F. Famà, J. Catani, A. Fioretti, C. Gabbanini, R.N. Bisset, L. Santos, and G. Modugno. "Observation of a Dipolar Quantum Gas with Metastable Supersolid Properties". *Physical Review Letters* 122 (2019), p. 130405.

[121] Fabian Böttcher, Jan-Niklas Schmidt, Matthias Wenzel, Jens Hertkorn, Mingyang Guo, Tim Langen, and Tilman Pfau. "Transient Supersolid Properties in an Array of Dipolar Quantum Droplets". *Physical Review X* 9 (2019), p. 011051.

[122] Mingyang Guo, Fabian Böttcher, Jens Hertkorn, Jan-Niklas Schmidt, Matthias Wenzel, Hans Peter Büchler, Tim Langen, and Tilman Pfau. "The low-energy Goldstone mode in a trapped dipolar supersolid". *Nature* 574 (2019), pp. 386–389.

[123] Karima Abbas and Abdelâali Boudjemâa. "Quantum liquid droplets in Bose mixtures with weak disorder". *Physical Review A* 107 (2023), p. 033306.

[124] Yoshihiro Machida, Ippei Danshita, Daisuke Yamamoto, and Kenichi Kasamatsu. "Quantum droplet of a two-component Bose gas in an optical lattice near the Mott insulator transition". *Physical Review A* 105 (2022), p. L031301.

[125] Alessio Recati and Sandro Stringari. "Coherently Coupled Mixtures of Ultracold Atomic Gases". *Annual Review of Condensed Matter Physics* 13 (Volume 13, 2022 2022), pp. 407–432.

[126] Eberhard Tiemann, Philipp Gersema, Kai K. Voges, Torsten Hartmann, Alessandro Zenesini, and Silke Ospelkaus. "Beyond Born-Oppenheimer approximation in ultracold atomic collisions". *Physical Review Research* 2 (2020), p. 013366.

[127] Alexander L. Gaunt, Tobias F. Schmidutz, Igor Gotlibovych, Robert P. Smith, and Zoran Hadzibabic. "Bose-Einstein Condensation of Atoms in a Uniform Potential". *Physical Review Letters* 110 (2013), p. 200406.

[128] Y-Q Zou, É Le Cerf, B Bakkali-Hassani, C Maury, G Chauveau, P C M Castilho, R Saint-Jalm, S Nascimbene, J Dalibard, and J Beugnon. "Optical control of the density and spin spatial profiles of a planar Bose gas". *Journal of Physics B: Atomic, Molecular and Optical Physics* 54 (2021), 08LT01.

[129] Y. Wang, S. Subhankar, P. Bienias, M. Łącki, T-C. Tsui, M. A. Baranov, A. V. Gorshkov, P. Zoller, J. V. Porto, and S. L. Rolston. "Dark State Optical Lattice with a Subwavelength Spatial Structure". *Physical Review Letters* 120 (2018), p. 083601.

[130] Claude Cohen-Tannoudji, Franck Laloe, and Bernard Diu. *Mécanique Quantique - Tome 1: Nouvelle édition*. EDP sciences, 2018. 1115 pp.

[131] David J. Griffiths. *Introduction to Quantum Mechanics*. Pearson Prentice Hall, 1995.

[132] *Nobel Prize in Physics 1929*. NobelPrize.org.

[133] F. Hund. "Zur Deutung der Molekelspektren. I". *Zeitschrift für Physik* 40 (1927), pp. 742–764.

[134] Ralph Howard Fowler and L. Nordheim. "Electron emission in intense electric fields". *The Royal Society Publisher* 119 (1997), pp. 173–181.

[135] G. Gamow. "Zur Quantentheorie des Atomkernes". *Zeitschrift für Physik* 51 (1928), pp. 204–212.

[136] Hermann Rohmann. "Elektrische Ströme durch Vakuumstrecken". *Zeitschrift für Physik* 31 (1925), pp. 311–325.

[137] Leo Esaki. "New Phenomenon in Narrow Germanium $p\ensuremath{-}n$ Junctions". *Physical Review* 109 (1958), pp. 603–604.

[138] B. D. Josephson. "Possible new effects in superconductive tunnelling". *Physics Letters* 1 (1962), pp. 251–253.

[139] G. Binnig, H. Rohrer, Ch. Gerber, and E. Weibel. "Tunneling through a controllable vacuum gap". *Applied Physics Letters* 40 (1982), pp. 178–180.

[140] G. Binnig, H. Rohrer, Ch. Gerber, and E. Weibel. "Surface Studies by Scanning Tunneling Microscopy". *Physical Review Letters* 49 (1982), pp. 57–61.

[141] Chester P. Rubbo, Salvatore R. Manmana, Brandon M. Peden, Murray J. Holland, and Ana Maria Rey. "Resonantly enhanced tunneling and transport of ultracold atoms on tilted optical lattices". *Physical Review A* 84 (2011), p. 033638.

[142] Christian Gross and Immanuel Bloch. "Quantum simulations with ultracold atoms in optical lattices". *Science* 357 (2017), pp. 995–1001.

[143] Markus Greiner, Olaf Mandel, Tilman Esslinger, Theodor W. Hänsch, and Immanuel Bloch. "Quantum phase transition from a superfluid to a Mott insulator in a gas of ultracold atoms". *Nature* 415 (2002), pp. 39–44.

[144] Michael Albiez, Rudolf Gati, Jonas Fölling, Stefan Hunsmann, Matteo Cristiani, and Markus K. Oberthaler. "Direct Observation of Tunneling and Nonlinear Self-Trapping in a Single Bosonic Josephson Junction". *Physical Review Letters* 95 (2005), p. 010402.

[145] B. P. Anderson and M. A. Kasevich. "Macroscopic Quantum Interference from Atomic Tunnel Arrays". *Science* 282 (1998), pp. 1686–1689.

[146] W. M. Liu, W. B. Fan, W. M. Zheng, J. Q. Liang, and S. T. Chui. "Quantum Tunneling of Bose-Einstein Condensates in Optical Lattices under Gravity". *Physical Review Letters* 88 (2002), p. 170408.

[147] F. S. Cataliotti, S. Burger, C. Fort, P. Maddaloni, F. Minardi, A. Trombettoni, A. Smerzi, and M. Inguscio. "Josephson Junction Arrays with Bose-Einstein Condensates". *Science* 293 (2001), pp. 843–846.

[148] Samuel Häusler, Shuta Nakajima, Martin Lebrat, Dominik Husmann, Sebastian Krinner, Tilman Esslinger, and Jean-Philippe Brantut. "Scanning Gate Microscope for Cold Atomic Gases". *Physical Review Letters* 119 (2017), p. 030403.

[149] Fujio Shimizu. "Specular Reflection of Very Slow Metastable Neon Atoms from a Solid Surface". *Physical Review Letters* 86 (2001), pp. 987–990.

[150] C. M. Fabre, P. Cheiney, G. L. Gattobigio, F. Vermersch, S. Faure, R. Mathevet, T. Lahaye, and D. Guéry-Odelin. "Realization of a Distributed Bragg Reflector for Propagating Guided Matter Waves". *Physical Review Letters* 107 (2011), p. 230401.

[151] T. A. Pasquini, Y. Shin, C. Sanner, M. Saba, A. Schirotzek, D. E. Pritchard, and W. Ketterle. "Quantum Reflection from a Solid Surface at Normal Incidence". *Physical Review Letters* 93 (2004), p. 223201.

[152] Alexander D. Cronin, Jörg Schmiedmayer, and David E. Pritchard. "Optics and interferometry with atoms and molecules". *Reviews of Modern Physics* 81 (2009), pp. 1051–1129.

[153] T. A. Pasquini, M. Saba, G.-B. Jo, Y. Shin, W. Ketterle, D. E. Pritchard, T. A. Savas, and N. Mulders. "Low Velocity Quantum Reflection of Bose-Einstein Condensates". *Physical Review Letters* 97 (2006), p. 093201.

[154] A. L. Marchant, T. P. Billam, M. M. H. Yu, A. Rakonjac, J. L. Helm, J. Polo, C. Weiss, S. A. Gardiner, and S. L. Cornish. "Quantum reflection of bright solitary matter waves from a narrow attractive potential". *Physical Review A* 93 (2016), p. 021604.

[155] J. Billy, V. Josse, Z. Zuo, W. Guerin, A. Aspect, and P. Bouyer. "Guided atom laser: a new tool for guided atom optics". *Annales de Physique* 32 (2007), pp. 17–24.

[156] Ramón Ramos, David Spierings, Shreyas Potnis, and Aephraim M. Steinberg. "Atom-optics knife edge: Measuring narrow momentum distributions". *Physical Review A* 98 (2018), p. 023611.

[157] Ramón Ramos, David Spierings, Isabelle Racicot, and Aephraim M. Steinberg. "Measurement of the time spent by a tunnelling atom within the barrier region". *Nature* 583 (2020), pp. 529–532.

[158] A. M. Martin, R. G. Scott, and T. M. Fromhold. "Transmission and reflection of Bose-Einstein condensates incident on a Gaussian tunnel barrier". *Physical Review A* 75 (2007), p. 065602.

[159] P. Manju, K. S. Hardman, M. A. Sooriyabandara, P. B. Wigley, J. D. Close, N. P. Robins, M. R. Hush, and S. S. Szigeti. "Quantum tunneling dynamics of an interacting Bose-Einstein condensate through a Gaussian barrier". *Physical Review A* 98 (2018), p. 053629.

[160] Dusty R Lindberg, Naceur Gaaloul, Lev Kaplan, Jason R Williams, Dennis Schlippert, Patrick Boegel, Ernst-Maria Rasel, and Denys I Bondar. "Asymmetric tunneling of Bose–Einstein condensates". *Journal of Physics B: Atomic, Molecular and Optical Physics* 56 (2023), p. 025302.

[161] P. Manju, K. S. Hardman, P. B. Wigley, J. D. Close, N. P. Robins, and S. S. Szigeti. "An atomic Fabry–Perot interferometer using a pulsed interacting Bose–Einstein condensate". *Scientific Reports* 10 (2020), p. 15052.

[162] F. Nogrette, H. Labuhn, S. Ravets, D. Barredo, L. Béguin, A. Vernier, T. Lahaye, and A. Browaeys. "Single-Atom Trapping in Holographic 2D Arrays of Microtraps with Arbitrary Geometries". *Physical Review X* 4 (2014), p. 021034.

[163] Takeshi Fukuhara, Adrian Kantian, Manuel Endres, Marc Cheneau, Peter Schauß, Sebastian Hild, David Bellem, Ulrich Schollwöck, Thierry Giamarchi, Christian Gross, Immanuel Bloch, and Stefan Kuhr. "Quantum dynamics of a mobile spin impurity". *Nature Physics* 9 (2013), pp. 235–241.

[164] G. Gauthier, I. Lenton, N. McKay Parry, M. Baker, M. J. Davis, H. Rubinsztein-Dunlop, and T. W. Neely. "Direct imaging of a digital-micromirror device for configurable microscopic optical potentials". *Optica* 3 (2016), pp. 1136–1143.

[165] Nir Navon, Robert P. Smith, and Zoran Hadzibabic. "Quantum gases in optical boxes". *Nature Physics* 17 (2021), pp. 1334–1341.

[166] Mohammadamin Tajik, Bernhard Rauer, Thomas Schweigler, Federica Cataldini, João Sabino, Frederik S. Møller, Si-Cong Ji, Igor E. Mazets, and Jörg Schmiedmayer. "Designing arbitrary one-dimensional potentials on an atom chip". *Optics Express* 27 (2019), pp. 33474–33487.

[167] Li-Chung Ha, Logan W. Clark, Colin V. Parker, Brandon M. Anderson, and Cheng Chin. "Roton-Maxon Excitation Spectrum of Bose Condensates in a Shaken Optical Lattice". *Physical Review Letters* 114 (2015), p. 055301.

[168] *DLPS6500 Data sheet.*

[169] Rudolf Grimm, Matthias Weidemüller, and Yurii B. Ovchinnikov. "Optical Dipole Traps for Neutral Atoms". *Advances In Atomic, Molecular, and Optical Physics.* Ed. by Benjamin Bederson and Herbert Walther. Vol. 42. Academic Press, 2000, pp. 95–170.

[170] "Optical Resonance and Two Level Atoms. Von L. Allen und J. H. Eberly. Band XXVIII der Wiley Serie Interscience Monographs and Texts in Physics and Astronomy, John Wiley and Sons LTD, Chichester/Sussex, 1975, 233 Seiten, 11.95 £". *Physik in unserer Zeit* 7 (1976), pp. 31–32.

[171] Joseph W. Goodman. *Introduction to Fourier Optics*. Roberts and Company Publishers, 2005. 520 pp.

[172] Patrik Schach, Alexander Friedrich, Jason R. Williams, Wolfgang P. Schleich, and Enno Giese. "Tunneling gravimetry". *EPJ Quantum Technology* 9 (2022), pp. 1–19.

[173] A. Boissé, G. Berthet, L. Fouché, G. Salomon, A. Aspect, S. Lepoutre, and T. Bourdel. "Nonlinear scattering of atomic bright solitons in disorder". *Europhysics Letters* 117 (2017), p. 10007.

[174] Christoph Weiss and Yvan Castin. "Creation and Detection of a Mesoscopic Gas in a Nonlocal Quantum Superposition". *Physical Review Letters* 102 (2009), p. 010403.

[175] S. L. Cornish, N. G. Parker, A. M. Martin, T. E. Judd, R. G. Scott, T. M. Fromhold, and C. S. Adams. "Quantum reflection of bright matter-wave solitons". *Physica D: Nonlinear Phenomena*. Nonlinear Phenomena in Degenerate Quantum Gases 238 (2009), pp. 1299–1305.

[176] Piero Naldesi, Juan Polo, Peter D. Drummond, Vanja Dunjko, Luigi Amico, Anna Minguzzi, and Maxim Olshanii. "Massive particle interferometry with lattice solitons". *SciPost Physics* 15 (2023), p. 187.

[177] I. Carusotto. "Nonlinear atomic Fabry-Perot interferometer: From the mean-field theory to the atom blockade effect". *Physical Review A* 63 (2001), p. 023610.

université PARIS-SACLAY

ÉCOLE DOCTORALE
Ondes et matière (EDOM)

(English version)

Title: Tunable Mean-Field and Beyond Mean-Field Interaction in a Coherently Coupled Bose-Einstein Condensate

Keywords: Bose-Einstein Condensate, Dressed state, Coherent Coupling, Ultra-Cold Atoms Tunneling, Magnetic Field Stabilization, Quantum Droplet

Abstract: This thesis explores mean-field and beyond mean-field interactions in a coherently coupled two-component Bose-Einstein condensate (BEC) of ^{39}K atoms. We first establish the theoretical framework describing the atomic structure of potassium-39, interatomic interactions, and Feshbach resonances. We then introduce the mean-field and beyond mean-field theories relevant to ultracold Bose gases. In addition, we describe the physics of coherently coupled two-level systems, including radio-frequency coupling, adiabatic sweeps, and scattering lengths in the dressed-state basis. A major part of the experimental work focuses on developing a high-precision magnetic field stabilization system, essential for accurate and reliable measurements in spinor BECs. We investigate the mean-field interaction energy of a coherently coupled two-component BEC in the lower dressed-state basis, both theoretically and experimentally. The results reveal nonlinearities and saturation effects as functions of density. We then explore the regime of quantum droplets, aiming at observing self-bound states stabilized by quantum fluctuations beyond the mean-field approximation. Finally, we present an experiment on BEC tunneling through optical barriers created using a Digital Micromirror Device and a blue-detuned laser, demonstrating the transition from classical to quantum tunneling and revealing Fabry–Pérot-like interference in matter waves.

université PARIS-SACLAY

ÉCOLE DOCTORALE
Ondes et matière
(EDOM)

(Version Français)
Titre: Interaction Réglable de Champ Moyen et au-delà du Champ Moyen pour un Condensat de Bose-Einstein dans un mélange cohérent de spin
Mots-clés: Condensat de Bose-Einstein, État habillé, Couplage cohérent, Tunneling d'atomes ultra-froids, Stabilisation du champ magnétique, Gouttelette quantique

Résumé: Cette thèse explore les interactions de champ moyen et au-delà du champ moyen dans un condensat de Bose–Einstein (BEC) à deux composantes de ^{39}K couplées de manière cohérente. Nous établissons d'abord le cadre théorique décrivant la structure atomique du potassium-39, les interactions interatomiques et les résonances de Feshbach. Nous présentons ensuite les théories de champ moyen et les corrections au-delà du champ moyen pertinentes pour les gaz de Bose ultrafroids. Nous décrivons également la physique des systèmes à deux niveaux couplés de manière cohérente, y compris le couplage radiofréquence, les balayages adiabatiques et les longueurs de diffusion dans la base des états habillés. Une grande partie du travail expérimental porte sur le développement d'un système de stabilisation du champ magnétique à haute précision, essentiel pour des mesures fiables et précises dans un BEC à deux composantes. Nous étudions l'énergie d'interaction de champ moyen dans un BEC à deux composantes couplé de manière cohérente, préparé dans l'état habillé, à la fois théoriquement et expérimentalement. Les résultats révèlent des non-linéarités et des effets de saturation en fonction de la densité. Nous explorons ensuite le régime des gouttelettes quantiques, dans le but d'observer des états autoliés stabilisés par les fluctuations quantiques au-delà de l'approximation de champ moyen. Enfin, nous présentons une expérience de tunneling d'un BEC à travers des barrières optiques créées à l'aide d'un dispositif à micromiroirs numériques (DMD) et d'un laser désaccordé vers le bleu, démontrant la transition entre les régimes de l'effet tunnel classique et quantique, ainsi que l'apparition d'interférences de type Fabry–Pérot dans les ondes de matière.